PLASMA SURFACE ENGINEERING AND CHARACTERISATION OF BIOMEDICAL STAINLESS STEELS

by JOSEPH BUHAGIAR

A thesis submitted to

The University of Birmingham

for the degree of

DOCTOR OF PHILOSOPHY

School of Metallurgy and Materials

College of Engineering and Physical Sciences

The University of Birmingham

June 2008

Nor do I doubt that whoever considers this well will fail to recognise a certain brutishness in it, for the founder is always like a chimney sweep, covered with charcoal and distasteful sooty smoke, his clothing dusty and half burned by the fire, his hands and face all plastered with soft muddy earth. To this is added the fact that for this work a violent and continuous straining of all a man's strength is required, which brings harm to his body and holds many definite dangers to his life. In addition, this art holds the mind of the artificer in suspense and fear regarding its outcome and keeps his spirit disturbed and almost continuously anxious. For this reason they are called fanatics and are despised as fools. But, with all this, it is a profitable and skilful art and in large part delightful.

The Pirotechnia of Vannoccio Biringuccio [1]

E anco non dubito che chi anderà tal arte ben considerando, che non conoscerà in essa una certa brutezza, perche sempre chi l' esercita, stà simile à un spazzacamino, tinti di carboni, e da dispiacevoli, e fulinginosi fumi con vesti polverose, e dal fuoco mezze abbruciate, e anco di molle, e fangosa terra le mani,e il viso tutto imbrattato. Al che si aggiunge di tutte le forze dell' huomo, che à tal esercito si richiede il violento, e continuo sforzamento, perilche molto nocumenoto viene à rendere al corpo, e oltre che molti particolar pericoli della vita tiene, e in oltre sempre tien tal arte sospesa per timor del suo fine, la mente dell'artifice egli fà l'animo torbido, e fastidioso quasi continuamente, perilche son chiamati fantastichi, e disprezzati per matti. Ma con tutto questo, como già hò detto, è arte utile, e ingegnosa, e in buona parte dilettevole.

Pirotechnia del signor Vannoccio Biringuccio [2]

---

[1] The Classic Sixteenth-Century Treatise on Metals and Metallurgy
Translated and Edited by Cyril Stanley Smith and Martha Teach Gnudi

[2] Premio del Libro Sesto – Dell' arte del gitto in universale, e in particolare

In memory of Prof. Tom Bell

(1941 – 2008)

Synopsis

Low temperature surface alloying with nitrogen (nitriding), carbon (carburising) and both (carbonitriding) has been successfully employed in hardening engineering grade AISI 316 by the formation of a modified layer better known as S-phase or expanded austenite. However little or no research has been directed towards the surface modification of medical grade austenitic stainless steels, such as ASTM F138, ASTM F1586 and ASTM F2581.

In this study, systematic plasma surface alloying treatments and characterisation were performed on Fe-Cr-Ni medical grade ASTM F138 and ASTM F1586 as well as engineering grade AISI 316 austenitic stainless steel for comparison in order to establish the optimised treatment conditions (especially temperature) which can maximise the hardened case depth without any detriment in corrosion resistance. Based on the first phase process condition optimisation results, the optimum treatment temperature for nitriding and carbonitriding is 430°C whilst for carburising it is 500°C

The established optimised treatment temperatures that formed precipitate free S-phase layers on the nickel-containing medical grade austenitic stainless steels were also performed on the nickel-free ASTM F2581 medical grade alloy. For the first time S-phase was created in the surface of nickel-free austenitic stainless steel by low temperature plasma surface alloying but only carburising yielded a precipitate free S-phase layer. This implies that nickel is not essential in the formation of S-phase and that manganese together with chromium plays an important part in precipitation kinetics of Ni-Free (Fe-Cr-Mn) alloys.

The surface of a biomaterial must not adversely affect its biological environment and return the material surface must not be adversely affected by the surrounding host tissue and fluids. Experimental results have shown that this duality of concern can be addressed by creating S-phase in the surface of medical grade austenitic stainless steel since biocompatibility, corrosion and wear studies have manifested positive results.

It has been shown that low-temperature nitriding, carburising and carbonitriding can improve the localised corrosion resistance of medical grade stainless steel as long as the threshold sensitisation temperature is not reached. The improvement seen after treating medical grade austenitic stainless steel was not limited only to electrochemical but also to mechanical-electrochemical properties. In fact all plasma surface alloyed medical grade austenitic stainless steels have shown a general improvement in wear-corrosion and fretting-wear resistance over the untreated materials.

Also since biocompatibility studies on N, C and hybrid C/N S-phase have proved, for the first time, that they are biocompatible under the realms of the tests conducted in this study therefore the use of hardened medical grade austenitic stainless steel might be suitable in implant applications. The renaissance in metal-to-metal implants and the high performance of the S-phase have raised the possibility of utilising stainless steel as an alternative joint bearing.

Acknowledgments

I would like to express my sincere gratitude to my supervisors, Dr. Hanshan Dong and the late Prof. Tom Bell for their invaluable guidance and supervision throughout this study.

I would like to thank, “The University of Malta Academic Scholarship Fund” and the University of Birmingham for their financial support throughout my study.

Special thanks go to the members of the Department of Metallurgy and Materials at the Faculty of Engineering of the University of Malta, especially Dr. Stephen Abela, Prof Maurice Grech, Dr. John Betts, Mr. Glenn Cassar, Mrs. Ann Zammit and Dr. Bertram Mallia.

I would like to express my appreciation for help throughout my course of study from members of the Birmingham Surface Engineering Group, especially Dr. Xiaoying Li, Dr. Jian Chen, Mr. Tom Bell Jr., Miss Wenwen Wu, Mr. Gerard Bell, Miss Theresa Wall and Mr. Nick Habibi.

Thanks also go to Dr. Rachel Sammons, Dr. Alison Davenport and Dr. David Book of the University of Birmingham for their kind assistance during the experiments performed in their laboratories. My gratitude goes to Prof Linmao Qian of the Southwest Jiaotong University, China for the fretting-wear tests. I would also like to thank Miss Nathalie Zahra for her guidance in ICP-MS testing, Miss Anne Jung for her help in corrosion-wear tests and Miss Iris Kretzschmar for assistance in sample preparation. I would also like to extend my thanks to Dr. Sukanta Ghosh, Mr Sean Fletcher, Miss Christine Hardy and Miss Huei-Yu Lee for their invaluable help.

I also owe a lot to my friends in “Grace House” for providing such a nice and affectionate atmosphere for living. I cannot end without thanking my family whose constant encouragement I have relied on through my study in the UK.

Publications

[1] J. Buhagiar, H. Dong and T. Bell: “Low temperature plasma surface alloying of medical grade austenitic stainless steel with carbon and nitrogen”, Surface Engineering **23** (2007), pp 313-317

[2] J. Buhagiar and H. Dong: “Low-temperature plasma surface modification of medical grade austenitic stainless steel to combat wear and corrosion”, Key Engineering Materials **373-374** (2008), pp 296-299

[3] J. Buhagiar and H. Dong: “S-phase in stainless steels: An overview”, in Surface Modification Technologies, Volume 21, T. S. Sudarshan and M. Jeandin, Editors (2008), Valar Docs, USA, pp 509-518

Terminology

PSA	Plasma Surface Alloying
LTPN	Low Temperature Plasma Nitriding (or PSA with N)
LTPC	Low Temperature Plasma Carburising (or PSA with C)
LTPCN	Low Temperature Plasma Carbonitriding (or PSA with C and N
SLTPCN	Sequential Low Temperature Plasma Carbonitriding (LTPC + LTPN)
PRE	Pitting Resistance Equivalent
GDOES	Glow Discharge Optical Emission Spectroscopy
E_*	Combined Modulus (GPa)
E_D	Modulus of Disc (GPa)
E_B	Modulus of Ball (GPa)
ν_D	Poisson Ratio of Disc
ν_B	Poisson Ratio of Ball
σ	Hertzian Contact Pressure (GPa)
a	Hertzian Contact Area Radius (mm)
$A_{N\ or\ C}$	Area under the GDOES plot of either N or C depth profile (μm)
N	Number of fretting-wear cycles
F_t	Tangential Force in fretting-wear (N)
D	Displacement in fretting-wear (μm)

Note: All data generated in this thesis was from annealed samples with the exception of biocompatibility tests where cold-worked disc samples were used.

Table of Contents

Chapter I
Introduction and Objectives

1-1 Introduction

During the last three decades, great efforts and significant progress have been made in the development of high performance prosthetic devices, which has greatly contributed to the improved quality of life of patients [1]. For half a century austenitic stainless steel has been widely used as material for orthopaedic implants due to its competitive price and relative ease of manufacturing [2]. For a long time AISI 316L was the most popular steel for orthopaedic implants; nevertheless, problems concerning localised corrosion such as pitting and crevice corrosion has been observed with implants of this grade [3].

The development of such new steel making techniques as vacuum arc remelting helped to minimise the inclusion content in stainless steel and therefore improved their localised corrosion resistance. For example, vacuum arc remelted 316LVM (ASTM F138) austenitic stainless steel has shown great benefits in a wide range of medical applications. However, it still has limitations with regard to ultimate tensile strength and localised corrosion resistance [3, 4]. Due to this, a new type of high-nitrogen (ASTM F1586) austenitic stainless steel with about 0.4 wt% nitrogen has been developed to improve the corrosion resistance and strength [3-5].

Notwithstanding the fact that both ASTM F138 and ASTM F1586 have been the material of choice for many body implants, nickel allergic hypersensitivity is still a major concern and this has led to the development of nickel-free austenitic stainless steel (such as ASTM F2581). The nickel in this alloy is completely replaced by other austenite stabilisers, manganese and nitrogen. This has resulted in enhancement of biocompatibility, strength and corrosion resistance [3, 6, 7], thus stirring interest amongst biomedical researchers and surgeons [8, 9].

However the low hardness and poor wear resistance of these austenitic stainless steels are their major limitations for tribological applications (such as joint bearing surfaces)[10]. In 1985 Zhang and Bell [11] developed a low temperature plasma nitriding treatment that can increase the hardness and wear resistance of austenitic stainless steels without any detriment to their corrosion resistance. This was achieved by creating a nitrogen-rich

modified layer so-called S-phase or expanded austenite. Later on, low temperature surface alloying with nitrogen (nitriding) [12], carbon (carburising) [13] and both (carbonitriding) [14] have proved to be promising in the formation of S-phase layers which have combined improvements in hardness, wear resistance and corrosion resistance.

Nonetheless, nearly all the research to-date was directed at the formation of S-phase in engineering grade Fe-Cr-Ni based austenitic stainless steel such as AISI 304 and AISI 316 [15-17] and limited work [18] was directed towards the hardening of medical grade ASTM F138 and ASTM F1586 austenitic stainless steels.

Furthermore, since early observations have indicated that S-phase can only be formed in Fe-Cr-Ni based austenitic stainless steels [19, 20], it was commonly believed that a certain amount of nickel was essential for the formation of S-phase in austenitic stainless steel. Therefore no work has been published on the formation of S-phase in nickel-free austenitic stainless steels.

1-2 Aims of the project

The overall aim of this PhD project was to investigate the response to plasma surface alloying in generating S-phase layers on medical grade austenitic stainless steels (ASTM F138, ASTM F1586 and ASTM F2581) in order to enhance their surface properties for potential biomedical applications. Specifically, the main objectives of the present study were:

(1) To conduct systematic plasma surface alloying with nitrogen, carbon and both in order to establish the optimal treatment temperatures which maximise the hardened S-phase case depth without any detriment in corrosion resistance.

(2) To fully characterise the S-phase layers formed during the optimised plasma surface alloying treatments in terms of phase constituents, microstructure, composition and hardness, thus advancing the scientific understanding of this layer

(3) To evaluate corrosion, dry sliding wear, corrosion-wear, fretting-wear and biocompatibility, of plasma surface alloyed medical grade austenitic stainless steels in simulated body environments, thus laying down the foundations for exploring their wider biomedical applications.

Chapter II
Literature Review

2-1 Austenitic Stainless Steels

2-1.1 The Stainless Steel Family

2-1.1.1 Stainless Steels

Stainless Steels are iron-based alloys that contain a minimum of approximately 11%Cr, the amount needed to prevent the formation of rust in unpolluted atmospheres [10]. The material must be a ferrous alloy and it must contain more than 50% iron [21]. They achieve their stainless characteristics through the formation of an invisible and adherent chromium-rich oxide surface film. This oxide forms and heals itself in the presence of oxygen. Other alloying elements such as nickel, molybdenum, carbon, titanium, aluminium, silicon, niobium, nitrogen, sulphur and selenium are added to improve particular characteristics [10].

2-1.1.2 History

The discovery of stainless steel dates back to a period just after the turn of the century when French, German, English and later US metallurgists began publishing the results of their studies on low carbon, chromium containing ferrous alloys. The industrial usefulness of stainless steel became evident between 1910 and 1915 when: Harry Brearley (England) developed martensitic stainless steels; Fredrick Becket and Christian Dantisizen (United States) developed ferritic stainless steels; and Edward Maurer and Benno Straus (Germany) developed austenitic stainless steel [10, 21, 22].

2-1.1.3 Classification of Stainless Steels

Stainless Steels can be divided into five groups. Four are based on the characteristic crystallographic structure / microstructure of the alloys in the family: ferritic, martensitic, austenitic or duplex (austenitic and ferritic). The fifth group the precipitation-hardenable alloys, is based on the type of heat treatment used, rather than microstructure [10, 23]. This thesis is concerned with the surface engineering of austenitic stainless steels therefore

martensitic, ferritic, duplex and precipitation-hardenable stainless will not be considered in this review.

2-1.1.4 Austenitic Stainless Steels

Austenitic stainless steels constitute the largest stainless family in terms of number of alloys and usage [10]. The austenitic alloys are non-magnetic, their structure is face-centred cubic (fcc) and they cannot be hardened by heat treatment but can be strained hardened by cold work [21]. These alloys have a rare combination of corrosion resistance, high temperature strength, oxidation resistance, ease of fabrication and weldability, good ductility and good impact resistance even at cryogenic temperatures [10, 21].

2-1.2 Metallurgy of Austenitic Stainless Steel

2-1.2.1 Physical Metallurgy

Austenitic stainless steels contain large amounts of chromium and iron, therefore the iron-chromium phase diagram provides the basis for understanding its basic metallurgy. As can be seen in Figure 2-1, the allotropic forms of iron constitute the iron end of the diagram. With increasing chromium content, the ferrite field expands and the austenite (γ) field contracts, thus providing the so-called γ loop since chromium is a ferrite stabilising element [10, 22, 24].

Next to chromium, nickel is the alloying element that mostly influences alloy design. The prototype ferritising element is chromium while the prototype austenising element is nickel. Since austenitic stainless steel compositions are based on a balance of alloying elements that promote ferrite formation and those that promote austenite formation they are best described in terms of the iron-chromium-nickel ternary alloy system in Figure 2-2. When comparing the ternary diagram with the iron-chromium binary diagram it can be clearly seen that nickel addition extends the austenite phase field. The phase diagram also indicates that as the chromium content increases above 18%, it also becomes necessary to raise the nickel content otherwise increasing amounts of ferrite will form [10, 22, 24].

In reality the commercial alloys also contain a certain amount of other alloying elements which might somewhat alter the phase balance, but by large the structure is determined by the three primary constituents: iron, chromium and nickel. In order to

broadly describe the effect of composition on microstructure in a wide range of stainless steels, the concept of chromium and nickel equivalent was developed to normalise the effect of these alloying elements on the microstructure evolution relative to the effects of chromium and nickel. The Schaeffler diagram shown in Figure 2-3 is a plot of chromium and nickel equivalents on opposing axis to provide a graphic depiction on the relationship between composition and microstructure for stainless steel. Molybdenum, silicon and niobium are considered as ferrite formers and therefore they are included in the chromium equivalent axis [10, 22]. Carbon is considered as a strong austenite former, while manganese does not seem to promote transformation of ferrite to austenite but promotes solubility of nitrogen in steel. Nitrogen also enhances the formation of austenite and its influence on phase equilibria in the Fe-Ni-Cr phase diagram is shown in Figure 2-4 [10, 22, 24]. It is for this reason that both carbon and manganese are found in the nickel equivalent axis [22].

Martensite may form in austenitic stainless steel during cooling below room temperature (i.e. thermally) or in response to cold work (i.e. mechanically). Besides extending the γ phase field nickel also lowers the martensite start (M_s) after cooling from solution annealing. In fact all the alloying elements commonly found in austenitic stainless steels lower the M_s, including chromium and molybdenum which at high temperatures promote the ferrite formation. Strain-induced martensite formation is a unique feature in austenitic stainless steels. This forms at higher temperatures than does martensite, which forms on cooling [10].

2-1.2.2 Inclusions and Precipitates

Lack of steel cleanliness and improper heat treatment can produce deleterious changes in the microstructure of austenitic stainless steels. These inclusions and precipitates also increase the susceptibility to localised corrosion and embrittlement.

Carbide Precipitation

Sensitization or carbide precipitation at grain boundaries can occur when austenitic stainless steels are heated for a period of time in the range of about 425°C to 870°C [10, 21, 22]. Time-temperature sensitization curves, as shown in Figure 2-5, provide a guidance to avoiding sensitization and illustrate the carbon content on this phenomenon [10, 21, 22,

24]. In the absence of stabilizing elements, $M_{23}C_6$ is the predominant carbide formed in austenitic stainless steels. $M_{23}C_6$ is mainly composed of chromium carbide, so the designation $Cr_{23}C_6$ is used frequently [10, 21, 22, 24]. However, since other elements can particularly substitute for chromium, the formula may be written as: $(Cr,Fe,Mo)_{23}C_6$, [10, 24] $(Cr,Fe)_{23}C_6$ [10], $(Fe,Cr)_2Mo_2C_6$ [25]. Austenitic Stainless steels which are alloyed with titanium and/or niobium resist better carbide precipitation and are called stabilised steels. These elements have an affinity for carbon and form MC type carbides readily; effectively reducing the matrix carbon content and thus protecting against the deleterious $M_{23}C_6$ precipitation [10, 21, 22, 24].

Nitride Precipitation

Nitrogen in solid solution is the most beneficial alloying element in promoting high strength of austenitic stainless steel without affecting their good ductility and toughness properties as long as the solubility of nitrogen in γ is not exceeded (<0.9wt%N). As the solubility is exceeded, Cr_2N precipitates at the grain boundaries of the austenitic stainless steel [24, 26].

Sulphides

Several types of sulphides have been observed in austenitic grades, the most common being MnS. However if the manganese content is low, chromium will replace some of the manganese in the sulphide [27, 28].

Other Phases

Z-Phase is a niobium rich nitride with a typical composition of $Cr_2Nb_2N_2$. Primary precipitation are frequently present as agglomerates and can be found at grain boundaries and at the triple point grain boundary of high-N stainless steel [5, 10, 29].

Sigma phase (σ) formed in austenitic stainless steels is a hard and brittle intermetallic phase which is rich in chromium and molybdenum. Sigma phase precipitates on grain boundary triple points and then grain boundaries after a long time at high temperature on incoherent twins and intergranular inclusions [10, 24].

Chi phase (χ) is a bcc phase of typical composition $Fe_{36}Cr_{12}Mo_{10}$. However the phase possesses an appreciable range of compositions with high tolerance of metal interchange. The nucleation sites for the χ phase are grain boundaries, incoherent twin boundaries and intergranular dislocations [10, 22, 24, 30].

Laves phase (η) is essentially Fe_2Mo and can form in austenitic stainless steels after long term high-temperature exposure. Alloys containing molybdenum, titanium and niobium are most susceptible. Laves precipitation is normally intergranular but it is occasionally found on grain boundaries [10, 24, 30].

2-1.2.3 Melting and Refining

Steel cleanliness of austenitic stainless steel is evaluated by inclusion type and count. As discussed in the previous section austenitic stainless steels might include a number of non-metallic inclusions which, as it will be discussed in the next section, influence adversely the localised corrosion properties of the austenitic stainless steel [4, 31].

The two most crucial properties of bio-materials are corrosion resistance and biocompatibility. In order to comply with the stringent requirements on micro-cleanliness it is a general practice to either use a conventional or a vacuum melting process. If the requirements are not met austenitic stainless steel which has been produced by any of these two processes may be refined using either vacuum arc remelting (VAR) [3, 4, 30, 31] or electron beam remelting or electroslag remelting (ESR) [4, 10].

Conventional Melting

Melting and refining of austenitic stainless steel is most commonly accomplished by electric arc furnace / argon oxygen decarburisation (EAF/AOD). The EAF/AOD process route involves melting the charge in basic lined electric furnace and transferring the molten metal into the AOD converter vessel. The AOD is a secondary refining process that offers improved metal cleanliness [4, 10, 31]. This can be followed by a ladle furnace / continuous casting route (LF/CC). This route is cost efficient and makes it possible to produce a variety of new types of austenitic stainless steels [10, 31]. In fact now with the EAF/AOD route it is possible to develop a high nickel, molybdenum-bearing austenitic stainless steel alloy containing nitrogen in the range of 0.1 to 0.2% without the formation of brittle second phases; to increase the strength of very low carbon types 304L and 316L

steels; to enhance resistance to chloride pitting, crevice corrosion, and certain acids; and to retard sensitization [10, 31].

Vacuum Melting

When the demands of the application justify the added cost it is possible to produce austenitic stainless steel of higher purity and lower non-metallic inclusion content using a method other than conventional EAF / AOD. Selected charge materials may be melted entirely under high vacuum to prevent oxidation in melting and removing any volatile impurities. Vacuum induction melting (VIM) is the most commonly used method, but electron beam melting (EBM) might also be used [10].

2-1.3 Types of Austenitic Stainless Steels

Austenitic stainless steels can be divided into two categories: Chromium-Nickel Alloys and Chromium-Manganese-Nitrogen alloys. Figure 2-6 gives a schematic depiction of these alloys.

2-1.3.1 Chromium-Nickel Alloys

These are probably the most common and the most known austenitic stainless steels that are available in the market [10]. The leanest of these austenitic stainless steels such as AISI 304 would have a composition of 18-20 wt% Cr, 8-10 wt% Ni and balance Fe [10, 21]. Addition of molybdenum to AISI 304 enhances pitting resistance and creates grades such as the AISI 316 and AISI 317 [10, 21]. To prevent intergranular corrosion after elevated-temperature exposure, titanium or niobium is added to stabilise the carbides in AISI 321 or AISI 347 [10, 21]. Also, lower carbon grades such as AISI 316L; have been established to prevent intergranular corrosion. To improve strength and pitting resistance nitrogen is added in 316N or 316LN [10, 21]. The addition of sulphur or selenium is used in order to improve the machinability of the steel while extra additions of chromium and Ni in types AISI 309 and AISI 330 improve strength and oxidation resistance [10, 21].

Another type is the superaustenitics which are austenitic stainless steels which contain ~6% molybdenum and ~0.2% nitrogen. They have been developed to improve the

resistance to chloride corrosion and to have higher strength than conventional AISI 316 stainless steel [10, 21].

2-1.3.2 Chromium-Manganese-Nitrogen Alloys

These steels are rich in chromium and manganese and are fully austenitic. They are heavily alloyed with nitrogen in order to keep their structure austenitic at room temperature. This austenitic stainless steel category can be further divided into two: The high-N austenitic stainless steels and the nickel free austenitic stainless steels.

2-1.4 Medical Grade Austenitic Stainless Steel

2-1.4.1 Low Vacuum Melted Austenitic Stainless Steels

Industrial grade AISI 316L austenitic stainless steel was the most popular steel used for orthopaedic implants such as fracture fixations and joint replacements. Nevertheless, problems concerning localised corrosion such as pitting, crevice corrosion and stress corrosion cracking haven been observed with implants of this grade. To control such corrosion important development work has been done by the steel industry by minimising the non-metallic inclusion content. This was done by a process called vacuum-arc remelting which produced a medical grade 316LVM austenitic stainless steel which falls under the ASTM F138 designation[3].

2-1.4.2 High-N Austenitic Stainless Steels

In order to improve the localised corrosion of 316L a higher alloyed stainless steel was developed. The nickel content was lowered while the chromium (~20wt%) and manganese (~4wt%) contents of the alloy were raised and up to 0.5% of nitrogen was also introduced to improve corrosion resistance and strength [3, 5, 29, 30]. The partial exchange of nickel by manganese was performed in order to enhance the nitrogen solubility [7]. This alloy is fully austenitic due to nitrogen's crucial ability to stabilise austenite [32]. Extra additions such as 0.5wt% niobium are introduced in order to reduce the chromium precipitation as carbides [33].

2-1.4.3 Nickel-free Austenitic Stainless Steels

A call for high strength, non-magnetic behaviour and corrosion resistance led to the development of a nickel-free austenitic stainless steel. The nickel in the alloy was completely replaced by manganese (~18wt %) in order to enhance nitrogen solubility.

In order to keep the structure austenitic nitrogen (0.5 – 0.9%) is added as an alloying element. Also to increase the corrosion resistance of this alloy 2-3wt% of molybdenum can be added. Since the alloy is completely nickel free it is considered as body friendly and is normally used for costume jewellery, watch handles and dental braces [6, 7].

2-1.4.4 Applications

Orthopaedic implant biomaterials are enormously successful in restoring the mobility and quality of life to millions of individuals each year [34]. Orthopaedic implants are generally used for either fracture fixation (fracture plates, wires, pins, screws etc.) or joint replacement [34]. The types of hip implants that exist today are either of the total hip arthroplasty [35] or of the surface replacement type [36].

The developer of new biomaterials for orthopaedic purposes faces the same duality of concerns present in all other implant use: the material must not adversely affect its biological environment and in return the material must not be adversely affected by the surrounding host tissues and fluids [34]. There are four principal metal alloys used in orthopaedics and particularly in total joint replacement: titanium-based alloys, cobalt-based alloys, refractory metals, and stainless steel alloys [34, 37, 38].

The form of stainless steel most commonly used in orthopaedic practice are: (1) 316LVM, designated as ASTM F138, (2) High-Nitrogen Austenitic Stainless Steel, designated as ASTM F1586 and (3) Nickel-Free Austenitic Stainless Steel [39-41], designated as ASTM F2581. Although the mechanical properties of stainless steels are generally less desirable than those of the other implant alloys (lower strength, wear and corrosion resistance), stainless steel do possess greater ductility indicated quantitatively by a threefold greater “percentage elongation fracture” when compared to other implant metals. This aspect of stainless steel has allowed it to remain popular as an implant material and a low-cost alternative to titanium and cobalt alloys [34, 37, 38].

An orthopaedic implant is considered to have failed if it has to be prematurely removed from the body. In every failure of an orthopaedic implant, the concerned patient

is made to experience the trauma of repeated surgeries, besides the pain experienced during the process of rejection of the device. Therefore it is highly desirable to keep the number of failures a minimum. Two common types of implant failures are corrosion and corrosion-wear [34, 42].

Electrochemical corrosion occurs to some extent on all metallic surfaces including implants. This is undesirable due to the fact that the degradative process may reduce the structural integrity of the implant and the release of products of degradation is potentially toxic (sensitizers or carcinogens) to the host[34, 42, 43].

The generation of wear debris, and subsequent tissue reaction to such debris, is central to the longevity of total joint replacements. Particulate debris generated by wear, fretting or fragmentation induces the formation of an inflammatory reaction resulting in progressive local bone loss[34, 44] that threatens the fixation of both cemented and cementless devices alike.

Current strategies designed to address the problem of biomaterial-related implant failure are primarily aimed at decreasing the amount of periprosthetic particulate burden and any subsequent effects. The complete elimination of polyethylene as a material for hip joint prosthesis [34] is an approach that came with the realization that early problems may have been related to design and not articulation, and because of this there has been a renew interest of metal-on-metal bearings [34, 40, 45, 46]. Metallic wear is also being addressed through techniques such as nitriding and nitrogen ion implantation to decrease the potential for articular, abrasive and fretting wear in stainless steel stems [34, 41, 42, 44, 47]. As it will be explained in the subsequent sections stainless steel have been hardened successfully by creating a hard and corrosion resistant modified layer called S-phase. An application for the S-phase emerged from the susceptibility of austenitic stainless steel prostheses to wear-corrosion attack. Although not yet applied to real prostheses, many independent studies [2, 18, 48] in the hardening of the femoral heads were conducted.

2-1.5 Corrosion of Austenitic Stainless Steel

The corrosion protection for austenitic stainless steel differs from that for carbon steels, alloy steels and other metals[10, 23]. Austenitic stainless steels like other related chromium bearing alloys rely largely on the phenomena of passivity. Passivity is a result of an invisible and thin passive film that forms on the surface of the austenitic stainless steel.

Chromium is the one element essential in forming the passive film [10]. This passive film has the property of ‘self-repair’ and will spontaneously re-form if the surface is broken or damaged mechanically, provided that there is a source of oxygen present.

This passive film acts as a barrier and separates the metal from the surrounding atmosphere and therefore the integrity of this film is essential in protecting the austenitic stainless steel against corrosion [10, 21, 23]. If passivity is destroyed under conditions that do not permit restoration of the passive film, then the austenitic stainless steel will corrode much like a carbon or low alloy steel would do [10]. In reality the total loss of the passive film is not a common occurrence but localised breakdown of the film is. This breakdown of the film leads to localised corrosion which is of great concern in austenitic stainless steel.

The forms of corrosive attack that most affect austenitic stainless steels include: general (uniform corrosion), galvanic corrosion, pitting corrosion, crevice corrosion, intergranular corrosion, stress-corrosion cracking and wear-corrosion [10, 23].

2-1.5.1 General Corrosion

General corrosion refers to corrosion dominated by uniform thinning that proceeds without appreciable localised attack. Passive materials like austenitic stainless steels are generally subject to localised attack however under specific conditions - high temperature corrosive environments - they are also susceptible to general corrosion [10].

2-1.5.2 Galvanic Corrosion

Galvanic corrosion results when two dissimilar metals are in electrical contact in a corrosive medium [10]. Galvanic corrosion behaviour of austenitic stainless steel is difficult to predict because of the influence of passivity. In fact austenitic stainless steels occupy two positions in the galvanic series, representing the active and passive states: close to steel when active and in a more noble state when passive [10, 21].

2-1.5.3 Pitting Corrosion

Pitting corrosion is a type of localised corrosion in which microscopic holes or cavities form on the surface of metals [28]. This attack occurs either due to direct corrosion of heterogeneities present on the surface, local discontinuity of the passive film or due to the localised damage of the protective passive film.

Under certain environmental conditions, particularly in the presence of aggressive ions such as halides, the protective passive film of austenitic stainless steel is damaged at weak sites either by adsorption and penetration or by penetration and migration of aggressive ions [28]. The preferential sites of attack are in the proximity of surface defects which are in the form of: inclusions, second phase precipitates, grain boundaries, slip steps and segregated interfaces [28]. It is for this reason why steel cleanliness in austenitic stainless steel is given so much importance.

Figure 2-7 shows a schematic diagram of a pit forming in the presence of halide ions. Pit initiation commences when aggressive chloride anions react with the metal atoms at the film-substrate interface to form metal chlorides. These in turn hydrolyse according to the reaction in Equation 2-1 to give metal hydroxide, but at the cost of increasing acidity at the reaction site [23, 28, 49].

$$M^{+}Cl^{-} + H_2O \rightarrow MOH + H^{+}Cl^{-} \qquad (2\text{-}1)$$

There is a decrease in pH at these pitting sites and this enhances further the metal dissolution according to the reaction in Equation 2-2 [28]. The rapid dissolution of metal within the pit produces an excess of positive charges in this area, causing migration of more chloride ions into the pit. Both hydrogen and chloride ions when acting together stimulate the dissolution even further and the entire process accelerates with time. Also because the solubility of oxygen is virtually zero in concentrated solutions, no reduction of oxygen occurs within a pit [23].

$$Fe \rightarrow Fe^{2+} + 2e^{-} \qquad (2\text{-}2)$$

The electrons released during dissolution are consumed by the cathodic reaction occurring on the passive film present further away from the pitting sites. There are two

types of reduction reactions that occur at the cathode: hydrogen evolution (equation 2-3) and reduction of oxygen (equations 2-4 and 2-5) [28].

$$2H^+ + 2e^- \rightarrow H_2 \quad (2\text{-}3)$$

$$2H^+ + ½\ O_2 + 2e^- \rightarrow H_2O \quad (2\text{-}4)$$

$$H_2O + ½\ O_2 + 2e^- \rightarrow 2OH^- \quad (2\text{-}5)$$

Cathodic reduction of oxygen on the surface areas adjacent to the pit tends to suppress corrosion on these surface and therefore isolated pits cathodically protect the surrounding metal surface [23]. When all of this occurs it is said that the pit has reached a stable stage, making the environment inside the pit more aggressive, and therefore penetrates the metal at an ever-increasing rate by an autocatalytic process [23, 28].

The chemical composition of the austenitic stainless steel plays a major role in affecting the pitting resistance. Chromium, molybdenum and to a lesser extent nickel are the main alloying elements required to improve the pitting resistance [23, 28] but nitrogen is also considered as an important alloying addition as it promotes passivity and widens the passive range in which pitting is less probable [28]. In fact, as it can be seen from Figure 2-8, the addition of nitrogen significantly improves the pitting corrosion resistance in acidic and neutral chloride media up to a temperature of 65°C (338K).

Pitting resistance of austenitic stainless steel is primary a function of the Cr, Mo and N levels. The pitting resistance equivalent (PRE) of an alloy, which also can be used for alloy ranking, is generally defined as:

$$PRE = \%Cr + 3.3(\%Mo) + x(\%N) \text{ were } x = 13 \text{ to } 30 \quad [4, 5, 28, 30, 32, 33]$$

The reason why nitrogen improves the pitting resistance of the alloy is not fully understood and the following mechanisms have been suggested to explain how nitrogen operates:

(1) Nitrogen in solid solution dissolves and produces NH_4^+, raising the pH and depressing oxidation inside a pit [49, 50].

(2) Concentrated nitrogen at the passive film-alloy surface stabilises the film, and prevents attack of the anions (Cl-) [49, 50].

(3) Nitrate ions are produced and these improve the resistance to pitting corrosion [28, 49, 50].
(4) Nitrogen addition stabilises the austenite phase [49, 50].
(5) Nitrogen blocks the kink, and controls the increase of electric current for pit production [49, 50].

2-1.5.4 Crevice Corrosion

Crevice corrosion is a form of localised attack that affects both active and passive metals but the attack is often more severe for passive alloys, particularly those in the stainless steel group [23]. This type of attack occurs at restricted regions, in occluded areas, in shielded areas, at narrow openings or gaps (spaces) between metal-to-metal or non-metal-to-metal components. In practice it is extremely difficult to avoid all crevices and these can be produced by design or accident. Crevices caused by design occur at gaskets, flanges, rubber O-rings and anywhere which has close fitting surfaces [23, 51]. Crevices caused by accident occur in occluded regions that are formed under tubercles, deposits, and below accumulation or biological materials. Similarly, unintentional crevices such as cracks, seams or any other metallurgical defect could serve as sites for corrosion [23].

This type of attack results from a concentration cell formed between the electrolyte inside the crevice, which is oxygen starved, and the electrolyte outside the crevice, where oxygen is more plentiful. Thus making the metal within the crevice an anode, and the exterior metal a cathode [23]. Based on the knowledge of the influence of various factors a unified crevice corrosion mechanism (Figure 2-9) has been proposed [51] and is described below:

Initially the cathodic reduction ($H_2O + ½O_2 + 2e^- \rightarrow 2OH^-$) and the anodic dissolution ($M \rightarrow M^+ + e^-$) processes occur uniformly over the entire metal surface, including crevice exterior. The oxygen in the shielded crevice area is consumed after some incubation period, but the decrease in cathodic reaction rate is negligible because of the small area involved. Consequently, the corrosion of the metal inside and outside the crevice continues at the same rate. With the cessation of the cathodic hydroxide producing reactions however, the migration of negative ions (e.g. chlorides) into the crevice is required to maintain charge balance. The resulting metal chloride hydrolyses to insoluble metal hydroxides and hydrochloric acid, which results in the progressive acidification of the

crevice ($M^+Cl^- + H_2O \rightarrow MOH + H^+Cl^-$). Both the chloride ions and low pH accelerate crevice corrosion in a manner similar to autocatalytic pitting while reduction reaction cathodically protects the exterior surface [51].

Pitting and crevice corrosion behave very similarly and both the corrosion initiation sites [51] within a crevice and the alloying elements [3, 23, 51] that resist crevice corrosion are similar to that of pitting. Apart from material related factors, the initiation of crevice corrosion can also be influenced by non-material related factors. Factors such as; crevice type, crevice geometry, number of crevices, exterior to interior crevice area ratio, bulk solution composition (chloride and oxygen content, pH and pollutants) , bulk solution environment (temperature, agitation, volume) and mass transport inside and outside of the crevice; influences greatly crevice attack [51].

2-1.5.5 Intergranular Corrosion

Intergranular corrosion is defined as the selective dissolution of grain boundaries, or closely adjacent regions, without appreciable attack of the grains themselves. This dissolution is caused by a potential difference between the grain-boundary region and any precipitates, intermetallic phases, or impurities that form at the grain boundaries [23].

Intergranular corrosion in austenitic stainless steels is generally the result of sensitization. This condition occurs when a thermal cycle leads to grain-boundary precipitation of carbide, nitride, or intermetallic phases without providing sufficient time for chromium diffusion to fill the locally depleted region [23]. The diffusion rate of chromium in austenite is slow at the precipitation temperatures; therefore the depleted zone persists. When the chromium level in the depleted area falls below that required for passivation the austenitic stainless steel becomes susceptible to intergranular corrosion [25]. This is because the depleted zones have higher corrosion rates than the matrix in many environments leading to a preferential dissolution at the grain boundary [23, 25].

2-1.5.6 Stress-Corrosion Cracking

Stress Corrosion cracking (SCC) is a corrosion mechanism in which the combination of: alloy susceptibility, tensile stress above a threshold value, and a particular environment leads to cracking [10, 21, 23, 52]. The overall SCC process can be divided into two stages:

the initiation process and the propagation process. During the initiation process, development of an occluded cell with its acidification and concentration of anionic species takes places. In fact, many SCC failures have been reported to initiate from pits [52].

2-1.6 Wear of Austenitic Stainless Steel

Wear, as defined by ASTM [53], is the damage to a solid surface: usually involving progressive loss of material, due to relative motion between that surface and a contacting substance or substances. Stainless steels are characterized as having relatively poor wear resistance, but they are often required for a particular application because of their corrosion resistance [10]. The types of wear described below include: abrasive, adhesive, oxidative, fatigue, corrosive and fretting. Austenitic stainless steels are subjective to any of these types of wear mechanisms.

2-1.6.1 Abrasive Wear

As defined by ASTM [53] abrasive wear occurs due to hard particles or hard protuberances forced against and moving along a solid surface. Generally, a material is seriously abraded or scratched only by a particle harder than itself [10]. Abrasion is typically categorized according to types of contact. Types of contact include two-body and three-body wear. The former occurs when anchored abrasives slide along a surface, and the latter, when an abrasive is caught between one surface and another.

Abrasive wear is manifested in the forms of scratches or grooves. Scratching is the mechanical removal or displacement (or both) of material from a surface by the action of abrasive particles or protuberances sliding across surfaces [53]. Wear in the form of grooves is divided into two: plowing or scoring. Plowing is the formation of grooves by plastic deformation of the softer of two surfaces in relative motion [53] while scoring, which is a severe kind of wear, is characterized by the formation of extensive grooves or scratches in the direction of sliding [53].

For austenitic stainless steels, abrasion resistance is highly dependable on two metallurgical variables: hardness and carbon content. Austenitic stainless steels with high carbon content and/or a high work-hardening rate, favours better abrasion wear resistance.

2-1.6.2 Adhesive Wear

As defined by ASTM [53], adhesive wear occurs due to localized bonding between contacting solid surfaces leading to material transfer between the two surfaces or loss from either surface. Adhesive wear occurs when two metallic components slide against each other under an applied load where no abrasives are present and wear results from shear failure of the weaker of the two metallic mating surfaces [10].

When the applied load is low enough, the surface oxide film characteristic of stainless steels can prevent the formation of metallic bonds between the asperities on the sliding surfaces, resulting in low wear rates. This form of wear is called mild wear, or oxidative wear, and can be tolerated by most moving components. When the applied load is high, metallic bonds will form between the surface asperities, and the resulting wear rates will be high.

Galling can be considered a severe form of adhesive wear and is defined by ASTM [53] as a form of surface damage arising between sliding solids, distinguished by macroscopic, usually localized roughening and creation of protrusions above the original surface, it often includes plastic flow or material transfer or both.

Materials that have limited ductility are less prone to galling, because under high loads surface asperities will tend to fracture when interlocked. Small fragments will be lost, but the resulting damage will be more similar to scoring (see abrasive wear) than to galling. For high ductile materials, asperities tend to plastically deform, thereby increasing the contact area of mated surfaces; eventually galling occurs [10].

Materials whose dislocations easily cross slip and hence have a high stacking-fault energy are prone to galling. Hcp structured material have a low dislocation slip rate and are less prone to galling. The opposite can be said about fcc materials since these materials easily cross slip. This explains why cobalt-base alloys resist galling while titanium alloys and austenitic stainless steels tend to gal [10].

In order to prevent adhesive wear of austenitic stainless steel parts proper design is required in order to minimize contact stresses. This can be achieved by minimizing the loading, increasing the contact area and utilization of lubricants. Design tolerance of the parts should be tight with sufficient clearance, because tight fit parts will be more prone to galling [10].

2-1.6.3 Oxidative Wear

This form of wear is considered as mild wear and is tolerated by most moving components [10]. Oxide particles are loosened and move about within the contact region, they loosen more particles, some of which leave the system as wear debris, but the oxides do not abrade the substrate in most systems. Wear by loosening of and loss of oxide should not be identified as abrasive wear [54].

2-1.6.4 Fatigue Wear

This kind of wear occurs when a surface is stressed in a cyclic manner. The fatigue wear rate of stainless steels is affected by surface conditions such as finish, residual stress, hardness and microstructure. Surface treatments such as: nitriding, carburising and shot peening, which increase surface hardness and improve residual stress distribution help in preventing this kind of wear [10].

2-1.6.5 Corrosion-wear

Corrosion-wear or tribo-corrosion involves the interaction between mechanical wear processes and electrochemical corrosion processes and leads to material loss [53, 55]. Corrosion-wear is often linked to the synergy resulting from the coupling of mechanical and environmental effects. According to Watson *et al.* [56] the total volumetric corrosion-wear rate (CW) can be regarded as the sum of all the surface damage due to the volumetric corrosion (C), the volumetric mechanical wear rate (W) and the volumetric rate of degradation due to the corrosion-wear synergy (S):

$$CW = C + W + S \qquad (2\text{-}6)$$

The synergy (S) [44, 57] can be regarded as the sum of the corrosion-enhanced wear (W_c) and the wear-enhanced corrosion (C_w):

$$S = W_c + C_w \qquad (2\text{-}7)$$

Possible wear-enhanced corrosion (C_w) mechanisms include [57]:

(i) Stripping of the protective corrosion film creating fresh reactive corrosion sites.

(ii) Local acidification at wear sites, prohibiting film formation and accelerating corrosion rates.

(iii) Anodic wear scars that can cathodically polarize the surrounding unworn surfaces and destabilizing passive film in these regions enhancing corrosion.

(iv) Roughening of the specimen surface increasing the corrosion rate.

(v) Increased mass transport by high turbulence.

Possible corrosion-enhanced wear (W_c) mechanisms include [57]:

(i) Removal of work hardened surfaces by corrosion processes and exposing the underlying base metal to wear mechanisms

(ii) Preferential corrosive attack at grain boundaries resulting in grain loosening and eventual removal

(iii) Lowering the fatigue strength of a metal by corrosion

(iv) Increase in the number of stress concentration defects resulting from micro-pitting.

(v) Detachment of plastically deformed flakes on the metal surface due to stress corrosion cracking.

However, in some instances negative synergy can also occur, called antagonistic effect. Possible antagonistic effects which reduce corrosion rates ($-C_w$) are: rapid corrosion film growth; scaling; the formation of a passive film; or thermally affected films. Whilst the reduction in wear rates can result from: the presence of a soft or loosely adherent corrosion film reducing contact stresses; or blunting of the crack tips by lateral dissolution and thus retarding the speed of crack propagation [57].

The synergy component in corrosion-wear is further complicated for surface engineered stainless steels where subsurface corrosion can occur at the interface with the substrate or interlayers. Dearnley and Aldrich-Smith [55] have proposed three major wear-corrosion mechanisms that affect 316L stainless steels when they are protected by hard cathodic surface coatings like S-Phase and CrN:

Type I: The removal of the coating passive film during sliding contact and its subsequent regeneration [55].

Type II: Galvanic attack of the substrate – leading to blistering and fracture followed by the removal of coating fragments during sliding contact [55].

Type III: Galvanic attack of the counterface material which causes it to roughen – this leads to mechanical damage (abrasion) of the coating during subsequent sliding contact [55].

Although these 3 mechanisms proposed by Dearnley and Aldrich-Smith [55] are related to coatings, mechanisms (I) and (III) apply for uncoated stainless steels involved in corrosion-wear.

Type I corrosion-wear occurs because stainless steels rely on a 1-10nm thick surface passive film for the protection from aggressive and corrosive environments. This passive film forms instantaneously when oxygen is available in the environment but abrasion can lead to a complete removal of this film exposing the substrate to the aggressive environment. Unless repassivation occurs accelerated dissolution will occur within the worn site. If the rate at which the stripping of this passive film is higher than its regeneration, the nascent bulk material is exposed longer to the corrosion environment and high dissolution rates may result. Therefore the corrosion-wear performance of stainless steel depends on the ability and rapidity of the passive film to self heal [10, 23, 57].

Type III corrosion-wear can occur in counterface materials which are composite (WC in cobalt binder) or are stainless steels that contain precipitates. For instance the presence of carbides in sensitized stainless steel establish a micro-corrosion cell as the carbide is likely to be cathodic with respect to the surrounding metal matrix. This can result in preferential anodic dissolution of the metal matrix close or at the matrix/carbide interface and thereby accelerate carbide removal from the surface which eventually roughens the surface [57].

2-1.6.6 Fretting Wear

Fretting wear occurs when material is removed from contacting surfaces when motion between the surfaces is restricted to very small amplitude oscillations (often, the relative movement is barely discernible) [23, 58, 59]. Although fretting wear can be regarded formally as reciprocating sliding wear with very small displacements, there are enough differences in both wear rates and mechanism to merit the use of a distinct term. Whereas sliding wear usually results from deliberate movement of the surfaces, fretting often arises in components those are considered fixed and are not expected to wear, but which nevertheless experience a small oscillatory relative movement [23]. These small displacements often originate from vibration.

Similarly to sliding wear, fretting wear can also occur in corrosive environments and when this occurs the term fretting corrosion-wear, fretting corrosion [43, 60] or mechanically assisted crevice corrosion (MACC) [60] is used. The micro-motion in corrosive environments creates the ideal site for the generation of fretting corrosion products. This motion results in increased rates of corrosion produced by the continual fracture and reformation of oxide layers (repassivation), which form over stainless steels [23].

For sphere-plane contact, under a normal load, the contact zone generated is circular and the contact pressure reaches maximum at the centre of the contact circle, and falls to zero at the edges. Figure 2-10 (a and b) illustrates this pressure distribution, and also shows a plan view of the area of contact respectively [59, 61].

If a small cyclic tangential force is superimposed on the normal force, some displacement may occur between the surfaces around the edges of the contact zone, where the normal pressure is lowest and the frictional stress opposing movement is therefore least (Figure 2-10c). The contact zone can then be divided into two regions: a central area where there is no relative tangential movement and an annular zone in which micro-slip occurs [59, 61].

As the cyclic tangential force is increased, the central area within which no slip occurs shrinks until eventually slip occurs over the whole contact area (Figure 2-10d). The tangential force can be translated into an equivalent macroscopic tangential displacement, which is a more convenient measure of the conditions of fretting.

The regimes of the normal load and displacement amplitude corresponding to stick, mixed stick-slip and gross-slip are plotted in Figure 2-11. At a fixed normal load, increasing the amplitude of the cyclic tangential displacement (or load) leads to an increase in the extent of slip; a similar effect results from increasing the normal load at fixed amplitude. These three different regimes are easily identified in the tangential load displacement plots (F_t-D) where gross slip is characterized by an open parallelogram shaped F_t-D plot; stick by a closed shaped F_t-D plot; and mixed stick-slip by an elliptical F_t-D plot [59, 61].

Fretting damage occurs in the micro-slip region. In the relative slip fretting process the applied normal load causes adhesion of asperities and as the contact areas slip, wear debris is produced which accumulate in the adjoining valley. These fine metal particles removed by adhesive wear oxidize and work-harden between the fretting surfaces. These hard particles then act like abrasives and increase the rate of material removal [23, 61].

2-2 S-phase in Austenitic Stainless Steels

2-2.1 Introduction

2-2.1.1 History

The S-phase was reported for the first time by Zhang and Bell in 1985 [11]. It was created in AISI 316 stainless steel by means of low temperature plasma nitriding carried out at 400°C. Zhang and Bell described the S-phase layer as being hard ($700HV_{0.05}$) and corrosion resistant.

In a parallel investigation by Ichii *et al.*[62] the S-phase was again created using low temperature nitriding at 400°C. The authors present XRD data which showed peak shifting to lower angles. These shifted peaks were not listed in the ASTM index and were denoted as S1-S5. Ichii et al. used the term 'S-phase' to describe this layer and thus the term was created.

The disagreement on the real structure of the S-phase started immediately. Zhang and Bell describe it as: "*mixed γ' + austenite surface layer which is completely free from CrN*" [11], whilst Ichii *et al.* presented it as a compound layer having a structure of type M_4N [M=(Fe, Cr, Ni …)][62]. This debate on the true structure of the S-phase is still ongoing, and as will be explained further down many different interpretations are given.

2-2.1.2 S-phase Names

There is a lack of agreement on the S-phase not only on the structure but also the name. Several authors use more than one name to describe the same phase, while others have invented terms of their own. Most of these names reflect the suggested crystal structure.

As indicated previously, the term S-phase was invented by Ichii et al., whilst '*expanded austenite'* [13] was used for the first time by Leyland *et al.* in 1993. These terms are the two most commonly used; they are sometimes interchanged within the same publication.

Although not strictly a name, the notation γ_N or γ_C is frequently used in order to describe a nitrogen or carbon S-phase respectively, and is commonly used for indexing peaks in XRD data [2, 63-66]. Similar terms are Y_N or Y_C [20], but these are seldom used.

Marchev *et al.* [67-69] used a completely new designation for the S-phase, namely "*m phase*". The reason for this was that they felt that the term S-phase had become too closely

attached in the literature to the incorrect fcc description. Makishi and Nakata [70] obtained a diffused layer on certain Ni-based materials alloyed with Ti, V, Nb, Cr and Mn. The authors performed XRD on these nitrided alloys and obtained similar peak shifts to those obtained in the S-phase in austenitic stainless steel. Makashi *et al.* [70] also name this phase as M-Phase, but the similarity to the name given by Marchev *et al.* [67] is purely coincidental.

Another name not commonly used is ε' [67, 71], which describes an S-phase which is tetragonally-distorted [71] or a hexagonal structure similar to ε nitride [67-69].

Higashi *et al.* [72] successfully applied the technology of low temperature salt bath nitriding to create the S-phase. Their process was trademarked Palsonite, and thus the name of P-Phase was assigned to their S-phase layer.

2-2.2 Characteristics of S-phase in Austenitic Stainless Steels

S-phase can be formed when large amounts of either nitrogen, carbon or both are dissolved in an austenitic stainless steel or other S-phase forming materials, forming a solid solution without the precipitation of chromium nitrides or carbides.

2-2.2.1 Microstructure

When a treated austenitic stainless steel is sectioned and etched with Marble's reagent, glyceregia, or an acidic etchant (50%HCl + 25%HNO_3 + 25%H_2O), the S-phase layer can be revealed. Under optical microscopy the precipitate-free S-phase layer appears as a featureless bright white layer separated from the matrix by a dark line [17, 18, 73-78]. This white appearance is indicative of a possible improvement in corrosion resistance to the etchant used over that of the original material [17, 18, 73, 75]. If there is a small amount of precipitation in the layer, dark phases can be seen extending from the substrate at the grain boundaries [74-76]; if there is a higher degree of precipitation, extensive dark areas can be observed at the top of the layer [74-76, 79].

It is impossible to distinguish between a nitrogen and carbon S-phase simply by looking under an optical microscope. The only clue is offered by the layer thickness, but this is not determining. A nitrogen-rich S-phase without any precipitates is normally

thinner (6-16μm) [73, 80, 81] than a carbon-rich precipitate-free S-phase (16-50μm) [73, 74, 80]. The layer thickness is also dependent both on time and temperature [79, 82].

2-2.2.2 Chemical Composition

Typical nitrogen concentrations in the surface of a nitrogen-rich S-phase layer range from 20-35at%,[14, 73, 79-81, 83, 84] whilst the carbon concentration of a carbon-rich layer ranges from 5-12at% [14, 73, 74, 76, 79-81, 84, 85]. The concentration profile is of a diffuse type and starts with a high concentration in the surface decreasing progressively to the concentration of the matrix.

Most of the chemical composition studies found in literature were performed using GDOES, but Menthe *et al.* [19] managed to confirm values of 23.5at% and 26.5at% using XPS and EDX respectively on a nitrogen-rich S-phase. Many authors who used the GDOES characterisation technique reported very high values of nitrogen or carbon at the surface [75]. These values might not be correct because the GDOES cannot read accurate stoichiometry at the surface. Weiss [86] in his review of GDOES explains that some elements have different sputtering rates, and thus the stoichiometry in the analysed plasma is different to that at the surface. The probability that some elements are sputtered preferentially is high.

Nitrogen or carbon is presumed to reside in the octahedral interstices of the fcc lattice. A high interstitial content of either carbon or nitrogen is obtained because of the relatively strong affinity of chromium atoms to nitrogen and, to a lesser extent, to carbon atoms, leading to a short range ordering of chromium and nitrogen or carbon [79-81, 84]. Due to the different nature of carbon and nitrogen atoms, the conditions leading to the formation, and the properties of, nitrogen and carbon S-phases are different [73].

2-2.2.3 S-phase Structure

The crystallographic structure of the S-phase has always been in debate. There is not much agreement between the researchers who worked on this phase throughout these two decades. It seems that the structure of the S-phase is very elusive and hard to decipher.

M_4N

On its first discovery, Zhang and Bell suggested that the structure of the S-phase consisted of a mixed phase of Fe_4N and an austenite surface layer, which was completely free of CrN [11]. This theory was backed up by Ichii *et al*. when they described the layer to be a type of M_4N [M = (Fe, Cr, Ni …)] having the same fcc crystal structure as Fe_4N [62]. Both these two theories were dismissed by several authors who argued that from their TEM analysis, no diffraction spots corresponding to the super lattice plane in γ' – M_4N could be identified in the majority of the S-phase layer [87-90].

New Phase on Austenite

Marchev *et al*. [68] stated that the S-phase seemed to grow as a new phase on austenite, rather than forming by the continuous incorporation of nitrogen in austenite. This statement is contradicted and not accepted by many authors. The S-phase cannot be a new phase because its grain size is the same as that of the untreated material [87, 89, 91-93]. It was also noticed that there is a clear continuity of the austenite grain boundaries through the inter-phase surface layer-substrate [75, 80, 87, 88, 94]. Therefore the S-phase is a modification of the parent austenite matrix without the formation of a new phase [95].

Peak Shifting

S-phase XRD peaks are similar to those produced by the untreated fcc austenite, except that all diffraction peaks are shifted to lower angles [18, 74, 75, 77, 85, 96] and appear to be broader [74, 75, 77, 85]. It is also observed that there is an unequal shift between the S(200) and S(111) XRD peak positions. In fact, when one compares the XRD data of the S-phase to that of the untreated material, one can notice that the S(200) peak shifts to lower angles when compared to its S(111) counterpart in relation to the γ(200) and γ(111) peaks of the untreated material [73, 81, 87, 89, 91, 97, 98].

The degree of peak shift also depends on the type and amount of the interstitials (C or N) in the S-phase. The greatest peak shift is observed in the nitrogen-rich S-phase layers with a calculated lattice expansion (based on fcc model) of between 6-10% [17, 99]. While the expansion of the carbon-rich S-phase is of only between 1.4-3% [75, 77, 95]. The peak shifts are lower for the carbon S-phase as would be expected from the lower supersaturation seen in the deeper chemical profiles [81].

Peak shift depends on the treatment temperature. The peak shift to lower angles stops when there is precipitation of chromium nitrides or carbides in the layer [75]. Both nitrogen and carbon-rich S-phase layers do not have a constant d-spacing throughout the layer: the lattice parameter is a maximum at the surface, and progressively decreases with depth in the layer. The peak shifting is thus also dependant on the interstitial concentration of the material. The higher the interstitial concentration, the greater the shift towards smaller angles [75, 77, 95].

FCC Structure with a High Density of Stacking Faults

Face centred structures are the best-recognised descriptions of the S-phase. Yet, as is clear from above, there are still too many unanswered questions.

From TEM, SEM and Optical Microscopy studies it was noticed that the S-phase had a high density of dislocations [2, 74-76, 87-89], slip lines [74, 75, 92, 94-96], deformation twins [75, 76, 88, 89, 100], and stacking faults [2, 74-76, 96, 98, 100]. These microstructural features and crystal defects are closely related to plastic deformation of the fcc crystallites [74, 81, 98, 100]. This plastic deformation is believed to be induced by the high compressive stress after treatment [89, 98, 101].

Blawert *et al*. [81] noticed a shift of the (200) peak in untreated stainless steel that had been cold worked. This led to the conclusion that stacking faults on the (111) plane created by cold working were responsible for this shift. A similarity was noticed between plastically deformed austenitic stainless steel and the S-phase. The authors acknowledged the fact that stacking faults were not the only influence in peak shifting, but were definitely responsible for the shifting of the (200) peaks to a greater degree that the (111) peaks. They also concluded that nitrogen S-phase had a stacking fault average over every 6th layer in the (111) plane, while carbon S-phase has it every 24^{th} and the untreated material every 50^{th} [81].

2-2.2.4 Interstitial Diffusion

A model was proposed whereby nitrogen is trapped at chromium sites resulting in the generation of a highly enriched layer. When all the trap sites become occupied, any additional incoming nitrogen diffuses rapidly to reach the leading edge of the nitrogen

depth profile where unoccupied trap sites are available [102]. Parascandola *et al.* [102] go further and give a trapping and a de-trapping model.

Williamson *et al.* noticed that carbon was always pushed in front of the nitriding front. This carbon was being introduced from the surface because of contamination in the furnace [103]. Authors who worked on the hybrid S-phase (i.e. with both nitrogen and carbon) [14, 17, 64, 73, 78, 99, 104, 105] also noticed this effect, which is called the carbon "push-in effect" or "uphill diffusion." This type of diffusion will be explained further on in the section *Hybrid S-phase,* and corresponds to Parascandola *et al.*'s [102] theory of trapping and de-trapping.

It is a known fact that carbon diffuses faster than nitrogen in austenitic stainless steel, but it was also noticed by many authors that both interstitial elements, carbon and nitrogen, always diffused more rapidly in the (200) plane. This is manifested in a thicker layer growth in the (200) orientation, which can be clearly seen both by using optical microscopy and XRD analysis [65, 103, 106].

The surface oxide layer which gives a good corrosion resistance to austenitic stainless steels acts as a diffusion barrier for nitrogen or carbon transport by diffusion. For this reason it is of paramount importance that this layer is removed before the diffusion treatment is started [102].

2-2.2.5 Metastability

The S-phase is a metastable phase which will decompose if it is subjected to a certain temperature for a certain length of time.

If a nitrogen S-phase is annealed at a temperature higher than the sensitization temperature (>450ºC) for a sufficient amount of time, it will eventually decompose into chromium nitrides, austenite and ferrite. A carbon S-phase held at its corresponding temperature range (>520ºC) will decompose into stable chromium carbides and austenite [88, 89, 107, 108].

If nitrogen and carbon S-phase are annealed at temperatures lower than their respective sensitization temperatures for very long times they will similarly decompose in the above-described manner [88, 89, 94, 107, 108].

When annealed the S-phase becomes thicker, with less interstitial solid solution; softer; and with XRD peaks shifted to larger angles. When precipitation occurs the corrosion resistance of the layer is completely lost [88, 107, 109].

It is as a consequence of its metastability that the S-phase, produced by the commercial Klosterising® process is recommended to be used at operating temperatures which are less than 300ºC [110].

2-2.3 S-phase Formation in Austenitic Stainless Steel

The S-phase as discussed above was discovered when a 316 austenitic stainless steel was plasma nitrided at a low temperature [11, 62]. Since then amounts of research were directed towards S-phase transformation in these alloys. Other stainless steels than austenitic ones have also been treated in order to create the hard and corrosion-resistant S-phase layer. Nickel-based alloys that contain chromium [70, 111-114] and cobalt-chromium alloys [91] also had their surfaces transformed into S-phase. As will be explained further, some have the basic requirements to form this phase whilst others do not.

2-2.3.1 Austenitic Stainless Steels

As long as the temperature of the treatment was kept under the chromium nitride and carbide precipitation threshold temperature, the S-phase was consistently formed in these alloys. Conventional austenitic stainless steels like 316, 304,[78, 92, 104, 115, 116] 303 [80] and 321[17, 75, 78, 117] together with the low carbon grades 316L [2, 63, 94, 118-120] and 304L [63, 97, 118, 121, 122] have had their surfaces successfully transformed into the S-phase. Recently medical grades such as ASTM F138 and F1586 have also been similarly treated successfully, with very promising results for the medical industry [18].

These materials are known to be fully austenitic and have an fcc structure. The high chromium content, generally greater than 16 wt%, is considered as being essential for S-phase formation [123]. This high concentration of chromium together with an iron base matrix is highly important for the solubility of both nitrogen and carbon, and the creation of a solid supersaturate of these elements. It was also reported that molybdenum, although not mandatory, has a positive effect on S-phase formation [110].

2-2.3.2 Duplex Stainless Steels

The microstructure of duplex stainless steels is made of austenite grains (fcc) dispersed in a ferritic (bcc) matrix [80, 83]. Several authors reported that when treated at low temperatures the surface of duplex stainless steel was transformed into the S-phase. The materials treated in five separate investigations where AISI 318 [117, 124], AISI 329 [80, 83], AL2205 [114] and the super duplex SAF 2507 [83]. All of these four materials had their surface transformed into the S-phase, except for the AL2205 grade, regarding which Williamson *et al.* [114] reported a layer made from both the S-phase and hcp phases.

According to these four separate investigations, the ferrite in the duplex stainless steel was transformed into austenite, which was then transformed into S-phase [80, 83, 117, 124]. Larisch *et al.* [124] suggest that this transformation in the ferrite occurred because of the 4wt% nickel in the alloy which assists the transformation into austenite. Christiansen *et al*. [80, 83] explain this phenomenon by implying that nitrogen is an austenite stabilizer, and that therefore ferrite can be transformed. It was also noted by the latter authors that the S-phase layer thickness in the duplex stainless steel was less in the grains which were formerly ferrite, due to different solubility and diffusability of nitrogen.

2-2.3.3 Precipitation-hardened Stainless Steels

The S-phase can only be formed in the fully austenitic alloys; the others; as will be explained; form mixed phases. Esfandiari *et al.* [125] nitrided at low temperature (≤420°C) a fully austenitic precipitation-hardened stainless steel with the designation A286. The authors successfully created a precipitation-free layer of S-phase without any other phases present.

Frandsen *et al.* [126] gas-nitrided two commercially precipitation-hardened alloys named Corax® and Nanoflex®. These materials consist of bcc α' (ferrite formed from austenite by martensite transformation) and fcc austenite. The S-phase was formed on the surface of these alloys together with nitrogen or carbon-containing martensite.

A 17/4 P-H stainless steel was nitrided at low temperature and carburised by Leyland et al. [13]. The surface of this stainless steel was full of precipitates, but when some of the layer was removed expanded austenite could be seen.

2-2.3.4 Martensitic Stainless Steel

In a carburising treatment at temperatures below 400°C Lewis *et al.* [127] reported that the S-phase could not be created in martensitic stainless steels (AISI 440 and 431). This is due to the fact that only carbides could be seen in the nitrided layer.

2-2.4 Processes

In order to create an S-phase layer it is necessary to introduce large quantities of either nitrogen or carbon (or both) in the surface of a material that can be transformed into S-phase. Researchers used different techniques in order to create this phase and this section will review these processes together with others which tried unsuccessfully to create this phase.

2-2.4.1 Plasma Diffusion Processes

The process which is used the most in the creation of S-phase on austenitic stainless steel is low temperature plasma nitriding. Variations of this process are low temperature plasma carburising, carbonitriding (nitrocarburising) and carburising followed by nitriding.

The equipment which is the most frequently used is dc (direct current) [79, 107, 128], pulsed dc [71, 121, 122, 129] and rf (radio-frequency) plasma nitriding [66, 99, 130]. Variations of these processes such as active screen [131-133], high pressure plasma [134], low pressure plasma arc source [135, 136] and anode metal screen plasma nitriding [82, 95, 96, 120] were also successful in the transformation of austenitic stainless steel surfaces into the S-phase.

Low temperature nitriding is the best way of producing a nitrogen S-phase. Nitrogen mixed with another carrier gas such as argon or hydrogen is generally used, although cracked ammonia may be an alternative. In order to produce a carbon S-phase low temperature carburising is employed, the carburising medium being a hydrocarbon gas, for example, methane, mixed with another carrier gas such as argon or hydrogen.

In order to have an S-phase without any precipitation in austenitic stainless steels, one must keep the temperature parameter under good control. A nitrogen-rich precipitate-free S-phase can be formed if the treatment temperature is kept below 450°C, [18, 79, 80, 84, 95, 99] whilst a carbon rich precipitate-free S-phase can be formed using temperatures

below 520°C [18, 74, 79, 80] or 550°C [84] (depending on the point of view of the authors concerned).

In literature there is little agreement on the ideal temperatures required to produce the thickest precipitate free S-phase, due to the fact that there are other factors which influence precipitation. Time and gas mixture compositions are two very important parameters. Different authors use different processes, time, gas mixture composition, pressure and materials. It is therefore impossible to reproduce their results exactly.

2-2.4.2 Gas and Liquid Diffusion Processes

It was believed that gas diffusion processes could not be used in the creation of the S-phase on austenitic stainless steels due to an oxide layer found on these steels that prevents the diffusion of nitrogen and carbon through the surface. Baranowska *et al.* [137-139] used cathodic sputtering to remove this oxide while Christiansen *et al.* [16, 80, 83, 140]removed this oxide layer using fluorides. With the successful removal of this oxide layer it was proved that S-phase can be created using a low temperature gas nitriding and carburising process [116].

Berns *et al*. [141, 142], using a commercial process trademarked Solnit-A®, which consisted of a gas nitriding process at 1050°C followed by quenching, were not successful in creating the S-phase as the diffusion rate was very high and there was no supersaturation of nitrogen.

Higashi *et al.* were successful in creating S-phase on austenitic stainless using low-temperature salt bath nitriding [72].

2-2.4.3 Ion Implantation Processes

Ion Implantation processes such as beam ion implantation (BII) [116], plasma ion implantation (PII) [116] and plasma immersed ion implantation (PI^3) [81, 116, 117, 143], which use higher energies than plasma nitriding processes, were also reported to be successful in the creation of S-phase.

2-2.4.4 PVD Processes

Dearnley *et al*. [144-146] reported that reactive magnetron sputtering enabled S-phase coatings to be produced with nitrogen contents ranging in the region of 8-32 at%.

2-2.5 Role of Crystal Structure and Alloying Elements

As could be perceived from the previous section in order to transform a materials surface into an S-phase some basic requirements are needed. Although austenitic stainless steel can help us understand to some extent which requirements these might be, it is the nickel base alloys together with cobalt-chromium alloys which will help us complete the picture in order to understand them better.

The basic requirements for an S-phase to form in a highly stressed state, with an aim to increase hardness of the untreated material considerably with an adequate thickness are:

- iron-based or cobalt-base alloys with a fcc structure (or a non-fcc structure which is at the limit of transformation into fcc with the addition of stabilizing elements such as nitrogen or carbon);
- a low concentration of nickel (sufficient to keep the material fcc);
- a high alloying content (including elements such as chromium).

2-2.5.1 Crystal Structure Requirement

It was generally believed that a fcc crystal structure was essential in order to form the S-phase [91, 114]. This argument has been supported by the fact that S-phase can not be formed in non-fcc structured ferritic (bcc) and martensitic (bct) stainless steels. However, this claim could not be retained when S-phase was formed in a Cobalt-Chromium alloy and duplex (ferrite-austenite) stainless steels.

As was seen in the previous section, the peak of the bcc ferrite of the duplex stainless steel was not visible anymore in the XRD analysis [80, 83, 117, 124]. Similarly, the peak of the hcp ε phase in the cobalt-chromium alloy could also not be seen [123].

The explanations given by the four researchers concerned were remarkably similar. In the case of duplex stainless steel they agreed that the ferrite transformed into austenite, and this in turn transformed to an S-phase [80, 83, 117, 124]. Similarly, Li *et al*. [123] concluded that the hcp ε was transformed into fcc α which in turn transformed into an S-phase.

The conclusion of these researchers was that both the ferrite and the ε-phase can be transformed into a fcc phase, as only some additional fcc stabilization elements such as nitrogen or carbon are needed for the transformation. This transformation into fcc then permits the material to change into the S-phase with the uptake of more nitrogen or carbon [80, 83, 123, 124].

In two independent studies Williamson *et al.* and Pedraza *et al*. [111, 114] treated two different materials, pure nickel and a NiCr20 alloy, with nitrogen. It should be noted that all these materials are fcc in structure. From XRD analysis it was concluded that the pure nickel alloy did not transform into an S-phase, whilst the NiCr20 alloy did. From this we can conclude that a fcc structure is not the only key requirement for S-phase transformation, and that alloying elements and solubility also play an important part in S-phase formation.

2-2.5.2 Alloying Elements

In this section the alloying elements present in the base material which will help in the formation of the S-phase: Nickel, Iron and Chromium will be discussed.

Nickel

Williamson *et al*. and Pedraza *et al*. [111, 114] treated three different materials with nitrogen: a control austenitic stainless steel sample, pure nickel and a NiCr20 alloy. Pure nickel is known for its low solid solubility with regards to nitrogen. From XRD analysis it was concluded that the pure nickel alloy did not transform into an S-phase, whilst the other two fcc alloys did. It can therefore be deduced that chromium plays a very important role in increasing the solubility of pure nickel. The S-phase layer formed in the NiCr20 alloy is still very thin compared to that formed in austenitic stainless steel, and one can therefore conclude that there are other alloying elements which will promote solubility of nitrogen and thus a thicker and more stressed S-phase layer.

Williamson et al. compare three other different alloys in the same publication: Invar (Fe65Ni34), Permalloy (Fe20Ni80) and Nichrome (NiCr20). S-phase is formed in all the three alloys, with the difference that Invar (Fe65Ni34) has a thicker layer. Thus from here we can conclude that a very high nickel content is not helping the solubility of nitrogen, whilst a high concentration of iron does [114].

Iron

Williamson *et al.* [114] compare 16 different fcc alloys divided into two groups: Nickel and Iron base alloys. With the exception of Invar (Fe65Ni34) and Permalloy (Fe20Ni80), all these materials have a high chromium content (>18wt%) as well as other alloying elements, and these two will therefore be ignored in this section.

The nickel-base alloys all formed a thin and not very stressed S-phase layer, whilst iron-base alloys formed stressed and thicker layers. This leads us to conclude once again that a high level of concentration of iron is beneficial for the formation of a stressed and thick S-phase layer [114].

On the other hand, when the iron base alloys with high alloying content are compared with Invar (Fe65Ni34), it can be concluded that alloying elements such as chromium are very important in promoting supersaturation and solubility. This is because only with iron-base alloys with a high concentration of alloying elements like chromium can one obtain a thick and stressed S-phase layer [114].

Chromium

In a research conducted by Makishi *et al*. [70] it was reported that when binary alloys of nickel were plasma nitrided only the alloys which included titanium, vanadium, niobium, chromium and manganese created an S-phase layer that could be seen with both XRD and optical microscopy.

Williamson *et al*. [114] confirm the results of Makishi *et al*.[70] by saying that alloying elements such as titanium, vanadium, niobium, chromium, manganese and molybdenum all increase the nitrogen solubility. These can be ranked in order of their ability to induce this increase for a given concentration, with titanium being the strongest [114].

It was also noticed that the two Fe-Ni alloys (Invar and Permalloy) had nearly identical lattice expansion and retained doses for the (111) and (200) planes. Thus the alloying elements, chromium in particular, seem to promote and enhance the retention of nitrogen in the (200) planes oriented parallel to the surface [114].

2-2.6 S-phase Properties

2-2.6.1 Hardness

Hardness values of both nitrogen-rich and carbon-rich S-phase have been reported in literature. As expected from XRD data, the nitrogen-rich S-phase is harder than its carbon counterpart. Values in the range of 1300-1500HV at the surface of the nitrogen-rich samples [64, 73, 79, 82, 84, 96] and in the range of 700-1000HV for the carbon-rich ones have been reported [64, 73, 76, 79, 84, 85, 127].

As suggested by XRD hardness varies with depth. A nitrogen S-phase presents a steep and sharp surface hardness profile between the case and core, whilst a carbon S-phase shows a gradual change in hardness from very high values at the surface down to the hardness of the original material [73, 79, 81, 84]. It is due to this fact that a carbon S-phase is described as having a better load bearing capacity than that of a nitrogen S-phase.

2-2.6.2 Fatigue

The S-phase produces an improvement of 25% [79, 84, 147, 148] in fatigue life when compared to untreated austenitic stainless steel. Thaiwatthana *et al*. [79, 84] report that the carbon-rich S-phase has a higher fatigue limit when compared to the nitrogen-rich S-phase. This is due to the fact that the nitrogen-rich S-phase is harder but also more brittle than the carbon-rich counterpart. An S-phase also shows an improvement in the fretting fatigue life time when compared to untreated austenitic stainless steel [79, 84, 147, 148].

2-2.6.3 Wear

Several papers have been written on the wear properties of the S-phase. The loading conditions, type of test, speed, sliding distance, material, treatment conditions, ball material and surface roughness vary from one report to another. It is therefore impossible to compare the reported results in this review [18, 48, 79, 84, 131, 149-151].

It has been indicated by many authors that according to their test conditions the wear resistance of austenitic stainless steel was improved drastically, and that the mechanism of wear changed [18, 84, 131, 149, 151]. It was also reported that the wear resistance of a nitrogen-rich S-phase is slightly better when compared to that of a carbon-rich S-phase

[84]. It is due to the high hardness of the S-phase that so much improvement in wear is manifested.

Most of the wear tests found in literature were carried out using pin-on-disc machines at very low loads. Sun *et al.* [150] reported a very low wear resistance of the S-phase to high loads applied on an Amstel wear tester. It was concluded that the S-phase should never be created in components where the loading conditions are very high. This is because S-phase layers are always very thin (<50μm) and the Hertzian stress at high loads are always a maximum under the S-phase layer. This leads to sub-surface deformation and, therefore, an inadequate wear resistance.

Thaiwatthana *et al*.[152] reported that both nitrogen and carbon rich S-phase can significantly improve the corrosion-wear resistance of austenitic stainless steel. Corrosion-wear experiments done at Leeds University on S-phase coatings by Aldrich-Smith and Dearnley [144] have demonstrated that when using a WC-Co balls as counterface in either 3%NaCl or pure H_2O the S-phase coatings improved the corrosion-wear resistance of the uncoated 316L stainless steel. On the other hand in a separate paper by Dearnley and Aldrich-Smith [55], but again in 3%NaCl, an S-phase coating with 23% nitrogen content rubbing again a WC-Co ball slightly improved the corrosion-wear resistance over the uncoated 316L stainless steel. However when rubbing against an alumina ball, two S-phase coatings with 10% and 25% nitrogen contents improved vastly the corrosion-wear resistance of the untreated 316L stainless steel. This reduction in wear material lost was attributed to Type III corrosion-wear mechanism [55, 145] that was explained in section 2-1.6.5. Work done by Dearnley *et al.* [44] on the corrosion-wear of S-phase coatings on Ortron 90 (ASTM F1586) against an alumina counterface in 0.89%NaCl and bovum serum have demonstrated that all S-phase coatings were effective in mitigating corrsion-wear of Ortron 90 in bovum serum, but only one S-phase coating (21%N) improved the wear resistance when tested in a 0.89% NaCl solution.

Dong *et al*. [153] reported that the erosion-corrosion resistance of austenitic stainless steel in a 20wt% Silica, 3.5% NaCl water slurry can be improved by 50% and 75% respectively for carbon- and nitrogen-rich S-phases.

2-2.6.4 Corrosion

As mentioned in the section on optical microscopy, the corrosion resistance of both carbon and nitrogen S-phases without any chromium nitride or carbide precipitates to corrosive attacks of acid mixture was generally reported to be higher than that of the substrate.

Electrochemical tests on the S-phase have given mixed results as to whether the layer improves, retains or diminishes the corrosion resistance of a stainless steel. It should be made clear that it is almost impossible to compare the corrosion results reported by different authors since the test methods, surface finish, treatment conditions, solution and materials used all vary.

After electrochemical testing it is generally believed that an S-phase without any precipitates does not diminish the corrosion resistance of the material. In some cases an improvement in corrosion resistance was also reported [2, 107, 132]. Surprisingly Gontijo *et al*. [121] report the exact opposite.

A number of authors reported that the nitrogen-rich S-phase layer inhibits pitting corrosion [2, 107, 121, 132, 154]. Nitrogen in the stainless steel is believed to dissolve during the corrosion process, consuming the acid in the pit by the reaction shown in Equation 2-6.

$$[N] + 4H^{+} + 3e^{-} \rightarrow (NH_4)^{+} \qquad \text{…….. (2-6)}$$

This would make the pit more alkaline, and therefore decreases its growth rate [2, 107, 120, 121, 132, 154]. Lei *et al*. [2] demonstrate that pitting can occur in the S-phase when the solution is more acidic. The latter carried out tests at 37°C in Ringer's solution at different pH levels. When the pH was between 5.5 and 7.2 no pitting was observed, but at a pH of 3.5 the opposite occurred. Nitrogen is also believed to be beneficial in the corrosion resistance of austenitic stainless steel because of its stabilizing effect on the oxide film at the surface, and by preventing attack from anions such as chlorides. The stabilisation of austenite by nitrogen is also believed to help [107, 132].

A carbon-rich S-phase without precipitates was also reported not to suffer from pitting corrosion [76, 84, 155]. The mechanism proposed by Martin *et al.* [155] described carbon as a mobile interstitial within the passive film which reduced the resistivity of this film and therefore reduced pitting corrosion.

It has been agreed on by many authors that the beneficial effect of nitrogen and carbon can only be achieved when they are in solid solution. Once either chromium nitrides or carbides precipitate, chromium in the matrix will be depleted. This prevents the formation of a dense and continuous oxide layer on the surface, and thus diminishes the corrosion resistance of the stainless steel. This type of corrosion is called sensitization and is manifested as a form of intergranular corrosion. It has been reported by many authors who carried out their treatments at high temperatures [2, 107, 120, 121, 132].

2-2.7 Hybrid S-phase

The incorporation of nitrogen and carbon, either simultaneously or sequentially, to create a layer which is made from both nitrogen- and carbon-rich S-phase will be called a Hybrid S-phase process for clarity. Since it is considered a novel process it will be considered as a distinct process to conventional individual nitrogen-rich and carbon-rich S-phase.

2-2.7.1 Introduction

In 1993 Leyland *et al*. [13] mentioned for the first time that austenitic stainless steels can be treated with nitrogen and carbon simultaneously, but failed to provide evidence that this type of S-phase can be created. In 2000 Blawert *et al*. [14] successfully created a hybrid S-phase layer on an austenitic stainless steel by applying PI^3 at a temperature of 400°C using a mixture of nitrogen and methane. In 2004 two independent publications [64, 104] reported a hybrid S-phase using a low temperature dc plasma process. Until the present, little research has been devoted to this novel process.

2-2.7.2 Parameters

Table 2-1 shows process parameters used by different authors. The process parameters vary considerably from one author to the other, and it is therefore difficult to compare their results. Table 2-1 lists only the processes which incorporate nitrogen and carbon simultaneously. It was reported in different papers that the same effect can be achieved if a material is first carburised and then post-nitrided [17, 80, 104, 105].

2-2.7.3 Characteristics

When a hyrbrid-treated austenitic stainless steel is sectioned and etched with an acidic etchant (50% HCl + 25% HNO_3 + 25% H_2O) a bright white layer resolvable into two sub-layers can be revealed [17, 64, 78, 104, 105].

Using GDOES it was reported by many authors that when carbon and nitrogen are diffused simultaneously they do not form a mixed S-phase. They instead tend to separate into two layers, with a nitrogen-rich layer close to the surface and a carbon rich-layer at a greater depth [14, 17, 64, 73, 78, 104, 105]. The nitrogen at the surface was reported to be between 24 to 30 at%, whilst the carbon S-phase underneath had a maximum carbon concentration of 3.5 to 6.5 at% [14, 17, 64, 73, 78].

The S-phase peaks obtained in hyrbrid S-phase are similar to the ones obtained after nitriding. The expansion of the lattice is slightly less than that of a nitrogen S-phase, but is much more expanded to that of carbon S-phase [17, 73]. Since the S-phase produced by hyrbrid treatment is not mixed, only the nitrogen peaks may be seen. This happens only when the thickness of the nitrogen-rich S-phase is thicker than the penetration of the X-Rays [73, 104, 105].

2-2.7.4 Interstitial Diffusion

The separation of the nitrogen and carbon in the chemical profiles discussed previously is due to a phenomenon in diffusion called trapping and de-trapping explained by Parascandola *et al*. [102]. During a hyrbrid treatment both carbon and nitrogen are introduced in the surface at the same time. Both carbon and nitrogen occupy the interstitial sites of the host material. A material like austenitic stainless steel has a number of interstitial sites which are considered to be trap sites due to the proximity of chromium atoms to these positions. Nitrogen has a higher affinity to chromium when compared to carbon, and therefore always fills up these trapping sites. If a carbon atom gets trapped in one of these sites it is always de-trapped and replaced by nitrogen if nitrogen is still in diffusion. Once all the trapping sites are filled up the rest of the interstitial elements diffuse more rapidly through the material. Since all the trapping sites are occupied with nitrogen, carbon moves ahead occupying new, as-yet unoccupied trapping sites. It is then de-trapped immediately as more nitrogen moves inwards. This combination of trapping and de-

trapping is the reason why carbon always diffuses more rapidly and always found ahead of the nitriding front in the material.

2-2.7.5 Hardness

The surface hardness observed for a hyrbrid S-phase layer is between 1200 and 1530HV [17, 64, 73, 78, 80]. There is no agreement as to whether this layer is harder or softer compared to nitriding carried out alone. Some authors report that it is slightly harder [17, 64, 80]; others say that it is similar [73]. Sun [78] reports it as being slightly softer. There is an agreement amongst authors that this layer gives a synergistic characteristic in hardness when compared to the individual nitrogen- and carbon-rich S-phase. The hardness profile of a hyrbrid S-phase is a superposition of the nitrogen and carbon S-phase profiles [17, 64, 73, 80]. The hyrbrid S-phase inherits the advantages of both carbon and nitrogen S-phase. It was further reported that a hyrbrid S-phase produced using the same treatment conditions is always thicker than a carburised layer [17, 73]. This leads to a better load-bearing capacity during wear and dynamic loading conditions.

2-2.7.6 Corrosion and Wear

There is no agreement on whether the corrosion resistance of the hybrid S-phase is better or worse than that of untreated stainless steel at temperatures low enough not to precipitate any chromium nitrides or carbides. It has been reported by a number of authors who performed electrochemical experiments that hybrid S-phase improves the corrosion resistance of austenitic stainless steel. Furthermore, the mechanism of corrosion is of a general type and no pitting can be seen [17, 64, 78].

The hybrid S-phase has an improved wear resistance similar to that of individual carbon and nitrogen rich S-phases [73, 105]. There is no real agreement on whether the Hyrbrid S-phase behaves better or worse than the individual nitrogen and carbon S-phases since the wear volume lost is very small and similar.

Chapter III
Materials and Experiments

3-1 Materials

3-1.1 Materials in Bar Form

The main materials used in this study are biomedical austenitic stainless steels in a 25mm diameter annealed bar form and are listed in Table 3-1 together with two other biomedical austenitic stainless steels in a 14mm diameter cold worked bar form which were only used for the biocompatibility studies. All the biomedical materials used in this study adhere to the standards indexed in Table 3-1 and contain no delta ferrite, chi or sigma phases when examined metallographically at a magnification of 100×. The microcleanliness of these steels is shown in Table 3-2 and their mechanical properties in Table 3-3. A more investigated, in terms of S-phase, industrial grade AISI 316 austenitic stainless steel in a 25mm diameter annealed bar form was used for comparison. The chemical compositions of these materials are listed in Table 3-4.

Coupon samples of 6mm in thickness were cut from the bar and one of the flat surfaces was wet ground using SiC paper from 120 down to 1200 grit. Prior to plasma surface alloying treatments, samples were ultrasonically cleaned in acetone and dried with hot air.

3-1.2 Materials in Sphere Form

Four materials used for wear tests were in the sphere form and are listed in Table 3-5. Only the AISI 316 spheres were plasma surface alloyed. Similarly to the coupon samples the spheres were ultrasonically cleaned in acetone and dried with hot air prior to plasma surface alloying.

3-2 Plasma Surface Alloying Treatments

Plasma surface alloying (PSA) was carried out in two Klöckner DC plasma units of 40 and 60kW. All nitrogen bearing processes were carried out in the latter while the rest were carried out in the former. The units consisted of a dc power supply with arc suppression, a vacuum system, a gas supply, a heat shield and a steel cold walled chamber (Figure 3-1). The working table voltage and current were varied between 400 to 650V and 1 to 10A

respectively in order to keep a stable plasma and hence a constant temperature during the process. A sample holder with a hole for a K-type thermocouple wire encased in an alumina ceramic sheath as shown in Figure 3-2 was used. The coupons were placed inside the jig shown in Figure 3-2 throughout the process in order to make sure that there was no edge effects and that the temperature of all the samples being treated was homogeneous.

In order to find the optimized parameters five kind of plasma surface alloying treatments were performed. The treatment parameters – time, temperature, gas composition and pressure – were selected after a literature survey on similar work on austenitic stainless steels. A special attention was given to the work done by Rayner *et al.* [18] since Blake Rayner, during his M.Res project, was the precursor to this work. The five plasma surface alloying treatments have been summarized below:

(1) Plasma surface alloying with nitrogen (Low temperature plasma nitriding – LTPN) at 5 different temperatures was performed and the treatment parameters are shown in Table 3-6.

(2) Plasma surface alloying with carbon (Low temperature plasma carburising – LTPC) at 6 different temperatures was performed and the treatment parameters are listed in Table 3-7.

(3) Plasma surface alloying with both carbon and nitrogen (Low temperature plasma carbonitriding – LTPCN) at a temperature of 460°C at 5 different methane gas compositions was performed and the treatment parameters are indexed in Table 3-8.

(4) Plasma surface alloying with both carbon and nitrogen (Low temperature plasma carbonitriding – LTPCN) at a methane gas composition of 1.5% was performed and the treatment parameters are listed in Table 3-9.

(5) Sequential plasma surface alloying with carbon for 7½ hours followed by plasma surface alloying with nitrogen for another 7½ hours (Sequential low temperature carburising followed by post nitriding - SLTPCN) was performed and the treatment parameters are listed in Table 3-10.

Once the optimized parameters were identified the treatments shown in Table 3-11 were performed. Three repeats in separate batches were done on the annealed AISI 316, ASTM F138 and ASTM F1586 coupons in order to assess the repeatability of the process and to do detailed testing. These parameters were also performed on the annealed ASTM F2581 and on both of the cold worked ASTM F138 and ASTM F1586. In the case of the cold-worked samples the C430 was the only treatment listed in Table 3-11 which was not performed and the sample holder shown in Figure 3-3 was utilized.

AISI 316 spheres were treated with all the parameters mentioned in Table 3-11 with the exception of low temperature carburising at 430°C. The sample holder used in this case is the one shown in Figure 3-4.

3-3 Post-Treatment Sample Surface Preparation for Testing

Table 3-13 lists all the experiments done and what kind of sample surface condition was used for the test. The polishing was done so that no back-deposited superficial layer are on the samples when testing and that the surface finish of all the samples treated and untreated was similar. In fact the surface roughness (Ra) of each tested sample was between 0.06-0.10μm. Throughout this work, after plasma surface alloying, the surface of the samples was tested in two completely different conditions:

(1) As-treated: Samples are tested in the as-treated condition without any post-polishing.

(2) Polished: Samples treated and untreated were polished using 6μm diamond paste for 5 minutes followed by a final polishing using 1μm diamond paste for another 5 minutes. Using this polishing technique for all the samples made sure that less than 1μm was removed from the treated sample surface.

Table 3-13 also lists the bulk material condition, whether annealed or cold worked, of every disc sample that underwent testing. All the data generated in this thesis was from annealed samples with the exception of biocompatibility were cold-worked disc samples were used.

3-4 Characterisation and Techniques

3-4.1 Metallography

Standard procedures were followed to prepare metallographic specimens to be examined under a Leitz DMRX optical microscope. This included cross-sectioning normal to the surface, mounting in phenolic resin, wet grinding with silicon carbide paper from 240 down to 1200 and polishing with diamond water based solutions of 6μm, 1μm and ¼μm sequentially. After polishing the samples were cleaned in acetone and etched in a solution containing 50ml of HCl (39% conc.), 25ml of HNO_3 (69% conc.) and 25ml of distilled water.

3-4.2 Composition Depth Profiling

The chemical composition depth-profile analysis was carried out using a LECO GDS-750 QDP glow discharge optical emission spectroscopy (GDOES). This equipment was calibrated for all the alloying elements found in stainless steel with a special attention to both nitrogen and carbon. The element of carbon was calibrated using a number of cast iron and stainless steel standards for the high and low end of the calibration curve respectively. Elemental nitrogen on the other hand was calibrated with a Coronite® standard and a number of stainless steel standards for the high and low end of the calibration curve respectively. In addition, the depth (using a profilometer) of the sputtered area was compared to the computed depth and were found to agree.

The data obtained was either presented in graphs of concentration (atomic weight %) against depth (μm) or as interstitial (nitrogen or carbon) species absorbed. The nitrogen or carbon species absorbed (gm^{-2}) was calculated using Equation 3-1:

$$\text{Species Absorbed}_{\text{N or C}} = \frac{1}{100} \times A_{\text{N or C}} \times \rho \qquad (3\text{-}1)$$

Where: $A_{\text{Nor C}}$ is the area (μm) under the graph of either nitrogen or carbon which was calculated using Simpson's rule. It is important to note that the graph used was of concentration (mass weight %) against depth (μm).

ρ is the density (gcm^{-3}) of the stainless steel used

3-4.3 Phase Structure Identification

3-4.3.1 X-Radiation Diffraction (XRD)

The phase constituents in the as-received and plasma treated surfaces were analysed with an X'Pert Philips X-Radiation diffractometer using Cu-Kα radiation (λ=0.154nm). The scanning step was of 0.02° at a dwelling time of 3 seconds. The diffraction patterns obtained were analysed and indexed using an X'Pert High Score analytical software for automated powder diffraction.

The XRD was calibrated every six months by a Philips engineer using a Silicon standard [156]. The XRD was also checked with a synthetic fluorophlogopite mica standard [157]. The XRD is accurate to 0.01° 2θ. Systematic errors have been accounted for by making sure that the sample surface lies exactly on the reference plane of the XRD specimen holder. This was achieved by using plasticine at the back of the sample and pressing hard till the sample surface stood exactly on the same plane as the reference plane of the sample holder.

3-4.3.2 Depth Profiling XRD (XSECXRD)

Phase constituents' depth-profiling was carried out using an in-house developed technique. The penetration of Cu-Kα X-rays in austenitic stainless steel is not deep enough to obtain the information from the whole modified layer. Therefore, after the first XRD measurement the sample was taken to the GDOES and was then sputtered for 90 seconds. This created a visible 4mm diameter hole which was 3±0.1μm deep. The top layer was then removed carefully by wet grinding using 1200 grit silicon carbide paper until the 4mm diameter sputtered hole was no longer visible. The freshly ground surface was then re-analysed in the XRD. These steps were repeated to the point where the entire S-phase layer was ground off.

In every step of this experiment, the nitrogen and carbon chemical composition of the new surface was recorded. This was obtained by calculating the average concentration between the intervals of 2.7 and 3μm that was gathered by the GDOES throughout the 90 second sputtering.

3-4.4 Hardness Measurements

Surface hardness was measured using a Mitutoyo MVK-H1 micro-hardness tester with a Vickers indenter at a range of loads varying between 0.025 to 1kgf with three repeats for each measurement. The same equipment but this time with a Knoop indenter and a load of 0.01kgf was used to measure the hardness-depth profile of the modified layer in cross-sectioned samples.

A computer controlled Nano-Test 600 machine (Micromaterials, UK) as shown in Figure 3-5 was used to evaluate the surface hardness (H) and elastic modulus (E) of the as-received and plasma surface alloyed samples. The indentation tests were carried out normal to the surface and 15 points were selected in order to determine the values of H and E.

3-4.5 Scanning Electron Microscopy and EDX

Wear tracks, corroded specimens and cell attachment on samples were examined using a field emission JEOL7000 scanning electron microscope (SEM) with an Energy Dispersive X-Ray (EDX) capability. The chemical compositions of selected wear and wear-corrosion samples were analysed using EDX during SEM examination. The analysis was carried out both qualitatively to determine the existence of certain elements and quantitatively to determine the amount of each element present.

3-4.6 Surface Topography Measurement

A stylus profilometer, Surf Corder SE 1700, was used to profile the wear tracks and to measure the surface roughness of the testing samples. To evaluate the roughness of the testing sample surface the measurements were taken on a distance of 2.5mm and the average surface roughness (Ra) was obtained. Three points on each sample were measured and the average value was reported.

A Laser Confocal Microscope, Olympus Lext OLS-3100, was used to measure the volume lost during fretting wear and to measure the surface roughness of the testing samples.

3-4.7 Inductive Coupled Plasma – Mass Spectroscopy (ICP-MS)

An ICP-MS (Thermo X Series) was used to analyse the concentration of ions of chromium, iron, nickel, manganese and molybdenum in solutions that were used for crevice corrosion experiments.

3-4.7.1 Calibration

A 100X dilution (solution A) was prepared by adding 70µL of each standard (1ppm of Fe, Ni, Cr, Mn and Mo) to 6650µL of 1%HNO_3. A second 500X dilution (solution B) was prepared by adding 1400µL of solution A to 5600µL of 1% HNO_3. A solution C containing 700µL of solution A, 70µL of Cs standard (1ppm) and 6230µL of 1% HNO_3 was created. Another solution D containing 700µL of solution B, 70µL of Cs standard (1ppm) and 6230µL of 1% HNO_3 was created. Both Solution C and D were then diluted (1 in 10) for another three times in 1% HNO_3. These solutions were then fed to the ICP-MS and a calibration curve for the elements of Fe, Ni, Cr, Mn, Mo and Cs (internal standard) at different concentrations was created.

3-4.7.2 Test Samples

According to ICP-MS practice, 700µL of each test sample was added to 70µL of 1ppm Cs standard and to 6230µL of HNO_3, was placed in a vial, mixed and then was fed into the ICP-MS for testing. Ion concentrations of Cr, Ni, Fe, Mn and Mo was obtained in parts per million (ppm).

3-4.8 TEM Analysis

TEM specimens were prepared oriented either parallel to the surface (planar section) or perpendicular to the surface (cross-section). The TEM samples were then examined using a Philips CM20 TEM.

3-4.8.1 Planar Section TEM Sample Preparation

The treated sample as shown in Figure 3-6 was: (1) cut parallel to the surface to a thickness of approximately 1mm; (2) ground from the back to an approximate thickness of 100µm; (3 and 4) punched out into a 3mm diameter disc and polished again from the back

side to a thickness of approximately 30μm; (5) dimpled on the backside using a copper disc, 6μm and 1μm diamond paste; (6) ion beam thinning using a Gatan 691 Precision Ion Polisher System (PIPS™) until a desired thin area was created.

3-4.8.2 Cross-Section TEM (XTEM) Sample Preparation

Figure 3-7 shows a schematic of XTEM sample preparation and the steps (1) to (5) will be explained. The treated sample was sectioned into 2 slabs, 2.2mm wide and 1.2mm thick. (1) These two slabs were then glued with the treated surface (red in Figure 3-7) facing each other. (2) The assembly was cut to a thickness of less than 1mm with the interface of the two glued treated layers in the centre followed by fine grinding and polishing until both surface become planar. (3) This thin assembly was then glued to a 3mm (o.d) and 1mm (i.d) brass reinforcing disc using G-1 epoxy. The exposed side was further polished to a thickness of approximately less than 20μm. (4) The sample is then placed in an ion beam miller - Gatan 691 Precision Ion Polisher System (PIPS™) - making sure that the milling is done in interface of the glued surface. (5) The milling is terminated once a desired thin area around the interface of the glued surfaces is created.

3-4.9 Corrosion Tests

3-4.9.1 Potentiodynamic Tests

Potentiodynamic tests were performed in a corrosion cell having two different configurations. The first configuration was that of an Avesta cell which prevents crevice corrosion by flushing distilled water at a flow rate of 15mLhr^{-1} in order to clean the potential crevice area (Figure 3-8). Later throughout this work it was discovered that flushing the crevice with distilled water was no longer necessary if another smaller O-ring was added as shown in Figure 3-9. For subsequent testing the flat cell configuration was used, which was found to be easier to work with and had less noise in the data collected when compared to the Avesta Cell. No crevice corrosion was visible after testing in both configurations.

The setup for both configurations consisted of a Ag/AgCl reference electrode, a platinum counter electrode and a heating jacket. All tests were conducted in full strength Ringer's solution (composition in Table 3-12) at a constant temperature of 37°C. Full

strength Ringer's solution is a simulated body fluid that mimics the liquid found in the synovial joint.

The sample to be tested was placed against a rubber o-ring at the bottom end of the flat cell, leaving a theoretical circle area of 1.327cm^2 on the sample surface in contact with the testing solution. The open circuit potential (OCP) was monitored for 5 minutes at which point a stable value was obtained. This was followed by a potentiodynamic sweep at a scan rate of 1mVs^{-1} in a voltage range of 0.1V before the OCP to 1V versus reference.

3-4.9.2 Test for Crevice corrosion

This test was performed according to the ASTM: G78-01 Standard guide for: "Crevice corrosion testing of Iron-Base and Nickel-Base alloys in Seawater or other Chloride Containing Aqueous Environments" [158].

Three different materials; ASTM F1586, ASTM F138 and AISI 316; in the untreated state were used throughout this test as control samples. Each material in three different treated states including: nitriding at 430°C, carbonitriding at 430°C and carburising at 500°C, were also used throughout the test. A repeat of each sample per condition was used making the total number of sample to 24. XRD was performed on all of the treated samples just after treatment together with their untreated counterparts.

The samples were then coated with 45-stopping-off lacquer (MacDermid) on their sides, backs and a very small portion of the surface leaving an exposed working area for each sample was of 314mm^2. All the lacquering was done in order to make sure that only the treated material was being tested and that no galvanic coupling effect were present. Three lacquering coatings for each sample were applied in order to make sure that the corrosive solution did not penetrate in the undesired areas.

A multiple crevice assembly washer (MCA) made from Teflon shown in Figure 3-10 was used. The crevice washer had 12 feet and had a 15.8mm outer diameter and a 6.7mm inner diameter. Each washer had an approximate contact area of 252mm^2.

Each coated coupon and MCA were wetted in the test solution and were then squeezed against each other using the polycarbonate sheets shown in Figure 3-11 creating a: crevice shielded to boldly exposed sample area ratio of 1.25. All the tightening was performed using a torque wrench in order to make sure that each crevice assembly had identical tightening. All the metallic fasteners used in these experiments were made from 304

Stainless Steel (RS) and 45-sopping-off lacquer (MacDermid) was again used by applying 3 protective coatings in order to avoid any corrosion products to be released from the screws and nuts. There was no physical contact between the metallic fasteners and the test specimen.

The solution used to conduct this test was composed of 500mls of 0.1M HCl mixed with 4 one quarter strength Ringer's solution tablets (composition in Table 3-12). The pH of the solution was of 0.77. Eight litres of this solution was prepared and then 150ml of it was poured into 24 identical glass beakers. The crevice tightened assembly was then placed in each of the beakers and Clingfilm was used in order to seal the beaker in order to avoid any evaporation of the quiescent solution. This solution was chosen in order to create an artificial crevice solution. An artificial crevice solution is normally very high in chloride content and also low in pH. This kind of aggressive solution cannot be found in the body (except for the stomach) but is necessary in order to obtain artificial crevices in the laboratory.

The beakers were then placed in a water bath at a temperature of 37°C for 10 days. The fluid in each beaker was then replaced with identical fresh corrosion solution. The beakers were then resealed and the new solution was left to proceed to corrode at room temperature for another 20 days. After a total of 30 days the 20 day old corrosion solution was poured out into marked plastic containers in order to be analysed at a later stage.

The samples were disassembled and the lacquer was peeled off. The uncoated specimens were then cleaned in acetone followed by rinsing in distilled water. XRD was then performed on the corroded samples together with micro-hardness measurements and observation of the surface using scanning electron microscopy and optical microscopy. Each corroded sample was then sectioned, polished and examined under the optical microscope. The corrosion products dissolved in the 20 day old solution was analysed using an ICP-MS (Thermo X Series) for ions of chromium, iron, nickel, manganese and molybdenum.

3-4.10 Wear Tests

3-4.10.1 Pin-on-disc

Figure 3-12 shows a schematic view of the pin-on-disc tribometer. Disc samples were made to rotate against a stationary WC-Co ball (Table 3-5) 8mm in diameter at a speed of 66revmin^{-1} (0.031ms^{-1}) for 3000m under non-lubricated conditions. The normal contact load acting on the pin was of 10N and a wear track of 9mm in diameter was produced. The wear loss volume was determined by measuring the cross-section of a wear track using a stylus profilometer. To obtain the wear volume, the area of the wear scar was calculated using Simpson's rule and then multiplying by the circumferential length of the wear track. Three measurements were performed for each wear track and the average value is reported.

WC-Co balls were used during this test because of their high hardness and high wear resistance. These properties were needed in order for the counterface material not to be worn too much. The calculated Hertzian contact pressure for this test was of around 1.55GPa (Table 3-14). This value is much higher than the proof stress (0.2%) of the untreated materials used in this work (Table 3-3).

3-4.10.2 Reciprocating-wear test

Figure 3-13 shows a schematic view of the reciprocating-wear tester. The polished (Ra = 0,06 to 0.1μm) treated and untreated coupons were cut into blocks 5mm by 7mm by 6mm. The samples were then glued to another block and the treated surface was masked using tape. The assembly was then clamped into the holder and was spray lacquered. When the lacquer dried the masking tape was removed and the sample surface was cleaned with acetone. Four kinds of tests were done:

Ni-Containing Stainless Steel versus WC-Cobalt

During this test, the sample was made to move linearly against a stationary WC-Cobalt ball (surface finish as supplied) of 12.7mm in diameter at an average speed of 6mms^{-1} (0.5Hz) for 200m under three conditions: non-lubricated, in full strength Ringer's solution and in distilled water. The normal contact load acting on the pin was of 54N and a wear scar of 6mm in length was produced. The test was repeated two times per condition. WC-Co balls

were used during this test because of their high hardness and high wear resistance. These properties were needed in order for the counterface material not to be worn too much.

Ni-Free Stainless Steel versus WC-Cobalt

During this test, the sample was made to move linearly against a stationary WC-Cobalt ball (surface finish as supplied) of 12.7mm in diameter at an average speed of 6mms^{-1} (0.5Hz) for 200m under two conditions: non-lubricated and in full strength Ringer's solution. The normal contact load acting on the pin was of 54N and a wear scar of 6mm in length was produced. The test was repeated six times per condition. WC-Co balls were used during this test because of their high hardness and high wear resistance. These properties were needed in order for the counterface material not to be worn too much.

ASTM F75 versus Stellite-6

During this test, the sample was made to move linearly against a stationary Stellite-6 ball (surface finish as supplied) of 12.7mm in diameter at an average speed of 12.5mms^{-1} (1Hz) for 200m in full strength Ringer's solution. The normal contact load acting on the pin was of 39N and a wear scar of 6mm in length was produced. The test was repeated two times per condition.

Ni-Containing Stainless Steel versus Ni-Containing Stainless Steel

In this test treated and untreated AISI 316 balls were used. Details of the treatments can be found in section 3-2. Before testing the treated balls were slightly polished with ¼μm diamond paste and then washed in acetone whilst the untreated balls were used as supplied. During this test, the sample was made to move linearly against a stationary treated or untreated stainless steel ball of 12.7mm in diameter at an average speed of 12.5mms^{-1} (1Hz) for 200m in full strength Ringer's solution. The normal contact load acting on the pin was of 39N and a wear scar of 6mm in length was produced. The test was repeated two times per condition.

Wear Loss Determination

The wear loss volume was determined by measuring the cross-section of a wear track using a stylus profilometer. To obtain the wear volume, the area of the wear scar was calculated using Simpson's rule and then multiplying by the length of the wear track. Three measurements were performed for each wear track and the average value is reported. The morphologies of the wear scars were characterised by a JEOL 7000 SEM with an EDX capability.

Hertzian Contact Pressure

The calculated Hertzian contact pressure for the reciprocating-wear tests are shown in Table 3-14. The lowest value obtained for contact pressure was for the stainless steel versus stainless steel tests were a value of 1.4GPa was obtained. Again this value is much higher than the proof stress (0.2%) of the untreated materials used in this work (Table 3-3). This pressure was selected in order to accelerate corrosion-wear process during the test, which is higher than the average contact pressures in human hip joint replacements which can be ~50-90MPa [44] for metal-on-metal designs under peak loading conditions.

3-4.11 Fretting-Corrosion tests

Fretting corrosion tests were carried out on a horizontal servo-hydraulic fretting test machine (DS20 PLINT, France). Owing to its suitable mechanical and corrosion properties, AISI 440C stainless steel balls 40 mm in diameter was selected as the counterpart moving horizontally against the stationary plate specimen. All the specimens for fretting tests were tested at a normal contact load acting on the ball was of 100N at a frequency of 5Hz in 150mL full-strength Ringer's solution simulating the fretting conditions in human body. The number of cycles were changed from $1x10^4$ to $2x10^4$ while keeping the displacement D=100μm.The fretting tests were repeated at least two times for the nickel-containing stainless steel and three times for the nickel-free stainless steel. The tangential force F_t and the number of cycles were recorded by the test machine. The profiles of the fretting pits were measured by a laser confocal microscope (Olympus Lext OLS-3100), and the morphologies of the wear scars were characterized by an optical microscope.

3-4.12 Biocompatibility

3-4.12.1 Preparation of Cell Suspensions

MCT3T3 (American Type Culture Collection™) CRL-2593 mouse Osteoblasts Cell Line were thawed from storage in liquid N_2 and transferred to: 200ml of McCoy's 5A Medium containing L-Glutamine (Gibco™); 20ml of Fetal Calf Serum (Sigma™); 5ml HEPES (Sigma™); and 2ml of Penicillin / Streptomycin (50 units mL^{-1} Sigma™) in a tissue culture flask. This was incubated in 5% (v/v) carbon dioxide (CO_2) at 37°C for 3-4 days until the cells were confluent, with a change of medium after the first 48 hours.

Cells were detached from the flask by removing the old media, adding 10mL of 0.25% Trypsin-EDTA (Sigma™) and then replacing the flask again in the incubator for 1 minute. 7mL of the enzyme was removed and the flask was replaced in the incubator for another 3 minutes. When complete detachment of the cells was observed the trypsin was diluted with 10mL fresh culture medium and the cells were then centrifuged at 1,500 rpm for 3 minutes, the remaining 3mL of Trypsin-EDTA was discarded and was replaced by 2mL of fresh McCoy's 5A medium. The cell number in the suspension was determined using a haemocytometer and was adjusted to100,000 cells mL^{-1} and 25,000 cells mL^{-1} for the viability assays and the cell attachment assays respectively.

3-4.12.2 Cell Proliferation Assays (MTT Test)

The number of viable cells on the samples was estimated using an MTT test. This test measures the production of formozan which is formed by reduction of tetrazolium salt MTT. The amount of formozan is proportional to the number of actively metabolising viable cells.

The metallic samples and the control plastic samples (Manufacturer - Thermanox® coverslips) were placed in the wells of 24-well plates (Costar®). 100,000 cells mL^{-1} were seeded in 1mL of media per well, covering the upper surface of the samples. The cells were then incubated in 5% (v/v) carbon dioxide (CO_2) at 37°C. Four wells per series were used on day 1, 2, 3 and 7 for cell viability measurements.

The cell proliferation assay was performed in the following way: 2mL of MTT solution - $5mgmL^{-1}$ of MTT (3-(4,5-Dimethylthiazol)-2,5-diphenyltetrazolium bromide) (Aldrich™) in Phosphate buffered saline – was prepared.

60μL of MTT solution were added to the wells containing the cells on the samples that were intended to be assayed. The 24-well plates containing the MTT were placed on a shaking table for 5 minutes and were then incubated for four hours in 5% (v/v) carbon dioxide (CO_2) at 37°C in order for the cells to metabolize the MTT. This was followed by carefully removing each sample into a new 24-well plate and adding 400μL of Dimethylsulphdioxide (Sigma™ Hybri-Max®) in order to solubilise the formazan. This re-suspension makes the solution turn blue. These wells were then placed on a shaking table for 5 minutes followed by a careful removal of the samples from each well without losing any of the blue coloured solution. An Elisa (ELX300) plate reader was used to read the absorbance at a wavelength of 570nm of each blue coloured solution. These intensities were later converted into the number of cells using a calibration curve.

For every condition and for every day interval the cells were fixed on the samples in order to view them under a scanning electron microscope. In order to prepare these samples the medium was pipetted off, and the implants were rinsed with phosphate-buffered saline (PBS). Samples were fixed for 3 minutes in a solution containing 1mL 25% Glutaraldehyde (EM Grade, Sigma™), 5mL of 0.2M Sodium Cacodylate buffer pH 7.3 (EM Grade, Agar Scientific ™) and 4mL of distilled water. The fixative was removed and was replaced with of 0.1M Sodium Cacodylate buffer pH 7.3 (Agar Scientific™). After 10 minutes the latter was removed and the cells were dehydrated in aqueous ethanol solutions of different concentrations (25, 50, 60, 70, 80, 90 and 100%) for a duration of 10 minutes per step. The 100% ethanol was removed and replaced with hexamethyldisilizane (Sigma ™) for another 10 minutes in a fume cupboard. This was then removed and the samples were left to dry for 1 hour in the fume cupboard. Samples were then coated with gold using a Poloron sputter coater.

3-4.12.3 Cell Attachment Assays

20mL of culture media containing 25,000 cells per ml was placed for 30 minutes recovery from the trypsin used to harvest cells in an incubator at 37°C in a 5% (v/v) carbon dioxide (CO_2) atmosphere. Three metal samples per condition were placed in a sterilized petridish and were exposed to approximately 500,000 recovered cells in 20mL of media. After 30 minutes of incubation at 37°C in a 5% (v/v) carbon dioxide (CO_2) atmosphere, the medium containing the unattached cells was pipetted out and the metal samples were rinsed with

phosphate-buffered saline to remove any unattached cells. The cells were then fixed, dehydrated and coated in gold as mentioned above.

The number of cells attached to implant surfaces was determined from 3 replicate experiments (3 samples per condition). Cells were classified according to 4 stages of attachment as described by Rajaraman *et al.*, [159]. In this classification, the first stage of attachment is characterized by rounded cells with a few filopodia, which progress to cells with focal cytoplasmic extensions or lamellipodia (stage 2), circumferential spreading (stage 3), and full spreading and flattening into a polygonal shape (stage 4).

Chapter IV
Experimental Results

It is well documented that low temperature plasma surface alloying with nitrogen, carbon or both can improve the wear resistance of austenitic stainless steel without loss of their corrosion resistance. However, there is no systematic work on medical grade austenitic stainless steel. Therefore this present study is aimed to improve the wear resistance of medical grade austenitic stainless steels - ASTM F138, ASTM F1586 and ASTM F2581 - without any deterioration on their corrosion resistance.

In this chapter, the microstructure of the as-received materials that were used in this study is presented, followed by a systematic approach of selecting the optimum treatment parameters for three low temperature treatments – nitriding, carburising and carbonitriding - using XRD analysis, GDOES, preliminary wear testing and corrosion testing. This is then followed by an in-depth analysis and comparison of each optimised treatment for all the three different materials.

Since there are only a handful of publications that mention the surface hardening of these three medical grade austenitic stainless steels, all the results mentioned in this research were continuously benchmarked against a more known and documented austenitic stainless steel – AISI 316.

4-1 Microstructure and Properties of the Untreated Materials

Medical grade austenitic stainless steels should be fully austenitic and without any presence of delta ferrite. Figure 4-1.1 presents the XRD profiles of all the austenitic stainless steel materials that have been used in this study. It can be seen that except for the "AISI 316 Balls" that were used in wear-corrosion experiments, all the materials are fully austenitic (Table A-1 and A-7). The "AISI 316 Balls", which are not medical grade, are dominated by austenite with a small amount of ferrite since an α (110) peak can be clearly seen at an angle of 45°. It is also noted that for some materials (such as ASTM F2581, ASTM F1586 and ASTM F1586-High Tensile) there is a slight shift in the peak positions

of austenite when compared to the peaks for the benchmark AISI 316 material. This could be related the fact that these materials have a higher interstitial content of nitrogen when compared to AISI 316.

The most important property of austenitic stainless steels is their superior corrosion resistance. Figure 4-1.2 shows a potentiodynamic plot of current density against voltage for four austenitic stainless steels and a Co-Cr alloy for comparison. Clearly, when tested in full strength Ringer's solution AISI 316 showed the worst corrosion properties when compared to the other materials used in the study. The OCP of this material is about -0.2V vs. Ag/AgCl with a current density in the region of $1X10^{-6}$ Acm^{-2}. The material then pits at a breakdown voltage around 0V vs. Ag/AgCl. ASTM F138 and ASTM F1586 behave very similarly to each other and have an OCP identical to that for AISI 316. These two medical grade austenitic stainless steels are passive at a current density of $1X10^{-6}$ Acm^{-2}; however, unlike ASTM F1586 which remains passive up to 1V vs. Ag/AgCl, the ASTM F138 reveals a breakdown voltage in the region of 0.8V vs. Ag/AgCl, indicating that it possesses an inferior corrosion resistance to the ASTM F1586. All these three medical grade austenitic stainless steel materials were compared with a high carbon cobalt-chromium alloy which is commonly used in medical applications. The OCP of the Co-Cr alloy shifted towards a less noble position (-0.4V vs. Ag/AgCl) and displayed a passive nature but had a slightly higher passive current density of $2X10^{-6}$ Acm^{-2} when compared to these medical grade stainless steels. In addition, this material also exhibited a larger increase in current density when the voltage was increase to above 0.5V vs. Ag/AgCl, which could be attributed to the dissolution of chromium ($Cr_2O_3 \rightarrow Cr^{6+} + 3e^-$).

Figure 4-1.3 shows the nano-hardness of the four austenitic stainless steels that were used throughout this research. It can be seen that the hardness and elastic modulus of AISI 316 and ASTM F138 are almost identical; compared with these two materials, the hardness increased and elastic modulus decreased in the order of ASTM F1586 and ASTM F2581. The increased hardness of ASTM F1586 and ASTM F2581 is in accordance with the XRD data showed in Figure 4-1.1 where ASTM F2581 and ASTM F1586 showed the greatest peak shift to lower angles. The higher hardness is due to the fact that these two alloys have higher nitrogen content. The elastic modulus of these stainless steels is very similar to that of Co-Cr alloys (225±25GPa); however, the latter is harder (about 6±1 GPa) than the former [160].

As evidenced in Figure 4-1.2 the medical grade stainless steels have excellent corrosion properties but their hardness as shown in Figure 4-1.3 leaves much to be desired. The combined properties of corrosion resistance and wear resistance are necessary if these materials are to be used in load-bearing medical applications such as hip-joint prosthesis. In the following sections a systematic approach of hardening these materials without deteriorating their superior corrosion properties will be presented.

4-2 Optimizing the Treatments

In order to identify the optimal treatment conditions, a series of low temperature plasma alloying treatments with N (nitriding), C (carburising) and both C and N (carbonitriding) were conducted at temperatures ranging from 400°C to 540°C for three materials (AISI 316, ASTM F138 and ASTM F1586). The treated materials were characterized using XRD, GDOES and potentiodynamic corrosion tests as well as preliminary pin-on-disc wear tests, and the results are presented in this section.

4-2.1 Plasma Alloying Using N (Nitriding)

Low temperature plasma alloying with N (i.e. nitriding) was performed on AISI 316, ASTM F138 and ASTM F1586 in the temperatures range from 420°C to 460°C. Figures 4-2.1.1, 4-2.1.2 and 4-2.1.3 show the nitrogen depth profiles of the treated materials. It can be seen that the alloying element, nitrogen, can diffuse deeper into substrate with increasing the temperature and that the average nitrogen absorbed at the surface was about 20 at%. It seems that there is no significant difference between the three alloys in nitrogen depth distribution and one can conclude that all the three materials showed a similar nitriding response.

Nitriding is governed by the laws of diffusion and therefore Fick's second law of diffusion applies. Since atomic diffusion involves atomic movements, it is to be expected that increasing the temperature of a diffusion system will increase the diffusion rate. It is for this reason that the depth of the composition profiles shown in Figures 4-2.1.1 to 3 increase in depth with an increase in temperature. This applies to all the other diffusion treatments (carburising and carbonitriding) presented in this work.

From Figures 4-2.1.1 to 3 it can be seen that the surface value of N varied between treatments. An explanation for this was given by Weiss [86] in his review about GDOES. The author explained that some elements have different sputtering rates, and thus the stoichiometry in the analysed plasma is different to that at the surface. The probability that some elements are sputtered preferentially is high. Light elements like nitrogen or carbon have a tendency to be sputtered preferentially and therefore have a tendency to yield very high values at the surface. It is for this reason that GDOES values in the first one micron of depth of light elements can be considered as inaccurate.

Figures 4-2.1.4, 4-2.1.5 and 4-2.1.6 show the XRD plots for the ASTM F1586, ASTM F138 and AISI 316 that were plasma nitrided at different temperatures. When compared to the untreated material one can notice that there is a shift in peaks to lower angles. This large shift is synonymous with the formation of S-phase in the surface of the material. In general, the peak shift increases with increasing the treatment temperature. In addition, two peaks at 37° and 42° can be observed in Figure 4-2.1.4, which might be indexed to $Cr_2N(110)$ and $Cr_2N(111)$ respectively (Table A-1 and A-5). No peaks of Cr_2N can be seen in the other two materials (Figures 4-2.1.5 & 6).

Figure 4-2.1.7 shows potentiodynamic curves for plasma nitrided ASTM F1586 at three different temperatures together with that for its untreated counterpart. When compared with the untreated material, the OCP of the treated samples was shifted to nobler potentials. Although the current density of the low-temperature (420°C and 440°C) treated samples are similar to that for the untreated material, higher current density was found for the 460°C treated sample because of sensitization. Therefore, the 420°C sample showed improved corrosion resistance in terms of both OCP and current densities when compared to the untreated material. The 440°C treated sample showed virtually the same corrosion resistance as the untreated material. However, the 460°C treated sample showed improved corrosion resistance when the voltage is below 0V vs. Ag/AgCl but reduced corrosion resistance in the higher voltage range.

Figure 4-2.1.8 shows the sweeps for plasma nitrided and untreated ASTM F138. The sample that was treated at a temperature of 460°C showed a shift in OCP to a more noble position but sensitization was manifested by a large increase of current. On the other hand, the samples treated at 420°C and 440°C showed slightly improved corrosion resistance because of the shift in OCP to a more noble voltage and no pitting.

Figure 4-2.1.9 shows the corrosion plot for treated and untreated AISI 316. While the 460°C treated sample exhibited sensitization, the samples treated at 420°C and 440°C demonstrated an improvement in corrosion resistance. It can be noticed that for the treated samples no pitting potential can be seen and that the OCP moved to a more noble position. This implies that for samples treated at 420°C and 440°C there is an improved corrosion resistance.

From the results obtained shown in the XRD plots, corrosion plots and nitrogen profiles it can be concluded that in order to obtain an S-phase layer without any detriment in corrosion resistance plasma nitriding should be performed no more than 440°C. Allowing a factor of safety of 10°C it was decided that the optimum temperature of 430°C should be used for the detailed experimentation.

4-2.2 Plasma Alloying with C (Carburising)

Low temperature plasma alloying using carbon (i.e. plasma carburising) was performed on AISI 316, ASTM F138 and ASTM F1586. The temperatures that were assessed ranged from 430°C to 540°C. Figures 4-2.2.1, 4-2.2.2 and 4-2.2.3 show the carbon depth profiles of the treated materials. These plots show that the thickness of the carburised cases increased with increasing the treatment temperature and that the average carbon absorbed at the surface was of 8 at%. It can be found by comparing Figures 4-2.2.1, 4-2.2.2 and 4-2.2.3 that all the three materials exhibited similar carburising response.

The XRD plots for the ASTM F1586, ASTM F138 and AISI 316 samples that were plasma carburised at different temperatures are shown in Figures 4-2.2.4, 4-2.2.5 and 4-2.2.6. When compared to the peaks for the untreated materials, the corresponding peaks of the plasma carburised materials were shifted to lower angles, implying the formation of carbon supersaturated austenite i.e. carbon S-phase. The shift of the carbon S-phase peaks increased initially with increasing temperature but then it reached a stable value when the temperature reached 460°C. Finally, the back shift of the peaks to higher angles occurred once precipitation started to occur. For these three alloys the precipitation of carbides occurred at 540°C as evidenced by the peaks of $C_{23}C_6$ (Table A-1 and A-6) shown in Figures 4-2.2.4 to 6. It was noticed that Fe_3C (Table A-1 and A-3) can be identified in all treated samples and Fe_5C_2 (Table A-1 and A-2) in some treatments. This was formed during plasma carburising through a back-deposition mechanism since such superficial

Fe_3C and Fe_5C_2 can be easily removed by post-treatment polishing. It was also noticed by comparing Figures 4-2.1.4 to 6 with Figures 4-2.2.4 to 6 that the degree of shifting for the carbon S-phase is less than that of the nitrogen S-phase.

Figure 4-2.2.7 shows the potentiodynamic curves for ASTM F1586. It can be seen that the OCP of all the treated samples shifted to a more noble voltage and that all the treatments except for carburising at 540°C showed similar current densities to the untreated material. Therefore, low-temperature (≤520°C) carburised samples possessed a similar or even slightly better corrosion resistance relative to the untreated material whilst the 540°C treated sample showed marginal deterioration of the corrosion resistance.

Figures 4-2.2.8 and 4-2.2.9 show the corrosion plots for ASTM F138 and AISI 316, respectively. Except for 540°C treatment, all other treatment can, more or less, improve the corrosion resistance of these two materials. It can be also noticed that no signs of pitting can be seen for the treated samples. The 540°C treated samples showed a severe intergranular attack, which are in agreement with the XRD results where chromium carbide precipitates could be seen (Figures 4-2.2.5 and 6).

Thus it follows based on the XRD, corrosion and chemical profiles results that in order to obtain a carbon S-phase layer without any detriment in corrosion resistance plasma carburising should be performed at temperatures below 520°C. Allowing a factor of safety of 20°C it was decided that 500°C should be used for the detailed experimentation.

4-2.3 Plasma Alloying Using C and N

4-2.3.1 Sequential Treatment

Figures 4-2.3.1, 4-2.3.2 and 4-2.3.3 show the variation of interstitial alloying element concentrations in the surface layers produced by sequential treatments (CN450-400) together with that produced by single nitriding and carburising for comparison. The GDOES charts consist of two pairs of nitrogen and carbon profiles. The first pair of nitrogen and carbon curves (see green and black curves respectively in Figures 4-2.3.1 to 3) are for sequential treated CN450-400 sample, which was first subjected to plasma carburising at 450ºC for 7.5h followed by post-nitriding at 400ºC for 7.5h. For the purpose of comparison, the second pair of nitrogen and carbon curves (see red and blue curves

respectively in Figure 4-2.3.1 to 3) are also provided for two separate processes: C450 (carburising at 450ºC for 7.5h) and N400 (nitriding at 400ºC for 7.5h).

It can be seen from the depth distribution of C and N that two separate layers were formed during the sequential treatments: a nitrogen rich layer close to the surface followed by a carbon rich layer at greater depths. This phenomenon, also known as the “push-in” effect, was observed from all the GDOES profiles obtained from the sequential treatments for all the three materials.

Figures 4-2.3.4, 4-2.3.5 and 4-2.3.6 show typical X-ray diffraction patterns of plasma surface alloyed ASTM F1586, ASTM F138 and AISI 316 with carbon, nitrogen and both. Each XRD plot consists of four diffraction patterns: the top one is for the CN450-400 sample which was first plasma carburised at 450ºC for 7.5h and then post-nitrided at 400ºC for 7.5h; the second one is for the C450 sample which was carburised at 450ºC for 7.5h; the third one is for the N400 sample which was nitrided at 400ºC for 7.5h; and the bottom one is for the untreated material. The XRD patterns for these three sequentially treated materials are very similar.

The XRD patterns of the treated material are similar to those produced by the untreated FCC austenite (Table A-7), except that all of the reflection peaks from the S-phase layer shifted to lower angles owing to the supersaturation of interstitial alloying elements. Carbon S-phase peaks were identified from the XRD pattern of the C450 sample. However, peaks from both nitrogen S-phase and austenite were identified for N400 sample. This is because the penetration depth of the X-ray in austenite was estimated to be about 6μm, which is larger than the thickness of the nitrogen S-phase produced by N400 treatment. For this reason, both nitrogen S-phase and carbon S-phase peaks were found from the XRD pattern of CN450-400 sample. In addition, a weak peak was found from the pattern, which could be assigned to Fe_3C (Table A-3).

4-2.3.2 Simultaneous Treatment (Carbonitriding)

Low temperature (430°C to 460°C) plasma alloying simultaneously with carbon and nitrogen was performed on ASTM F1586, ASTM F138 and AISI 316. Figures 4-2.3.7 to 9 show the nitrogen and carbon depth-profiles of the treated materials. It is of great interest to find that carbon and nitrogen do not mix in expanded austenite layers and indeed they tend to form two separate layers: a nitrogen rich layer close to the surface followed by a

carbon rich layer at greater depths. The chemical depth profiles obtained from the carbonitriding treatments match to the ones obtained from sequential treatments (Figures 4-2.3.1 to 3). The mechanism involved in the formation of two separate layers will be discussed in Chapter 5.

Figures 4-2.3.10 to 12 show the XRD plots of ASTM F1586, ASTM F138, and AISI 316, respectively. When compared to the untreated material one can notice that there is a shift in peaks to lower angles. In all the plots a peak of Fe_3C (211) can be seen (Table A-3), which was also observed from carburised samples as shown before.

Figures 4-2.3.13 to 15 show XRD profiles for carbonitrided ASTM F1586, ASTM F138 and AISI 316, respectively as a function of CH_4 content (0, 0.5, 1, 1.5, 2 and 3% CH_4) used in the carbonitriding treatments. Apart from the nitrogen S-phase peaks, Fe_3C peaks (Table A-3) were indentified from the XRD plots, the intensity of which increased with increasing CH_4%.

Figure 4-2.3.16 shows the corrosion curves for treated and untreated ASTM F1586 samples. Compared with the untreated material, the OCP of all the treated samples was shifted a nobler value. The low-temperature (430°C and 440°C) treated samples showed similar corrosion current density to the untreated material; on the other hand, the treatments performed at 450°C and 460°C showed large current densities, which is a sign of intergranular corrosion. As shown in Figure 4-2.3.17, the corrosion behaviour of ASTM F138 is very similar to that of ASTM F1586 with less deterioration in corrosion resistance for the latter than for the former when they were treated at temperatures above 440°C. Figure 4-2.3.18 shows the potentiodynamic curves for treated and untreated AISI 316. All the samples had their OCP shifted to a nobler position and improved corrosion resistance as compared with the untreated sample. However, the treatments above 440°C led to slightly elevated corrosion currents as compared to the low-temperature treated material.

In summary, in order to ensure retained good corrosion resistance plasma surface alloying treatments with both carbon and nitrogen should be performed at temperatures below 440°C. Therefore, it was decided that 430°C should be used for the detailed experimentation. Also it was decided that sequential treatments will not be included in the detailed experimentation for the fact that these involve two separate processes, thus making this process economically not feasible.

4-2.4 Preliminary Pin-On-Disc Wear Tests

In the previous section it was concluded that it is possible to retain the good corrosion resistance of medical grade austenitic stainless steels provided the plasma treatment temperature is below 440°C for nitriding and carbonitriding and below 520°C for carburising. The next step was to assess whether these treatments can improve the wear resistance of these materials. Figure 4-2.4.1 shows a bar chart of untreated and plasma surface alloyed (nitriding, carburising, carbonitriding and sequential treatments) ASTM F138, ASTM F1586 and AISI 316 at temperatures lower than the critical temperatures mentioned above. From the chart it can be easily seen that all the surface treatments have improved the wear resistance of the materials considerably and it is therefore necessary to test these treatments at optimum conditions in greater detail.

4-3 Optimized Treatments

In the following sections three optimized treatments, plasma alloying with nitrogen at 430°C (nitriding), carbon at 500°C (carburising) and both carbon and nitrogen (carbonitriding) at 430°C will be fully investigated together with an extra treatment, plasma carburising at 430°C for comparison. In addition, a Ni-free medical grade austenitic stainless steel, the ASTM F2581 will also be introduced.

Systematic characterization will be divided into three sections: General characterization (Optical microscopy, chemical analysis, phase analysis and transmission electron microscopy analysis); Mechanical and electrochemical properties (Hardness, corrosion, wear, corrosion-wear and corrosion-fretting-wear); and biocompatibility.

4-3.1 Optical Microstructure

The cross-section microstructures shown in Figures 4-3.1.1 to 4 reveal a very similar surface layer formed in all the four materials investigated. The surface modified layer in most treated samples appears to be bright white. This is an indication that the surface layer has superior corrosion properties to the untreated material when etched. The exceptions are for the plasma nitrided ASTM F1586 (Figure 4-3.1.1a) and ASTM F2581 (Figure 4-3.1.4a) where black areas can be seen in the top region. The distinct line at the substrate-layer interface, especially in the nitrided and carbonitrided layers and to a lesser extent in the

carburised layers, is due to a grinding and polishing artefact where a step was formed by the difference in hardness between the hard S-phase layer and the soft substrate.

4-3.2 Chemical Analysis

The depth distributions of nitrogen and carbon for all the surface treated materials were probed using a GDOES machine and the results for the four different materials can be seen in Figures 4-3.2.1 to 4. The thickness of the nitrogen- and carbon-diffused layers as determined from the nitrogen and carbon depth profiles is in good agreement with those measured from the optical microscope cross-section microstructures shown in Figures 4-3.1.1 to 4.

For all the four treated materials, the 430°C nitrided layer is about 10μm thick with a surface nitrogen content of 15 to 20 at% while the 430°C carburised layer is about 15μm thick with surface carbon content between 5 and 10 at%. The thickness of the 500°C carburised layers are of 30 to 35μm. The chemical compositions of the carbonitrided layers have indicated that the S-phase layer formed was divided into two sublayers: a top nitrogen-rich (~15 at%) sublayer followed by a carbon-rich (7 to 10 at%) sublayer. The thickness of the nitrogen-rich sublayer and the total layer is around 10 and 20 to 22μm, respectively.

It is noted that for all the four materials treated at the same temperature (430°C) for the same period (15hrs), the thickness of the total modified surface layer decreased in the order of the carbonitrided, carburised and nitrided samples. Figure 4-3.2.5 summarises the alloying species absorbed in the plasma modified cases by integrating the areas under the corresponding GDOES curves. The alloying species absorbed during the three treatments (nitriding, carburising and carbonitriding) at 430°C for 15hrs decreased in the order of the carbonitrided, nitrided and carburised samples, which is different from the layer thickness order as discussed above. It is interesting to note that the 430°C carbonitrided layer absorbed almost the same amount of species as the 500°C carburised layer.

4-3.3 XRD Phase Analysis

Figures 4-3.3.1, 4-3.3.2 and 4-3.3.3 show the X-ray diffraction patterns of plasma surface alloyed Fe-Cr-Ni austenitic stainless steels (ASTM F1586, ASTM F138 and AISI 316) with nitrogen (nitriding 430°C for 15h), carbon (carburising at 430°C and 500°C for 15h) and both C and N (carbonitriding 430°C for 15h). It can be seen by comparing these three figures that the XRD patterns for these three Fe-Cr-Ni austenitic stainless steels are very similar, implying their response to plasma surface alloying with C, N or C/N is generally alike.

As reported in Section 4-2, the XRD patterns for the treated material and the untreated FCC austenite are very similar but the reflection peaks from the S-phase layer shifted to lower angles when compared to the corresponding austenite FCC peaks. The peak shifting is an indication that the lattice of FCC austenite was expanded and thus stressed and the larger the peak shifting the more the layer is expanded and stressed. The peaks of the 430°C carbonitrided layers are at a point between the corresponding peaks for the carburised (430°C and 500°C) and the 430°C nitrided samples. It seems that the diffusion of nitrogen was probably hindered by carbon atoms which already occupied interstitial sites.

In the carbonitrided samples extra weak peaks can be seen in the XRD profiles, which are correspondent to Fe_3C (cementite - Table A-3). Whilst in the carburised samples both Fe_3C (cementite – Table A-3) and Fe_5C_2 (Hagg-carbide – Table A-2) are found at every sample surface.

Figure 4-3.3.4 shows the X-ray diffraction patterns from as-treated and polished plasma surface alloyed ASTM F2581. On the as-carburised samples Fe_3C (cementite – Table A-3) and Fe_5C_2 (Hagg-Carbide – Table A-2) can be identified but these peaks disappeared after polishing away the first 1μm of the surface. This indicates that these iron carbides are at the very surface of the carburised material. However, Mn_3N_2 (Table A-4) and Cr_2N (Table A-5) were identified on the nitrided FN430 and carbonitrided FNC430 samples respectively even after polishing, indicating that these precipitates are within the surface treated layer.

The plots depicted in Figures 4-3.3.5 and 4-3.3.6 show the variation of the lattice parameter calculated from the 111 plane against the depth of the layer for treated ASTM F1586 and ASTM F138 samples, respectively. The lattice parameter of the 430°C nitrided

specimen drops abruptly at the layer-core interface. Whilst that of the carburised materials (430°C and 500°C) has a gradually decreasing lattice parameter profile although the lattice parameter at the surface is not as large as the corresponding nitrided layer. The 430°C carbonitrided layer has a large lattice parameter at the surface as for nitrided layer, which reduce slowly with the depth as for carburised layer.

The 111 peak is not the ideal peak to calculate the lattice parameter from since its diffraction lies at a low 2θ angle. Since the largest gradient of the sinθ curve is at low values of θ, a small error in the recorded angle of the diffraction peak will cause a significant error in the calculated lattice parameter. At high values of θ the error in the calculated sinθ value will be reduced and leads to a smaller error in the calculated value of the lattice parameter [161]. In this work the 111 peak was selected for two reasons: (1) this peak has the highest intensity and is easily identifiable whilst the other high angle diffraction peaks with the exception of the 200 peak are not easily identifiable since they have very low intensities and are extremely broad; (2) the structure of the S-phase is not a pure fcc and therefore the assumption of using an fcc equation to calculate the lattice parameter is by itself inaccurate. Therefore the 200 peak was not selected because this peak was found to deviate more from the fcc structure than the 111 peak.

4-3.4 TEM Analysis

4-3.4.1 XTEM of Carbonitrided ASTM F138 and ASTM F1586 Samples

Cross-section TEM (XTEM) studies were conducted on carbonitrided ASTM F138 and ASTM F1586 specimens. XTEM observations revealed that a typical carbonitrided layer consisted of a very thin fine-grained outer layer, a N-rich S-phase layer with a d-spacing of 0.2193nm close to the surface and a C-rich S-phase layer with a d-spacing of 0.212nm close to the N-rich interface (See Table 4-1 and Appendix).

Outer Layer

The outer layer structure for plasma carbonitrided ASTM F1586 is shown in Figure 4-3.4.1. The outer layer had a thickness of approximately 50nm and consisted of very fine equiaxed grains. The selected area diffraction (SAD) pattern of the layer at Area A (Figure 4-3.4.1) revealed sharp diffraction rings which can be assigned to a fcc structure M(N,C)

(M=Fe, Cr, Ni, Mo and Mn). The structure was found to be similar to that of CrN and the rings observed indicate that the grain size of this layer is very fine. The weak diffraction spots in Figure 4-3.4.1b were contributed from the S-phase layer just beneath the outer layer. The SAD pattern of the N-rich S-phase layer (Area B) is given in Figure 4-3.4.1c.

S-phase Layer

Plenty of twins, slip bands and entangled dislocations were observed in the S-phase layer. Figure 4-3.4.2 shows the dislocations and Figure 4-3.4.3 shows many twins and slip bands found in the S-phase layer.

Figure 4-3.4.4a shows a typical XTEM microstructure of the S-phase layer created on ASTM F138 by plasma carbonitriding. The ion milling of this sample was performed at a very small offset such that a thin interface area between the N-rich and C-rich S-phase (S_N and S_C, respectively) can be viewed. TEM observations revealed that the interface between the S_N and S_C sublayers is within an original grain since the SAD patterns from B and C are almost the same. However, difference in interstitial content made the N- and C-rich S-phase have different crystal constants. The SAD patterns obtained in Area B (Figure 4-3.4.4b) gave a lattice parameter of circa 0.3817nm which can be attributed to the N-rich S-phase. While the SAD pattern in Area C (Figure 4-3.4.4c), which was 2μm away from Area B revealed a smaller lattice parameter of circa 0.3703nm, which can be assigned to the C-rich S-phase.

4-3.4.2 XTEM of Carburised ASTM F138 Samples

Figure 4-3.4.5a shows a XTEM microstructure of S-phase layer created on ASTM F138 by plasma carburising at 500°C. A layer of chromium was applied to the surface using PVD in order to protect the surface of the modified layer from damage during sample preparation. The SAD patterns (Figure 4-3.4.5b) obtained from Area (i) in Figure 4-3.4.5a can be assigned to C-rich S-phase. Lamellar precipitates very close to the surface can be seen in Area (ii) in Figure 4-3.4.5a and the SAD (Figure 4-3.4.5c) can be assigned to Hagg-carbides (Fe_5C_2) although weak diffraction spots from the chromium protective layer were also picked up.

4-3.4.3 Plane-view TEM of ASTM F2581 Ni-free Austenitic Stainless Steel

The XRD data suggested that S-phase was created for the first time in Nickel-free austenitic stainless steel, ASTM F2581, and more detailed TEM crystallographical analysis was carried on 430°C nitrided, 430°C carbonitrided and 500°C carburised samples.

430°C Plasma Nitrided Samples

TEM observation of the plasma nitrided ASTM F2581 sample revealed that the dominant phase of the layer is N S-phase. Figure 4-3.4.6 shows the S-phase microstructure and corresponding SAD pattern of (111) zone. Dislocations and slip bands evidenced by the weak spots along the [112] directions in Figure 4-3.4.6b can be seen. However, in some areas, although no apparent precipitates could be recognized, SAD analysis revealed two sets of diffraction patterns (Figure 4-3.4.7b). The diffraction patterns of S-phase and Mn_3N_2 were superimposed together and their orientation relationship was as follows:

$$[011]s \,//\, [331]Mn_3N_2$$
$$(\bar{1}\bar{1}1)s \,//\, (1\bar{1}0)Mn_3N_2$$

High resolution TEM showed a tweed microstructure which indicated a fine lamellar precipitation of Mn_3N_2 within the S-phase (Figure 4-3.4.7a).

430°C Plasma Carbonitrided Samples

Figure 4-3.4.8 represents the microstructure of the plasma carbonitrided ASTM F2581. Plenty of entangled dislocations and slip bands, which are characteristic of S-phase, can be observed in Figure 4-3.4.8a. SAD patterns revealed that this surface layer consisted mainly of S-phase.

500°C Carburised Samples

TEM study of plasma carburised ASTM F2581 sample was conducted and the typical microstructure and SAD patterns are given in Figure 4-3.4.9. The SAD pattern revealed that only a single carbon S-phase was present in the layer and it was precipitate free. In addition, systematic TEM observations also demonstrated that the grain boundaries as

shown in Figure 4-3.4.9a can be traced to those in the substrate, indicating that the surface layer kept the original austenite grains.

4-3.5 Mechanical Properties

4-3.5.1 Hardness: Nano-hardness

Figure 4-3.5.1 summarizes the nano-indentation results for four different materials treated using four different processes. It can be clearly seen that all the four materials can be hardened significantly using any of these surface alloying processes. For a given treatment, all the four materials exhibited very similar hardening effect; for a given material treated at 430°C, the surface hardness decreased in the order of nitrided, carbonitrided and carburised layers. The hardness of carburised materials increased with the increase in the treatment temperature.

4-3.5.2 Hardness: Load Bearing Capacity

Figures 4-3.5.2 to 4 show the load bearing capacity of the three different materials treated using four different processes. It can be seen by comparing these figures that all the three Fe-Ni-Cr alloys showed very similar load bearing capacity as a function of different treatment conditions.

The surface hardness of the nitrided specimen decreased quickly when the indentation load was above 100g, indication of its relatively low load bearing capacity. The 430°C carburised layer behaved similarly to the nitrided layer but with much lower surface hardness. On the other hand, the 500°C carburised layer showed a lower surface hardness relative to nitrided layer but the highest load-bearing capacity at higher loads. This is due to the fact that the carburised layer formed at 500°C is much thicker than the nitrided layer and therefore can support the indentation load better. With the strong support by the underlying C-enriched layer, the carbonitrided treated surfaces exhibited a much enhanced load bearing capacity as compared to both the 430°C nitrided and 430°C carburised surfaces.

Figure 4-3.5.5 shows the load bearing capacity of the Ni-free ASTM F2581 stainless steel. It can be seen that the nitrided layer and the carbonitrided layer showed similar high load bearing capacity, which is followed by that of carburised layers.

4-3.5.3 Hardness: Profiles

Figures 4-3.5.6, 4-3.5.7 and 4-3.5.8 shows the hardness depth profiles of plasma surface alloyed ASTM F1586, ASTM F138 and AISI 316.

The hardness of the 430°C nitrided specimen is nearly constant across the nitrided layer and drops abruptly at the layer-core interface. Such an abrupt hardness drop may account for the observed brittleness and poor load bearing capacity of the nitrided specimen. The low temperature (430°C) carburised sample behaved in a similar manner but it also came with the disadvantage of low surface hardness. On the other hand, high-temperature (500°C) carburised sample produced a thicker layer with a gradually decreasing hardness profile although its peak hardness is not as high as the corresponding nitrided layer. The hardness depth profiles of the 430°C carbonitrided samples showed the synergetic characteristics of both nitriding (430°C) and carburising (430°C). The hardness depth profiles of the carbonitrided treatments are characterized by a high surface hardness, a deep layer and a gradually decreasing hardness.

4-3.6 Corrosion: Potentiodynamic Polarisation Tests

Figures 4-3.6.1 to 4-3.6.4 represent the corrosion results for plasma surface alloyed and untreated ASTM F1586, ASTM F138, AISI 316 and ASTM F2581, respectively. No crevice corrosion similar to the one shown in Figure 4-3.6.6 and Figure 4-3.6.7 could be seen in any of the tested samples.

As shown in Figure 4-3.6.1, the OCP for all plasma surface alloyed as well as the untreated ASTM F1586 is almost the same (-0.2V vs. Ag/AgCl). The carburised samples exhibited virtually the same corrosion behaviour to the untreated material. The nitrided and carbonitrided samples showed an increase in passive current when the voltage reached 0 and 0.3V vs. Ag/AgCl, respectively. This increase in current can be attributed to intergranular corrosion as evidenced by the SEM image shown in Figure 4-3.6.8. It must be indicated that no pitting could be observed in both treated and untreated material after the corrosion tests.

It seems from Figure 4-3.6.2 that all the plasma treated samples possess similar corrosion performances to the untreated material since these potentiodynamic curves coincided together. However, it is noted that a sharp increase in current appeared at a voltage around 0.8V vs. Ag/AgCl on the potentiodynamic curve for the untreated material,

implying that pitting occurred to the untreated material; however, no such current increase was observed from the potentiodynamic curves for the plasma treated material. Therefore, it follows that the pitting corrosion resistance of ASTM F138 has been improved after the treatments.

It can be seen from Figure 4-3.6.3 that the OCP for all the AISI 316 samples tested is almost the same (-0.2V vs. Ag/AgCl). No pitting occurred for all the treated samples throughout the entire test sweep but the untreated material pitted (Figure 4-3.6.5) at an early stage (~ 0V vs. Ag/AgCl). Clearly, all the plasma surface alloying treatments can effectively improve the pitting corrosion resistance of AISI316.

For ASTM F2581, except for the 430°C nitrided sample all other treated samples showed similar corrosion performances to the untreated material (Figure 4-3.6.4). An increase in the passive current at a voltage of 0.5V vs. Ag/AgCl was recorded and the SEM image of the corroded surface revealed intergranular corrosion (Figure 4-3.6.9).

4-3.7 Corrosion: Immersion Crevice Corrosion Tests

Three different materials, ASTM F1586, ASTM F138 and AISI 316, treated and untreated were subjected to immersion crevice corrosion tests. All corroded samples or their respective corrosion solutions were analysed using XRD, ICPMS, micro-hardness, optical microscopy and scanning electron microscopy. Throughout this section each material will be reported separately in order to know what might have happened during the immersion corrosion tests. Then a general comparison of the untreated and treated layers will be presented.

4-3.7.1 ASTM F1586

Initial visual inspection revealed that all the tests samples appeared uncorroded, and staining could only be seen on the untreated specimens where the feet of the multiple crevice washer were pressed. When hardness measurements were taken inside and outside the crevice area it was established that the surface layer had survived for all the treated samples. The surface of the samples was then examined under SEM and surface attack was only observed in the nitrided and the carbonitrided samples in the form of intergranular corrosion. In some cases on the nitrided samples grain pullout and peeling of the surface

(Figure 4-3.7.2) was observed while for the carbonitrided samples in addition to grain pullout (Figure 4-3.7.1) bulging of the surface was also observed.

A lot of information was obtained from the XRD analysis before and after the crevice tests. Figure 4-3.7.3 shows the XRD results for all the ASTM F1586 samples before and after the corrosion tests. As expected, the XRD peaks before and after the test of the untreated material were the same. For the nitrided samples their peaks moved slightly to higher angles and a very faint peak from the substrate material can be seen. There was no difference in peak position for the carbonitrided material and no changes were observed for the S-phase peaks of the carburised samples but the cementite peak was no longer visible since the surface was polished prior to the corrosion test.

Of great interest was the cross-section of the ASTM F1586 nitrided sample. In fact as can be seen from Figure 4-3.7.2 the layer was almost entirely peeled off but still just hung to the substrate. Had the test lasted slightly longer the layer would have been completely lost and only the untreated peaks would have been registered after the XRD analysis. This is in agreement with the XRD results since the S-phase peaks observed were generated by the almost peeled off nitrogen S-phase layer.

Figure 4-3.7.4 shows the ICPMS results and it can be seen that the concentration of metal ion released in the solution after 20 days of corrosion was much higher for the untreated and the carburised (C500) samples than for the nitrided (N430) and carbonitrided (NC430) samples. These results at a first glance appear to be quite strange since the samples that showed less corrosion leached a higher concentration of ions while the samples that seemed to be corroded more leached less metal ions. But it must be borne in mind that the corrosion observed on the untreated and carburised sample was completely uniform while the corrosion observed on the nitrided and carbonitrided sample was localised in the form of intergranular corrosion. Intergranular corrosion may release fewer ions into the solution than uniform corrosion but the damage caused by the former could be more severe than by the latter.

4-3.7.2 ASTM F138

Visual inspection revealed a very rough surface morphology (Figure 4-3.7.5b) on the carbonitrided samples whilst the other samples appeared not to be attacked by the corrosive liquid. The only attack on the untreated material was manifested as very light

staining on which the multiple crevice washer feet were pressed during the crevice tests, Figure 4-3.7.5a.

Hardness measurements were taken inside and outside the crevice area and the results indicated that the surface layer may have survived for all the treatment conditions except for nitriding where the hardness of the substrate material was registered after the corrosion tests. SEM observations revealed corrosion to all three treated surfaces. The carburised samples showed the least attack followed by the nitrided samples, both of which revealed a very slight etch. On the other hand, the carbonitrided samples showed an attack where the slip lines were very strongly demarked (Figure 4-3.7.6). No intergranular attack was visible in any of the ASTM F138 samples.

Figure 4-3.7.7 shows the XRD results of all ASTM F138 samples before and after the corrosion tests, which are to a larger extent similar to that for ASTM F1586 (Figure 4-3.7.3). However, it was noted by comparing Figure 4-3.7.7 with Figure 4-3.7.3 that for the nitrided samples a large shifting of the (111) S-phase peaks to higher angles and very high intensity substrate peaks were observed. This gave enough evidence to conclude that the majority of the S-phase layer on the nitrided samples was almost completely lost.

The ICPMS results in Figure 4-3.7.4 indicates that compared with the untreated sample, all the treated samples released more metal ions into the solution; the carbonitrided sample leached the lowest level of metal ions among all the treated samples. This is in agreement with the attacks observed on the treated materials under SEM. In fact the untreated material did not appear corroded at all, whilst on all the treated samples corrosion in the form of light etching and strongly demarked slip lines was observed.

4-3.7.3 AISI 316

It seems from visual inspection that except for the carburised sample all other samples appeared to be completely corroded with roughened surfaces (Figure 4-3.7.8). However, hardness measurements inside and outside the crevice area implied that all the surface layers (except for the nitrided one) survived from the corrosion tests.

The surface of the samples was examined under the SEM and different kinds of corrosion attack were observed on these samples. The untreated material (Figure 4-3.7.9) showed general corrosion with very fine pits outside the crevice area (Figure 4-3.7.9a) whilst staining and pitting could be observed inside the crevice area (Figure 4-3.7.9b). The

nitrided material showed strong etching outside the crevice area (Figure 4-3.7.10a marked B) whilst in the area under the crevice washer pits (Figure 4-3.7.10a marked A), uncorroded areas and dark etching was observed. The carburised sample showed slight etching under the crevice area (Figure 4-3.7.10b marked A) and strong demarking of slip line outside of the crevice area (Figure 4-3.7.10b marked B). The carbonitrided sample, as shown in Figure 4-3.7.11, had evidence of pitting and uncorroded areas under crevice former (Figure 4-3.7.11a marked A) and strong demarking of slip lines at the exposed area (Figure 4-3.7.11b).

The XRD analysis was carried out before and after the corrosion tests and the results are given in Figure 4-3.7.12. No appreciable changes to the XRD profiles of the untreated and carburised material after the corrosion tests were observed. The greatest change in the XRD profiles occurred to nitrided sample following the corrosion test as evidenced by the large intensity reduction and shifting of the S_N(111) peak, very high substrate peaks and the complete disappearance of the S_N (200) peaks. This indicates that the S-phase layer on the nitrided samples was almost completely removed by corrosion. For the carbonitrided sample, the S-phase (111) and (200) peaks moved slightly to higher angles, indicating that a small part of the nitrogen S-phase might have been corroded away.

The cross-sections of the untreated sample revealed a corrosion mechanism involving grain pull-out, peeling of the surface and pitting (Figure 4-3.7.13). The nitrided sample showed peeling of the nitrided layer and pitting of areas where the nitrided layer no longer existed any more. The tested carbonitrided section showed bulging of the surface and pits growing in the substrate material (Figure 4-3.7.14). The carburised sample showed the least corrosion in the form of uniform corrosion although slight peeling could be observed in very few areas.

The ICPMS results shown in Figure 4-3.7.4 indicate that the untreated and the carburised samples released a low level of ions to the corroding solution whilst the nitrided and the carbonitrided samples produced a large amount of ions. Compared with the medical grade ASTM F1586 and F138, the engineering grade AISI 316 leased a much higher level of metal ions regardless treatment conditions.

4-3.8 Wear and Wear-Corrosion (Stainless Steel versus WC-Cobalt)

4-3.8.1 Wear Lost

Figure 4-3.8.1 depicts the wear and wear-corrosion properties of untreated and 430°C carbonitrided ASTM F1586, ASTM F138 and AISI 316 Fe-Ni-Cr austenitic stainless steels. The test was performed in three different conditions – dry (air), corrosive (Ringer's solution) and wet (distilled water).

When tested in air (dry), the wear volume loss of both the untreated and carbonitrided materials increased in the order of AISI 316, ASTM F138 and ASTM F1586. However, it is impressive that carbonitriding can significantly improve the wear resistance of all these three materials. The higher wear resistance of AISI 316 relative to ASTM F138 and ASTM F1586 could not be simply related to their hardness since AISI316 is indeed softer than ASTM F138 and ASTM F1586 under both untreated and carbonitrided conditions (Figure 4-3.5.1). This difference may be attributed to the fact that compared with AISI 316, ASTM F1586 and ASTM F138 have a much lower content of inclusions (especially soft sulphides), which could act as lubricants under unlubricated conditions (Table 3-2).

When tested in Ringer's solution and distilled water, the untreated materials showed a much more reduced wear loss. This is probably due to the fact that the Ringer's solution and the distilled water can act as a lubricant and therefore reduce wear. However, the wear loss was larger when tested in Ringer's solution than in distilled water because of synergetic effect of corrosion action of the Ringer's solution and mechanical action of sliding. In addition, all the carbonitrided samples have shown an improvement in their wear resistance in corrosive and wet environments. The percentage improvement over the untreated material is less distinct in the distilled water than in the Ringer's solution, which produced an improvement of up to 100%.

Figure 4-3.8.2 depicts the wear volume lost of treated and untreated ASTM F2581 in dry-wear and corrosion-wear tests. Although all the treatments can improve the wear resistance of this material under both tests conditions, the wear improvement can be best seen in the dry wear conditions where the nitrided sample showed an improvement of 1500% over the untreated one. As described previously in Figure 4-3.8.1, the wear loss for the untreated ASTM F2581 in the Ringer's solution was again lower than in air (dry). All the treated samples showed an improvement over the untreated in the wear resistance of the material in Ringer's solution. It should be noted though that the wear loss of the treated

samples (except for the 430°C carburised) was slightly higher in Ringer's solution than in air (dry).

Since the hardening of ASTM F2581 has never been attempted before and no publications on this subject can be found, Figure 4-3.8.3 was included in order to compare the performance of this material in dry-wear and corrosion-wear scenarios with stainless steels that are well studied. From this chart it can be clearly seen that ASTM F2581 has similar wear losses to AISI 316 stainless steel in dry conditions but when tested in Ringer's solution its wear loss was the highest among all the untreated materials. When treated and tested in dry-conditions this treated material has showed the best performance when compared to the other three materials. Whilst in the corrosion-wear conditions its performance was not the best but was in line with the other treated material.

4-3.8.2 Wear Track Morphology

Untreated ASTM F138

Dry Conditions: The back scattered images in topography and composition mode, for the centre part of the wear track in untreated ASTM F138 after dry wear test, are given in Figures 4-3.8.4 (a) and (b), respectively. Similar photos are shown in Figures 4-3.8.5 (a) and (b) for the end part of the wear track of untreated ASTM F138 in dry wear conditions. In both Figures 4-3.8.4 and 4-3.8.5 galling and smearing can be seen. The galling seen on this sample is characterised by localised tearing and roughening. EDX results on the dark areas (smearing) in Figures 4-3.8.4b and 4-3.8.5b have revealed a high presence of tungsten and oxygen, whilst the lighter areas had the composition of stainless steel. This leads to a conclusion that the wear between the untreated ASTM F138 and WC-cobalt ball is governed mainly by adhesive wear mechanism together with mild oxidation wear.

In Ringer's solution: The mechanism of wear for untreated ASTM F138 against WC-cobalt ball was completely changed when tested in Ringer's solution. As can be seen from Figure 4-3.8.6, the wear observed on this surface is of an abrasion mechanism type which is evidenced by deep parallel grooves in the direction of sliding. EDX in the wear track has revealed a presence of oxygen within the wear track. Rust at the edges of the wear track could be noted in Figure 4-3.8.6 (a) but was easily removed using acetone as shown in Figure 4-3.8.6 (b). This change in wear mechanism from severe (adhesive) to mild

(abrasive) is the reason for the improvement in wear loss (Figure 4-3.8.1) for the untreated ASTM F138 samples tested in dry and lubricated conditions, respectively.

Untreated ASTM F2581

Dry Conditions: The type of wear that is manifested in untreated ASTM F2581 against WC-Cobalt is similar to that of untreated ASTM F138. The SEI SEM images at two different magnifications in Figures 4-3.8.7 (a) and (b) give evidence of galling and smearing again. EDX spot analysis within the wear track has revealed a high presence of tungsten and oxygen. This is an indication that adhesive wear is present since the ball material contains large amounts of tungsten and oxidation wear may have also played a role in the wear process.

In Ringer's solution: Deep parallel grooves in the direction of sliding can be seen in Figure 4-3.8.8 (a), which are representative for abrasive wear. Therefore, abrasive wear is again the mechanism for the untreated stainless steel tested in Ringer's solution. In the right part of the SEM photo (Figure 4-3.8.8b) rust similar to that found on ASTM F138 can be seen. It is believed that this patch of rust was created from oxidised wear debris which was pushed out of the wear track and eventually deposited on the surface of the material.

Treated ASTM F138

Ringer's solution: After treatment ASTM F138 revealed a similar wear morphology to the untreated alloy in Ringer's solution but with a difference that the grooves seen were not very deep explaining the improved wear-corrosion properties over the untreated shown in Figure 4-3.8.1. SEM and EDX results of the wear track shown in Figure 4-3.8.9 shows an abrasive type of wear together with a slight oxidation of the surface. Intergranular corrosion can also be seen within the wear track. Since the image was taken using back scattered electrons (topography mode) the wear track appears to be rough due to this type of corrosion around the grain boundaries.

Treated ASTM F1586

Ringer's solution: Treated ASTM F1586 also suffered from a similar wear mechanism to that of treated ASTM F138. Figure 4-3.8.10 (a) shows an overview of the wear track which is appears to have shallow grooves and a polished appearance explaining the improved wear-corrosion resistance over the untreated. Figures 4-3.8.10 (b) and (c) show grain boundary attack at the end part of the wear scar which is similar to that observed in treated ASTM F138.

Treated AISI 316

Ringer's solution: The wear mechanism in this case is governed by abrasive wear and slight oxidation of the surface. The back scattered electron (topography) SEM image shown in Figure 4-3.8.11a reveals shallow grooves in the direction of sliding which is representative of mild abrasive wear. While the dark features present in Figure 4-3.8.11b are rich in oxygen, indication of oxidation wear.

Treated ASTM F2581

Dry conditions: The wear morphology of treated ASTM F2581 in air (dry conditions) is reported in Figure 4-3.8.12. It can be seen from Figure 4-3.8.12 (b) that the tested surface seemed covered by a thin black film. EDX analysis revealed that the thin film on the wear track was rich in oxygen and doped with tungsten. This indicates that a this oxide film was formed during the wear of plasma treated ASTM F2581 and its wear was dominated by a oxidation wear mechanism together with transfer of tungsten from the counterpart WC ball. When compared to untreated samples (Figure.4-3.8.7), no tearing (adhesive wear) or deep grooves (abrasive wear) can be seen in the wear scar and this explains the greatly improved wear resistance of the alloy.

Ringer's solution: The typical wear track morphologies of treated ASTM F2581 formed in Ringer's solution are given Figure 4-3.8.13. As depicted in 4-3.8.13 (a), the surface appears to be polished with very fine scratches. Figure 4-3.8.13 (b) represents the end part of the wear track of treated ASTM F2581 in Ringer's solution. Rust deposits similar to that seen in the untreated material could be seen at the end of the wear scar.

4-3.9 Stainless Steel versus Stainless Steel

As reported in the preceding sections, the S-phase layers have demonstrated significantly enhanced wear properties when sliding against WC-Cobalt balls. However, no information is openly available in the literature on the wear behaviour of a tribo-pair both made from S-phase layers. This is both scientifically and technologically important since the S-phase may have the potential for metal-on-metal joint prostheses.

To this end, commercial AISI 316 balls were plasma surface alloyed with nitrogen, carbon and both of them. Figures 4-3.9.1 (a), (b) and (c) show S-phase layers on the AISI316 stainless steel balls which were generated by nitriding at 430°C, carbonitriding at 430°C and carburising at 500°C, respectively. As it can be seen from Figure 4-3.9.1a that the S-phase layer is not completely white and probably some precipitates are present. Figure 4-3.9.1b shows a hybrid S-phase layer with some precipitation in the top part of the layer whilst the carburised layer shown in Figure 4-3.9.1c on the other hand seems to be precipitate free.

4-3.9.1 Wear Loss of Discs

Wear of Untreated Disc Samples

As shown in Figure 4-3.9.2a, the wear loss of untreated ASTM F138 disc against untreated AISI 316 balls is very high whilst the wear loss of untreated ASTM F1586 and AISI 316 discs is only about 1/3 that of untreated ASTM F138 disc when tested under the same conditions. The wear loss of the untreated ASTM F138 discs is still much higher than that of untreated ASTM F1586 and AISI 316 discs when sliding against C500 and N430 treated AISI 316 balls. However, when sliding against NC430 treated ball, all three untreated discs showed almost the same wear. Therefore, it follows that among all the untreated discs, the ASTM F138 disc showed the highest wear whether is was against untreated or treated (except for NC430 treated) AISI 316 balls.

It is of interest to note that the wear loss of the untreated ASTM F138 discs was larger when sliding against the untreated soft AISI 316 balls than against treated hard ones; on other hand, the wear loss of the untreated ASTM F1586 and AISI 316 discs was smaller when sliding against the untreated soft AISI 316 balls than against treated hard ones except for untreated AISI316 disc against NC430 treated ball). Furthermore, it is interesting that the wear of all three untreated discs is larger when wearing against C500 treated AISI 316

balls than N430 and NC430 treated ones although the latter is normally harder than the former.

Wear of Plasma Alloyed Discs Samples

The wear loss of surface treated disc samples can be compared from Figure 4-3.9.2a. For C430 treated discs, no significant counterface effect can be observed when the experimental errors were taken into account; however, the treated AISI 316 discs were always worn more than the other two treated discs (ASTM F138 and ASTM F1586) regardless the treatment conditions used. Similarly, the counterfaces did not play significant effect on the wear of three types of NC430 treated discs when sliding against NC430 and N430; however, the wear loss of NC430 treated ASTM F1586 disc was much lower than that for NC430 treated ASTM F138 and AISI 316 discs. However, no clear trend can be observed for the C500 treated materials with the type of disc materials and the treatments of counterface.

4-3.9.2 Wear of Balls

The wear loss of the AISI316 balls sliding against discs made from three different materials and treated by four different conditions is summarised in Figure 4-3.9.2b. It can be clearly seen that the wear loss of untreated ball was much larger when rubbing against the untreated discs than against the treated ones no matter what treatments were used. This could be attributed to the similar tribo-compatibility between the ball and the discs.

In addition, it is also clear that all three plasma surface treatments, C500, N430 and NC430, can effectively improve the wear resistance of AISI316 balls in Ringer's solutions against three different austenitic stainless steels (ASTM F138, ASTM F1586 and AISI 316) treated using four different plasma alloying conditions (C430, C500, NC430, N430). It is noticed that the wear of plasma treated balls depended also on the type of the counterface materials; much larger wear was recorded when the treated balls were rubbed against treated ASTM F1586 than against treated ASTM F138 and AISI 316 except for N430 treated balls against C430 and C500 treated discs.

4-3.9.3 Combined Wear

The combined wear volume loss of the balls and discs together is illustrated in the stacked bar chart as shown in Figure 4-3.9.3. The following observations can be made from the combined wear:

- For all the samples tested, whether they were surface treated or not, the wear of the AISI 316 balls is much less than that of the counterface discs, whether they are plasma treated or not;
- Larger wear occurred to the tribopair when one of the two surfaces was not plasma treated than the tribopair when both of the surfaces were treated with the exception of N430 treated AISI316 tribopair;
- For treated tribopairs, their combined wear volume loss for ASTM F1586 and ASTM F138 is less than that for AISI 316. This is probably related to the relatively poor corrosion resistance of AISI 316 as compared with ASTM F1586 and ASTM F138;
- The combined wear of four plasma treated tribopairs made of ASTM F1586 and one plasma treated tribopair (C500 | N430) made of ASTM F138 is close to that of Co-Cr tribopair, which is the material of choice for metal-on-metal joint prostheses.

4-3.9.4 Wear Morphologies

Against Untreated Balls

Figure 4.3.9.4 illustrates the typical wear morphologies for untreated tribopair consisting of ASTM F1586 disc against untreated AISI 316 ball in Ringer's solution. The wear track was characterised by a mixture of severe adhesive and abrasive wear as evidenced by tearing and deep parallel grooves in direction of sliding motion (Figure 4-3.9.4b). EDX spot analysis has revealed a high level of oxygen in the dark areas of the wear track. Therefore, the wear of the ASTM F1586 disc against untreated AISI 316 ball was dominated by severe adhesive and abrasive wear together with mild oxidation wear. Similar wear morphologies were observed in the wear track in the untreated ASTM F138 disc after sliding against the untreated AISI 316 ball (Figure 4-3.9.5a). The SEM image of the wear scar observed on the ball also gives evidence of adhesive wear since severe smearing and tearing can be seen in Figure 4-3.9.5b.

On the other hand, the wear morphology of the untreated Co-Cr disc after sliding against untreated Co-Cr ball were featured only by fine and shallow scratches in the direction of motion as shown Figure 4-3.9.6. The wear of this untreated Co-Cr tribopair was dominated by mild abrasion mechanism, which is in line with the very low wear of the tribopair (Figure 4-3.9.3).

Against Carburised Balls

The wear test results have demonstrated that the wear loss of ASTM F138 discs can be effectively reduced by treating the surface of the ball counterparts (Figure 4-3.9.3). In order to investigate the mechanism involved, the wear morphologies of the tested discs were examined by SEM/EDX.

Figure 4-3.9.7a represents the wear scar on the untreated ASTM F138 disc after sliding against 500°C carburised AISI 316 ball counterpart. Deep grooves in the direction of sliding can be seen within the wear track; however, no macro-scale tearing or adhesion was detected from the wear track. EDX analysis has revealed that the wear track is rich in oxygen. As shown in Figure 4-3.9.7b, the damage to the carburised counterpart ball was very mild with very fine scratches and patches of dark areas, indicative of oxidation wear in conjunction with mild abrasive wear. Clearly, severe adhesive wear as shown in Figure 4-3.9.5b for untreated ball against the same untreated ASTM F138 disc was eliminated by the carburising treatment. Therefore, the mechanisms involved are a mixture of oxidative and abrasive wear for this tribopair.

When both the AISI 316 ball and ASTM F138 disc were carburised, the combined wear of the tribopair was significantly reduced (Figure 4-3.9.3) and the wear morphologies changed accordingly. Figure 4-3.9.8 shows representative wear morphologies observed from the wear track in the 500°C carburised ASTM F138 disc after sliding against 500°C carburised AISI 316 ball counterpart. Only very fine abrasion grooves as observed from untreated Co-Cr against untreated Co-Cr (Figure 4-3.9.6) were found in the wear track, indication of very mild abrasive wear.

Very low combined wear similar to that untreated Co-Cr against untreated Co-Cr was recorded for 500°C carburised AISI 316 ball rubbing against 500°C carburised ASTM F1586 disc (Figure 4-3.9.3). SEM/EDX studies revealed that the corrosion-wear of the tribopair resulted in an oxidative wear together with mild abrasive wear. Figure 4-3.9.9

shows dark areas within the wear track which were high in oxygen. This oxide was smeared along the whole wear scar and in the lighter areas parallel scratches could be seen. These scratches were not very wide or deep implying that the two surfaces were resistant to abrasive wear.

4-3.9.5 Effect of Solution

Wear Lost

It was observed that most treated samples showed excellent wear resistance when sliding against treated balls. In fact some of the treated balls against treated ASTM F1586 and ASTM F138 discs were comparable to the cobalt-chromium benchmark. The only exception was found in AISI 316 where the nitrided AISI 316 ball against nitrided AISI 316 disc behaved very similarly to an untreated disc against a nitrided ball. Due to this discrepancy further tests were conducted in both Ringer's solution and in distilled water as well for nitrided samples and the results are given in Figure 4-3.9.10.

It can be seen from Figure 4-3.9.10 that when tested in Ringer's solution the wear loss of the nitrided AISI 316 disc against nitrided AISI 316 ball was larger than that of the untreated AISI 316 disc against untreated AISI 316 ball; however, when tested in distilled water, the wear of the disc in the nitrided tribopair was less than in the untreated tribopair. This demonstrates that the corrosion-wear of nitrided AISI 316 disc was governed more by corrosion effect than by the mechanical effect.

For the untreated balls, the corrosion-wear in Ringer's solution was almost the same as in distilled water. This implies that the corrosion-wear of the untreated ball was dominated by the mechanical effect. On the other hand, the corrosion-wear of the nitrided ball was larger in Ringer's solution than in the distilled water. Therefore, corrosion effect may have played an important role in the corrosion-wear of the nitrided ball.

Wear Morphologies of Untreated AISI 316 Tribopair

Figure 4-3.9.11 shows typical corrosion-wear morphologies of untreated AISI 316 disc after rubbing the untreated AISI 316 ball in Ringer's solution. Severe adhesion tearing together with dark areas was observed at the end of the wear track (Figure 4-3.9.11a) and deep grooves in the direction of motion together with corrosion attack were observed in the

middle of the wear track (Figure 4-3.9.11b. EDX analysis has also revealed a high presence of oxygen within the wear track. Therefore, the possible mechanisms governing the wear of untreated AISI 316 tribopair were abrasive, adhesive and oxidative.

The wear morphologies of the untreated AISI 316 disc against the untreated ball formed in distilled water in general seems similar to the one formed in Ringer's solution (Figure 4-3.9.12). It can be found by comparing Figure 4-3.9.11 with Figure 4-3.9.12 that although adhesive and abrasive wear are still the major wear mechanism the wear track had less corrosion attack and appeared to be smoother.

Wear morphologies of nitrided AISI 316 tribopair

The wear track for nitrided tribopair is characterised by abrasive wear. Figure 4-3.9.13 reveals parallel grooves in the direction of sliding which are characteristics for abrasive wear. EDX analyses, has revealed that no oxygen was detected within the wear track.

The wear track, shown in Figure 4-3.9.14, shows mild abrasive wear and EDX analysis revealed that the dark areas are rich in oxygen. The kind of wear on this track is less severe than that observed in Ringer's solution and this explains why the wear volume loss (Figure 4-3.9.10) is much lower.

4-3.10 Fretting wear

The 3-dimensional fretting-wear F_t-d-N curve for ASTM F2581 in the untreated and 500°C carburized condition is shown in Figures 4-3.10.1 (a) and (b) respectively. The parallelogram shape of the curves indicates a gross-slip fretting-wear mechanism. All the materials (ASTM F138, ASTM F1586 and ASTM F2581) treated and untreated showed similar 3-dimensional fretting-wear curves indicating that all the samples have a gross-slip fretting-wear mechanism.

The micrographs in Figure 4-3.10.2 show the wear scars of all the samples that were tested in the fretting-wear tribometer. The volume loss of material calculated from the areas of the wear scar did not show any significant difference between treated and untreated samples. Therefore, laser confocal microscopy was utilized in order to get a more accurate value of wear volume lost.

Figure 4-3.10.3 shows a typical 3-dimensional laser confocal image which was used to calculate the wear volume loss after fretting-wear. This technique can more accurately measure the volume loss of material under the sample surface as opposed to calculating the wear volume loss using the projected area of a 2-dimensional image. This is because a wear scar might have a larger area but very shallow if the ball counterface was worn and flattened. This might be the case of the treated samples since they are harder than the counterface material. Therefore, the 2-dimensional technique is difficult, if not impossible, to reliably measure the wear volume loss since it does not take in consideration the depth of the wear scar.

Figure 4-3.10.4 shows the wear volume lost on untreated and 500°C carburized medical grade austenitic stainless steel samples (ASTM F138, ASTM F1586 and ASTM F2581) which were subjected to fretting wear for 1×10^4 and 2×10^4 cycles. After 1×10^4 cycles, all the 500°C carburized samples showed an improvement over the untreated ones; however, when subjected to 2×10^4 cycles, although the 500°C carburised ASTM 1586 and ASTM F2581 still showed improved fretting resistance, the 500°C carburised ASTM F138 sample showed reduced fretting resistance when compared with the untreated materials.

Figure 4-3.10.5 shows the wear lost after fretting wear test of 1×10^4 and 2×10^4 cycles on ASTM F138 and ASTM F1586 in untreated, nitrided (N430), carbonitrided (NC430) and carburised (C500) conditions. It is evident that for ASTM F1586 all the treated samples outperformed the untreated ones for the both fretting cycles. However for ASTM F138, although all the treated samples still showed improved fretting resistance after 1×10^4 cycles, the opposite was observed for the N430 and C500 treated samples when tested up to 2×10^4 cycles.

4-3.11 Biocompatibility

All biocompatibility testing was performed on High-Tensile versions of ASTM F138 and ASTM F1586. Post-treatment characterisation on these samples has revealed that there is no difference to the plasma alloying treatments when compared to annealed samples. Similarly to the annealed samples a back deposited layer of iron nitrides and carbides was observed from the XRD profiles. It is because of this layer close to the surface that it was decided to polish of the first 1μm layer close to the surface. This approach gave us a 100% confidence that throughout this work only the biocompatibility of S-phase and not any

other phase was tested. The polishing was also done so that the surface finish of the material between treated and untreated samples was exactly the same and also due to the fact that the bearing surface of metal implants are always polished.

4-3.11.1 Cell Proliferation

Figures 4-3.11.1a and b represent the number of viable osteoblasts following a period of 7 days on ASTM F1586 and ASTM F138 respectively. Figure 4-3.11.2 combines the results as shown in Figures 4-3.11.1 (a) and (b) together for comparison.

Day 1: After just 1 day it seems that all the surfaces used in this study support cell growth and proliferation. It can be seen clearly that there are more cells growing on the carbonitrided surfaces than on other treated surfaces. Figure 4-3.11.3 and 4-3.11.4 show the SEM cell attachment micrographs on ASTM F1586 and ASTM F138, respectively. For comparison, the micrographs for the control specimen can be seen in Figures 4-3.11.3e and 4-3.11.4e. From these images it can be seen clearly that even at an early stage there are a lot of cells which have spread and flattened on all surfaces. It can be seen by comparing Figures 4-3.11.3c and 4-3.11.4c for the carbonitrided samples to the other conditions that there are a higher number of cells on the carbonitrided surface. This is in agreement with the results presented in Figures 4-3.11.1 to 2.

Day 2: After 2 days of incubation there seems to be an increase in cell proliferation for almost all samples except the carbonitrided ASTM F1586 surface and carburised ASTM F1586 and ASTM F138 surfaces. It seems that the cells have reached a plateau after two days for both carburised surfaces. It can be seen from the SEM images shown in Figures 4-3.11.5 and 6 that the cells appear to be lying on top of each other; they have become narrower and are more fibroblastic (elongated) when compared to cells after 1 day.

Day 3: At day 3 the results are similar to day 2 and from the SEM images shown in Figures 4-3.11.7 and 4-3.11.8 it can be seen that there are more cells on the samples but according to the MTT test they are less actively metabolising. It is possible that the cells have stopped actively dividing and started

differentiating, for example, the production of collagen, although this is not yet visible in the micrographs.

Day 7: At day 7 on the ASTM F138 samples the cells seem to have reached a plateau and are therefore not proliferating anymore. On the ASTM F1586 samples in most of treated cases there are a reduced number of active cells as indicated by the lower MTT results. The SEM images in Figures 4-3.11.9 and 4-3.11.10 show that the number of cells has not reduced and therefore it can be concluded that there is no cell death but as on day 3 the cells are less metabolically active. The only case of cell death observed under the SEM was in the case of the carbonitrided ASTM F1586 stainless steel (Figure 4-3.11.9c) at the top left hand corner of the micrograph. The reason for cell death in this case is not because the material is toxic to the cells but because the proliferation of the cells on this surface was so high that there were too many cells on the surface. The cells appear to have less integrity and have started to lyse.

4-3.11.2 Cell Attachment

Figure 4-3.11.11 shows images at different stages in cell attachment. As shown in Figure 4-3.11.11a Stage 1 attachment is characterised by rounded cells with a few filopodia. Figure 4-3.11.11b shows the second stage of attachment where lamellipodia or focal cytoplasmic extensions can be seen. Stage 3, shown in Figure 4-3.11.11c is characterised by a circumferential spreading of the cytoplasm. Figure 4-3.11.11d depicts Stage 4 which is also the last stage of attachment of the cell. In this stage cells are now fully spread and flattened into a polygonal shape.

Figures 4-3.11.12 and 4-3.11.13 show the different stages in cell attachment on ASTM F1586 and ASTM F138, respectively after incubating for 30 minutes. By comparing the images visually there seems to be no clear difference in cell attachment on the different surfaces at the initial stage of attachment. Also the wetability and surface roughness (Figure 4-3.11.14) experiments performed on the surfaces of treated and untreated ASTM F1586 and ASTM F138 showed no differences in any of the surfaces. Since no difference was seen in initial cell attachment, roughness and also wetability it was concluded that the

high number of cells after just one day of incubation is due to the high proliferation rate on the material surface rather than a more efficient cell attachment.

Chapter V
Discussion

5-1 Response to Plasma Surface Alloying

5-1.1 Medical Grade vs Engineering Grade Austenitic Stainless Steel

The major difference between medical grade ASTM F138 and engineering grade AISI 316 lies in their production route and carbon content. As discussed in Section 2, AISI 316 is produced by conventional electric melting while medical grade ASTM F138 is refined by vacuum re-melting to reduce the amount of inclusions. In addition, in order to avoid intergranular corrosion, carbon content in ASTM F138 is lower than that of AISI 316 (Table 3-4). This has greatly contributed to improved microstructural cleanliness (Figures 4-3.1.2 vs. Figures 4-3.1.3) and electrochemical corrosion resistance (Figure 4-1.2).

The experimental results reported in this work have shown that compared with the engineering counterpart AISI 316, the medical grade ASTM F138 has a slightly better response to the plasma surface alloying treatments (especially for C430 and NC430) in terms of the interstitials absorbed (Figure 4-3.2.5) and improved surface hardness (Figure 4-3.5.1) of the S-phase layers.

As will be discussed in detail in the next section, the response of austenitic stainless steels to plasma surface alloying is to a large extent determined by their alloying elements. It can be found from Table 3-4 that the chromium content for both materials is very close, but the medical grade ASTM F138 contains more Ni (+2.55%), Mo (+0.75%) and Mn (+0.23%) but less carbon (-0.06%) as compared with the engineering grade AISI 316.

5-1.2 ASTM F1586 versus ASTM F138

The response of ASTM F1586 to plasma surface alloying seems quite similar to that of ASTM F138 but there are some small differences. As it can be seen in Figure 4-3.2.5 ASTM F138 has a tendency to absorb more carbon during carburising and carbonitriding than ASTM F1586. This is also reflected in their nano-surface hardness (Figure 4-3.5.1) where the hardness of ASTM F138 is higher than that of ASTM F1586 in the case of carburising. However, for carbonitriding, ASTM F1586 is actually marginally harder than

ASTM F138 although the total absorbed species are less in the former than in the latter. This seemingly contradictory result could be attributed to the fact that the surface hardness of S-phase case depends mainly on the interstitial level at the near surface. As has been shown in Figures 4-3.2.1 to 2, after carbonitriding the surface nitrogen and carbon contents are higher in treated ASTM F1586 than in ASTM F138; this is in line with the results shown in Figures 4-3.3.5 and 6 were the lattice parameter of the S-phase formed in carbonitrided ASTM F1586 is 0.382nm while that of carbonitrided ASTM F138 is 0.380nm.

It is also of interest to have found from Figure 4-3.2.5 that the nitrogen absorbed during nitriding is less for ASTM F138 ($2.2gm^{-2}$) than for ASTM 1586 ($2.6gm^{-2}$). This difference could be caused by the higher initial nitrogen content in ASTM 1586 (0.39 wt%) than in ASTM 138 (0.08 wt%). However, the quantitative calculation has revealed that this difference in the original nitrogen content only accounts for 0.24 gm^{-2} (See Apendix), which is much smaller than the difference in the absorbed nitrogen (0.40 gm^{-2}).

Hence, it follows that these two alloys' response to plasma surface alloying treatments is slightly different and it is also process dependent. This difference in response to plasma surface alloying could be related to the difference of alloying elements in these two materials. ASTM F1586 is higher in chromium (+3.37 wt%), manganese (+2.12wt%) and nitrogen (+0.30wt%) content but lower in nickel (-3.93 wt%) when compared to ASTM F138. Nitrogen is absorbed easier in the surface when the alloying content of manganese and chromium are high and nickel is low. Carbon on the other hand is absorbed easier when the nickel content is high and the content of manganese and chromium is low. Therefore, ASTM F1586 and ASTM F138 are favourable for nitrogen and carbon intake respectively.

5-1.3 Ni-Free versus Ni-Containing Austenitic Stainless Steels

The advances in S-phase have always been directed toward nickel containing austenitic stainless steels such as AISI 316. This is probably because early experimental observation [19, 20] has given the impression that a certain amount of chromium and nickel are essential in the formation of S-phase in austenitic stainless steel. Contrary to these claims or believes the results of this work have demonstrated for the first time that S-phase can be produced in the surface of a nickel-free austenitic stainless steel. Interesting results have

been reported in Chapter 4. Some differences in the layers created in the nickel-free stainless steel when compared to nickel-containing stainless steel were noticed.

From the optical cross-section microstructure of the low temperature plasma surface alloyed Ni-free samples (Figures 4-3.1.4 b, c and d) a featureless white layer can be seen in the samples which were alloyed with carbon (FC430 and FC500) and both nitrogen and carbon (FNC430). This is in agreement with the results obtained for the Ni-containing stainless steels where similar white layers were observed. Yet for the nitrogen alloyed samples (FN430) the layer consisted of an outer black sub-layer and inner white layer, which is different from the nitrogen S-phase layers produced in the Ni-containing alloys (Figure 4-3.1.1a, 2a and 3a) which were treated under the same conditions. These results were in fact in agreement with the potentiodynamic curves shown in Figure 4-3.6.4 indicating that the corrosion resistance was not affected for all the treated Ni-Free samples except for FN430.

XRD results have shown that all the Ni-containing austenitic stainless steel used in this study after nitriding (N430), carbonitriding (NC430) and carburising (C430 and C500) had their surface transformed into S-phase without any precipitates. For the Ni-free austenitic stainless steel only carburising (FC430 and FC500) yielded and S-phase without any precipitates. This was confirmed by XRD (Fig. 4-3.3.4) and TEM (Figure 4-3.4.9) results and accounts for the higher hardness and wear resistance of the alloy without any detriment in corrosion resistance.

Nitriding in the Ni-free stainless steel have also proved to be different to the Ni-containing stainless steels in terms of precipitation. Both XRD and TEM analysis has revealed that the layer is composed of S-phase and precipitates of Mn_3N_2. These precipitates are laminar and are within the S-phase forming a ‘tweed’ structure. It is believed that the dissolution of these precipitates is responsible for the increase in current at a voltage of +0.5V vs. Ag/AgCl (Figure 4-3.6.4). Work done by Suter *et al*. [162, 163] on microelectrochemical analysis of MnS inclusions also showed similar current transients in the region of +0.4V SCE to the one observed in the potentiodynamic curves on FN430.

The precipitates noticed in both nitrided (FN430) and carbonitrided (FNC430) layers of Ni-free austenitic stainless steel occur within the layer because this alloy (ASTM F2581) has a large quantity of manganese and this element, like chromium, has a high affinity to nitrogen and a tendency to form nitrides [70]

The layer thickness obtained both from GDOES (Figure 4-3.2.4) and optical microscopy (Figure 4-3.1.4) has not shown much difference when compared to the layer thickness obtained from Ni-containing stainless steel. Species absorbed on the other hand, differed greatly for nitrided (FN430) and carburised (FC430 and FC500) layers. Carbon and nitrogen were absorbed much less and much more respectively in the Ni-Free materials (Figure 4-3.2.5). The high intake of nitrogen for ASTM F2581 is very high compared to the Ni-containing austenitic stainless steels due to the fact that nitrogen solubility is hindered by the alloying element of nickel and enhanced by manganese [164]. On the other hand nickel increases the solubility of carbon while alloying elements such as manganese decrease its solubility [165]. Since in carbonitriding both nitrogen and carbon are absorbed simultaneously the hindering and enhancing effect cancel each other and therefore the Ni-free alloy behaves similarly to the Ni-containing one. This difference in solubility of carbon in Ni-free austenitic stainless steel has resulted in lower hardness for carburised samples when compared to the Ni-containing austenitic stainless steel (Figure 4-3.5.1).

5-2 Alloying Element Effect

5-2.1 Interaction between Carbon and Nitrogen

It has been clearly manifested in Figure 4-3.2.5 that when treated at the same temperature of 430°C the intake of total species (nitrogen and carbon) is higher than those registered by nitriding (N430) or carburising (C430). Except for AISI 316 the total intake of species, for all the other materials, during 430°C carbonitriding treatment is even larger than those registered for 500°C carburising. From the GDOES curves (Figures 4-3.2.1 to 4) together with the optical micrographs (Figures 4-3.1.1 to 4) it can be clearly seen that the layer thickness is greater for carbonitriding (NC430) than for nitriding (N430) and carburising (C430). The higher amount of species absorbed is due to the fact that the combination of both nitrogen and carbon, entails an even stronger ordering of chromium atoms [165], leading to the highest interstitial solubility of both nitrogen and carbon. The reason for a thicker case for carbonitriding (NC430) when compared to nitriding (N430) and carburising (C430) can be explained by the trapping and de-trapping theory of Parascandola *et al.* [102]. Since nitrogen has a higher affinity to chromium when compared

to carbon, the former always fills the trapping sites therefore carbon can diffuse faster since it has less resistance to diffusion by the trapping sites. This in turn helps carbon to diffuse more rapidly inwards of the nitriding front making the layer thicker.

5-2.2 Formation of Dual Layer

Carbonitriding results in the formation of a dual layer: a nitrogen-rich top layer followed by a carbon-rich just below (Figures 4-3.2.1 to 4). Since stainless steel strongly absorbs X-Rays, the intensity of the incident beam is reduced to almost zero in a very short distance (6μm) and the diffracted beams therefore originate chiefly from only a 6μm thin surface layer [161]. Therefore the penetration of the X-Rays used in this work is not deep enough to obtain information from the carbon S-phase due to the fact that the top nitrogen-rich S-phase layer is thicker than 6μm (blue line in Figures 4-3.2.1 to 4). Consequently the XRD data revealed that after carbonitriding only nitrogen S-phase can be seen in the surface (Figures 4-3.3.1 to 4). On the other hand the thickness of the nitrogen S-phase layer formed in the sequential treatments is smaller than the penetration depth of the X-Rays, peaks from both the carbon and nitrogen S-phase layer and can be indexed (Figures 4-2.3.4 to 6).

The XTEM result, shown in Figure 4-3.4.4, has further supported the observation that nitrogen- and carbon- rich S-phase did not mix and formed two sublayers. Although the interface is not clearly visible by the XTEM, SAD from two areas 2μm apart on the cross-section revealed a face centred cubic structure with two completely different lattice parameters. These two lattice parameters matched those of the nitrogen-rich S-phase (0.3817nm) and that of the carbon-rich S-phase (0.3703nm). This result was also in agreement with the results (Figures 4-3.3.5 and 6) obtained from depth profiling XRD by grinding the surface at interval depths of 3μm. Nitrogen S-phase at a lattice parameter of circa 0.38nm only registered at the surface whilst carbon S-phase at a smaller lattice parameter of circa 0.37nm can only be seen deeper in the layer.

In the works by Sun and Sun *et al*. [17, 64, 78, 166] layers similar to the ones reported in this work have been produced. Chemical profiling reported by the authors generally reveals a nitrogen-rich part, which is deeper than 10μm, close to the surface. The XRD data presented by these authors is indexed as having both nitrogen and carbon S-phase peaks. Based on the XRD and XTEM findings of this work there is a disagreement with the work of these authors. As discussed previously when nitrogen is present carbon-rich S-

phase never forms on the surface. Therefore if their nitrogen-rich S-phase layer thickness is greater than the penetration depth of their X-Rays no carbon S-phase peaks should be detected. It is believed that the indexing of the carbon S-phase peak (111) found at an angle of 43° by Sun and Sun *et al.* [17, 64, 78, 166] is wrong since from this work, as shown in Figures 4-2.3.13 to 15, that peak was confidently indexed to Fe_3C (102). In other cases the authors [64, 166] also index another carbon S-phase peak (200) at an angle of 48° which is not visible in any of our XRD results.

This separation of nitrogen- and carbon-rich S-phase that has been observed not only by simultaneous alloying with carbon and nitrogen i.e. carbonitriding (Figures 4-2.3.7 to 9) but also in alloying with carbon first followed by nitrogen i.e. sequential carburising and nitriding (Figures 4-2.3.1 to 3). This can be explained using the trapping and de-trapping theory by Parascandola *et al.* [102] which has been outlined in chapter 2. In sequential carburising and nitriding (Figures 4-2.3.1 to 3), carbon that had diffused throughout the carburising treatment had occupied both regular and trapping interstitial sites. When this carburised sample was post-nitrided: carbon that was occupying the trapping sites got de-trapped and was replaced by nitrogen. This meant that the de-trapped carbon had to move inward in order to occupy other regular or trapping interstitial sites. This combination of trapping and de-trapping is the reason why carbon is always found deeper ahead of the nitriding front.

Baranowska *et al.* [137-139] and Czerwiec *et al.* [106] in their work on nitriding have indexed two sets of peaks for nitrogen-rich S-phase: one set at a lower angle and the other set at a higher angle. This was not observed in our work but can be explained using the above theory. The second set of peaks at higher angles noticed by the mentioned authors belongs to carbon S-phase. The carbon could have come from the following sources: (1) carbon impurity in the hydrogen gas; (2) the residual carbon in the furnace wall if carburising was performed some time before the nitriding treatment; and the carbon in the substrate alloy. In the cases of 1 and 2, carbon diffused into the alloy in a similar way to carbonitriding and in case 3, carbon was pushed ahead the nitriding front similar to the diffusion in the sequential treatment. From our chemical depth profiles it was noticed that a weak carbon peak is always present at the nitriding front.

5-2.3 Summary

The critical importance of interstitial elements such as carbon and nitrogen in austenitic stainless steels has been identified in this thesis. In fact below their solubility limit, their presence can have a drastic influence on the steels mechanical properties, as they build strong interactions with the lattice defects present in the austenitic matrix.

From the previous discussion and the results in Figure 4-3.2.5 the nitrogen solubility is enhanced by manganese but impeded by that of nickel whilst the carbon solubility is increased by nickel and reduced by manganese. This is related to the belief that manganese and carbon contribute to the decrease of free electrons which in turn decreases the solubility of carbon in the alloy [167].

The role of chromium although considered as an essential element for S-phase to form [19, 20] is considered, like manganese, to also contribute in the decrease of free electrons [167] and therefore should also decrease the solubility of carbon in the alloy. Nickel on the other hand increases the concentration of free electrons [167] but is always used in conjunction of chromium and therefore when these two elements are in the same alloy they cancel each others' negative effect. This is the reason why no obvious reduction or enhancement in nitrogen and carbon uptake (Figure 4-3.2.5) can be seen in Cr-Ni austenitic stainless steels.

5-3 Corrosion Properties

Although it has been well documented that plasma nitriding or carburising can be used to significantly increase the hardness and wear resistance of austenitic stainless steel, the improved mechanical properties are usually at the price of impaired corrosion resistance. This problem was not solved until the mid-1980s, when Zhang and Bell [168] developed a low temperature plasma process that could harden the surface of austenitic stainless steel whilst improving or retaining the corrosion resistance of the steel.

However the formation of S-phase by thermochemical treatment is diffusion-controlled process. Therefore in order to produce a thick S-phase layer some researchers tend to use an as-high as possible temperature provided no significant loss of corrosion resistance occurs. This strategy would be intensified for most engineering applications where wear is a major concern. Conversely the application of this work is for the

biomedical sector and there is no point in improving the wear resistance if the corrosion resistance was impaired since both wear and corrosion will lead to metal ion release.

Indeed, Kamachi Mudali *et al*. [42] have reported that among 50 failures of stainless steel implants, 12 failed due to corrosion attack and 3 failed due to severe wear. Therefore, it is highly desirable to keep the number of failures to a minimum by improving the wear resistance without reducing the corrosion resistance of the starting alloy. Accordingly, the corrosion behaviour of surface modified medical grade austenitic stainless steels, were investigated using the untreated materials as benchmarks.

5-3.1 Untreated

5-3.1.1 AISI 316

The electrochemical corrosion test results (Figure 4-1.2) have indicated that AISI 316 stainless steel suffers from pitting. Pitting on AISI 316 occurred consistently at 0V vs. Ag/AgCl. From the reverse potentiodynamic sweeps a repassivation potential at -0.2V vs. Ag/AgCl was registered. This means that this material does not repassivate easily once a pit has initiated. The poor pitting resistance of engineering grade AISI 316 is related to its high sulphur and inclusion content. This in turn creates manganese sulphides, which are considered as probable pit initiation sites. The relative high content of carbon in AISI 316 may also cause potential intergranular corrosion. However, because pitting occurred at a very early stage, features related to intergranular corrosion could not be observed from the corrosion curves.

5-3.1.2 ASTM F138

The potentiodynamic sweeps conducted on untreated ASTM F138 (Figure 4-1.2) reveal that this material may be susceptible to pitting. Pitting occurred at 0.8V vs. Ag/AgCl at a single initiation site. This high breakdown potential is due to the fact that this steel has a much lower inclusion and sulphur content as compared to the engineering counterpart AISI 316. Pitting attack was not always observed and in some cases this material did not exhibit pitting at all. This is because pitting is a probabilistic and stochastic event and there were instances where pitting initiation sites were not present. There were also instances during the potentiodynamic scans where only metastable pits were visible which repassivated

immediately. On reverse scans applied after the pitting current density reached 10^{-4} Acm^{-2} it was noticed that the repassivation potential was also very close to 0.8V vs. Ag/AgCl, indicating that the material repassivates easily and is an ideal candidate for biomedical applications.

The pitting voltage of 0.8V vs. Ag/AgCl was not in agreement with the work done by Pan *et al.* [3] and Bou-Saleh *et al.* [169] on similar ASTM F138 material. The pitting voltage reported by the former was of 0.36V vs. Ag/AgCl and the latter 0.3V vs. Ag/AgCl. Contrary to our work both authors used Phosphate buffered saline (PBS) solutions but this should not make much difference in pitting because the pH value and the chloride content is similar to the electrolyte used throughout this work. The discrepancy in pitting voltage might be attributed to the different surface roughness of the samples since Bou-Saleh *et al.* [169] and Pan *et al.* [3] used ground surfaces of 600-grit and 1200-grit respectively while mirror polished samples was used in the electrochemical tests performed in this study. This is because a rougher surface [163], causes a high number of occluded sites on the metal surface, were critical Cl^- concentration can be attained facilitating pitting.

The increase in the pitting voltage from 0V vs. Ag/AgCl to 0.8V vs. Ag/AgCl for AISI 316 and ASTM F138 respectively has demonstrated the importance of steel cleanliness to combat localised corrosion. This result is in agreement with the report by Haraldson *et al.* [4] and Wallén [31] where the importance on the cleanliness of Sandvik's ASTM F138 stainless steel were highlighted.

5-3.1.3 ASTM F1586 and F2581

According to the potentiodynamic sweeps (Figure 4-1.2) no pitting was observed in both ASTM F1586 and ASTM F2581. This high pitting resistance of these alloys is in complete agreement with the works of Zardiackas *et al.* [170], Haraldsson *et al.* [5], Windler *et al.* [29, 171] and Pan *et al.* [3] where pitting, if any, always occurs at voltages which are over that of 1V vs. Ag/AgCl.

The higher pitting potential of these materials compared to that for ASTM F138 can be mainly attributed to the high-nitrogen content that these alloys contain in solid solution since it is well documented that nitrogen can effectively improve the pitting corrosion resistance of austenitic stainless steels. The reason why nitrogen improves the pitting resistance of the alloy is not fully understood and the following mechanisms have been

suggested to explain how nitrogen operates: (1) Nitrogen in solid solution dissolves and produces NH_4^+, raising the pH and depressing oxidation inside a pit [49, 50]; (2) Concentrated nitrogen at the passive film-alloy surface stabilises the film, and prevents attack of the anions (Cl^-) [49, 50]; (3) nitrate ions are produced and these improve the resistance to pitting corrosion [28, 49, 50]; (4) Nitrogen addition stabilises the austenite phase [49, 50]; (5) Nitrogen blocks the kink, and controls the increase of electric current for pit production [49, 50].

The superior localised corrosion resistance of both ASTM F1586 and ASTM F2581 when compared to ASTM F138 is outlined in Figure 4-1.2. Table 3-2 shows that the high-nitrogen stainless steels (ASTM F1586 and ASTM F2581) have higher inclusion content when compared to ASTM F138. This means that the improvement in localised corrosion resistance is attributed to the fact that this steel has higher nitrogen content compared to ASTM F138, rather than being a cleaner material.

5-3.2 Treated Materials

As it can be seen from Figure 4-1.2 this excellent pitting resistance is comparable with the corrosion resistance of the Co-Cr alloy which is commonly used alloy in hip joint replacement. Both ASTM F1586 and ASTM F2581 showed excellent corrosion resistance even when compared to their major competitor - the cobalt-chromium alloy. As it has been presented in section 4-3.6, after treatments at temperatures lower than the threshold sensitisation temperature, both ASTM F138 and AISI 316 have showed an improvement in localised corrosion resistance. However the corrosion resistance of both ASTM F2581 and ASTM F2581 can be hardly improved since these alloys already have shown excellent localised corrosion resistance in the untreated state. In this section four types of localised corrosion mechanisms that could possibly occur during the experiments performed in this study will be discussed.

5-3.2.1 Testing Methods

In order to quickly assess the corrosion resistance of plasma treated surface layers a simple etching test on the cross-section of the treated sample was performed (Figures 4-3.1.1 to 4). From this test only the nitrided ASTM F1586 (Figures 4-3.1.1a) and ASTM F2581

(Figures 4-3.1.4a) and the carbonitrided ASTM F1586 (Figure 4-3.1.1c) showed some signs of impaired corrosion resistance. This technique can give a quick idea whether the corrosion resistance of the material was maintained or not but it cannot be used as definite answer. This is because the immersion time is too short for any real corrosion to occur.

Potentiodynamic testing can give a better indication whether the alloy has been sensitised or not. The subsequent section will give an interpretation of the potentiodynamic test results in terms of intergranular corrosion. It should be emphasised at this point that potentiodynamic testing alone is not enough to assess whether a layer can resist this type of corrosion when subjected to a long term corrosion test. Long term corrosion tests were also conducted in this work and will be explained in section 5-3.2.3. It is suggested that Electrochemical potentiodynamic reactivation (EPR) test to be used in order to check whether an alloy has become sensitised or not.

5-3.2.2 Intergranular Corrosion

As can be seen in the set of corrosion curves of samples treated at different process temperatures and using different plasma processes (Figures 4-2.1.7, 4-2.1.8, 4-2.1.9. 4-2.2.7, 4-2.2.8, 4-2.2.9, 4-2.3.16, 4-2.3.17 and 4-2.3.18) the corrosion resistance of the treated alloy is degraded if the threshold sensitisation temperature is reached and surpassed. As it has been explained in Section 2, the S-phase layer is corrosion resistant only when it is not accompanied by secondary precipitations of the chromium nitride and carbide type. As was illustrated in the results section, chromium nitrides (Cr_2N) in austenitic stainless steel tends to form at temperatures above 430°C while chromium carbides ($Cr_{23}C_6$) tend to form at temperatures higher than 500°C. It is therefore essential that all plasma surface alloying in nitrogen containing atmospheres (nitriding and carbonitriding) are preformed at temperatures of 430°C and that all carbon containing treatments (carburising) are performed at temperatures of not more than 500°C.

Current Transients

During the anodic potentiodynamic scans throughout this work it was noticed that there was an increase in current at specific voltages. This current increase was sometimes in the form of blimps at voltages between 0.3V to 0.5V vs. Ag/AgCl and 0.5V to 0.7V vs. Ag/AgCl (Figure 4-3.6.1). In other cases at voltages of 0.5V vs. Ag/AgCl the current

increase did not form a hump and instead there was a steady current increase (Figure 4-2.1.7 and 4-3.6.4). These current increases or transients can be easily interpreted as pitting but in reality they are due to dissolution or oxidation of a particular phase or element. It was observed that the samples whose potentiodynamic curves had these current blimps also suffered from sensitisation. Post examination after corrosion testing of these samples revealed intergranular attack along the grain boundaries (Figures 4-3.6.8 and 9). Similar current transients have been reported in a number of different publications [76, 107, 132] on austenitic stainless steel that have been plasma nitrided at high temperatures or have been annealed at certain temperatures for long times after plasma nitriding. Hence the importance of understanding such current transients as the first signs of sensitisation is highlighted in the current research.

Transpassive dissolution has been reported in many papers which deal with the corrosion of austenitic stainless steel but is rarely linked with intergranular corrosion. The current transients that were noticed in this work are probably related to the transpassive oxidation of Cr^{3+} to Cr^{6+} [3, 5, 33, 169, 172, 173]. Other possible causes attributed to this increase in current is the dissolution of molybdenum at 0.7V vs. Ag/AgCl [173] and the dissolution in areas where MnS or Mn_3N_2 precipitates are present at voltages of +0.4V vs. SCE [162, 163].

The intergranular corrosion attack observed in this work, manifested with an increase in current, could be related to the dissolution of the chromium depleted zone. This happens because the solute-depleted (in particular Cr) solid solution adjacent to the grain boundary precipitate is anodic and the cathodic reaction is supported by the precipitate particle and the unaltered solid solution within the grain resulting in a localised corrosive attack in the region near the precipitate. Large corrosion rates usually occur due to the large cathode-to-anode ratios. As a result, the localised corrosion rate may be several orders of magnitude greater than that of a homogenous alloy.

Effect of Manganese

The alloys which are high in manganese such as ASTM F1586 and ASTM F2581 (Figures 4-3.6.1 and 4) were found to be more susceptible to intergranular corrosion after treatment in nitrogen atmospheres when compared to the low manganese alloys (AISI 316 and ASTM F138). Post-corrosion SEM observations revealed that these samples were suffering

from intergranular corrosion (Figures 4-3.6.8 and 9) and that the formation of manganese nitrides (Mn_3N_2) is the cause of this kind of intergranular corrosion. Work done by Suter *et al.* [162, 163] on microelectrochemical analysis of MnS inclusions showed similar current transients reported in this work (Figures 4-3.6.1 and 4) in the region of 0.4V vs. SCE. This similar result by Suter *et al.* [162, 163] makes us believe that the increase in current at a voltage of 0.5V vs. Ag/AgCl could be related to the precipitation of Mn_3N_2. Manganese, similar to chromium, has a high affinity to nitrogen and therefore alloys which are high in manganese tend to form Mn_3N_2 if nitrided or carbonitrided at a high temperature. It is generally advisable to use temperatures lower than 430°C during nitriding or carbonitriding of these high-manganese alloys.

5-3.2.3 Pitting Corrosion

It has been found that the pitting resistance of all four austenitic stainless steels in chloride containing solutions can be increased by low temperature nitriding, carbonitriding and carburising. No pitting potentials were observed in all the potentiodynamic sweeps of the treated materials and post-corrosion SEM observations revealed surfaces free from pits. This result is in complete agreement with the work of other authors where pitting was not observed for nitrogen [2, 84, 120, 121, 132], carbon [76, 84, 88, 155] and hybrid [17, 64, 73] S-phase.

The beneficial influence requires that nitrogen or carbon or both must be in solid solution. From the results presented in this study it is clear that when the temperature for nitriding and carbonitriding was kept below 430°C there were no signs of intergranular corrosion and pitting. This means that both nitrogen and carbon interstitial elements are beneficial in pitting resistance.

As has been discussed in chapter 2 researchers working on nitrogen S-phase and high-nitrogen austenitic stainless steel tried to give several mechanisms of why nitrogen is beneficial. The most common mechanism, is the formation of ammonia inside the pit that neutralises the acidic solution which is dissolving the metal inside the pit. This mechanism can explain why nitrogen is beneficial for combating pitting of austenitic stainless steels but is unable to explain why carbon is also beneficial.

Currently there is no well-accepted theory to explain the beneficial effect of carbon in improving the pitting corrosion resistance of austenitic stainless steel. However, it is

believed that carbon and nitrogen residing in the oxygen vacancy sites of the passive film are mobile. Since the oxygen vacancy sites are responsible for charge transport within the passive film the mobility of either carbon or nitrogen makes the passive film less resistive. Therefore both nitrogen and carbon maintain the oxygen vacancy motion and thus retarding pitting. This hypothesis, using XPS measurement of carbon in the passive film, was proposed by Martin *et al.* [155] but requires further investigation.

5-3.2.4 Corrosion in Crevice Test

As reported in section 4-3.7 no typical crevice corrosion was observed to a great extent on the tested samples during the immersion crevice corrosion tests as evidenced by the fact that the corrosion attack was occurring on the exposed areas rather than the occluded areas under the multiple crevice assembly (MCA) washers.

However, it would be a bit presumptuous at this point to conclude that crevice corrosion does not occur on these materials in this specific environment because results from other researchers have indicated otherwise [163]. Because of the many interrelated metallurgical and environmental and geometric factors known to affect crevice corrosion, results from any given test may or may not be indicative of actual performance in service application where the conditions may be different from those of the test.

It has to be mentioned that whether crevice corrosion occurs depends on the artificial crevices created on the sample surfaces during the experiment. Simulating a crevice forming condition depends on the test solution, the sample geometry and the performance of the crevice former. The solution used was high in chloride content and low in pH, this in theory [3] should favour the formation of crevices. But unfortunately, because of the limitation of sample and crevice former size the crevice to sample area ratio was only 1.25 and this value might be too low, since in order to get a crevice attack started the cathode to anode ratio must be high. Also the crevice formers were too soft, so with the application of torque they deformed and narrowed the crevice gap to an extent that was not sufficient to initiate crevice.

Although crevice corrosion was not found on any of these samples, the resultant outcome of this experiment can still be useful as it represents a long term immersion corrosion experiment. Therefore a short discussion on the results gathered from these long term corrosion tests will be given below.

From the ion release bar charts for the untreated samples (Figures 4-3.7.4) it is clear that AISI 316 released the largest amount of metal ions amongst all the treated materials. This is also supported by the corrosion morphology observed: The engineering grade AISI 316 suffered from pitting and severe general corrosion (Figure 4-3.7.9 and 13) whilst no pitting was observed on medical grade ASTM F138 and ASTM F1586.

After plasma surface treatments, the engineering grade AISI 316 still showed the highest ion release among all the three surface treated materials independent of the treatments process. This is probably because the existence of inclusions (such as MnS) in the S-phase deteriorates its corrosion resistance. It is also of interest to note that metal ions released (Figure 4-3.7.4) from all treated AISI 316 surfaces are all higher than from the untreated material. This is due to the fact that the corrosion mechanism governing the untreated is pitting while that on treated samples, especially 500°C carburised (GC500) is general corrosion. The corrosion during general attack happens on the whole sample surface so the amount of ions released is high. While the attack in pitting is localised and therefore limited ions can be released from such a small surface area.

When the results are compared to the potentiodynamic tests there is a slight disagreement in results. ASTM F138 samples which were nitrided at 430°C showed no impairment in corrosion resistance when tested potentiodynamicaly (Figure 4-3.6.2) but suffered from intergranular corrosion when subjected to a long time immersion test. This discrepancy in results emphasis the limitations of potentiodynamic testing in intergranular corrosion detection.

5-3.2.5 Localised Slip Band Attack

Potentiodynamic results obtained during this work indicate that the corrosion of precipitate free S-phase is of uniform corrosion type. This is because intergranular corrosion only occurs with the presence of precipitates in the layer. Localised corrosion in the form of pitting does not occur in Ringer's solution due to the beneficial effect of nitrogen and carbon and cleanliness of the medical grade austenitic stainless steel.

When observed under the SEM, the electrochemically tested precipitate-free samples showed no signs of corrosion. On the other hand, the samples which were long term tested in an acidic solution had corrosion attack along slip bands (Figure 4-3.7.6). This type of attack was also noticed by other authors like Lei *et al.* [2] and Li *et al.* [132].

It is a well known fact and it was also presented in this thesis that the S-phase layer is highly stressed and slip bands tend to form. Therefore localised attack on slip bands possibly occurs due to the fact that deformation by slip produces in the surface and offset that cracks the passive film and exposes clean surface (Figure 5-1) [174]. This exposed region actively corrodes and then passivates blocking propagation.

5-4 Tribological Properties

5-4.1 Dry Sliding

As it can be seen in Figures 4-2.4.1, 4-3.8.1, 4-3.8.2 and 4-3.8.3 all low temperature plasma surface alloying treatments have been successful in improving the dry sliding wear behaviour of all the austenitic stainless steels that were used in this work. This huge improvement in terms of wear lost can be attributed to a change in wear mechanism from severe adhesive and abrasive (Figures 4-3.8.4, 5 and 7) in untreated samples to mild abrasive and oxidative in the treated ones (Figure 4-3.8.12).

Adhesive wear is considered to be a severe mode of wear whilst oxidative on the other hand is considered as mild. In fact the material lost due to wear of the adhesive type is much greater than that in oxidative. This is the reason why there is a huge difference in terms of material lost between treated and untreated.

The high surface hardness of the treated samples when compared to the untreated ones (Figure 4-3.5.1) is the reason behind this change in wear mechanism. As it was explained in the literature review section adhesive wear occurs when the surface asperities of two components slide against each other and eventually cold weld together if the oxide film in the surface of these asperities breaks due to lack of mechanical support from the substrate. Therefore factors like hardness and alloying additions which increase the stability and maintain the integrity of the oxide film are critical for adhesive wear resistance.

The creation of S-phase on the surface of austenitic stainless steel increases the surface hardness and this hardened layer gives strong support to the overlying oxide film. This means that the oxide film on top of the S-phase is more stable and less prone to breakage when compared to the oxide layer formed on a soft austenitic substrate.

In addition, adhesive wear also depends on the growth of junctions, which is related to the plastic deformation and ductility of the surface. Therefore adhesive wear can be

eliminated by promoting elastic deformation and reducing the plastic deformation [54]. It is well known that hardness to modulus ration (H/E) is a measure of elastic deformation capability of a surface and consequently a high H/E ratio is also beneficial for enhancing adhesive wear resistance. Figure 5-2 shows a plot of the H/E ratio of the untreated austenitic stainless steel compared to the treated ones. It can be seen that all the plasma surface treatments can effectively increase the H/E ratio of the four austenitic stainless steels. This is in good agreement with the dry sliding wear tests results (Figure 4-3.8.3). Figure 5-3 shows a correlation plot of wear loss (in untreated and 430°C carbonitrided samples) versus H/E. It can be seen that for every untreated sample whose H/E was increased after treatment the wear volume lost always decreased. There is no direct correlation between the different untreated materials but as it was explained before there are other factors such as inclusion content which also affect the “dry” wear resistance.

In addition, it is also evident that a higher H/E ratio is achieved by nitriding (N430), then by carburising (C430, C500). This is also generally in line with the dry sliding wear results (Figure 4-3.8.2). Figure 5-4 shows another correlation plot for treated and untreated ASTM F2581 which were tested in “dry” reciprocating wear conditions. Again it is very clear that an increase in H/E increases the wear resistance. Figure 5-5 shows the same correlation plot to Figure 5-4 but the Y-axis is shown in log scale. A direct correlation between wear lost and H/E can now be seen in Figure 5-5.

As it was explained in the literature section another key factor for a tendency of a material to suffer from adhesive wear is the ease by which dislocations cross slip over more than one plane during plastic deformation. The S-phase microstructure (Figures 4-3.4.2, 4-3.4.3, 4-3.4.6 and 4-3.4.8) is composed of entangled dislocations and a high density of stacking faults and this decreases the tendency of cross slip. Since dislocation cross slip is hindered by the presence of stacking faults and entanglement of dislocations and therefore the S-phase layer is beneficial in the resistance against adhesive wear

The severe abrasive wear seen in the untreated was less pronounced in the treated samples. This reduction in abrasive wear is related to the increase in hardness of the treated surface because hardness is a key factor in abrasive wear resistance.

5-4.2 Corrosion Wear

5-4.2.1 Metal-on-WC

As it was explained in the literature review most corrosion-wear work done on S-phase was performed on S-phase coatings [44, 55, 144-146] and not on nitrided or carburised layers. In fact the only work done on nitrided and carburised layers was by Thaiwatthana *et al.* [152]. In general, S-phase, when tested in saline corrosion-wear environments, even if marginal, always proved to be superior to the untreated or uncoated austenitic stainless steel. This is in agreement with the work on corrosion-wear presented in this study.

Lubrication Effect

As has been shown in Figures 4-3.8.1 to 3 when the reciprocating wear test was conducted under lubricated (wet) conditions the wear of untreated and treated samples can be effectively reduced as compared with wear under dry conditions. In addition post-test SEM wear track observations also revealed that the dominant wear mechanism has been changed from severe adhesive and abrasive wear to mild abrasive and oxidative wear. This meant that the adhesive wear seen in the wear scars of the untreated samples tested under dry conditions changed into mild abrasive (Figure 4-3.8.6) or oxidative wear (Figure 4-3.8.8) when tested in wet conditions. This has contributed to the significantly reduced wear for the untreated materials (Figures 4-3.8.1 to 3).This is mainly because adhesive wear has been effectively suppressed by the liquid media (Ringer's solution or distilled water) which acted as a lubricant and reduced direct contact between the tribopair. This lubrication effect has also contributed to the reduced wear of all the treated samples in distilled water. However the reduction in wear is much less for the treated samples than for the untreated materials. This is mainly because the wear of the treated samples were dominated by an oxidative wear even under dry conditions.

Synergism: Mechanical and Electrochemical effects

Distilled water is considered to be a non-corrosive solution so it is assumed that the material lost during wear tests in this solution were predominantly due to mechanical wear. Ringer's solution on the other hand is considered as a corrosive-solution and therefore the material lost is due to a synergistic effect of both mechanical wear and electrochemical corrosion. The material lost in the wear tests (Figure 4-3.8.1) conducted in distilled water

is only slightly lower than that conducted in Ringer's solution indicating that the material lost in these tests was dominated more by mechanical wear than by corrosive-wear.

The mechanical and electrochemical effects within a corrosion-wear system are easily separated by performing two tests: one under OCP and the other under cathodic protection [175-177]. When under OCP (similar to tests conducted in this work) both mechanical and electrochemical components are acting against together. On the other hand under cathodic protection only the mechanical-wear component is acting. In this work cathodic protection experiments were not done because this equipment is not available within the University of Birmingham. Work done by Dearnley *et al*.[44] on S-phase coatings has demonstrated that the corrosion effect during corrosion-wear is very high. In fact the authors report that corrosion plays a very important role in the corrosion wear of uncoated and S-phase coated Ortron 90 (ASTM F1586) in saline solution. The authors conclude that the sum of the synergy and the corrosion-enhanced wear constitutes 97.6% and 99.5% of the total corrosion-wear for uncoated and S-phase coated ASTM F1586.

It was observed that the wear volume lost for all the samples (treated and untreated) tested in distilled water was always less than that for the samples that were tested in Ringer's solution (Figure 4-3.8.1). This is in agreement with the work by Aldrich-Smith *et al.* [144] were both uncoated and S-phase coated 316L showed less wear in distilled water than in 3wt% NaCl. As has been explained in the previous section, this discrepancy is mainly due to the fact that the material removed in Ringer's solution could be related to a synergistic attack from both mechanical and electrochemical effects.

Electrochemical attack in stainless steel occurs most commonly as localised corrosion in the form of pitting but within the wear track the corrosive attack was not manifested as pitting but rather as a rust deposit and intergranular corrosion.

Pitting: Wear-corrosion is a synergistic attack consisting of both electrochemical and mechanical material removal. The electrochemical tests performed on the materials tested have shown good corrosion results but these are not representative to the conditions that the material was subjected to during the wear-corrosion reciprocating tests. During the electrochemical corrosion test there was no mechanical disruption to the passive film; after the corrosion-wear tests no pitting was observed in the wear scars for both treated and untreated material but in the electrochemical tests pitting was observed in the untreated

AISI 316 and ASTM F138 samples. The reason for not seeing any pitting in the wear tracks of all the samples is due to the fact that conditions for pit initiation are not available throughout the wear-corrosion tests. The movement of the sample relative to the pin and the rubbing of the pin with the sample surface create movement in the solution and therefore stagnant conditions are not available. Electrochemical attacks such as pitting require stagnant conditions in order for them to occur and therefore pitting is unlikely to occur within the wear scar because stagnant conditions are not available.

Rust Deposits: The corrosion resistance of stainless steel depends on the integrity of the passive film (Type I corrosion-wear mechanism by Dearnley *et al.* [55]). The rubbing action of the sphere during the wear test removes this thin passive film and corrosion by dissolution occurs and stops only once a new passive film is recreated. This continual removal of material by both wear and corrosion creates a suspension of wear debris. Eventually these wear debris composed mostly of iron ions react with the oxygen and water in the solution and become oxidized particles such as rust. The reciprocating motion of the ball creates a flow in the solution and these particles are then transferred to the edge of the wear track. This debris then settles down at the outside edge of the wear track and is chemi-absorbed onto the surface (Figures 4-3.8.6 and 4-3.8.8).

Intergranular Corrosion: When the S-phase layer has some precipitates the attack during wear-corrosion is manifested as intergranular corrosion. This kind of attack was observed in the ASTM F1586 sample which was carbonitrided at 430°C (Figures 4-3.8.10) and this is in line with the electrochemical corrosion results (Figures 4-3.6.1 and 4-3.6.8). This kind of attack within the wear track is also mentioned in the review by Wood [57] when the author mentions micro-galvanic activity and selective phase corrosion. Dearnley *et al*. [55] in Type III corrosion-wear mentions that a galvanic attack occurring on the counterface might lead to roughening. This Type III corrosion-wear mechanism can be extended to sensitized S-phase discs were the surface is roughened by intergranular attack.

From Figures 4-3.8.1 it is observed that this sensitized sample showed the best wear-corrosion volume lost when compared to the other samples that did not suffer from this attack. This very good wear-corrosion resistance is probably due to the fact that the precipitates formed along the grain boundaries of this material are harder than the S-phase

matrix itself and therefore make the surface of the material more resistant to mechanical wear.

5-4.2.2 Stainless Steel-on-Stainless Steel

The implication of polyethylene wear debris in aseptic loosening has led in recent years to a re-examination of alternative wear couples. In particular, there has been a resurgence of interest in metal-to-metal hips which can be partly attributed to the observation that retrieved metal-to-metal hips show few signs of wear after more than two decades of use. CoCr-against-CoCr implants are a very popular choice since they have a low wear rate in this articulating combination. In fact the appearance of cups retrieved after more than 20 years of service is very striking since there are virtually no signs of wear, and little staining of the surrounding tissue [46]. This renaissance in metal-to-metal hips leads us to the investigation of testing stainless steel against stainless steel with a special interest in S-phase layers against S-phase layers. In literature one cannot find any work of S-phase-against-S-phase tribo-pairs so comparisons cannot be made.

Wear of Untreated Discs

As has been reported in Section 4-3.9, the highest wear is of untreated discs when reciprocating against untreated and treated AISI 316 ball in Ringer's solution (Figure 4-3.9.2a). The wear mechanisms observed in the untreated stainless steel discs against untreated stainless steel balls was dominated by severe adhesive wear together with abrasive and oxidative wear (Figures 4-3.9.4 to 5).

This is mainly because the untreated austenitic stainless steels are very soft and ductile. Therefore, the surface oxide films on the untreated austenitic stainless steels tribo-pairs will easily break down under the mechanical interaction due to the lack of the necessary mechanical support from the substrate. This leads to direct rubbing of metal-against-metal, which in turns creates adhesion of the asperities of the two rubbing faces. Because austenitic stainless steels are very ductile, growth of adhesive junctions is fast, thus giving rise to material transfer and severe adhesive wear of the untreated surfaces (Figure 4-3.9.5). Work hardening of the transferred material to the counterpart ball will occur during the sliding process due to the low stack fault energy and strong work hardening tendency

of austenitic stainless steels. These hardened transferred materials will abrade the soft disc, thus leading to abrasive wear as observed in Figure 4-3.9.4.

Some interesting wear results were reported in Section 4-3.9.1 for the wear of untreated discs against AISI 316 balls. First, it has been noted that untreated ASTM F138 discs were worn more as compared with other two untreated materials. As has been discussed above, this could be related to its relatively low hardness as compared with ASTM F1586 and AISI 316 (Figure 4-3.5.1). In addition, the high amount of sulphur in AISI 316 (Table 3-4) may also help to reduce its wear owing to the lubricating effect of MnS. Second, wear of all three untreated discs is larger when reciprocating against C500 treated AISI 316 balls than N430 and NC430 treated ones although the latter are harder than the former. This seemingly abnormal wear can be explained by the fact that as discussed in Section 4-3.9.2 wear of treated ball can also occur and more wear was observed from C500 treated AISI 316 balls than N430 and NC430 treated ones (Figure 4-3.9.2). Accordingly, the damaged ball will in turn cause more wear to the counterpart disc.

Wear of Treated Discs

As has been shown in Figure 4-3.9.2, the wear of discs can be effectively reduced by plasma surface alloying the surfaces. Such improvement in wear performance can be explained from the change of the wear mechanism.

As discussed above, the wear mechanisms noticed in untreated stainless steel samples against untreated stainless steel balls was governed by adhesive wear together with abrasive and oxidative wear while the treated discs against the treated balls experienced a very mild abrasive wear with some oxidation (Figures 4-3.9.8 and 9).

This change in mechanisms is attributed to the strong mechanical support from hardened S-phase layer to the surface passive film, which could avoid direct metal-on-metal contact in stainless steel tribo-pairs. In the untreated tribo-pair the oxide film would be easily removed by the rubbing of the hard asperities from the ball and the plastic deformation in the disc, resulting in the rubbing of metal against metal and thus adhesive wear.

In the case of a treated discs against untreated balls the oxide layer on the untreated ball may fail whilst the oxide film on the hardened disc can survive. This means that in the treated against untreated tribo-pairs the rubbing of the two surfaces would be metal against

oxide and adhesive wear could be reduced. Similarly, if both the discs and balls are hardened by S-phase, there would be even less chance for direct metal-on-metal contact and adhesive wear. Accordingly, mild oxidation wear and abrasive wear are expected, which is supported by the wear morphologies shown in Figures 4-3.9.13 and 14.

Wear of Balls

As has been shown in Figure 4-3.9.2, the wear loss of untreated ball was much larger when rubbing against an untreated disc than of a treated ball against an untreated disc. Firstly, this could be partially attributed to the fact that the untreated balls and the discs have very similar metallurgical characteristics and thus high metallurgical compatibility. According to Rabinowicz's [54, 160] adhesive wear theory, severe adhesive wear will occur because of the very large metallurgical compatibility between them. Secondly, as has discussed above, the untreated disc surfaces could be easily damaged through severe adhesive wear; the transferred materials will be work hardened by further rubbing, which caused more wear to the untreated ball.

When plasma surface alloyed, the wear of the balls significantly reduced as compared with the untreated ones. This is partially because of increased surface hardness and thus the strong support to the surface oxide film and partially because of the reduced metallurgical compatibility owing to the formation of S-phase layer.

It is also observed that much larger wear occurred when the treated balls reciprocated against treated ASTM F1586 than against treated ASTM F138 and AISI 316 except for N430 treated balls against C430 and C500 treated discs. This could be related to the fact that after N430 and NC430 treatments, the surface hardness of treated ASTM F1586 is higher than that of treated ASTM F138 and AISI316. However, the surface hardness of C430 and C500 treated ASTM F1586 is actually lower than that for C430 and C500 treated ASTM F138.

Combined wear

It has been noticed from Figure 4-3.9.3 that the wear lost from the untreated discs against treated balls is always higher than the treated disc against the treated balls (except for nitrided AISI 316 ball against untreated AISI 316 disc).

As has been discussed before, the wear mechanism for treated ball against untreated discs is dominated by abrasive and oxidative wear. It also well-know that hardness difference plays a key role in determining the abrasive wear in a tribo-pair [54]. Therefore, much larger abrasive wear would be expected when hardened ball against the soft untreated discs than against hardened discs since the hardness difference is much larger for the former tribo-pair than for the latter one.

In addition, it has also observed from Figure 4-3.9.3 that for treated tribo-pairs, the combined wear volume loss for ASTM F1586 and ASTM F138 is less than that for AISI 316. This could be related to the relatively poor corrosion resistance of treated AISI 316 as compared with treated ASTM F1586 and ASTM F138. It can be seen by comparing Figure 4-3.6.3 with Figures 4-3.6.1 & 2 that although plasma surface alloying can effectively enhance the corrosion resistance of AISI 316, the current density of surface treated AISI 316 samples is still about 1-2 orders magnitude higher than treated ASTM F1586 and ASTM F138. Therefore, corrosion may have also played a role in the reciprocating wear of stainless steel against stainless steel in Ringer's solution.

The above discussion is supported by the experimental results shown in Figure 4-3.9.10. When nitrided AISI 316 balls reciprocate against nitrided AISI 316 discs, the wear was higher in Ringer's solution than in distilled water.

S-phase versus Co-Cr Tribo-pairs

The wear results of S-phase layers on medical stainless steel (ASTM F138 and ASTM F1586) sliding against each other proved to be successful and the wear volume loss was similar to that for the Co-Cr combination. In fact the combined wear of four plasma treated tribopairs made of ASTM F1586 and one tribopair of ASTM F138 is equal or less than that of a Co-Cr tribopair. This result highlights the possibility that in the future the articulating surfaces of hip joint replacements could be potentially made from S-phase hardened medical grade stainless steels.

5-4.3 Fretting Wear

As has been shown in Figures 4-3.10.4 and 5, almost all surface treatments, except at 2×10^4 cycles for the 430°C nitrided (N430) and 500°C carburised (C500) ASTM F138 samples have been to good effect successful in improving the fretting-wear behaviour of all the medical austenitic stainless steels tested in the Ringer's solution.

Comparison to other author's work on fretting-wear properties of S-phase is not possible since it has never been attempted before and published. In our work the fretting-wear mechanism observed was in the gross-slip regime due to the open parallelogram shape of the F_t-d-N curve (Figure 4-3.10.1). This open parallelogram curve was also observed by other authors who were doing similar fretting wear tests but on different materials [59, 61, 178].

Because the fretting tests were carried out in the Ringer's solution, both mechanical fretting and chemical corrosion might have contributed to the fretting wear behaviour of these medical grade austenitic stainless steels. However, as has been shown in Figures 4-3.6.1 to 4, no appreciable improvement in the corrosion resistance of these three medical grade austenitic stainless steels (ASTM F138, 1586 and 2581) can be achieved by the low-temperature plasma surface processes investigated in this study. Therefore, it seems that the mechanical fretting may have played a more important role than the chemical corrosion in the fretting wear of these samples in the Ringer's solution. This is further supported by the experimental observations that although the electrochemical corrosion resistance of 500°C carburised ASTM F1586 is better than 430°C nitrided and carbonitrided ASTM F1586 (Figure 4-3.6.1), the fretting wear resistance of the former is worse than the latter (Figure 4-3.10.4). Therefore, it is reasonable to assume that the improvement in fretting wear by plasma surface alloying could be attributed to the enhanced surface mechanical properties in terms of the hardness and layer thickness of the treated surfaces.

It is known that fretting wear is not a basic wear mechanism but a complex wear mode including abrasion, adhesion and oxidation processes. This is evidenced by the parallel scratches along the fretting directions, adhesive craters and black/brown surface colours observed from the fretting craters shown in Figure 4-3.10.2. As has been shown in Figures 4-3.10.1, under the current fretting wear conditions, the 3-dimensional fretting-wear F_t-d-N curves are characterised by open parallelogram, indicative of a gross-slip mechanism. In essence, this is a micro-scale reciprocating sliding wear and therefore some

discussion given in Section 5-4.2 may to some extent applicable to the gloss-slip region fretting wear.

Similar to macro-scale sliding-wear, improvement in surface hardness can reduce abrasive wear and adhesive wear and thus reduce fretting wear. This is because increased surface hardness can reduce the penetration depth of the hard asperities and the abrasive wear. Equally, the hardened surface can effectively support the overlying oxide film, thus making the oxide film more stable and less prone to breakage when compared to the oxide layer formed on soft austenite. This protection of the oxide film in turn avoids metal-on-metal sliding which is the cause for the detrimental adhesive wear and also protects the fretting surface from corrosive attack.

For the treated ASTM F1586 samples, for both 1×10^4 and 2×10^4 cycles, the best fretting-wear properties is given by the 430°C carbonitrided (NNC430) sample followed by 430°C nitriding (NN430) and 500°C carburising (NC500) samples. The different fretting wear performance of these three treated samples could be related to both the hardness (Figure 4-3.5.1) and the depth of the surface modified layers (Figure 4-3.2.1). Among them the carburised sample has the thickest layer (Figure 4-3.2.1) but is also the softest (Figure 4-3.5.1) whilst the nitrided layer is the hardest but also the thinnest. The thin nitrided layer therefore can only offer limited protection before the layer is completely worn while for the carburised layer, since its hardness is lower, the layer removal occurs and fretting-wear is faster. The 430°C carbonitrided layer on the other hand has the characteristics of both the carburised and nitrided layers and therefore has a prolonged protection against fretting-wear. It is of interest to note that the rank of the fretting wear resistance of these three samples is the same as the rank of their load bearing capacity in terms of the surface hardness under a load between 50 and 200g (Figure 4-3.5.2).

For the treated ASTM F138 after 2×10^4 cycles of fretting-wear against the 430°C carbonitrided (MNC430) sample showed the best fretting-wear characteristics. On the other hand the 430°C nitrided (MN430) and 500°C carburised (MC500) samples showed respectively similar or even worse fretting-wear resistance when compared to the untreated material. Again this result can be attributed to the combination of both the surface hardness (Figure 4-3.5.1) and the layer thickness (Figure 4-3.2.2). It seems that because the 430°C nitrided layer was very thin, after some cycles between 1×10^4 and 2×10^4, the S-phase layer was almost completely worn out and thus it could not provide the fretting-wear resistance.

The 500°C carburised sample suffered the highest wear loss and indeed underperformed the untreated material. This might be attributed to the fact that since the S-phase layer is relatively soft it was worn out quicker leaving an unprotected surface somewhere in between 1×10^4 to 2×10^4 cycles. The reduced fretting wear resistance could be ascribed to the relatively hard S-phase fragments trapped in the contact area, which may act as abrasives and lead to strong abrasion.

The 430°C carbonitrided sample on the other hand has a combination of both high hardness and thick layer (Figure 4-3.5.7) and thus it managed to survive even after 2×10^4 cycles.

5-5 Biocompatibility

Since in literature the only reference to biocompatibility of the S-phase was in 1996 by Bordji *et al.* [179] a proper comparison of the results is not possible. In their paper the authors compared three different surface treatments performed on austenitic stainless steels. From the three treatments S-phase was only referenced in conjunction with the low temperature nitrided layer. It is not clear whether ion implantation created an S-phase layer but there is a possibility that it did. The carbon doped stainless steel definitely did not create a carbon S-phase since the authors say and I quote: “These deposits had an amorphous phase and were between 12.5μm and 15.5μm thick” [179]. Therefore we can only attempt to compare our results with the low temperature nitriding that these authors performed since this nitrided layer that they describe is very similar to the layer we used throughout this test. This comparison cannot be entirely equivalent since the authors used a human osteoblast cell line while in our experiment we used a mouse osteoblast cell line. Also the authors conducted their test over 21 days while we conducted our test over a period of 7 days. However, it is unlikely that the different cell types could account for any differences.

The results of the biocompatibility tests (Figure 4-3.11.1 and 4-3.11.2) reported in this work have demonstrated that both treated and untreated samples did not show any adverse cytotoxic effect on the mouse osteoblast cells used. This result is not in agreement with work done by Bordji *et al.* [179] since they concluded that the cells growing on the nitrided samples showed a high degree of cytoincompatibility. There are many speculative reasons

that can be given to explain why the results by Bordji *et al.* do not agree with our results but the main one might be the fact that we polished our samples and removed 1μm from our surface. Bordji *et al.* might have been not testing only the S-phase but also some iron nitrites that can be present in the exact surface after the nitriding treatment. But as mentioned above there are several other differences between their experiments and ours and it would be futile to even try to explain why our results do not agree.

In our work it was also noticed that the treated samples had more cells attached to the samples when compared to the untreated samples. Figure 4-3.11.2 shows a general repeating pattern with cell viability being highest for carbonitriding (NC430) followed by nitriding (N430), carburising (C500) and untreated.

This high proliferation of the cells on the treated samples might be due to the chemical nature of the treated surface. A higher concentration of interstitial elements in the face centred cubic structure of austenitic stainless steel seems to be beneficial for osteoblast cell proliferation. In fact as it can be seen from Figure 4-3.11.2 the amount of cells found on the surface of untreated ASTM F1586 was always higher than that on untreated ASTM F138 except for day 7. The difference between ASTM F138 and ASTM F1586 is mostly in the alloying elements of manganese and nitrogen. In addition the treated samples have a very high interstitial content in the surface. In fact the interstitial elements in the nitrided (N430), carburised (C500) and carbonitrided (NC430) layers can reach up to 20 at% nitrogen, 8 at% carbon and 20 at% nitrogen + 2 at% carbon respectively. Also the high proliferation of the cells on the carbonitrided (NC430) samples might give us an indication that osteoblast cells prefer surfaces that are both rich in nitrogen and carbon.

Wetability tests and surface roughness (Figure 4-3.11.14) conducted on the treated and untreated samples did not reveal any differences and similarly the initial cell attachment experiment also did not show any differences in the initial cell behaviour between the treated and untreated samples. Therefore these two variables are not key factors that are contributing to the difference in cell proliferation. The osteoblast cells used in the initial cell attachment experiment adhered well to all the surfaces tested and this result is in agreement with the work of Bordji *et al.* [179] where in their paper they say: “Cell attachment experiments during the first few hours of culture showed that fibroblasts and osteoblasts adhered as well on nitrided SS as on the other surfaces” [179].

The only factor that might be causing a difference in cell growth between treated and untreated is the surface residual stress caused by the S-phase. This in hindsight cannot be attributed to this difference because it is a known fact that nitriding and carbonitriding have a similar surface stress but cell proliferation was found to be always higher in the carbonitrided samples.

Chapter VI
Conclusions

Response to Plasma Surface Alloying & Formation of S-phase

(1) The present work has shown for the first time that precipitate-free S-phase can be produced in the surface of nickel-free (Fe-Cr-Mn) ASTM F2581 austenitic stainless steel by low-temperature plasma surface alloying with carbon (i.e. carburising).

(2) S-phase layers without any precipitates can be formed in Fe-Cr-Ni medical grade ASTM F138 and ASTM F1586 by plasma surface nitriding and carbonitriding at 430° and by carburising at 500°C.

(3) Compared with engineering grade AISI 316, medical grade ASTM F138 has a slightly better response to the low temperature plasma surface alloying treatments in terms of the interstitials absorbed and surface hardness although both are based on the Fe-Cr-Ni system with similar alloying elements.

(4) When plasma nitrided and carbonitrided at 430°C, precipitation of nitrides occurred in high-N, high-Mn ASTM F1586 and ASTM F2581 stainless steels. This is probably because of their high contents of nitrogen and manganese and the strong affinity between manganese and nitrogen.

(5) For all three medical grade austenitic stainless steels, Ni can increase the uptake of C in carburising but suppress the uptake of N in nitriding; on the other hand, Mn will suppress the uptake of C in plasma carburising but increase the uptake of N in nitriding.

Characteristics of S-phase in Medical Grade Austenitic Stainless Steels

(6) Nitrogen and carbon can be dissolved in the austenitic lattice of the medical grade austenitic stainless steel during plasma surface alloying, thus forming a interstitial (C, N) supersaturated solid solution i.e. S-phase with plenty of twins, slip bands and entangled dislocations.

(7) A dual layered S-phase case, consisting of an outer N-rich sublayer followed by an inner C-rich sublayer, can be formed in all three medical grade austenitic stainless steel by low-temperature plasma surface alloying with both carbon and nitrogen simultaneously (carbonitriding) or sequentially (sequential treatment). This could be related to the stronger affinity between Cr and N than between Cr and C.

(8) Cross-sectional TEM (XTEM) studies conducted on carbonitrided ASTM F138 and ASTM F1586 have revealed, for the first time, that the dual layered S-phase case consisting of a N-rich S-phase sublayer with a lattice parameter of 0.3817nm close to the surface and a C-rich sublayer with a lattice parameter of 0.3703nm close to the top N-rich sublayer.

(9) Low temperature carbonitriding inherits all the advantages of the individual plasma nitriding and carburising treatments. The synergistic effect creates a hybrid S-phase case with superior properties to individual nitrogen and carbon S-phase layers in terms of harder surface, thicker layer and smoother hardness-depth distribution.

Properties of S-phase in Medical Grade Austenitic Stainless Steels

(10) Low-temperature nitriding, carburising and carbonitriding can improve the localised corrosion resistance of medical grade austenitic stainless steels as long as the threshold sensitisation temperature is not reached. Current transients or blimps observed on the potentiodynamic curves are due to transpassive dissolution and are an indication of intergranular corrosion.

(11) All plasma surface alloyed medical grade austenitic stainless steel have shown significantly improved wear resistance over the untreated materials under both pin-on-disc and reciprocating dry sliding wear conditions. This can be attributed to significantly increased surface hardness, enhanced load bearing capacity and increased hardness to elastic modulus ratio (H/E). The wear mechanism changed from severe abrasive and adhesive wear for the untreated materials to mild oxidative and abrasive wear for the plasma surface alloyed surfaces. It should be pointed out that these conditions are unrepresentative of the joint replacement operating environment.

(12) Fretting-wear tests have revealed that plasma surface alloying can in general improve fretting-wear resistance of medical grade austenitic stainless steels in Ringer's solution.

(13) The combined wear of S-phase against S-phase for four plasma treated tribopairs made of ASTM F1586 and one tribopair made of ASTM F138 is close to that of CoCr against CoCr tribopair under reciprocating sliding wear conditions in Ringer's solution at a maximum contact pressure of about 1.4GPa. It should be indicated that these tests were carried out under extreme pressure which is beyond the yield point of some of the untreated materials. Also the synergistic influence of corrosion is an important factor in the joint replacement application and in this work it was not possible to quantify this influence, in the tests made, due to the predominance of mechanical effects brought upon by the use of these extreme pressures. Therefore the corrosion-wear results presented in this work are

unrepresentative of the joint replacement operating environment and this work can not be used as a basis for recommending or not recommending the use of nitrided, carbonitrided or carburised stainless steel for joint replacement applications.

(14) Biocompatibility studies on N, C and hybrid C/N S-phases have proved, for the first time that they are biocompatible under the realms of the tests conducted in this study.

Chapter VII
Future Work

This study has clearly shown that S-phase can be formed in medical grade austenitic stainless steel, which can effectively improve their surface properties. To fully realize its potential, the following topics are considered worthy for further attention.

Corrosion-Wear

A better understanding of the synergism of wear and corrosion on the surface of the treated sample is necessary and therefore detailed work on corrosion-wear should be conducted on the plasma alloyed medical stainless steels under: cathodic protection, open circuit potential and anodically polarised conditions.

Role of Cr

The results from this study has revealed that like Mn, Cr can increase the uptake of N in nitriding and decrease the uptake of C in carburising in high-N, low-Ni ASTM F1586; however, the opposite occurred in Ni-free, high-N ASTM F2586. Therefore, it is important to investigate the interaction among Cr, Ni and Mn.

Simulator tests

The renaissance in metal-to-metal implants and the high performance of the S-phase layers has raised the possibility of utilising stainless steel as the alternative joint bearings. It is therefore necessary to test the combination of S-phase against S-phase in hip joint simulators.

Chapter VIII
References

1. Hench, L.L. *Biomaterials: a forecast for the future*. in *European Materials Research Society Meeting*. 1997.

2. Lei, M.K. and X.M. Zhu, *In vitro corrosion resistance of plasma source ion nitrided austenitic stainless steels.* Biomaterials, 2001. **22**(7): p. 641-647.

3. Pan, J., C. Karlén, and C. Ulfvin, *Electrochemical study of resistance to localized corrosion of stainless steels for biomaterial applications* J. Electrochem. Soc., 2000. **147**(3): p. 1021-1025.

4. Haraldsson, C. and M. Newman, *Sandvik Bioline High-N; a new alloy for orthopaedic implants and fracture fixation devices*, in *Orthopaedic Product News*. 2000.

5. Haraldsson, C. and S. Cowen, *Characterization of Sandvik Bioline High-N - A comparison of standard grades F1314 and F1586*, in *Stainless Steels for Medical and Surgical Applications*, G.L. Winters and M.J. Nutt, Editors. 2003, ASTM International: Pittsburg, PA, USA p. 3-12.

6. Stein, G. and V. Diehl. *High nitrogen alloyed steels on the move-fields of application*. in *7th International Conference on High Nitrogen Steels*. 2004. Ostend, Belgium: GRIPS media.

7. Berns, H. *Alloy development and processing*. in *7th International Conference on High Nitrogen Steels*. 2004. Ostend, Belgium: GRIPS media.

8. Ciapetti, G., et al., *Quantative assessment of the response of osteoblast- and macrophage-like cells to particles of Ni-Free Fe-base alloys.* Biomaterials, 2005. **26**(8): p. 849-859.

9. Montanaro, L., et al., *Promising in vitro performances of a new nickel-free stainless steel.* J. Mater. Sci.: Mater. Med. , 2006. **17**(3): p. 267-275.

10. Davis, J.R., ed. *Stainless Steels*. 1994, ASM International: Ohio.

11. Zhang, Z.L. and T. Bell, *Structure and corrosion resistance of plasma nitrided stainless steel.* Surf. Eng., 1985. **1**(2): p. 131-136.

12. Rolinski, E., *Effect of plasma nitriding temperatures on surface properties of austenitic stainless steel.* Surf. Eng., 1987. **3**(1): p. 35-40.

13. Leyland, A., et al., *Low temperature plasma diffusion treatment of stainless steels for improved wear resistance.* Surf. Coat Technol., 1993. **62**(1-3): p. 608-617.

14. Blawert, C., et al., *Characterisation of duplex layer structures produced by simultaneous implantation of nitrogen and carbon into austenitic stainless steel X5CrNi189.* Surf. Coat Technol., 2000. **128-129**: p. 219-225.

15. Gemma, K., et al., *Prospects of rapid nitriding in high Cr austenitic alloys*, in *Stainless Steel 2000: Thermochemical Surface Engineering of Stainless Steel*, T. Bell and K. Akamatsu, Editors. 2000, Maney: Osaka, Japan. p. 159-166.

16. Christiansen, T. and M.A.J. Somers, *On the crystallographic structure of S-phase.* Scr. Mater., 2004. **50**(1): p. 35-37.

17. Sun, Y. and E. Haruman, *Effect of carbon addition on low-temperature plasma nitriding characteristics of austenitic stainless steel* Vacuum, 2006. **81**(1): p. 114-119

18. Rayner, B., X.Y. Li, and H. Dong, *Preliminary study on plasma surface modification of medical grade 316LVM and high nitrogen austenitic stainless steels.* Surf. Eng., 2006. **22**(2): p. 103-108.

19. Menthe, E., et al., *Structure and properties of plasma-nitrided stainless steel.* Surf. Coat. Technol., 1995. **74-75**(1-3): p. 412-416.

20. Yasumaru, N., *Nature of Y_N phase formed with low temperature plasma nitriding of austenitic stainless steels,* in *Stainless Steel 2000: Thermochemical Surface Engineering of Stainless Steel*, T. Bell and K. Akamatsu, Editors. 2000, Maney: Osaka, Japan. p. 229-245.

21. Dillon, C.P., *Corrosion resistance of stainless steels*. 1995, New York, USA: Marcel Dekker.

22. George, G. and H. Shaikh, *Introduction to austenitic stainless steels*, in *Corrosion of Austenitic Stainless Steels - Mechanisms, Mitigations and Monitoring* H.S. Khatak and B. Raj, Editors. 2002, Alpha Science International Ltd.: Pangbourne, UK. p. 1-36.

23. Davis, J.R., ed. *Corrosion: Understanding the basics*. 2000, ASM International: Ohio.

24. Marshall, P., *Austenitic Stainless Steels: Microstructure and Mechanical Properties*. 1984, Essex: Elsevier Applied Science Publishers Ltd.

25. Parvathavarthini, N., *Sensitization and testing for intergranular corrosion,* in *Corrosion of Austenitic Stainless Steels - Mechanisms, Mitigations and Monitoring* H.S. Khatak and B. Raj, Editors. 2002, Alpha Science International Ltd.: Pangbourne, UK. p. 117-138.

26. Wallinder, D., et al., *EIS and XPS study of surface modification of 316LVM stainless steel after passivation.* Corros. Sci., 1999. **41**: p. 275-289.

27. Shahryari, A. and S. Omanovic, *Improvement of pitting corrosion resistance of a biomedical grade 316LVM stainless steel by electrochemical modification of the passive film semiconducting properties.* Electrochem. Commun. , 2007. **9**: p. 76-82.

28. Kamachi Mudali, U. and M.G. Pujar, *Pitting corrosion of austenitic stainless steels and their weldments*, in *Corrosion of Austenitic Stainless Steels - Mechanisms, Mitigations and Monitoring* H.S. Khatak and B. Raj, Editors. 2002, Alpha Science International Ltd.: Pangbourne, UK. p. 74-105.

29. Windler, M., R. Steger, and G.L. Winters, *Quality aspects of high-nitrogen stainless steel for surgical implants*, in *Stainless Steels for Medical and Surgical Applications*, G.L. Winters and M.J. Nutt, Editors. 2003, ASTM International: Pittsburg, PA, USA p. 72-81.

30. Örnhagen, C., J.-O. Nilsson, and H. Vannevik, *Characterization of nitrogen-rich austenitic stainless steel used for osteosynthesis devices.* J. Biomed. Mater. Res., 1996. **31**: p. 97-103.

31. Wallén, E. and O. Sundqvist, *Cleanliness of vacuum-arc remelted 316LVM*, in *Semicon Southwest*. 1997: Austin Texas, USA.

32. Simmons, J.W., *Overview: High-nitrogen alloying of stainless steels.* Mater. Sci. Eng., 1996. **A207**: p. 159-169.

33. Villamil, R.F.V., et al., *Comparison electrochemical studies of F1586-95 and F138-92 stainless steel in sodium chloride, pH=4.0 medium*, in *Stainless Steels for Medical and Surgical Applications*, G.L. Winters and M.J. Nutt, Editors. 2003, ASTM International: Pittsburg, PA, USA p. 168-175.

34. Hallab, N.J., J.J. Jacobs, and J.L. Katz, *Orthopedic applications*, in *Biomaterials Science: An Introduction to Materials in Medecine*, B.D. Ratner, et al., Editors. 2004, Elsevier Inc. : London, UK. p. 526-555.

35. Maloney, W.J., *Polymethylmethacrylate*, in *Hip Surgery Materials and Developments*, L. Sedel and M.E. Cabanela, Editors. 1998, Mosby: London, UK. p. 57-65.

36. Amstutz, H.C. and P. Grigoris, *Surface replacement of the hip*, in *Hip Surgery Materials and Developments*, L. Sedel and M.E. Cabanela, Editors. 1998, Mosby: London, UK. p. 383-392.

37. Salvati, E. and E. Gomez-Barrena, *Wear: Osteolysis related to metallic debris*, in *Hip Surgery Materials and Developments*, L. Sedel and M.E. Cabanela, Editors. 1998, Mosby: London, UK. p. 333-340.

38. Hildebrand, H.F. and J.-C. Hornez, *Biological response and biocompatibility*, in *Metals As Biomaterials*, J.A. Helsen and H.J. Breme, Editors. 1998, John Wiley & Sons Ltd: Chichester, UK. p. 265-290.

39. Eschbach, L., et al., *Fatigue of small bone fragment fixation plates made from low-nickel steel*, in *Stainless Steels for Medical and Surgical Applications*, G.L. Winters and M.J. Nutt, Editors. 2003, ASTM International: Pittsburg, PA, USA p. 93-106.

40. Büscher, R. and A. Fischer. *Tribological performance of austenitic high-nitrogen steels for biomedical applications* in *7th International Conference on High Nitrogen Steels*. 2004. Ostend, Belgium: GRIPS media.

41. Singh, R. and N.B. Dahotre, *Corrosion degradation and prevention by surface modification of biometallic materials.* J. Mater. Sci., 2007. **18**: p. 725-751.

42. Kamachi Mudali, U., et al., *Failures of stainless steel orthopaedic devices - causes and remedies.* Corros. Reviews, 2003. **21**(2-3): p. 231-267.

43. Blackwood, D.J., *Biomaterials: Past successes and future problems.* Corros. Reviews, 2003. **21**(2-3): p. 97-124.

44. Dearnley, P.A., C.G. Figueiredo Pina, and J. Fisher, *Assessment of S-Phase coated medical grade stainless steel (Orton 90) for use in the human joing replacement corrosion-wear environment.* J. Phys. D: Appl. Phys., 2008. **41**: p. 9pp.

45. Helsen, J.A. and H.J. Breme, *Selection of materials*, in *Metals As Biomaterials*, J.A. Helsen and H.J. Breme, Editors. 1998, John Wiley & Sons Ltd: Chichester, UK. p. 1-35.

46. Scott, R., *Metal on metal*, in *Hip Surgery Materials and Developments*, L. Sedel and M.E. Cabanela, Editors. 1998, Mosby: London, UK. p. 21-29.

47. Dearnley, P.A., *A brief review of test methodologies for surface-engineered biomedical implant alloys.* Surf. Coat Technol., 2005. **198**: p. 483-490.

48. Saklakoglu, N., et al., *Tribological behavior of PIII treated AISI 316L austenitic stainless steel against UHMWPE counterface.* Wear, 2006. **261**(3-4): p. 264-268.

49. Bayoumi, F. and W.A. Ghanem, *Effect of nitrogen on the corrosion behavior of austenitic stainless steel in chloride solutions* Mater. Lett., 2005. **59**: p. 3311-3314.

50. Baba, H., T. Kodama, and Y. Katada, *Role of nitrogen on the corrosion behavior of austenitic stainless steels* Corros. Sci., 2002. **44**: p. 2393-2407.

51. Dayal, R.K., *Crevice corrosion of stainless steels* in *Corrosion of Austenitic Stainless Steels - Mechanisms, Mitigations and Monitoring* H.S. Khatak and B. Raj, Editors. 2002, Alpha Science International Ltd.: Pangbourne, UK. p. 106-116.

52. Muraleedharan, P., *Metallurgical influences on stress corrosion cracking*, in *Corrosion of Austenitic Stainless Steels - Mechanisms, Mitigations and Monitoring* H.S. Khatak and B. Raj, Editors. 2002, Alpha Science International Ltd.: Pangbourne, UK. p. 139-165.

53. *Standard terminology relating to wear and erosion*, in *ASTM Standard G 40-02*. 2002, Anual Book of ASTM Standards: West Conshohocken, PA, USA. p. 165-172.

54. Ludema, K.C., *Friction, Wear, Lubrication A Textbook in Tribology* 1996, Washington DC: CRC Press. 257.

55. Dearnley, P.A. and G. Aldrich-Smith, *Corrosion-wear mechanisms of hard coated austenitic 316L stainless steels.* Wear, 2004. **256**: p. 491-499.

56. Watson, S.W., et al., *Methods of measuring wear-corrosion synergism.* Wear, 1995. **181-183**(Part 2): p. 476-484.

57. Wood, R.J.K., *Tribo-corrosion of coatings: a review.* J. Phys. D: Appl. Phys., 2007. **40**: p. 5502-5521.

58. Hoeppner, D.W. and V. Chandrasekaran, *Fretting in orthopaedic implants: a review.* Wear, 1994. **173**: p. 189-197.

59. Zhou, Z.R. and L. Vincent, *Mixed fretting regime.* Wear, 1995. **181-183**: p. 531-536.

60. Hallab, N.J. and J.J. Jacobs, *Orthopedic implant fretting corrosion.* Corros. Reviews, 2003. **21**(2-3): p. 183-213.

61. Ju, X., PhD Thesis: "*The ceramic conversion treatment and tribological characterizations of NiTi shape memory alloys."* The University of Birmingham, 2007.

62. Ichii, K., K. Fujimura, and T. Takase, *Structure of the Ion-nitrdided layer of 18-8 stainless steel.* Technol. Rep. Kansai Univ., 1986. **27**: p. 135-144.

63. Poirier, L., Y. Corre, and J.P. Lebrun, *Solutions to improve surface hardness of stainless steels without loss of corrosion resistance.* Surf. Eng., 2002. **18**(6): p. 439-442.

64. Sun, Y., *A hybrid low temperature surface alloying process for austentic stainless steel.* Transactions of Materials And Heat Treatment Proceedings of The 14th IFHTSE Congress, 2004. **25**(5).

65. Ozturk, O. and D.L. Williamson, *Phase and composition depth distribution analyses of low energy, high flux N implanted stainless steel.* J. Appl. Phys., 1995. **77**(8): p. 3839-3850.

66. Leigh, S., et al., *The influence of ion energy on the nitriding behaviour of austenitic stainless steel.* Surf. Coat Technol., 1996. **85**(1-2): p. 37-43.

67. Marchev, K., et al., *The metastable m phase layer on ion-nitrided austenitic stainless steels: Part 2: crystal structure and observation of its two-directional orientational anisotropy.* Surf. Coat Technol., 1999. **112**(1-3): p. 67-70.

68. Marchev, K., et al., *The m phase layer on ion nitrided austenitic stainless steel (III): an epitexial relationship between the m phase and the (gamma) parent phase and a review of structural identifications of this phase.* Surf. Coat Technol., 1999. **116-119**: p. 184-188.

69. Marchev, K., et al., *Conditions for the formation of a martensite single-phase compound layer in ion-nitrided 316L austenitic stainless steel.* Surf. Coat Technol., 1998. **99**: p. 225-228.

70. Makishi, T. and K. Nakata. *Feature of M phase formed by plasma nitriding of Ni-base alloys - surface engineering of Ni-base alloys by means of plasma nitriding.* in *Stainless Steel 2000: Thermochemical Surface Engineering of Stainless Steel.* 2000. Osaka, Japan: Maney.

71. Gontijo, L.C., et al., *Study of the S phase formed on plasma-nitrided AISI 316L stainless steel.* Mater. Sci. Eng. A, 2006. **431**(1-2): p. 315 - 321.

72. Higashi, M., K. Shinkawa, and K. Kurosawa. *Low temperature palsonite salt bath nitriding of austenitic stainless steel SUS304.* in *Stainless Steel 2000: Thermochemical Surface Engineering of Stainless Steel.* 2000. Osaka, Japan: Maney.

73. Cheng, Z., et al., *Low temperature plasma nitrocarburisig of AISI 316 austenitic stainless steel.* Surf. Coat Technol., 2005. **191**(2-3): p. 195-200.

74. Sun, Y., X. Li, and T. Bell, *Structural characteristics of low temperature plasma carburised austenitic stainless steel.* Mater. Sci. Technol., 1999. **15**(10): p. 1171-1178.

75. Sun, Y., X.Y. Li, and T. Bell, *X-ray diffraction characterisation of low temperature plasma nitrided austenitic stainless steels.* J. Mater. Sci., 1999. **34**(19): p. 4793-4802.

76. Sun, Y., X. Li, and T. Bell, *Low temperature plasma carburising of austenitic stainless steels for improved wear and corrosion resisitance.* Surf. Eng., 1999. **15**(1): p. 49-54.

77. Farrell, K., et al., *Characterization of a carburized surface layer on an austenitic stainless steel* J. Nucl. Mater., 2005. **343**(1-3): p. 123-133.

78. Sun, Y., *Enhancement in corrosion resistance of austenitic stainless steels by surface alloying with nitrogen and carbon.* Mater. Lett., 2005. **59**(27): p. 3410 - 3413.

79. Thaiwatthana, S., et al., *Comparison studies on properties of nitrogen and carbon S phase on low temperature plasma alloyed AISI 316 stainless steel.* Surf. Eng., 2002. **18**(6): p. 433-437.

80. Christiansen, T. and M.A.J. Somers, *Low temperature gaseous nitriding and carburising of stainless steel.* Surf. Eng., 2005. **21**(5-6): p. 445-455.

81. Blawert, C., et al., *Nitrogen and carbon expanded austenite produced by PI*^{3} Surf. Coat Technol., 2001. **136**(1-3): p. 181-187.

82. Fossati, A., et al., *Glow-discharge nitriding of AISI 316L austenitic stainless steel: influence of treatment time.* Surf. Coat Technol., 2006. **200**(11): p. 3511-3517.

83. Christiansen, T. and M.A.J. Somers, *Characterisation of low temperature surface hardened stainless steel.* Structure, 2006(9): p. 1-17.

84. Thaiwatthana, S., et al., *Mechanical and chemical properties of low temperature plasma surface alloyed 316 austenitic stainless steel.* Surf. Eng., 2002. **18**(2): p. 140-144.

85. Aoki, K. and K. Kitano, *Surface hardening for austenitic stainless steels based on carbon solid solution.* Surf. Eng., 2002. **18**(6): p. 462-464.

86. Weis, Z., *Emission yields adn the standard model in glow discharge optical emission spectroscopy: Links to the underlying physical and analytical interpretation of the experimental data.* Spectrochim. Acta, Part B, 2006. **61**: p. 121-133.

87. Li, X.Y., *Low temperature plasma nitriding of 316 stainless steel - Nature of S-phase and its thermal stability.* Surf. Eng., 2001. **17**(2): p. 147-152.

88. Li, X.Y., et al., *Thermal stability of carbon S phase in 316 stainless steel.* Surf. Eng., 2002. **18**(6): p. 448-452.

89. Li, X.Y. and Y. Sun, *Transmission electron microscopy study of S phase in low temperature plasma nitrided 316 stainless steel*, in *Stainless Steel 2000: Thermochemical Surface Engineering of Stainless Steel*, T. Bell and K. Akamatsu, Editors. 2000, Maney: Osaka, Japan. p. 215-228.

90. Bell, T. and Y. Sun, *Low temperature plasma nitriding and carburising of austenitic stainless steels*, in *Stainless Steel 2000: Thermochemical Surface Engineering of Stainless Steel*, T. Bell and K. Akamatsu, Editors. 2000, Maney: Osaka, Japan. p. 275-288.

91. Li, X.Y., et al., *Microstructural characterisation of a plasma carburised low carbon Co-Cr alloy.* Surf. Eng., 2007. **23**(1): p. 45-51.

92. Xu, X., et al., *Phase depth distribution characteristics of the plasma nitrided layer on AISI 304 stainless steel.* Surf. Coat Technol., 2003. **162**(2-3): p. 242-247.

93. Renevier, N., et al., *Low temperature nitriding of AISI 316L stainless steel and titanium in a low pressure arc discharge* Surf. Coat Technol., 1999. **111**(2-3): p. 128 - 133.

94. Nosei, L., et al., *Stability under temperature of expanded austenite developed on stainless steel AISI 316L by ion nitriding.* Thin Solid Films, 2004. **468**(1-2): p. 134-141.

95. Borgioli, F., et al., *Glow-discharge nitriding of AISI 316L austenitic stainless steel: influence of treatment temperature.* Surf. Coat Technol., 2005. **200**(7): p. 2474-2480.

96. Borgioli, F., et al., *Glow discharge nitriding of AISI 316L austenitic stainless steel: Influence of treatment pressure* Surf. Coat Technol., 2006. **200**(18-19): p. 5505-5513.

97. Menthe, E. and K.T. Rie, *Further investigation of the structure and properties of austenitic stainless steel after plasma nitriding.* Surf. Coat. Technol., 1999. **116-119**: p. 199-204.

98. Sun, Y., X.Y. Li, and T. Bell, *The formation and decomposition of nitrogen and carbon fct austenite in austenitic stainless steel,* in *Stainless Steel 2000: Thermochemical Surface Engineering of Stainless Steel,* T. Bell and K. Akamatsu, Editors. 2000, Maney: Osaka, Japan. p. 263-273.

99. Abd El-Rahman, A.M., et al., *Effect of N_2 to C_2H_2 ratio on r.f. plasma surface treatment of austenitic stainless steel* Surf. Coat Technol., 2004. **183**(2-3): p. 268-274.

100. Sun, Y. and L.Y. Chin, *Residual stress evolution and relaxation in carbon S phase layers on AISI 316 austenitic stainless steel.* Surf. Eng., 2002. **18**(6): p. 443-447.

101. Sun, Y., et al., *The response of austenitic stainless steels to low-temperature plasma nitriding.* Heat Treat. Met., 1999. **26**(1): p. 9-16.

102. Parascandola, S., W. Moller, and D.L. Williamson, *Successful nitriding of austenitic stainless steel: The diffusion mechanism of nitrogen and the role of the surface oxide layer*, in *Stainless Steel 2000: Thermochemical Surface Engineering of Stainless Steel,* T. Bell and K. Akamatsu, Editors. 2000, Maney: Osaka, Japan. p. 201-214.

103. Williamson, D.L., et al., *Role of ion-beam processing time in the formation and growth of high-nitrogen phase in austenitic stainless steel*, in *Stainless Steel 2000: Thermochemical Surface Engineering of Stainless Steel*, T. Bell and K. Akamatsu, Editors. 2000, Maney: Osaka, Japan. p. 333-352.

104. Tsujikawa, M., et al., *Behavior of carbon in low temperature plasma nitriding layer of austenitic stainless steel.* Surf. Coat. Technol. , 2004. **193**(1-3): p. 309-313

105. Tsujikawa, M., et al., *Surface material design of 316 stainless steel by combination of low temperature carburizing and nitriding.* Surf. Coat. Technol., 2005. **200**(1-4): p. 507-511

106. Czerwiec, T., N. Renevier, and H. Michel, *Low-temperature plasma-assisted nitriding.* Surf. Coat Technol., 2000. **131**(1-3): p. 267-277.

107. Li, X.Y. and H. Dong, *Effect of annealing on corrosion behaviour of nitrogen S phase in austenitic stainless steel.* Mater. Sci. Technol., 2003. **19**(10): p. 1427-1434.

108. Li, X.Y., Y. Sun, and T. Bell, *The stability of the nitrogen S-phase in austenitic stainless steel.* Z. Metall., 1999. **90**(11): p. 901-907.

109. Ozturk, O. and D.L. Williamson, *Thermal stability of the high-N solid-solution layer on stainless steel* Surf. Coat Technol., 2002. **158-159**: p. 288 - 294.

110. Rey, O. and P. Jacquot. *Klosterising(r): the hardening of austenitic stainless steel* in *4th European Stainless Steel Science and Marketing Congress* 2002. Paris.

111. Pedraza, F., et al., *Low energy, high-flux nitridation of face centred cubic metallic matrices.* Thin Solid Films, 2007. **515**(7-8): p. 3661-3669.

112. Pedraza, F., et al., *Low-energy high-flux nitriding of Ni and Ni20Cr substrates* Surf. Coat Technol., 2004. **176**(2): p. 236-242.

113. Williamson, D.L., et al., *Metastable phase-formation and enhanced diffusion in fcc alloys under high-dose, High-flux nitrogen implantation at high and low ion energies.* Surf. Coat Technol., 1994. **65**(1-3): p. 15-23.

114. Williamson, D.L., J.A. Davis, and P.J. Wilbur, *Effect of austenitic stainless steel composition on low-energy, high-flux, nitrogen ion beam processing.* Surf. Coat Technol., 1998. **103-104**: p. 178-184.

115. Xiaolei, X., et al., *A comparative study on microstructure of the plasma-nitrided layers on austenitic stainless steel and pure Fe.* Surf. Coat Technol., 2005. **192**(2-3): p. 220- 224.

116. Wei, R., et al., *A comparative study of beam ion implantation, plasma ion implantation and nitriding of AISI 304 stainless steel* Surf. Coat Technol., 1996. **83**(1-3): p. 235-242.

117. Blawert, C., et al., *Plasma immersion ion implantation of stainless steel: austenitic stainless steel in comparison to austenitic-ferritic stainless steel* Surf. Coat Technol., 1996. **85**(1-2): p. 15-27.

118. Chen, F.-S. and C.-N. Chang, *Effect of CH_4 addition on plasma nitrocarburizing of austenitic stainless steel.* Surf. Coat. Technol., 2003. **173**(1): p. 9-18.

119. Czerwiec, T., et al., *On the occurrence of dual diffusion layers during plasma-assisted nitriding of austenitic stainless steel.* Surf. Coat Technol., 2006. **200**(18-19): p. 5289-5295

120. Fossati, A., et al., *Corrosion resistance properties of glow-discharge nitrided AISI 316L austenitic stainless steel in NaCl solutions* Corros. Sci., 2006. **48**(6): p. 1513-1527.

121. Gontijo, L.C., et al., *Corrosion resistance of the layers formed on the surface of plasma-nitrided AISI 304L steel* Thin Solid Films, 2006. **515**(3): p. 1093-1096

122. Menthe, E., et al., *Improvement of the mechanical properties of austenitic stainless steel after plasma nitriding.* Surf. Coat. Technol., 2000. **133 -134**: p. 259-263.

123. Li, X.Y., *Microstructural Characterisation of a Plasma Carburised Low Carbon Co-Cr alloy.* Surf. Eng., 2007. **23**(1): p. 45-51.

124. Larisch, B., U. Brusky, and H.J. Spies, *Plasma nitriding of stainless steels at low temperatures.* Surf. Coat Technol., 1999. **116 -119**(-): p. 205-211.

125. Esfandiari, M. and H. Dong, *Improving the surface properties of A286 precipitation-hardening stainless steel by low-temperature plasma nitriding.* Surf. Coat Technol., 2007. **201**(14): p. 6189-6196.

126. Frandsen, R.B., T. Christiansen, and M.A.J. Somers, *Simultaneous surface engineering and bulk hardening of precipitation hardening stainless steel* Surf. Coat Technol., 2006. **200**: p. 5160-5169.

127. Lewis, D.B., et al., *Metallurgical study of low-temperature plasma carbon diffusion treatments for stainless steels.* Surf. Coat Technol., 1993. **60**(1-3): p. 416-423.

128. Bell, T., *Surface engineering of austenitic stainless steel.* Surf. Eng., 2002. **18**(6): p. 415-422.

129. Mingolo, N., A.P. Tschiptschin, and C.E. Pinedo, *On the formation of expanded austenite during plasma nitriding of an AISI 316L austenitic stainless steel* Surf. Coat Technol., 2006. **201**(7): p. 4215-4218

130. Fewell, M.P., et al., *The nature of expanded austenite.* Surf. Coat Technol., 2000. **131**(1-3): p. 300-306.

131. Li, C.X. and T. Bell, *Sliding wear properties of active screen plasma nitrided 316 austenitic stainless steel.* Wear, 2004. **256**(11-12): p. 1144-1152.

132. Li, C.X. and T. Bell, *Corrosion properties of active screen plasma nitrided 316 austenitic stainless steel.* Corros. Sci., 2004. **46**(6): p. 1527-1547.

133. Li, C.X., J. Georges, and X.Y. Li, *Active screen plasma nitriding of austenitic stainless steel.* Surf. Eng., 2002. **18**(6): p. 453-458.

134. Ueda, M., et al., *Grazing incidence X-ray diffraction of SS304 steel surfaces modified by high- and low-pressure ion nitriding processes.* Surf. Coat Technol., 2004. **186**(1-2): p. 291-294.

135. Liang, W., S. Juncai, and X. Xiaolei, *Low pressure plasma arc source ion nitriding compared with glow-discharge plasma nitriding of stainless steel* Surf. Coat Technol., 2001. **145**(1-3): p. 31-37.

136. Liang, W., et al., *Characteristics of low pressure plasma arc source ion nitrided layer on austenitic stainless steel at low temperature* Thin Solid Films, 2001. **391**(1): p. 11-16.

137. Baranowska, J., et al., *Surface modification of austenitic steel by low-temperature plasma.* Vacuum, 2005. **78**(2-4): p. 389-394.

138. Baranowska, J., S.E. Franklin, and C.G.N. Pelletier, *Tribological behaviour and mechanical properties of low temperature gas nitrided austenitic steel in relation to layer morphology.* Wear, 2005. **259**(1-6): p. 432-438.

139. Baranowska, J., *Characteristic of the nitride layers on the stainless steel at low temperature.* Surf. Coat Technol., 2004. **180-181**: p. 145-149.

140. Christiansen, T. and M.A.J. Somers. *Kinetics of microstructure evolution during gaseous thermochemical surface treatment*. in *The 1st International Conference on Difusion in Solids and Liquids*. 2005. University of Aveiro, Aveiro, Portugal.

141. Berns, H., *Solution nitriding of stainless steels*, in *Stainless Steel 2000: Thermochemical Surface Engineering of Stainless Steel*, T. Bell and K. Akamatsu, Editors. 2000, Maney: Osaka, Japan. p. 111-115.

142. Berns, H., et al., *Solution nitriding of stainless steels - A new thermocemical heat treatment process.* Heat Treat. Met., 2000. **2**: p. 39-45.

143. Li, X., et al., *Crosss-sectional transmission electron microscopy characterisation of plasma immersion ion implanted austenitic stainless steel* Surf. Coat Technol., 1996. **85**(1-2): p. 28-36.

144. Aldrich-Smith, G., D.G. Teer, and P.A. Dearnley, *Corrosion-wear response of sputtered CrN and S-Phase coated austenitic stainless steel* Surf. Coat Technol., 1999. **116-119**: p. 1161-1165.

145. Dearnley, P.A., *Corrosion wear response of S-phase coated 316L.* Surf. Eng., 2002. **18**: p. 429-432.

146. Dearnley, P.A., K.L. Dahm, and G. Aldrich-Smith, *The nature of S phase coatings and their wear and corrosion-wear behaviour when applied to 316L,* in *Stainless Steel 2000: Thermochemical Surface Engineering of Stainless Steel,* T. Bell and K. Akamatsu, Editors. 2000, Maney: Osaka, Japan. p. 317-331.

147. Allen, C., et al., *The fretting fatigue behaviour of plasma nitrided AISI 316 stainless steel,* in *Stainless Steel 2000: Thermochemical Surface Engineering of Stainless Steel,* T. Bell and K. Akamatsu, Editors. 2000, Maney: Osaka, Japan. p. 353-360.

148. Allen, C., et al., *The effect of fretting fatigue behaviour of plasma nitrided Stainless Steel.* Wear, 2003. **254**: p. 1106-1112.

149. Sun, Y. and T. Bell, *Dry sliding wear resistance of low temperature plasma carburised austenitic stainless steel.* Wear, 2002. **253**(5-6): p. 689-693.

150. Sun, Y. and T. Bell, *Effect of layer thickness on the rolling-sliding wear behavior of low-temperature plasma-carburized austenitic stainless steel.* Tribol. Lett., 2002. **13**(1): p. 29-34.

151. Sun, Y. and T. Bell, *Sliding wear characteristics of low temperature plasma nitrided 316 austenitic stainless steel.* Wear, 1998. **218**(1): p. 34-42.

152. Thaiwatthana, S., et al., *Corrosion wear behaviour of low temperature plasma alloyed 316 austenitic stainless steel.* Surf. Eng., 2003. **19**(3): p. 211-216.

153. Dong, H., et al., *Improving the erosion–corrosion resistance of AISI 316 austenitic stainless steel by low-temperature plasma surface alloying with N and C.* Mater. Sci. Eng. A, 2006. **431**(1-2): p. 137-145

154. Zhu, X.M. and M.K. Lei, *Pitting corrosion resistance of high nitrogen f.c.c. phase in plasma source ion nitrided austenitic stainless steel* Surf. Coat. Technol., 2000. **131**(1-3): p. 400-403.

155. Martin, F.J., et al., *Carburization-induced passivity of 316L austenitic stainless steel.* Electrochem. Solid-State Let. , 2007. **10**(12): p. C76-C78.

156. Hubbard, C.R., *Certification of Si powder diffraction standard reference material 640a.* J. Appl. Cryst., 1982. **16**(3): p. 285-288.

157. Hubbard, C.R., *Standard reference material 675 - Low 2θ (large d-Spacing) standard for X-Ray powder diffraction*, in *National Bureau of Standards Certificate*. 1982, National Bureau of Standards: Washington D.C.

158. *Standard guide for crevice testing of iron-base and nickel-base stainless alloys in seawater and other chloride-containing aqueous environments*, in *ASTM Standard G 78-01*. 2001, Anual Book of ASTM Standards: West Conshohocken, PA, USA.

159. Rajaraman, R., et al., *A scanning electron microscope study of cell adhesion and spreading in vitro.* Exp. Cell Res., 1974. **88**: p. 327-339.

160. Chen, J., PhD Thesis: "*Plasma surface alloying of CoCr alloys to combat wear."* The University of Birmingham, 2008.

161. Cullity, B.D. and S.R. Stock, *Elements of X-Ray Diffraction*. 3rd ed. 2001, New Jersey, USA: Prentice Hall. 678.

162. Suter, T. and H. Boehni, *Critical factors of localised corrosion II.* Electrochem. Soc. Proc., 1996. **95-15**: p. 127.

163. Szklarska-Smialowska, Z., *Pitting and Crevice Corrosion*. 2005, Houston: NACE International.

164. Gemma, K., et al., *Abnormal nitriding behaviour of a high chromium, high manganese austenitic steel.* Surf. Eng., 1995. **11**(3): p. 240-245.

165. Shanina, B.D., et al., *Concept of a new high-strength austenitic stainless steel.* Steel Research, 2002. **73**(3): p. 105-113.

166. Sun, Y. and E. Haruman, *Influence of processing conditions on structural characteristics of hybrid plasma surface alloyed autenitic stainless steels.* Surf. Coat Technol., 2008. **202**(17): p. 4069-4075.

167. Berns, H., *Stainless steels suited for solution nitriding* Mat. -wiss. u. Werkstofftech., 2002. **33**: p. 5-11.

168. Zhang, Z.L. and T. Bell. *Structure and corrosion resistance of plasma-nitrided AISI 316 Stainless Steel*. in *Third International Congress on Heat Treatment of Materials*. 1983. Shanghai: The Metals Society.

169. Bou-Saleh, Z., A. Shahryari, and S. Omanovic, *Enhancement of corrosion resistance of a biomedical grade 316LVM stainless steel by potentiodynamic cyclic polarization.* Thin Solid Films, 2007. **515**: p. 4727-4737.

170. Zardiackas, L.D., et al., *Comparison of anodic polarization and galvanic corrosion of a low-nickel stainless steel to 316LS and 22Cr-13Ni-5Mn stainless steel,* in *Stainless Steels for Medical and Surgical Applications,* G.L. Winters and M.J. Nutt, Editors. 2003, ASTM International: Pittsburg, PA, USA p. 107-118.

171. Windler, M. and R. Steger, *Mechanical and corrosion properties of forged hip stems made of high-nitrogen stainless steel*, in *Stainless Steels for Medical and Surgical Applications*, G.L. Winters and M.J. Nutt, Editors. 2003, ASTM International: Pittsburg, PA, USA p. 39-49.

172. Hodgson, A.W.E., et al., *Passive and transpassive behaviour of CoCrMo in simulated biological solutions.* Electrochim. Act, 2004. **49**: p. 2167-2178.

173. Ghosh, S. and T. Ramgopal, *Effect of chloride and phosphoric acid on the corrosion of alloy C-276, UNS N08028, and UNS N08367.* Corrosion 2005. **61**(6): p. 609-619.

174. Stansbury, E.E. and R.A. Buchanan, *Fundamentals of Electrochemical Corrosion.* 2004, Ohio: ASM International. 487.

175. Yan, Y., et al., *Tribocorrosion in implants - assessing high carbon and low carbon Co-Cr-Mo alloys by in situ electrochemical measurements* Tribology International, 2006. **39**: p. 1509-1517.

176. Yan, Y., A. Neville, and D. Dowson, *Understanding the role of corrosion in the degradation of metal-on-metal implants.* Proc. IMechE Part H: J. Engineering in Medecine, 2006. **220**: p. 173-181.

177. Yan, Y., A. Neville, and D. Dowson, *Biotribocorrosion - an appraisal of the time dependence of wear and corrosion interactions: I. The role of corrosion.* J. Phys. D: Appl. Phys., 2006. **39**: p. 3200-3205.

178. Geringer, J., B. Forest, and P. Combrade, *Wear analysis of materials used as orthopaedic implants.* Wear, 2006. **261**: p. 971-979.

179. Bordji, K., et al., *Evaluation of the effect of three surface treatments on the biocompatibility of 316L stainless steel using human differentiated cells.* Biomaterials, 1996. **17**(5): p. 491-500.

Table 2-1 Process parameters for hybrid S-phase

Process	Temp	Time	Pressure	Gas Mixture %			Material	Ref
	°C	hrs	Pa	N_2	CH_4	H_2		
PI[3]	400	3	0.3	bal	25, 50, 75		X5CrNi189	[14]
dc	350-450	≥40	500	n.g.	n.g.	n.g.	316, 321	[64]
dc	400	8	600	80	5	15	304	[104
dc	450	12	500	bal	0.5, 1, 2, 5, 8	75	316	[73]
dc	450	8	600	80	5	15	316	[105]
dc	420	5	500	95	5		321	[17]
dc	380-430	15-40	n.g.	95	5		316, 304, 321	[78]

Process Parameters (n.g. = not given)

Table 3-1 Trade names and standards of biomedical materials used in this study

Trade Name	Condition	Diameter (mm)	UNS	Code	ASTM Stadard	ISO Standard	BS Standard
Sandvik Bioline 316LVM	Annealed Bar	25	S 31673	M	F 138-03	5832-1	7252/1
Sandvik Bioline 316LVM	Cold Worked Bar	14	S 31673	MT	F 138-03	5832-1	7252/1
Sandvik Bioline High-N	Annealed Bar	25	S 31675	N	F 1586-02	5832-9	7252/9
Sandvik Bioline High-N	Cold Worked Bar	14	S 31675	NT	F 1586-02	5832-9	7252/9
Böhler P558	Annealed	25	S 29225	F	F 2581-07	-	-
Co29Cr5Mo (Smith & Nephew)	Cast Bar	40	R 30075	Co-Cr	F75	5832-4	7252/4

Table 3-2 Inclusion content of the biomaterials used

Material	Condition	A (Sulphide)		B (Alumina)		C (Silicate)		D (Globular Oxide)	
		Thin	Heavy	Thin	Heavy	Thin	Heavy	Thin	Heavy
ASTM F138	Annealed Bar	0.0	0.0	0.1	0.0	0.0	0.0	0.8	0.0
ASTM F138	Cold Worked Bar	0.0	0.0	0.8	0.0	0.0	0.0	0.9	0.1
ASTM F1586	Annealed Bar	0.0	0.0	0.7	0.0	1.3	1.3	1.2	0.2
ASTM F1586	Cold Worked Bar	0.0	0.0	0.8	0.0	0.0	0.0	1.0	0.3
ASTM F2581	Annealed Bar	1.5 max	1.0 max	1.5 max	1.0 max	1.5 max	1.0 max	1.5 max	1.0 max

Table 3-3 Properties of the biomaterials used

Material	Condition	Grain Size	Ultimate Tensile Stress	Proof Stress (0.2%)	Elongation 4D	Reduction in Area	Hardness
		No.	MPa	MPa	%	%	HB
ASTM F138	Annealed	6	593	300	55	86	149
ASTM F138	Cold Worked	6	961	766	21	73	300
ASTM F1586	Annealed	8	885	587	42.5	67	241
ASTM F1586	Cold Worked	11	1271	1032	19.5	60	363
ASTM F2581	Annealed	≥5	827 min	482 min	40 min	50 min	-
ASTM F75	Cast	-	665 min	450 min	8 min	-	257-333

Table 3-4 Composition of the materials used

MATERIAL	Composition [wt%]												
	Type	C	Si	Mn	P	S	Cr	Ni	Mo	Cu	N	Nb	W	Bal.
AISI 316 Annealed Bar	Spec.	0.08 max	1.0 max	2.0 max	0.045 max	0.03 max	16-18	10-14	2 -3	-	-	-	-	Fe
AISI 316 Cold Worked Ball	Spec.	0.08 max	1.0 max	2.0 max	0.045 max	0.03 max	16-18	10-14	2-3	-	-	-	-	Fe
AISI 440C Cold Worked Ball	Spec.	0.95 – 1.20	1.0 max	≤1.0	0.04 max	≤0.015	16-18	-	0.4 -0.8	-	-	-	-	Fe
ASTM F138 Annealed Bar	Cert.	0.019	0.5	1.87	0.018	0.001	17.43	13.75	2.72	0.059	0.084	-	-	Fe
ASTM F138 Cold Worked Bar	Cert.	0.021	0.49	1.68	0.018	0.001	17.43	14.22	2.77	0.082	0.055	-	-	Fe
ASTM F1586 Annealed Bar	Cert.	0.037	0.47	3.99	0.018	0.0013	20.80	9.82	2.33	0.1	0.39	0.28	-	Fe
ASTM F1586 Cold Worked Bar	Cert.	0.032	0.48	4.05	0.016	0.0008	20.7	9.7	2.33	0.1	0.38	0.26	-	Fe
ASTM F2581 Annealed Bar	Spec.	0.15 – 0.25	0.2-0.6	9.5-12.5	0.02 max	0.01 max	16.5-18	0.05 max	2.7-3.7	0.25 max	0.45-0.55	-	-	Fe
ASTM F75 Cast Bar	Spec.	0.35 max	1.0 max	1.0 max	0.02 max	0.01 max	26.5–30	0.5 max	4.5-7	-	0.25 max	-	1.0	Co
Stellite® 6 PM Ball	Cert.	1.24	0.77	-	-	-	29.3	2.6	-	-	-	-	4.5	Co
AISI 316 Annealed Bar	EDX	-	0.27	1.64	-	-	17.02	11.15	2.02	-	-	-	-	Fe
ASTM F2581 Annealed Bar	EDX		0.39	10.06	-	-	16.72	-	3.2	-	-	-	-	Fe

Type: Spec. is according to standard specification; Cert. is according to supplier material certificate; EDX is according to in-house analysis using Energy Dispersive X-rays

Table 3-5 Spheres used

	Diameter (mm)	Hardness	Standard Grade	Treated / Untreated	Composition	Purpose
WC in cobalt binder	8	90.5-91.5 HRA	100	Untreated	93-95% WC; 5-7% Co	Pin-on-disc wear
WC in cobalt binder	12.7	90.5-91.5 HRA	100	Untreated	93-95% WC; 5-7% Co	Reciprocating-wear
AISI 316	12.7	25-39 HRC	100	Both	See Table 3-4	Reciprocating-wear
Deloro Stellite® 6 Ball	12.7	40 HRC	40	Untreated	See Table 3-4	Reciprocating-wear
AISI 440C	40	57-60 HRC	100	Untreated	See Table 3-4	Fretting-wear

Table 3-6 PSA with Nitrogen (temperature effect)

Code	Process Parameters						
	Furnace	Temperature	Time	Pressure	Gas Mix [%]		
	kW	[°C]	[hrs]	[Pa]	CH_4	N_2	H_2
N400	40	400	15	400	0	25	75
N420	40	420	15	400	0	25	75
N430	40	430	15	400	0	25	75
N440	40	440	15	400	0	25	75
N460	40	460	15	400	0	25	75

Table 3-7 PSA with Carbon (temperature effect)

Code	Process Parameters						
	Furnace	Temperature	Time	Pressure	Gas Mix [%]		
	kW	[°C]	[hrs]	[Pa]	CH_4	N_2	H_2
C430	60	430	15	400	1.5	0	98.5
C450	60	450	15	400	1.5	0	98.5
C460	60	460	15	400	1.5	0	98.5
C500	60	500	15	400	1.5	0	98.5
C520	60	520	15	400	1.5	0	98.5
C540	60	540	15	400	1.5	0	98.5

Table 3-8 PSA with Carbon and Nitrogen (composition effect)

Code	Process Parameters						
	Furnace	Temperature	Time	Pressure	Gas Mix [%]		
	kW	[°C]	[hrs]	[Pa]	CH_4	N_2	H_2
NC460 (0.5)	60	460	15	400	0.5	25	74.5
NC460 (1.0)	60	460	15	400	1.0	25	74.0
NC460 (1.5)	60	460	15	400	1.5	25	73.5
NC460 (2.0)	60	460	15	400	2.0	25	73.0
NC460 (3.0)	60	460	15	400	3.0	25	72.0

Table 3-9 PSA with Carbon and Nitrogen (temperature effect)

Code	Process Parameters						
	Furnace	Temperature	Time	Pressure	Gas Mix [%]		
	kW	[°C]	[hrs]	[Pa]	CH_4	N_2	H_2
NC400	60	400	15	400	1.5	25	73.5
NC430	60	430	15	400	1.5	25	73.5
NC440	60	440	15	400	1.5	25	73.5
NC460	60	460	15	400	1.5	25	73.5

Table 3-10 PSA with nitrogen, carbon and both (Carburising followed by post-nitriding)

Code	First Process							Second Process						
	Furnace	Temperature	Time	Pressure	Gas Mix [%]			Furnace	Temperature	Time	Pressure	Gas Mix [%]		
	kW	[°C]	[hrs]	[Pa]	CH_4	N_2	H_2	kW	[°C]	[hrs]	[Pa]	CH_4	N_2	H_2
N400 (7.5)	60	400	7.5	400	0	25	75	-	-	-	-	-	-	-
C450 (7.5)	40	450	7.5	400	1.5	0	98.5	-	-	-	-	-	-	-
CN450-400	40	450	15	400	3.0	25	72.0	60	400	15	400	0	25	75

Table 3-11 PSA with nitrogen, carbon and both (Optimised Treatments)

Code	Process Parameters						
	Furnace	Temperature	Time	Pressure	Gas Mix [%]		
	kW	[°C]	[hrs]	[Pa]	CH_4	N_2	H_2
N430	60	430	15	400	0	25	75
C430	40	430	15	400	1.5	0	98.5
NC430	60	430	15	400	1.5	25	73.5
C500	40	500	15	400	1.5	0	98.5

Table 3-12 Composition of full strength Ringer's solution

	Ringer's Solution		Simulated Crevice Solution	
	gL^{-1}	Molarity	gL^{-1}	Molarity
NaCl	9	0.1540	9	0.1540
KCl	0.42	0.0056	0.42	0.0056
$CaCl_2$	0.48	0.0043	0.48	0.0043
$NaHCO_3$	0.2	0.0024	0.2	0.0024
HCl	-	-	3.65	0.1

Table 3-13 Surface condition of the surface and bulk material condition of the disc samples together with the corresponding testing technique

Technique or Experimental testing	Surface Condition	Bulk Material Condition
Metallography (disc)	As-Treated	Annealed
GDOES	As-Treated	Annealed
XRD (Untreated)	Polished	Annealed & Cold Worked
XRD (Treated)	As-Treated, Polished	Annealed
XRD (Corrosion Specimen)	Corroded Surface	Annealed
XSEC-XRD (1^{st} Step)	As-Treated	Annealed
SEM	Worn or Corroded Surface	Annealed
SEM (biocompatibility)	Adhered cells on polished surface	Cold-Worked
Surface Micro-Hardness (Vickers)	Polished (Ra=0.06-0.10µm)	Annealed
Surface Nano-Indentation	Polished (Ra=0.06-0.10µm)	Annealed
Hardness-Depth Profile (Knoop)	As-Treated	Annealed
Surface Roughness (Stylus)	Polished and Worn Surfaces	Annealed
Surface Roughness (Confocal)	Polished	Cold Worked
Planar TEM	As-Treated	Annealed
XTEM	As-Treated	Annealed
Potentiodynamic Corrosion Testing	Polished (Ra=0.06-0.10µm)	Annealed
Crevice Corrosion Testing	Polished (Ra=0.06-0.10µm)	Annealed
Pin-on-disc	As-Treated	Annealed
Reciprocating-Wear	Polished (Ra=0.06-0.10µm)	Annealed
Fretting-Corrosion Wear	Polished (Ra=0.06-0.10µm)	Annealed
Biocompatibility	Polished (See Fig 4-3.11.14)	Cold Worked

Table 3-14 Hertzian contact stress analysis of the different wear tests conducted throughout this work

Test	Load (N)	Ball Material	Disc Material	Ball diameter (mm)	Maximum Contact Pressure (GPa)	Contact Area (mm)
Pin on disc	10	WC – Co	Stainless Steel	8	1.55	0.06
Reciprocating	54	WC – Co	Stainless Steel	12.7	1.99	0.11
Reciprocating	39	Stellite® 6	Co-Cr	12.7	1.44	0.11
Reciprocating	39	Stainless	Stainless Steel	12.7	1.40	0.12

See Appendix for equations, values and calculations used

Table 4-1 TEM analysis of Figure 4-3.4.4 together with XRD data acquired from Figure 4-3.3.6 at a depth of 6μm

No.	(h k l)	R (cm)	d-spacing from TEM (nm)	d-spacing from XRD (nm)	TEM Data Notes	XRD Data Notes
1	$\bar{1}1\bar{1}$	0.57	0.2193	0.217703	Nitrogen S-phase Refer to Figure 4-3.4.4b	Refer to XRD Depth Profile Figure 4-3.3.6
2	$\bar{2}00$	0.65	0.1923	0.197152		
3	$02\bar{2}$	0.94	0.1330	0.133409		
1	$\bar{1}1\bar{1}$	0.59	0.2120	0.213898	Carbon S-phase Refer to Figure 4-3.4.4c	Refer to XRD Depth Profile Figure 4-3.3.6
2	$\bar{2}00$	0.67	0.1866	0.187524		
3	$02\bar{2}$	0.96	0.1302	0.130866		

Camera Constant (Lλ) used is 1.25nm

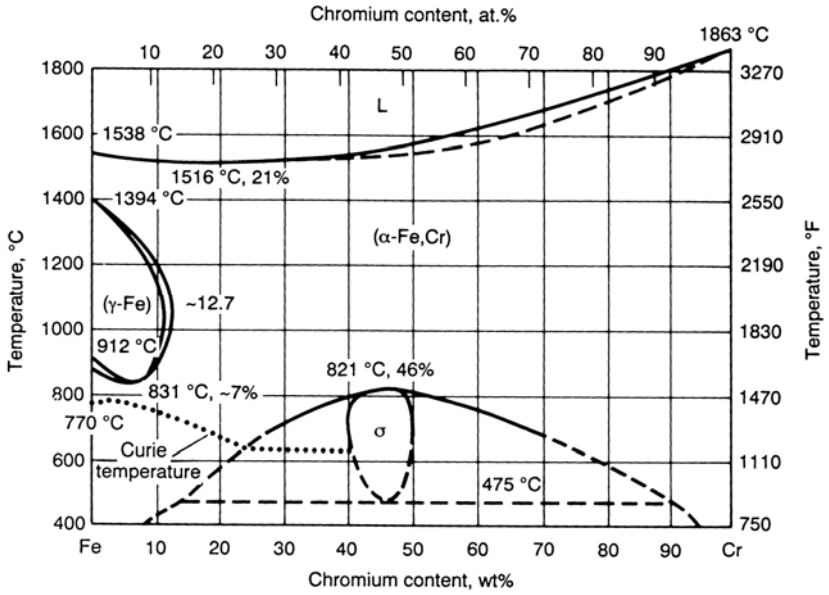

Figure 2-1 Binary iron-chromium equilibrium phase diagram. Source: Ref [10]

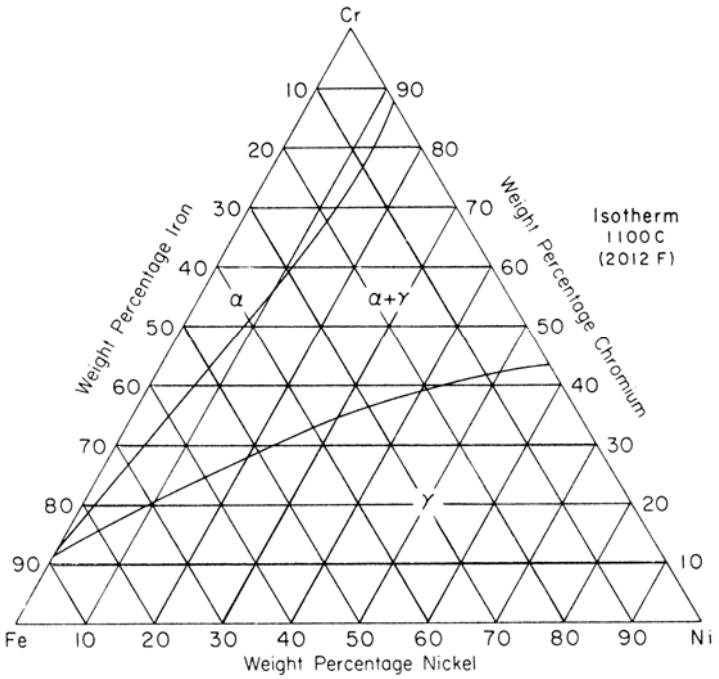

Figure 2-2 The iron-nickel-chromium system at 1100°C. Source: Ref [10]

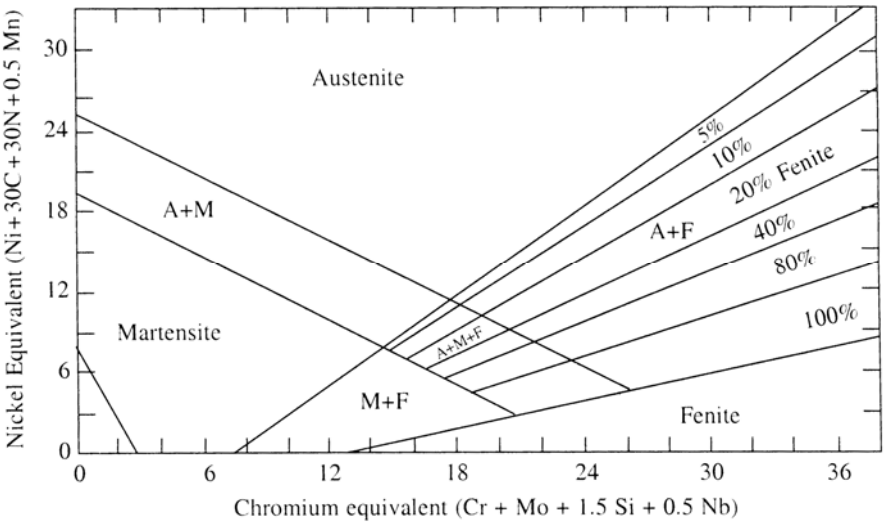

Figure 2-3 Schaeffler constitution diagram for stainless steel. Source: Ref [22]

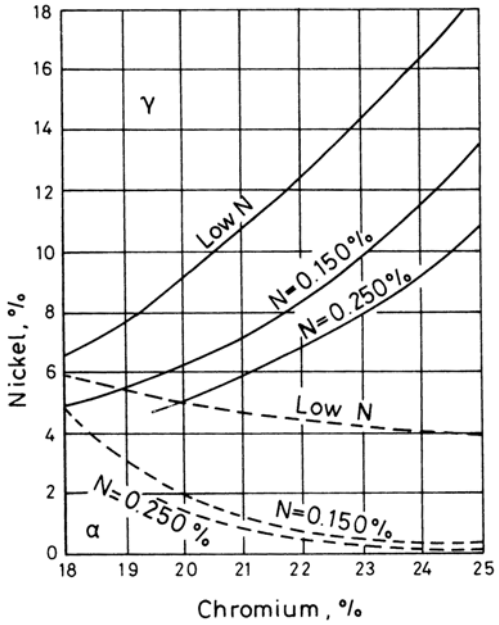

Figure 2-4 Effect of nitrogen on austenite loop. Source: Ref [24]

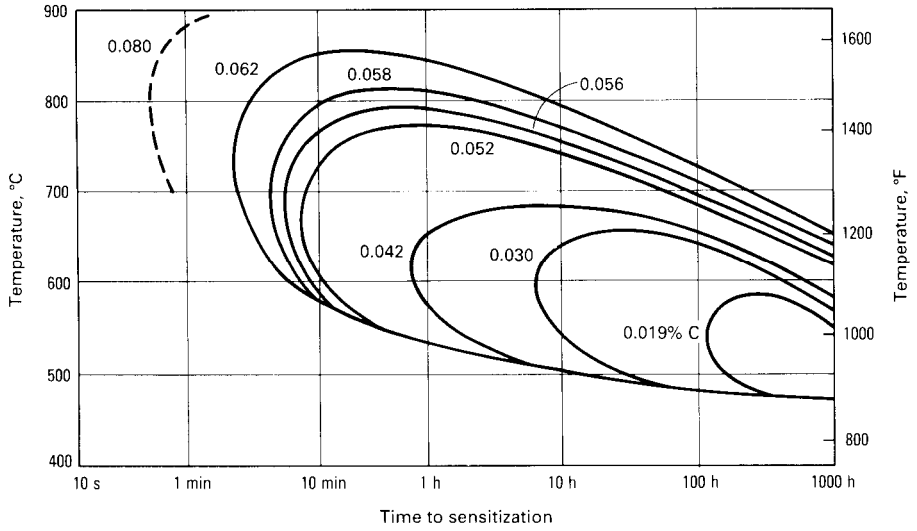

Figure 2-5 Time-temperature curves showing effect of carbon content on carbide precipitation, which forms in the areas to the right of the various carbon-content curves. Source: Ref [10]

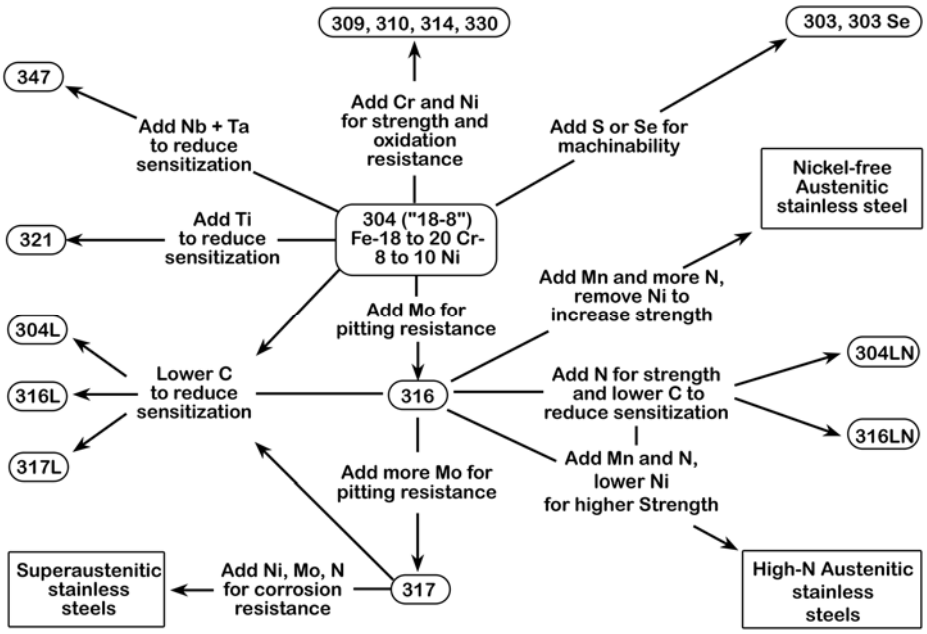

Figure 2-6 Compositional and property linkages in stainless steel family of alloys. Redrawn from: Ref [6, 7, 10]

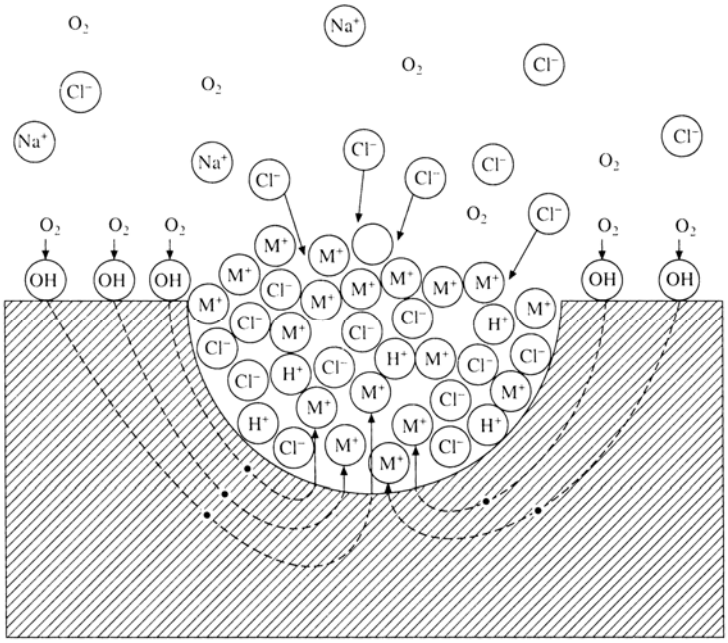

Figure 2-7 Schematic of the various events occurring during the growth of pits. Source: Ref [10, 28]

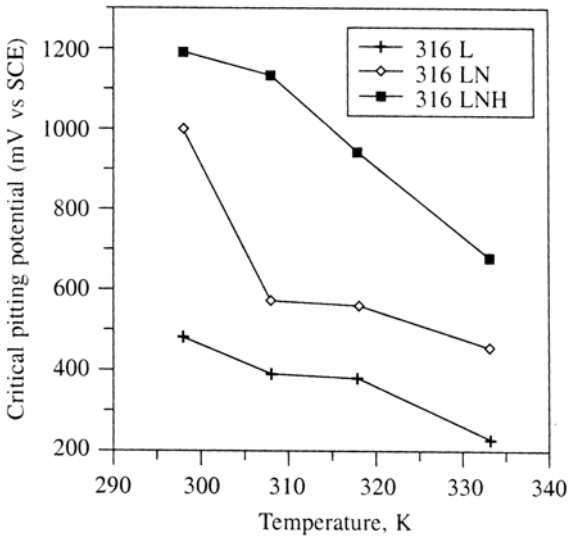

Figure 2-8 Influence of nitrogen addition on pitting corrosion resistance at various temperatures. Source: Ref [28]

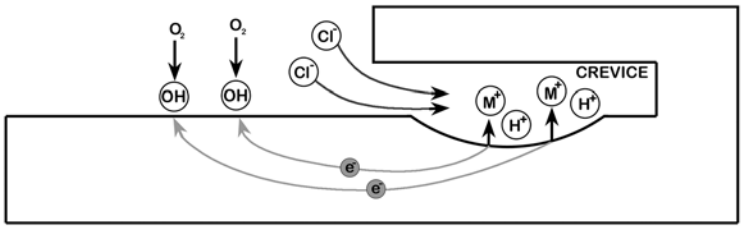

Figure 2-9 Schematic of the various events occurring during crevice corrosion

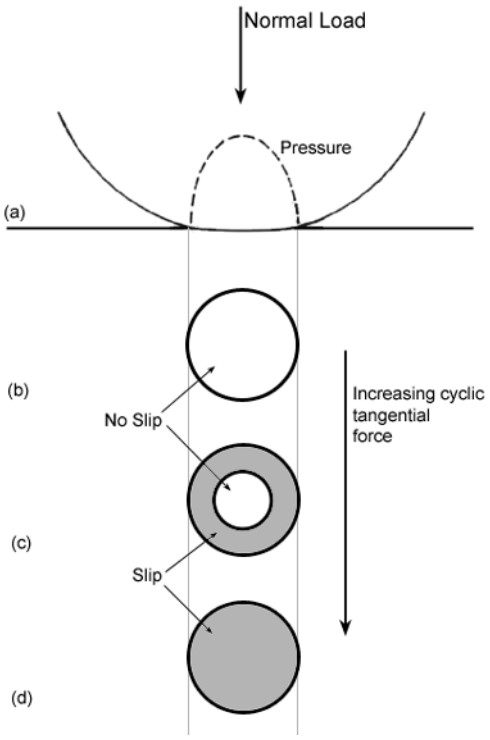

Figure 2-10 (a) The distribution of elastic normal stress beneath a sphere against a flat. (b) to (d) show plan views of the area of contact with increasing values of applied cyclic tangential force. Source: Ref [61]

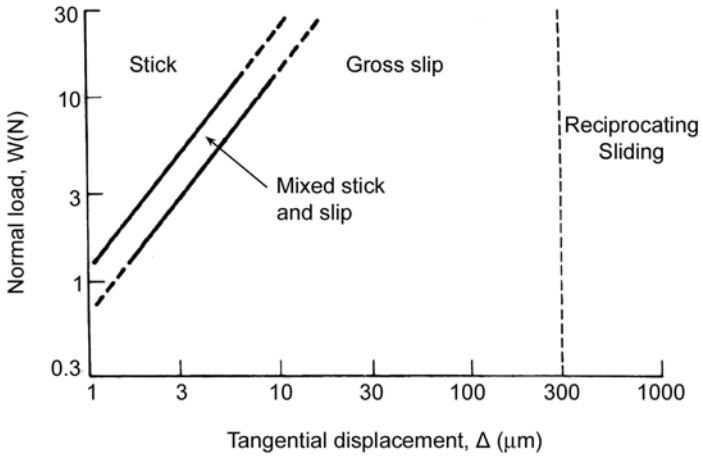

Figure 2-11 Schematic illustration of fretting regimes for counterformal contact between stainless steel surfaces (sphere-on-flat geometry). Normal load W is plotted against tangential displacement Δ. Source: Ref [61]

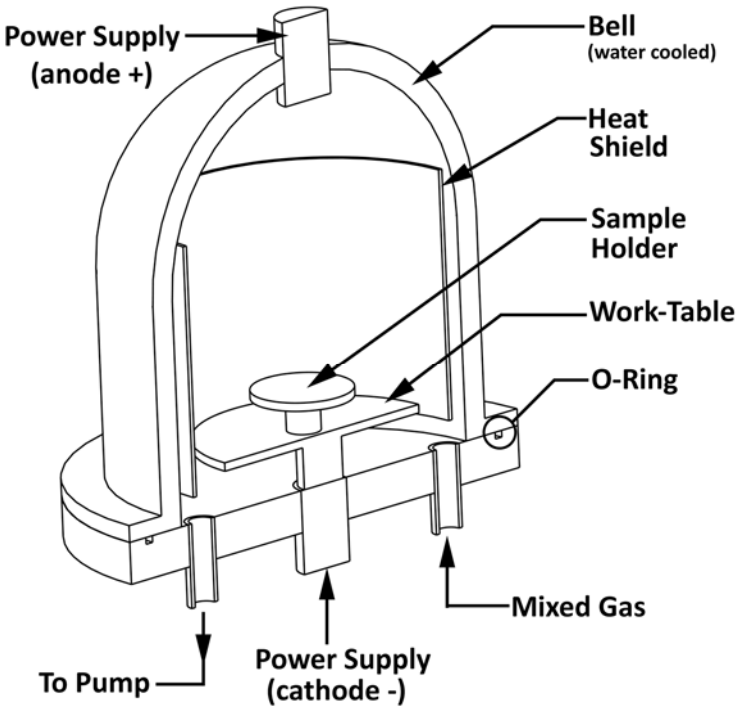

Figure 3-1 Schematic diagram of plasma furnace unit

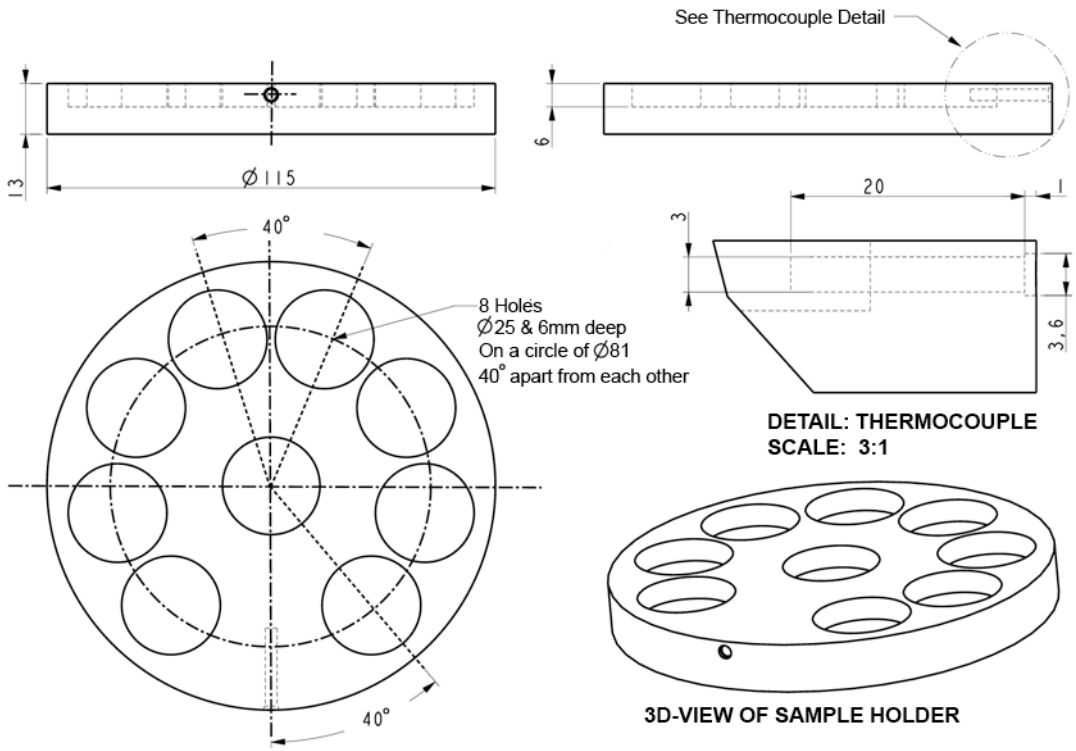

Figure 3-2 (a) Schematic view of sample holder (9 X Ø25mm samples)

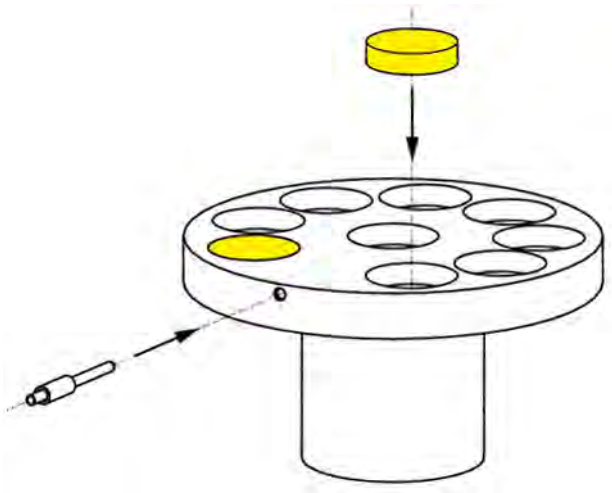

Figure 3-2 (b) Assembly of thermocouple sheath and Ø 25mm samples into holder

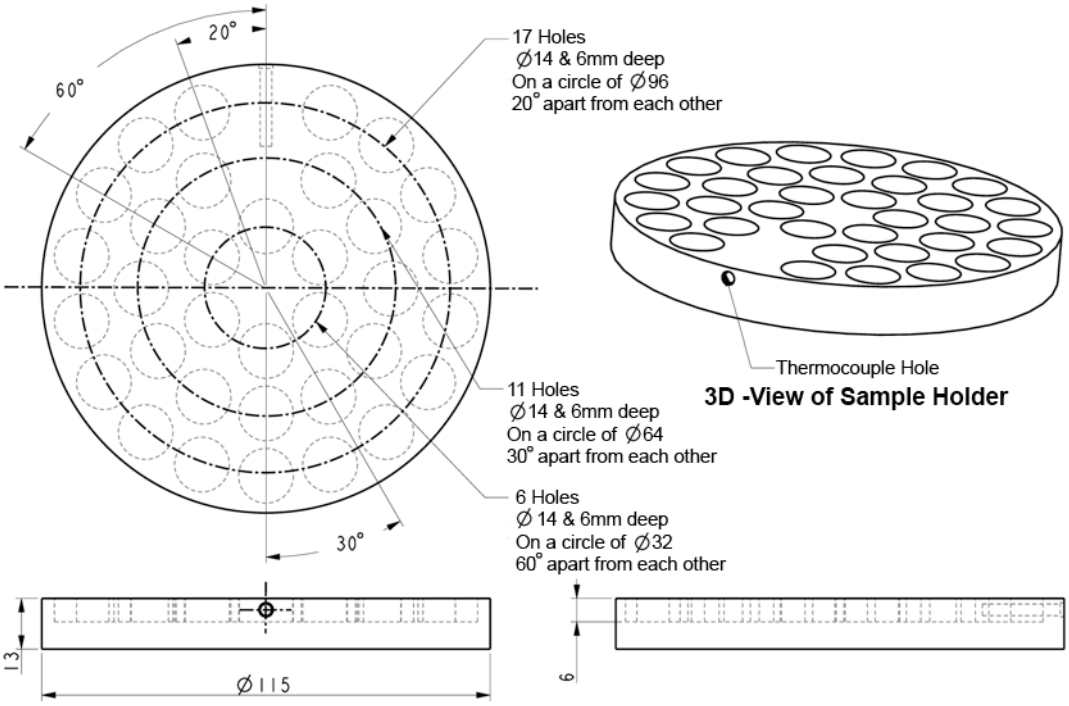

Figure 3-3 (a) Schematic view of sample holder (34 X Ø14mm samples)

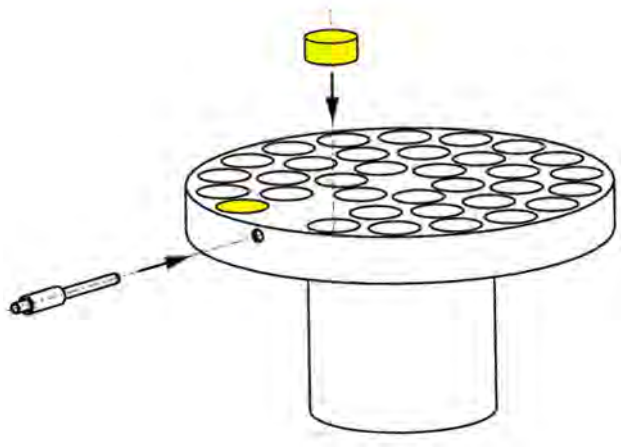

Figure 3-3 (b) Assembly of thermocouple sheath and Ø 14mm samples into holder

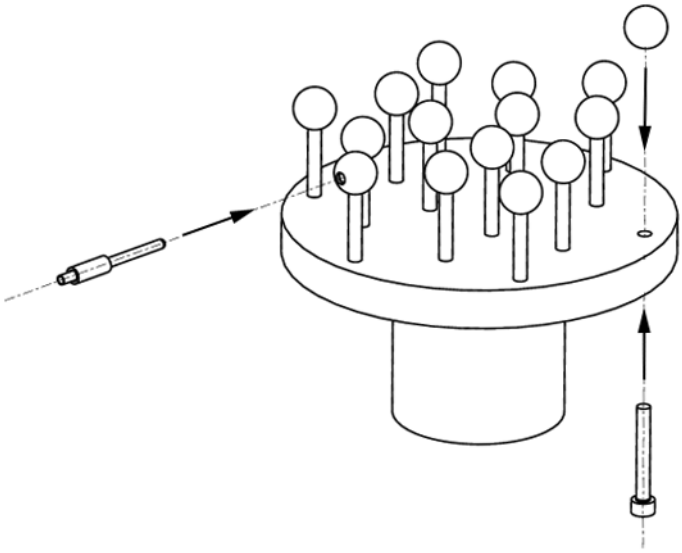

Figure 3-4 Assembly of thermocouple sheath and spherical samples into holder

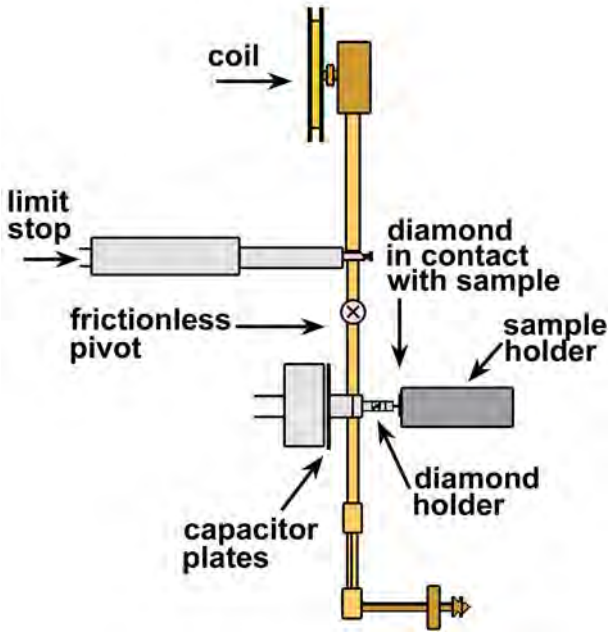

Figure 3-5 Schematic view of nano-hardness testing machine

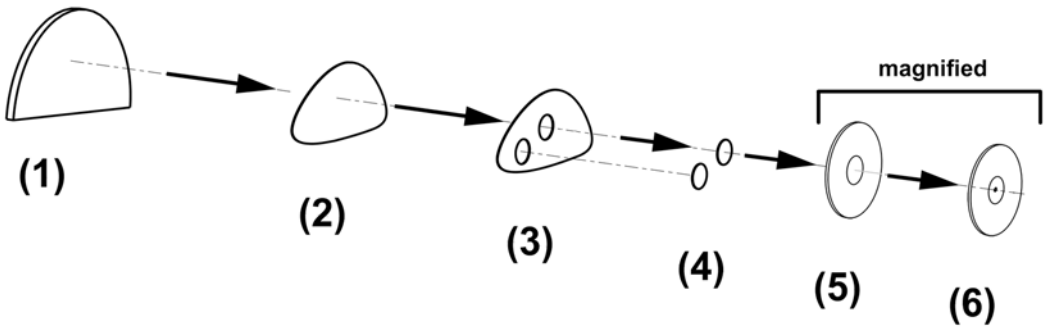

Figure 3-6 Schematic view of the steps involved in the preparation of a plane-TEM sample preparation.

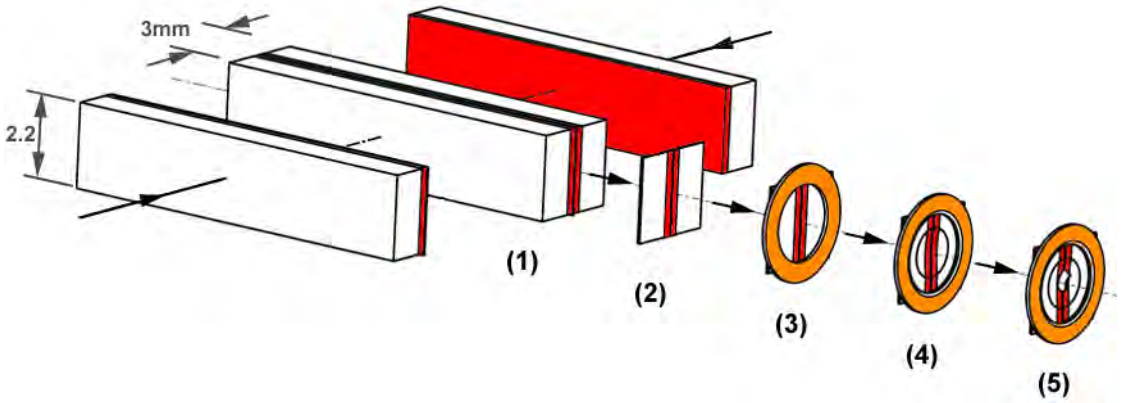

Figure 3-7 Schematic view of the steps involved in the preparation of a Cross-section-TEM sample preparation

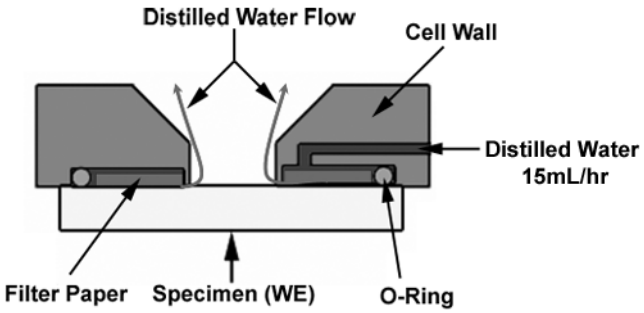

Figure 3-8 Schematic view of the Avesta corrosion cell setup

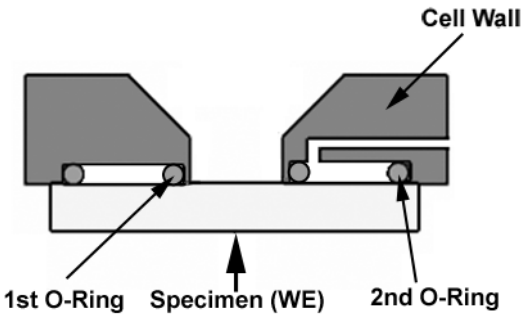

Figure 3-9 Schematic view of the flat cell corrosion setup

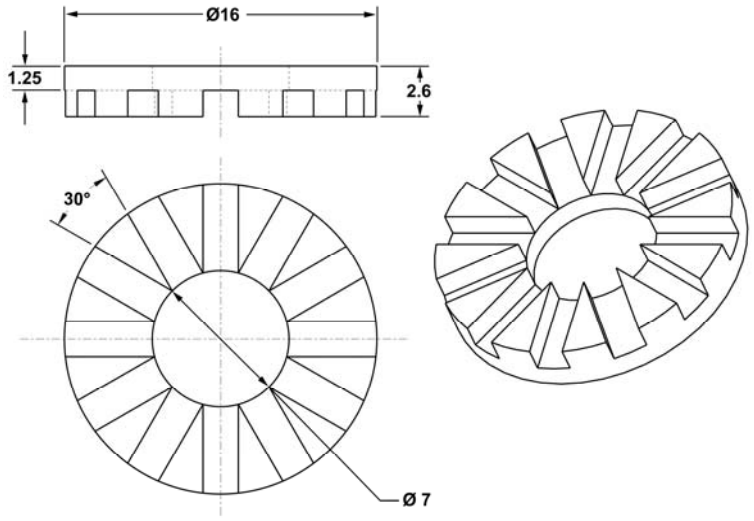

Figure 3-10 Multiple crevice assembly (MCA) washer used in crevice corrosion test

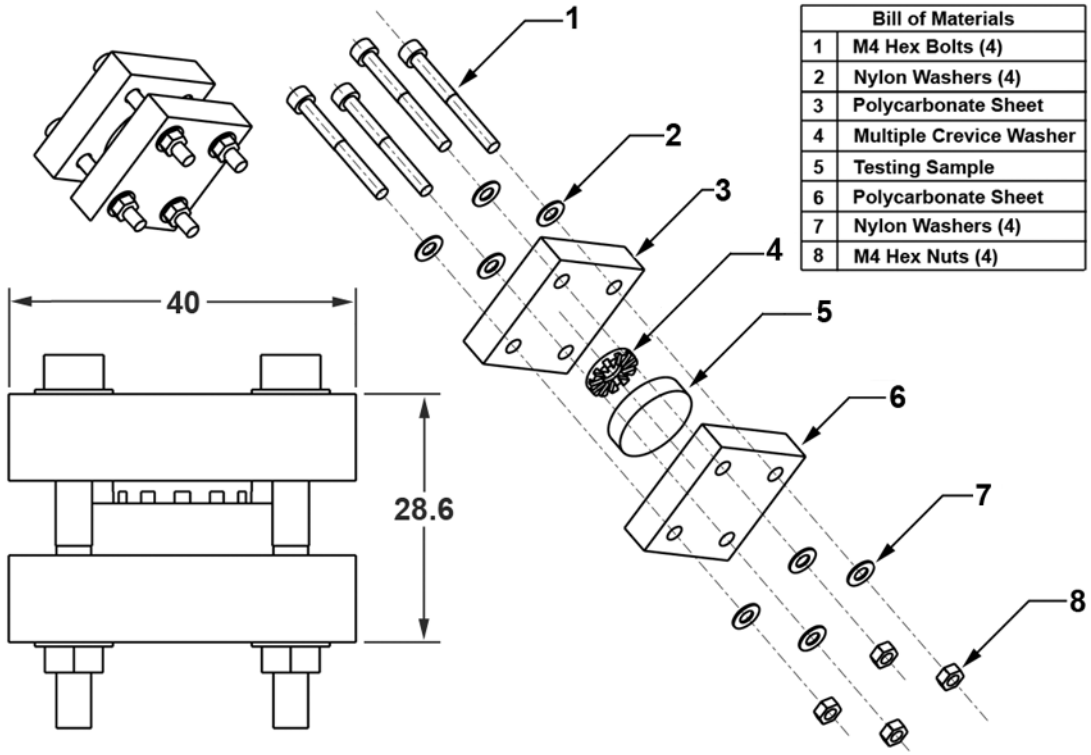

Figure 3-11 Assembly drawing of crevice corrosion experimental setup

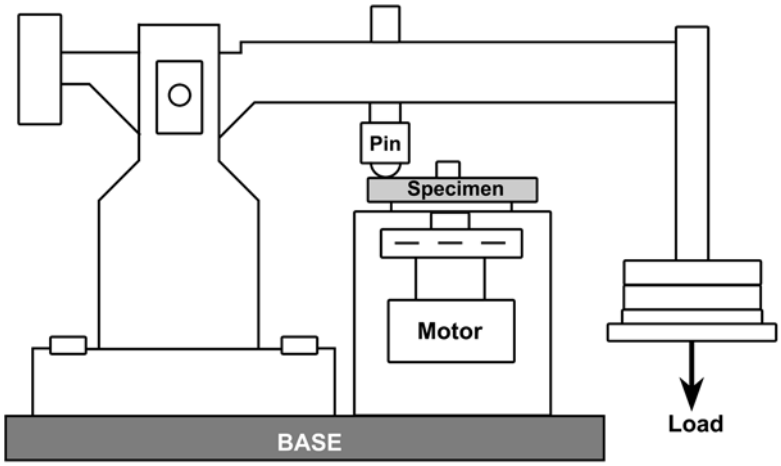

Figure 3-12 Schematic view of pin-on-disc tribometer

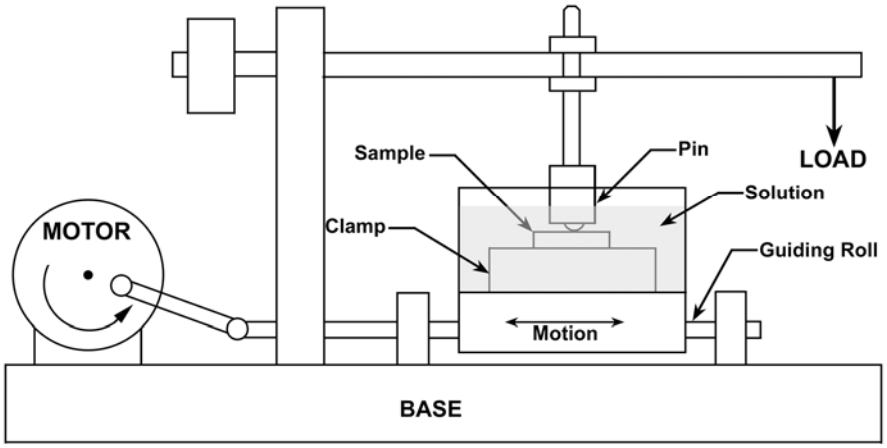

Figure 3-13 Schematic view of reciprocating-wear tribometer

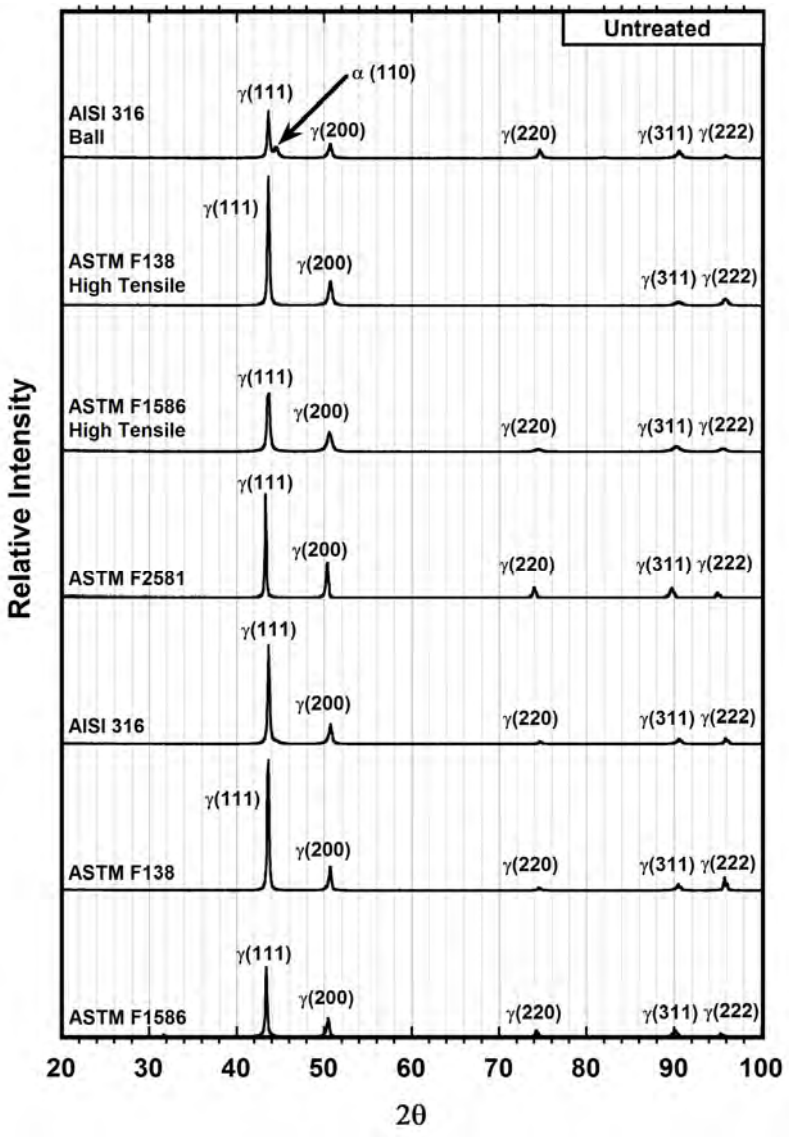

Figure 4-1.1 XRD Profiles of the untreated materials used in this work: ASTM F1586 (annealed condition); ASTM F138 (annealed condition); AISI 316 (annealed condition); ASTM F1586 (high-tensile condition); ASTM F138 (high-tensile condition); and AISI 316 (spherical).
Cu Kα Radiation

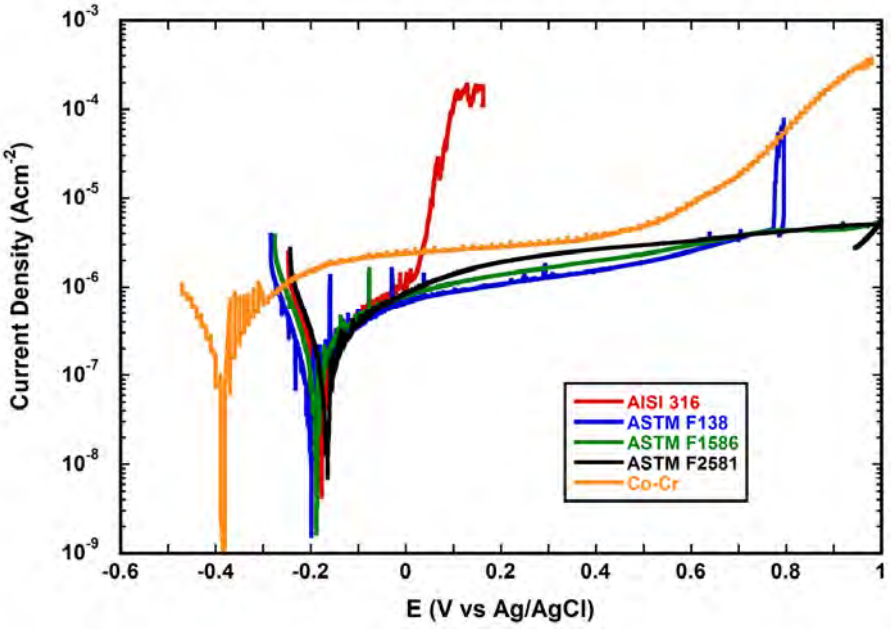

Figure 4-1.2 Potentiodynamic curves of untreated materials in full strength Ringer's solution

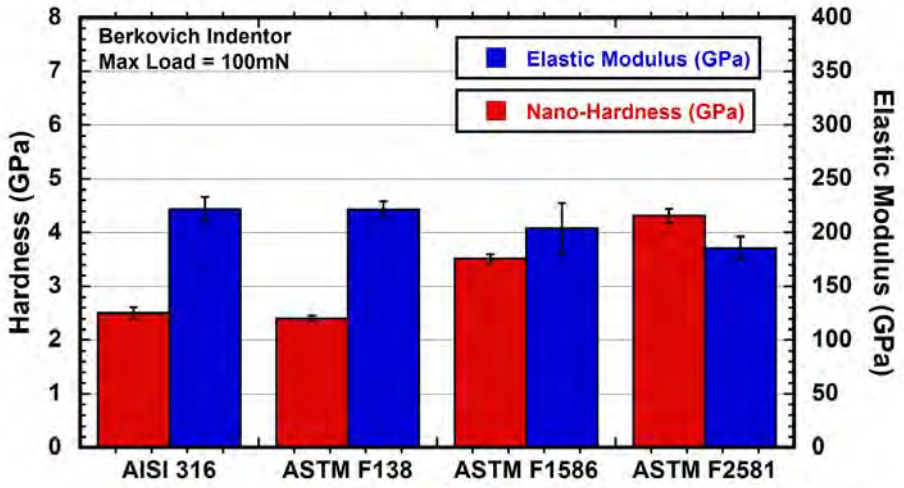

Figure 4-1.3 Elastic modulus and nano-hardness measurements of untreated material. Standard deviation of 15 points.

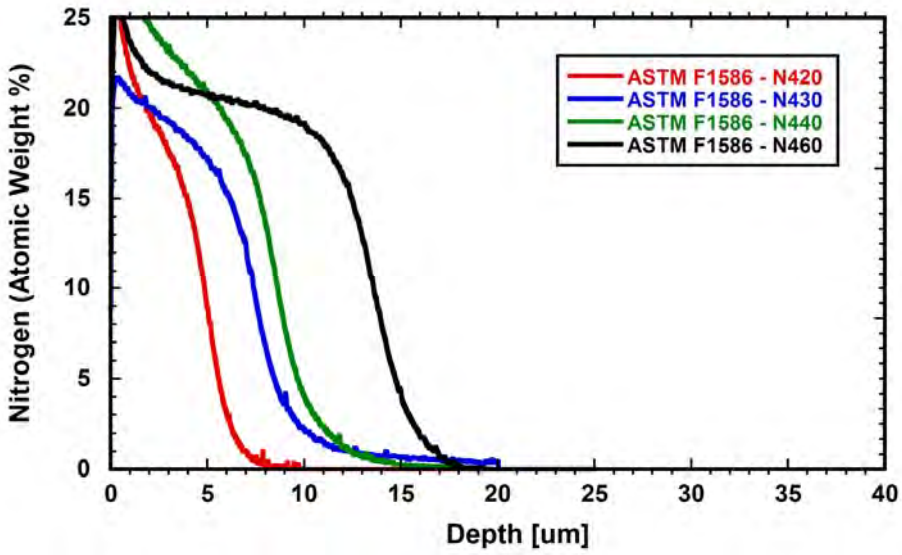

Figure 4-2.1.1 Nitrogen depth profiles of plasma nitrided ASTM F1586 samples at different temperatures

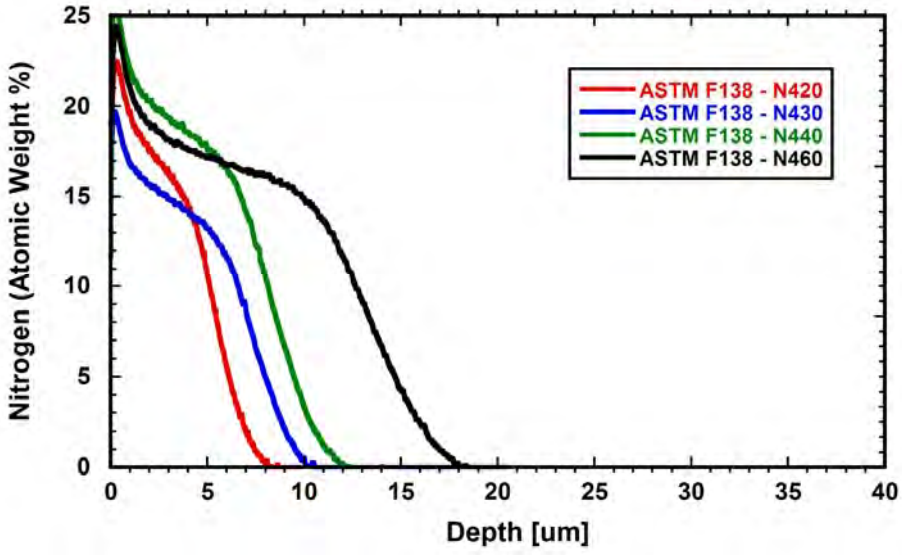

Figure 4-2.1.2 Nitrogen depth profiles of plasma nitrided ASTM F138 samples at different temperatures

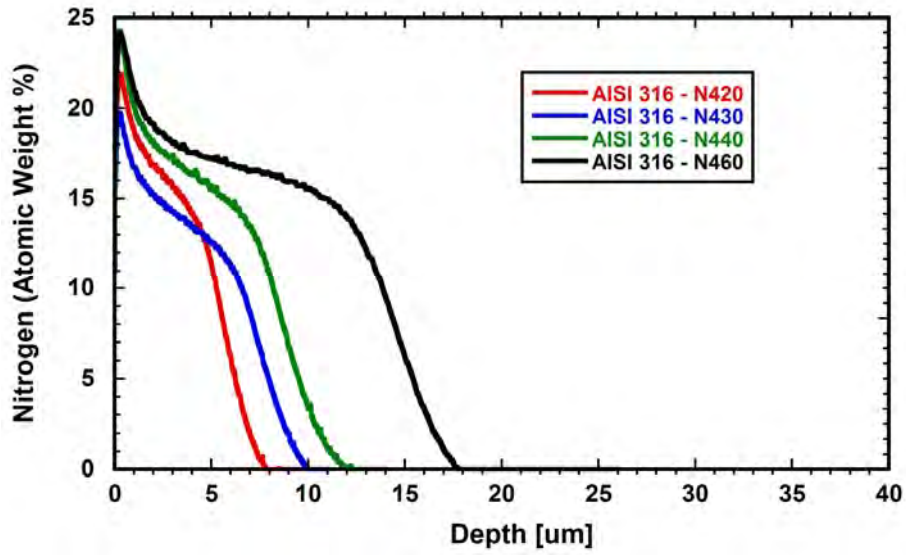

Figure 4-2.1.3 Nitrogen depth profiles of plasma nitrided AISI 316 samples at different temperatures

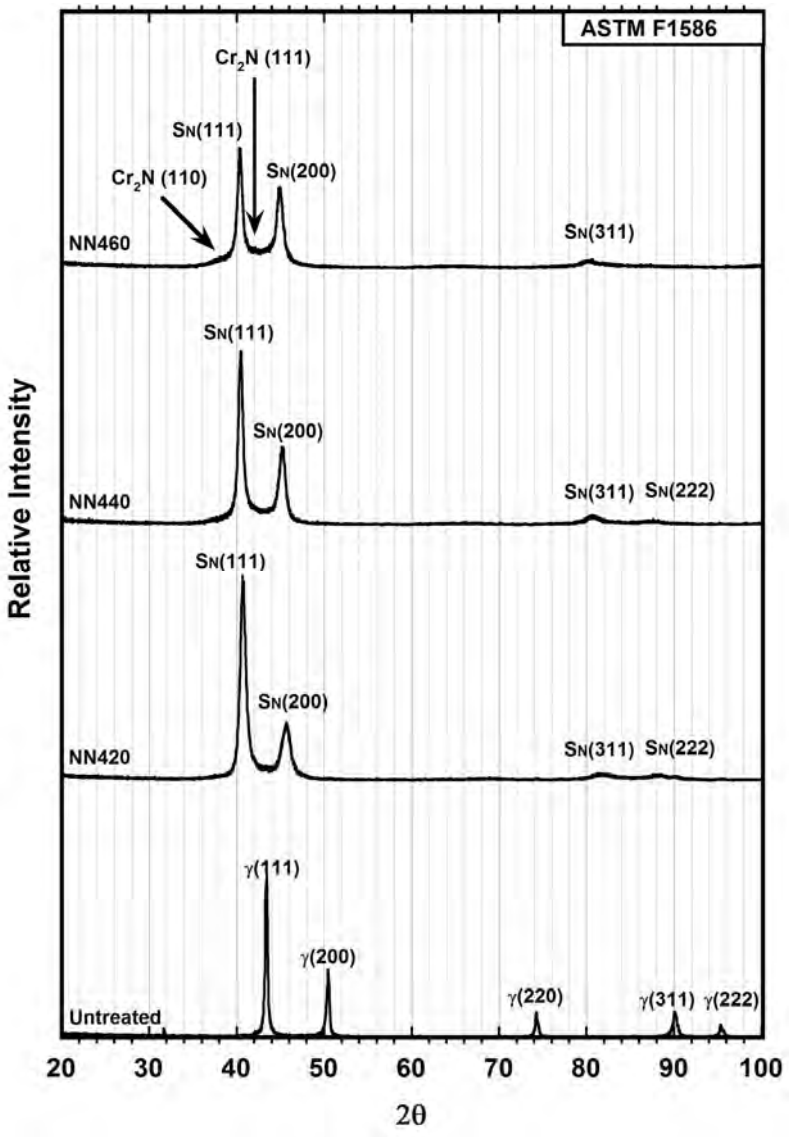

Figure 4-2.1.4 XRD profiles of ASTM F1586 samples nitrided at different temperatures as compared to that of the untreated material Cu Kα Radiation

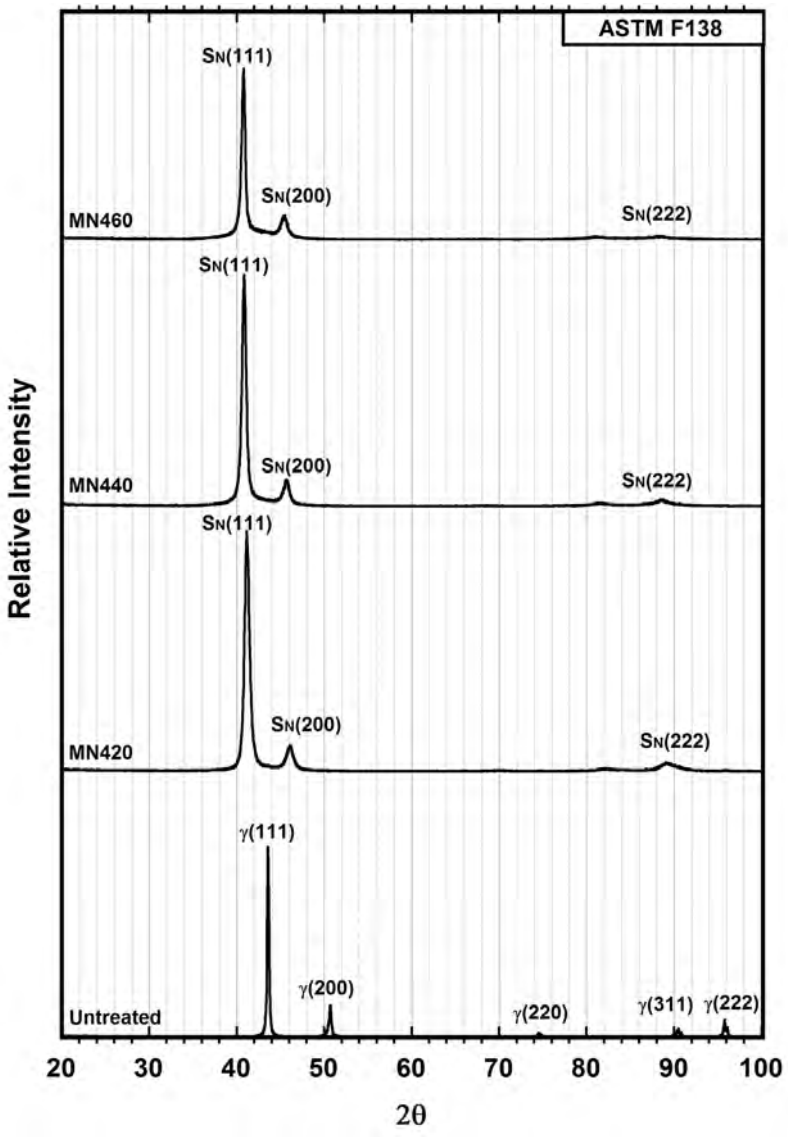

Figure 4-2.1.5 XRD profiles of ASTM F138 samples nitrided at different temperatures as compared to that of the untreated material Cu Kα Radiation

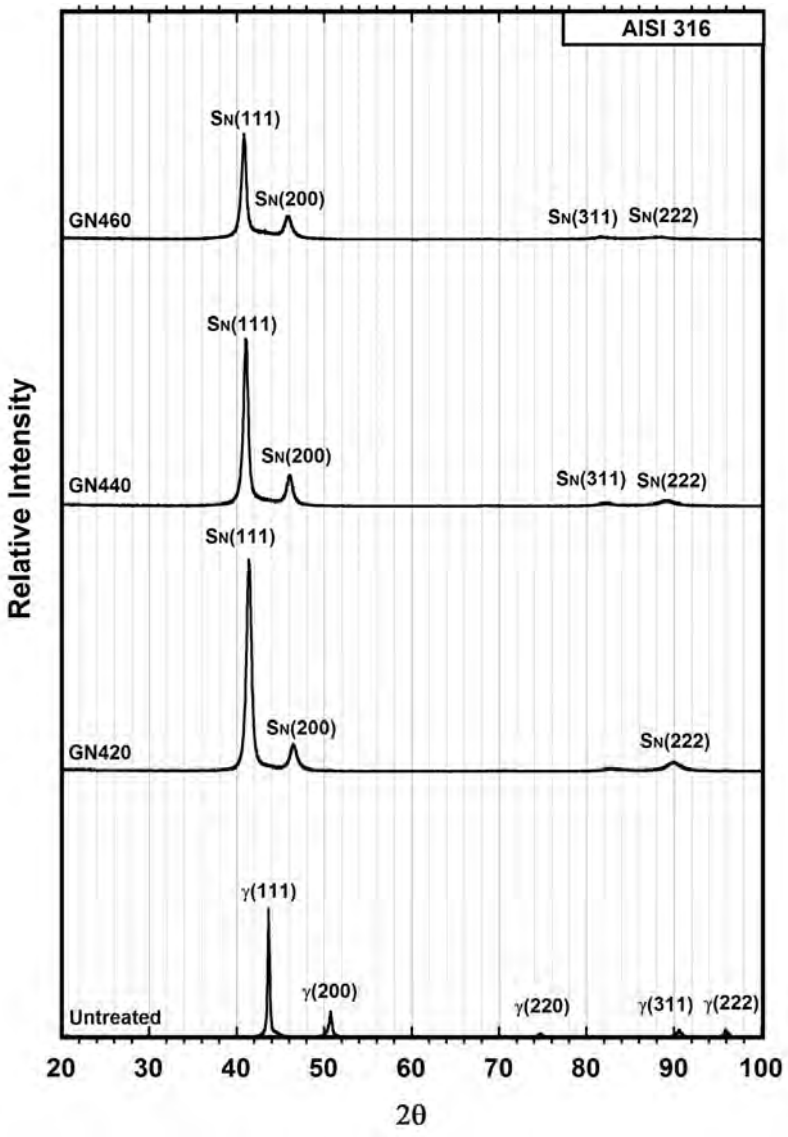

Figure 4-2.1.6 XRD profiles of AISI 316 samples nitrided at different temperatures as compared to that of the untreated material
Cu Kα Radiation

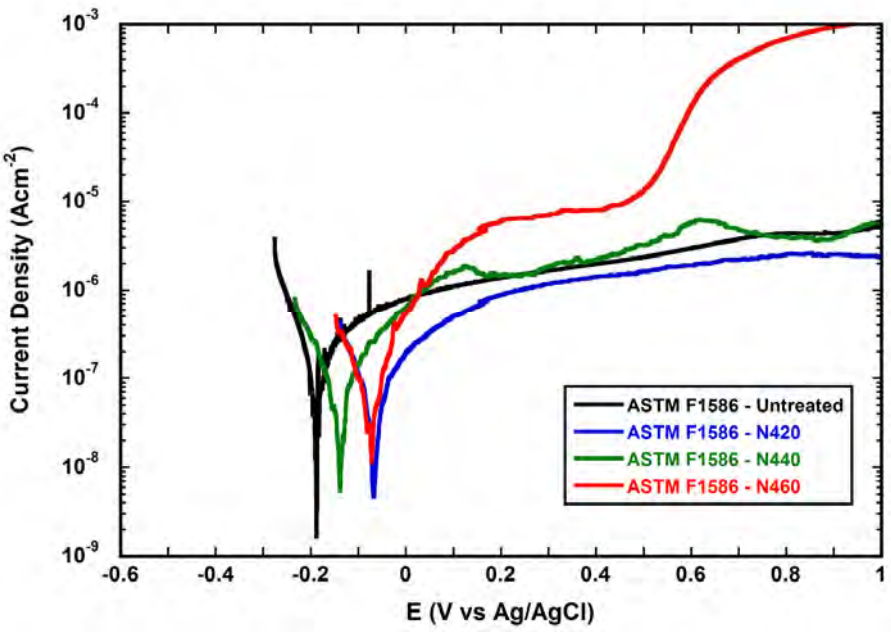

Figure 4-2.1.7 Potentiodynamic curves of ASTM F1586 samples plasma nitrided at different temperatures and electrochemically tested in full strength Ringer's solution

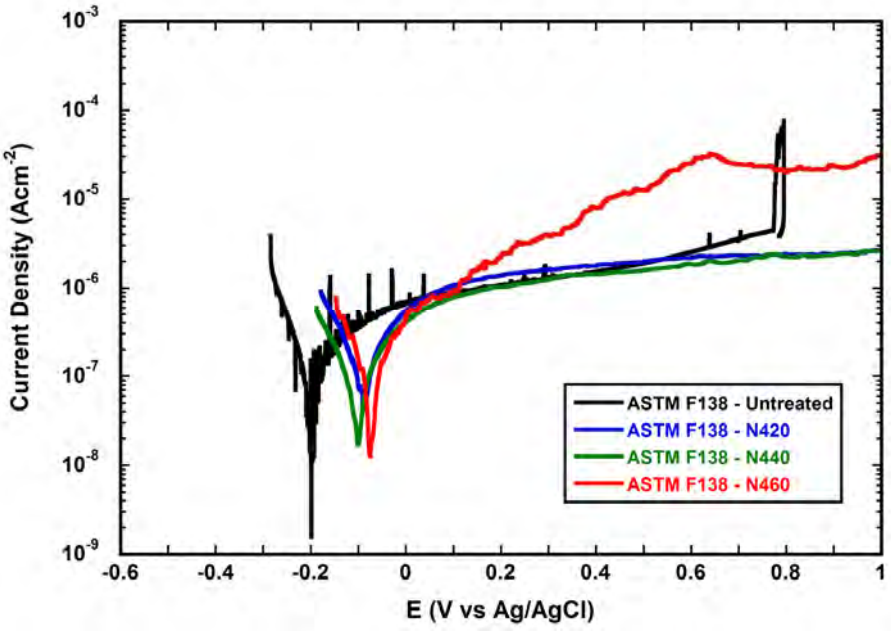

Figure 4-2.1.8 Potentiodynamic curves of ASTM F138 samples plasma nitrided at different temperatures and electrochemically tested in full strength Ringer's solution.

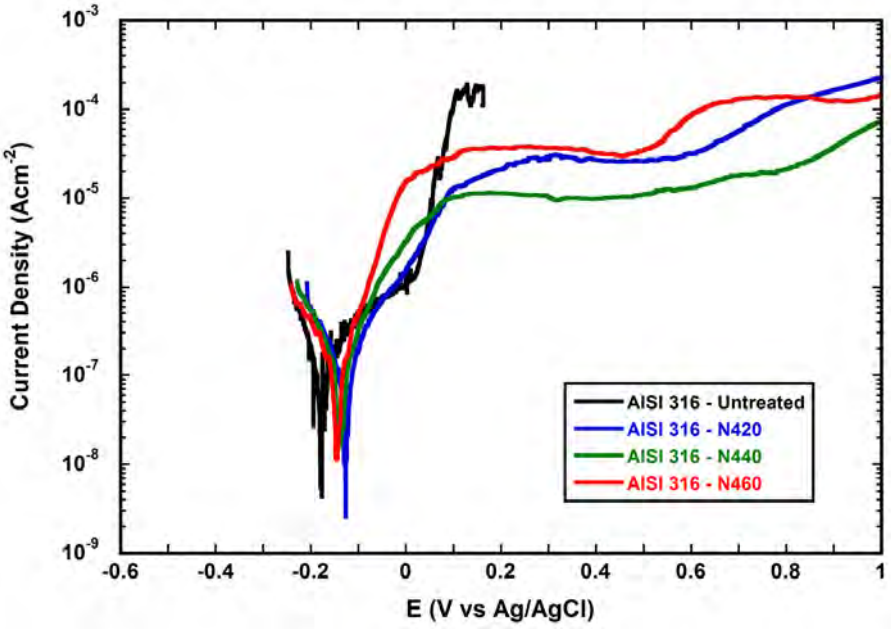

Figure 4-2.1.9 Potentiodynamic curves of AISI 316 samples plasma nitrided at different temperatures and electrochemically tested in full strength Ringer's solution.

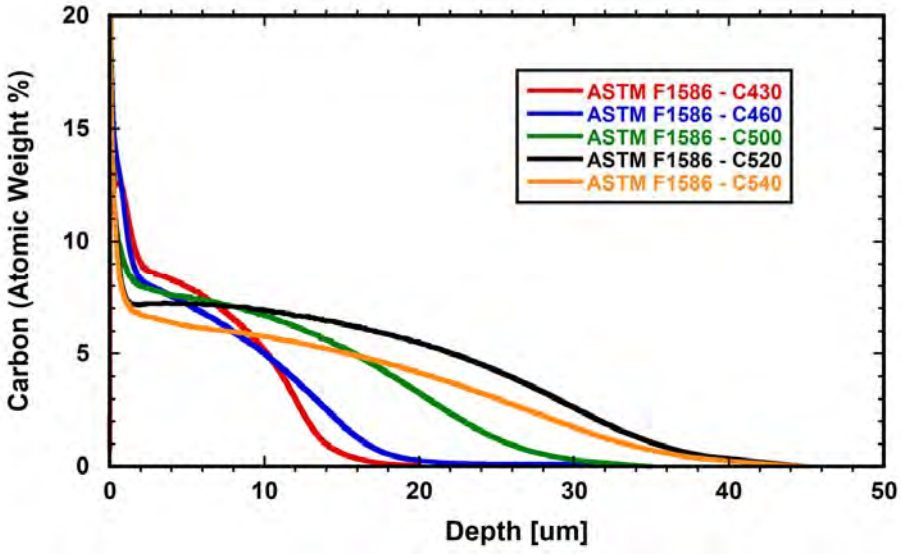

Figure 4-2.2.1 Carbon depth profiles of plasma carburised ASTM F1586 samples at different temperatures

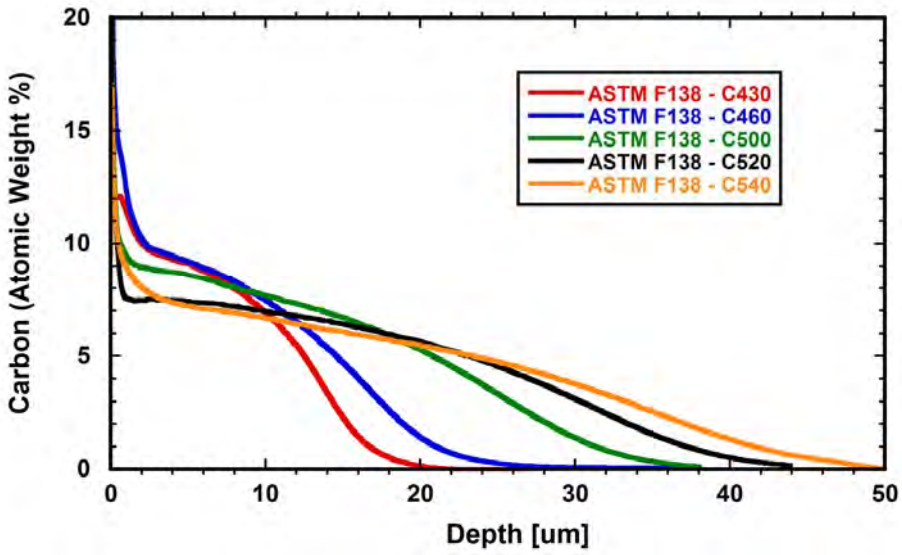

Figure 4-2.2.2 Carbon depth profiles of plasma carburised ASTM F138 samples at different temperatures

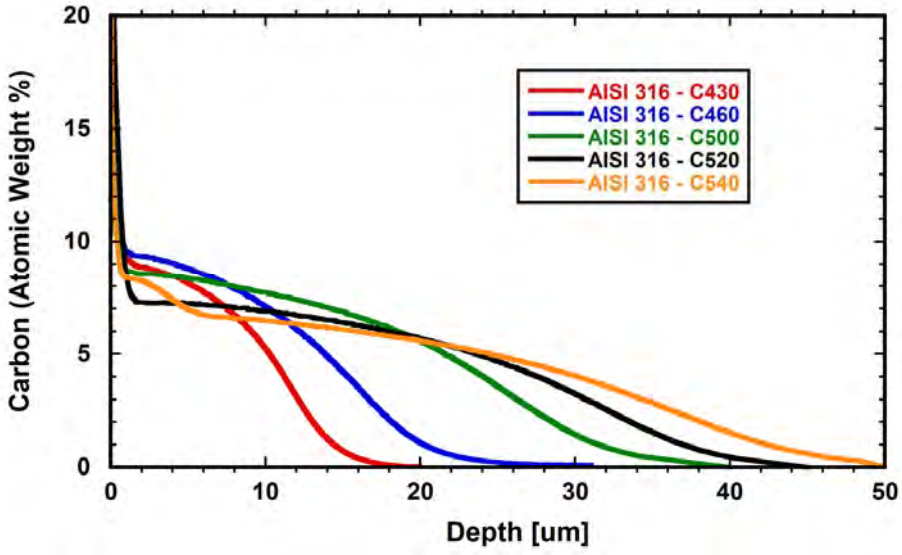

Figure 4-2.2.3 Carbon depth profiles of plasma carburised AISI 316 samples at different temperatures

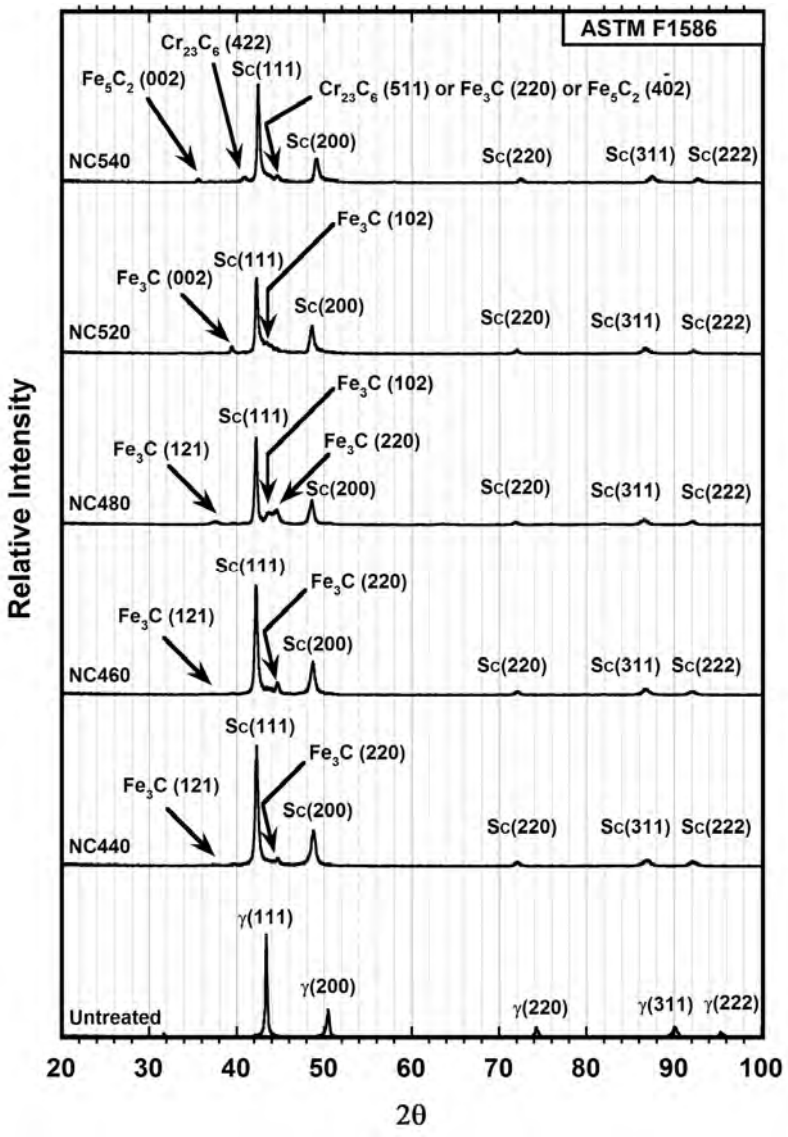

Figure 4-2.2.4 XRD profiles of ASTM F1586 samples carburised at different temperatures as compared to that of the untreated material
Cu Kα Radiation

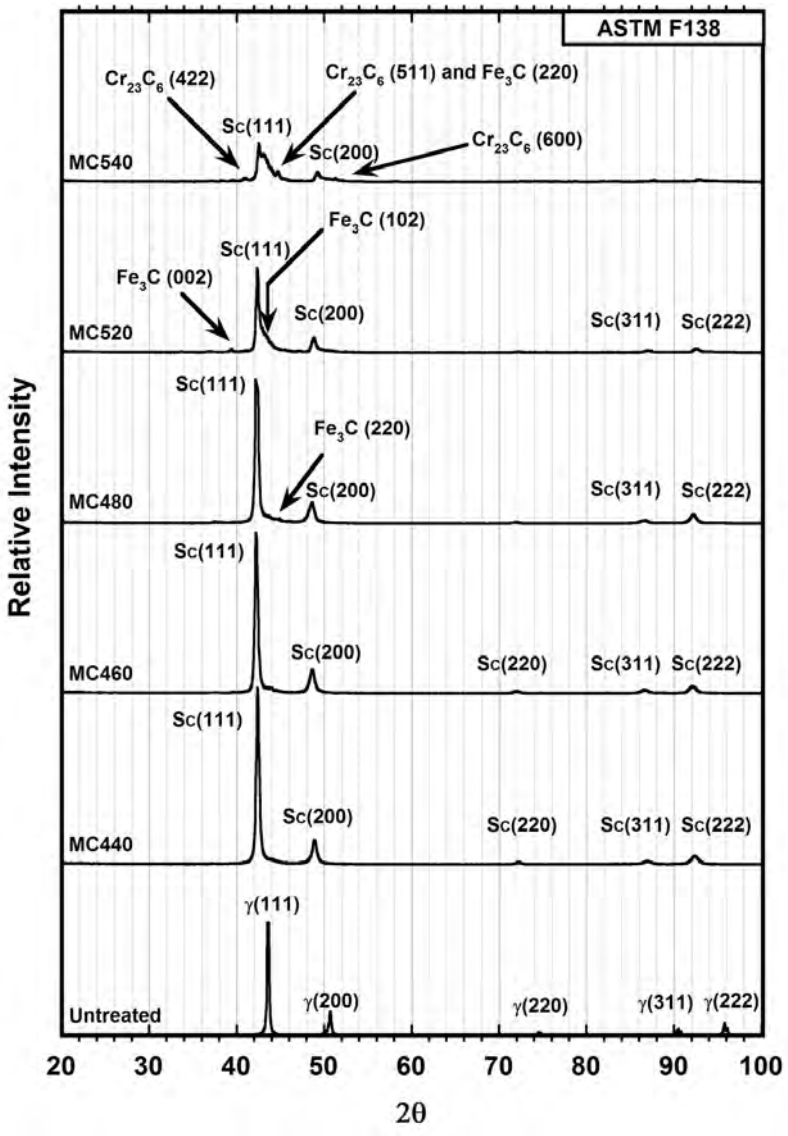

Figure 4-2.2.5 XRD profiles of ASTM F138 samples carburised at different temperatures as compared to that of the untreated material
Cu Kα Radiation

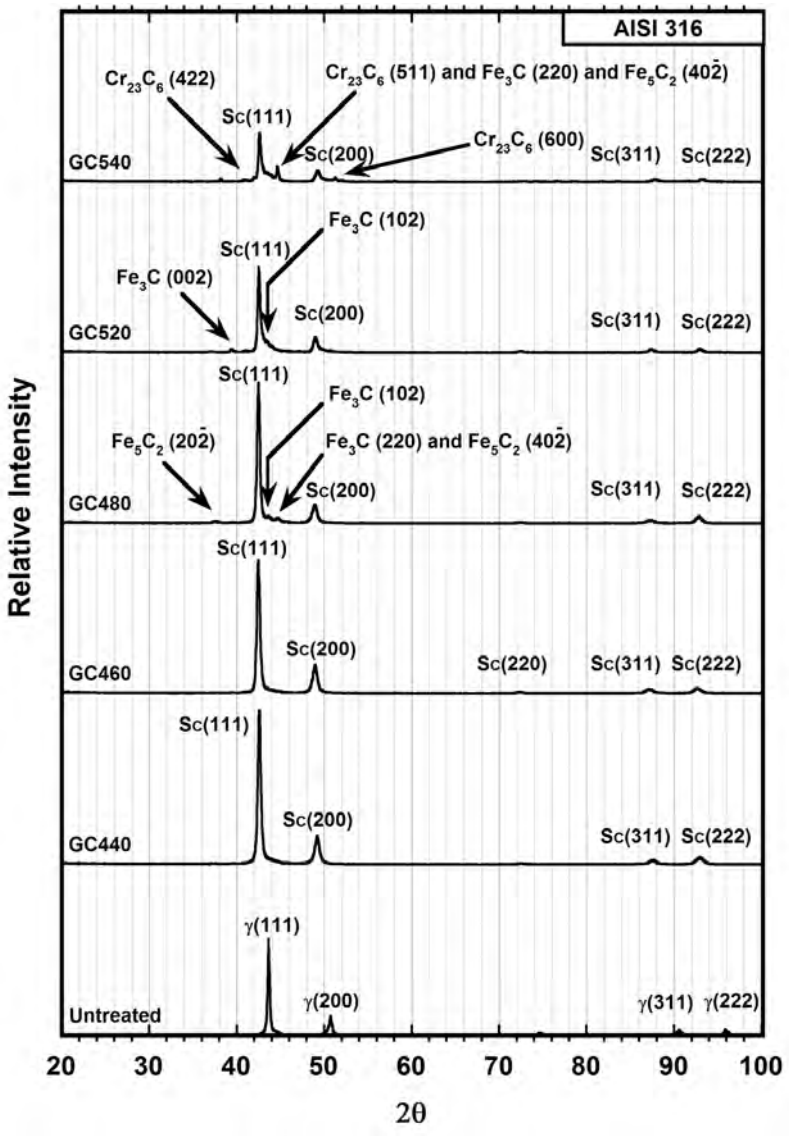

Figure 4-2.2.6 XRD profiles of AISI 316 samples carburised at different temperatures as compared to that of the untreated material Cu Kα Radiation

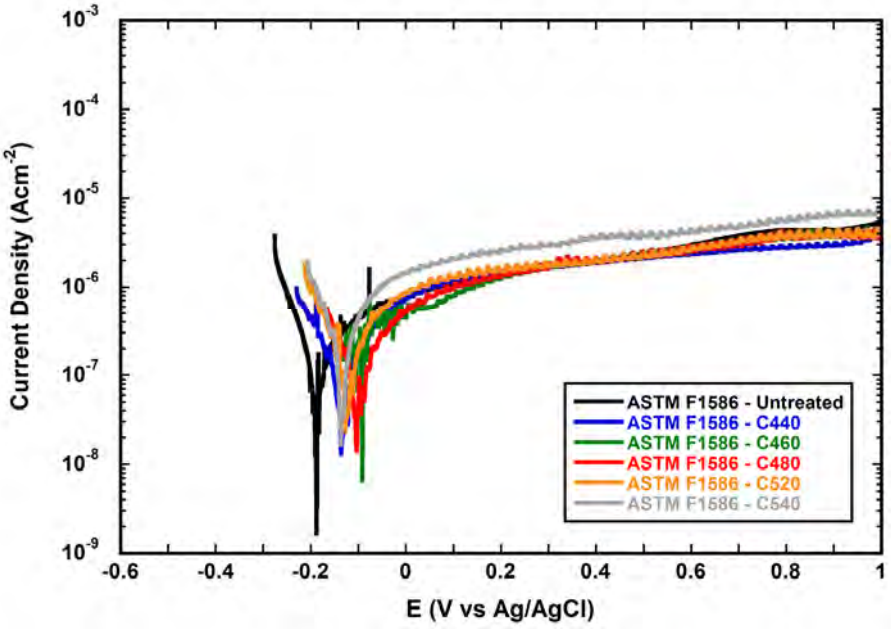

Figure 4-2.2.7 Potentiodynamic curves of ASTM F1586 samples plasma carburised at different temperatures and electrochemically tested in full strength Ringer's solution

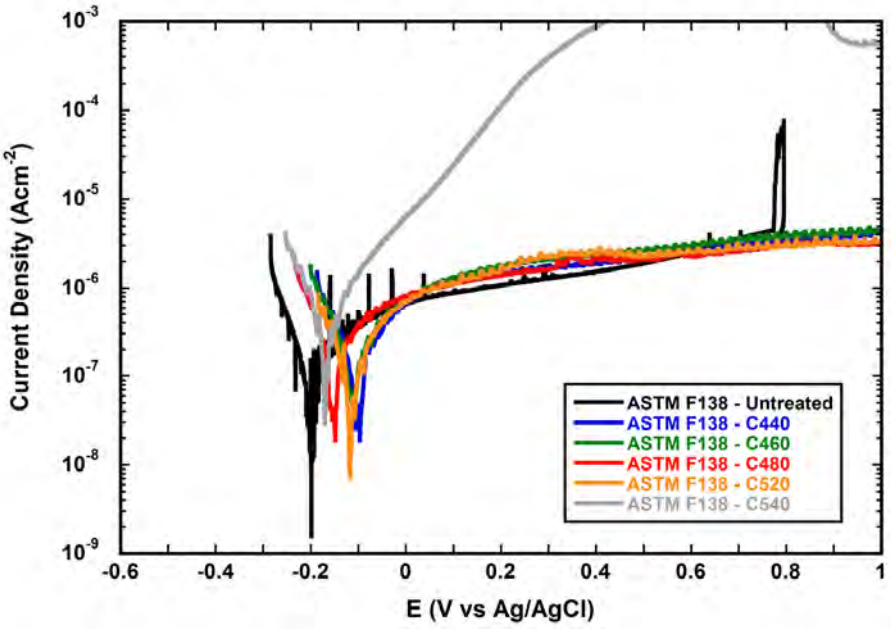

Figure 4-2.2.8 Potentiodynamic curves of ASTM F138 samples plasma carburised at different temperatures and electrochemically tested in full strength Ringer's solution

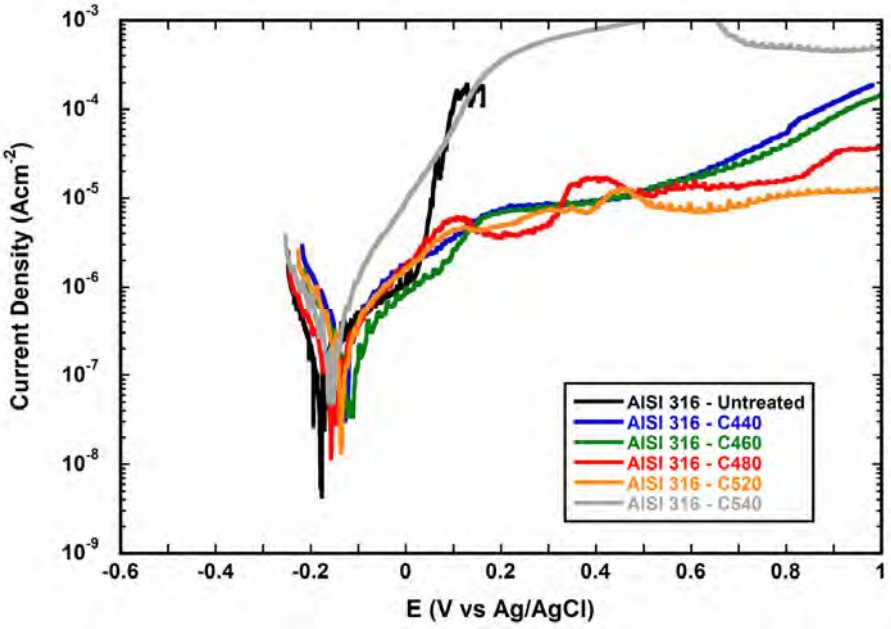

Figure 4-2.2.9 Potentiodynamic curves of AISI 316 samples plasma carburised at different temperatures and electrochemically tested in full strength Ringer's solution

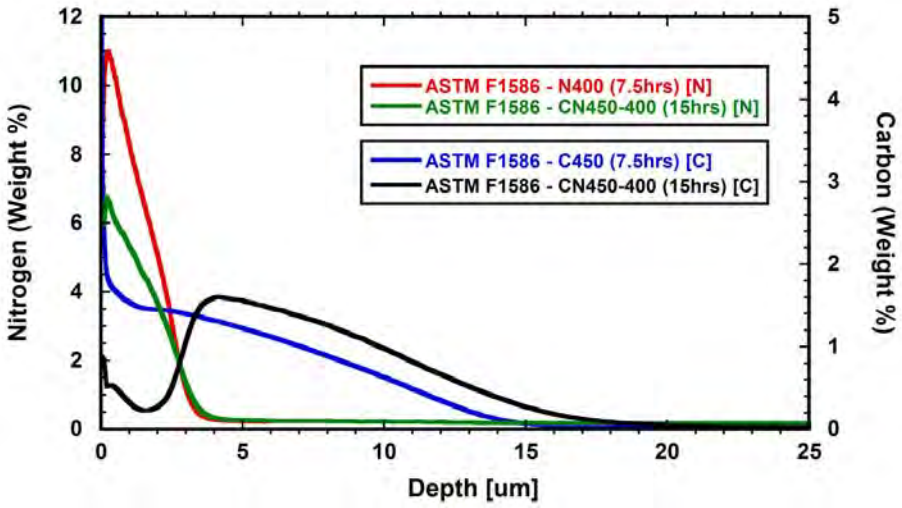

Figure 4-2.3.1 Chemical profiles on treated ASTM F1586 samples: nitrided at 400°C for 7.5hrs (N400); carburised at 450°C for 7.5hrs (C450); and sequentially treated by carburising at 450°C for 7.5hrs followed by post-nitriding at 400°C for 7.5hrs (CN450-400)

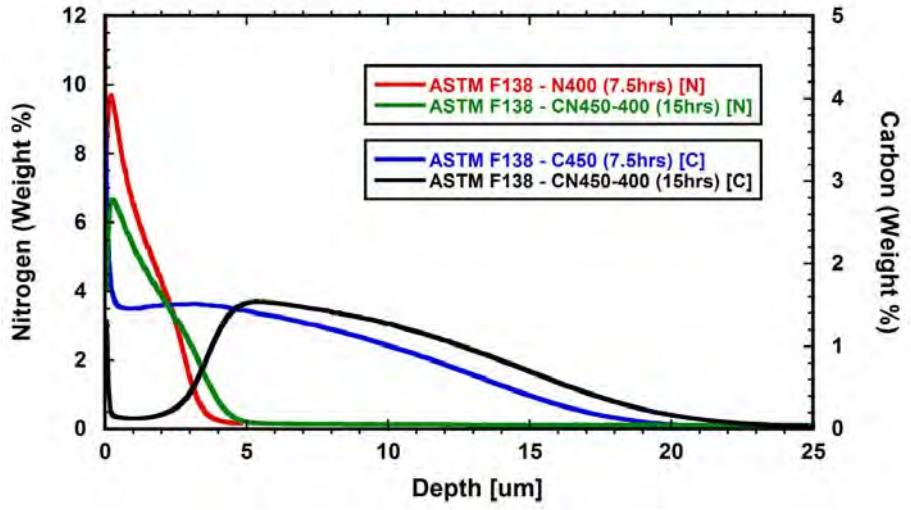

Figure 4-2.3.2 Chemical profiles on treated ASTM F138 samples: nitrided at 400°C for 7.5hrs (N400); carburised at 450°C for 7.5hrs (C450); and sequentially treated by carburising at 450°C for 7.5hrs followed by post-nitriding at 400°C for 7.5hrs (CN450-400)

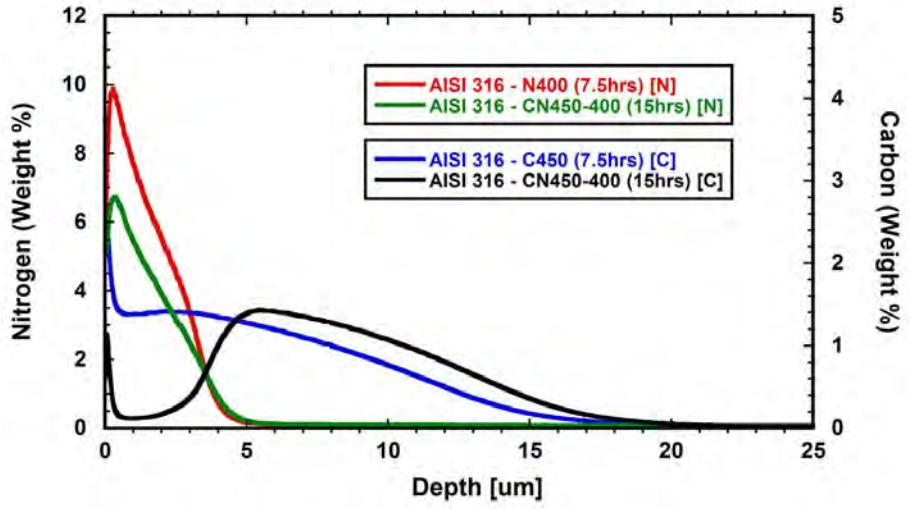

Figure 4-2.3.3 Chemical profiles on treated AISI 316 Samples: nitrided at 400°C for 7.5hrs (N400); carburised at 450°C for 7.5hrs (C450); and sequentially treated by carburising at 450°C for 7.5hrs followed by post-nitriding at 400°C for 7.5hrs (CN450-400)

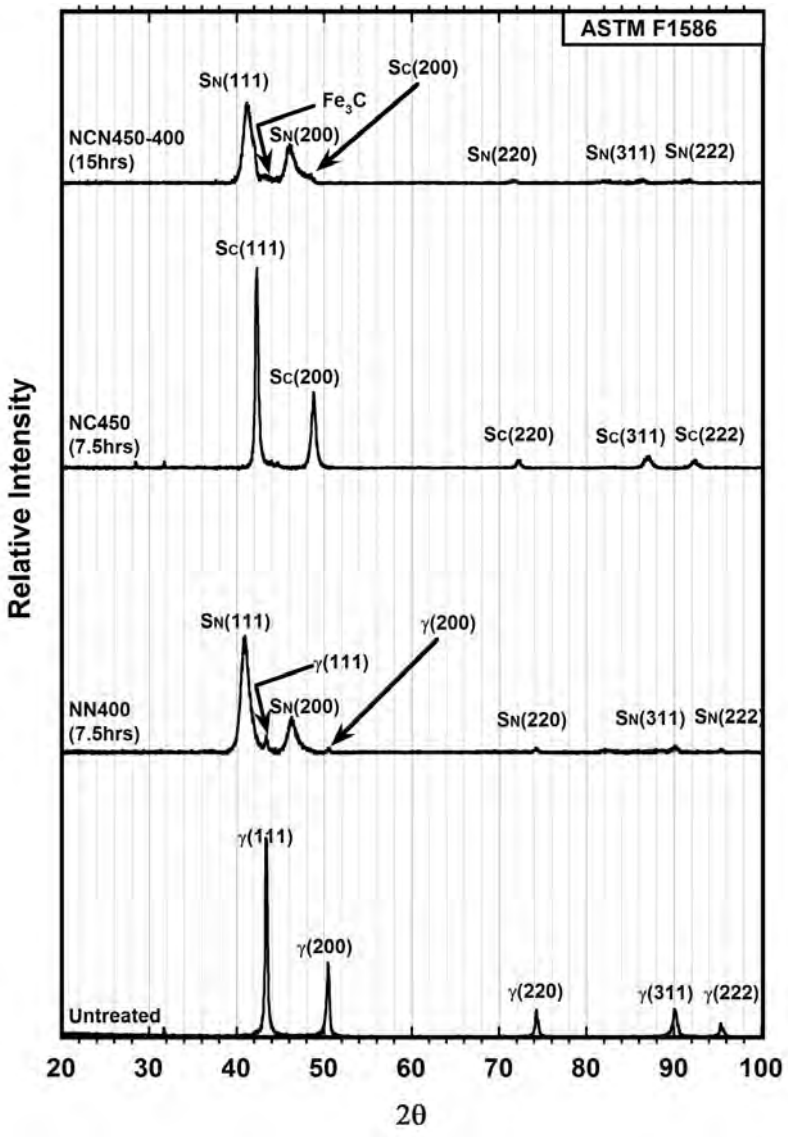

Figure 4-2.3.4 XRD patterns of ASTM F1586 samples: Untreated; nitrided at 400°C for 7.5hrs (NN400); carburised at 450°C for 7.5hrs (NC450); and sequentially treated by carburising at 450°C for 7.5hrs followed by post-nitriding at 400°C for 7.5hrs (NCN450-400)
Cu Kα Radiation

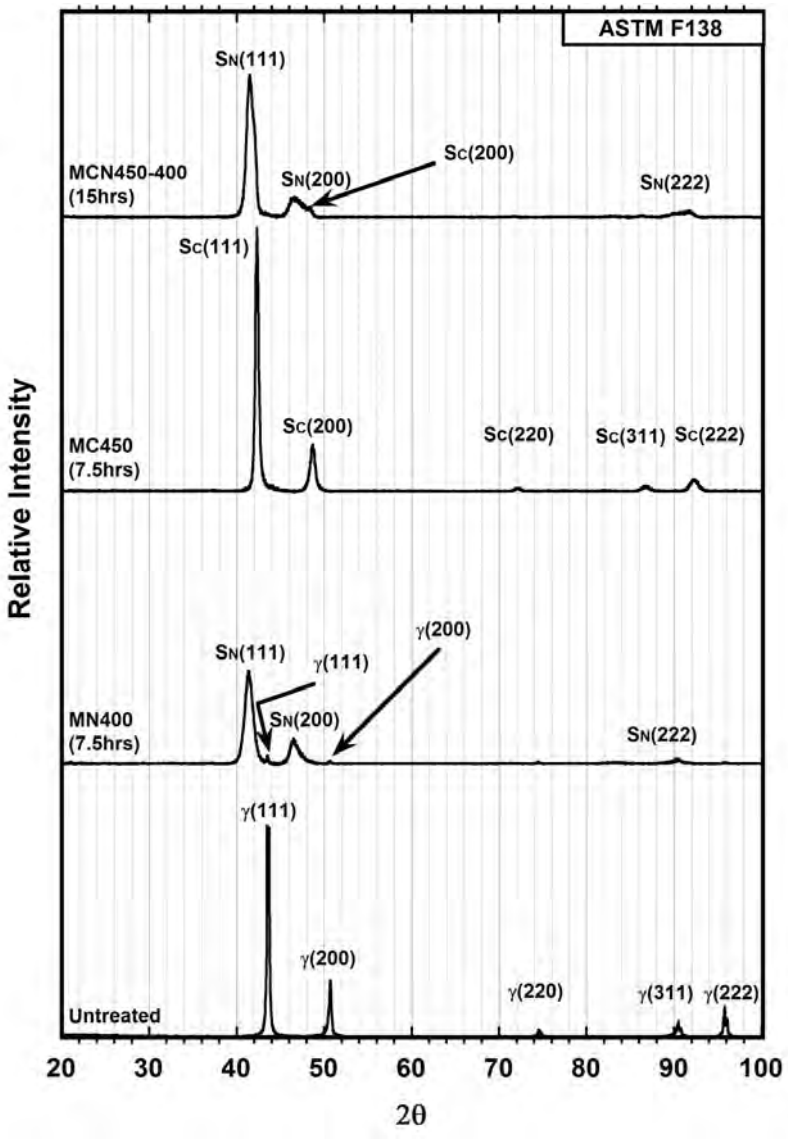

Figure 4-2.3.5 XRD patterns of ASTM F138 samples: Untreated; nitrided at 400°C for 7.5hrs (MN400); carburised at 450°C for 7.5hrs (MC450); and sequentially treated by carburising at 450°C for 7.5hrs followed by post-nitriding at 400°C for 7.5hrs (MCN450-400)
Cu Kα Radiation

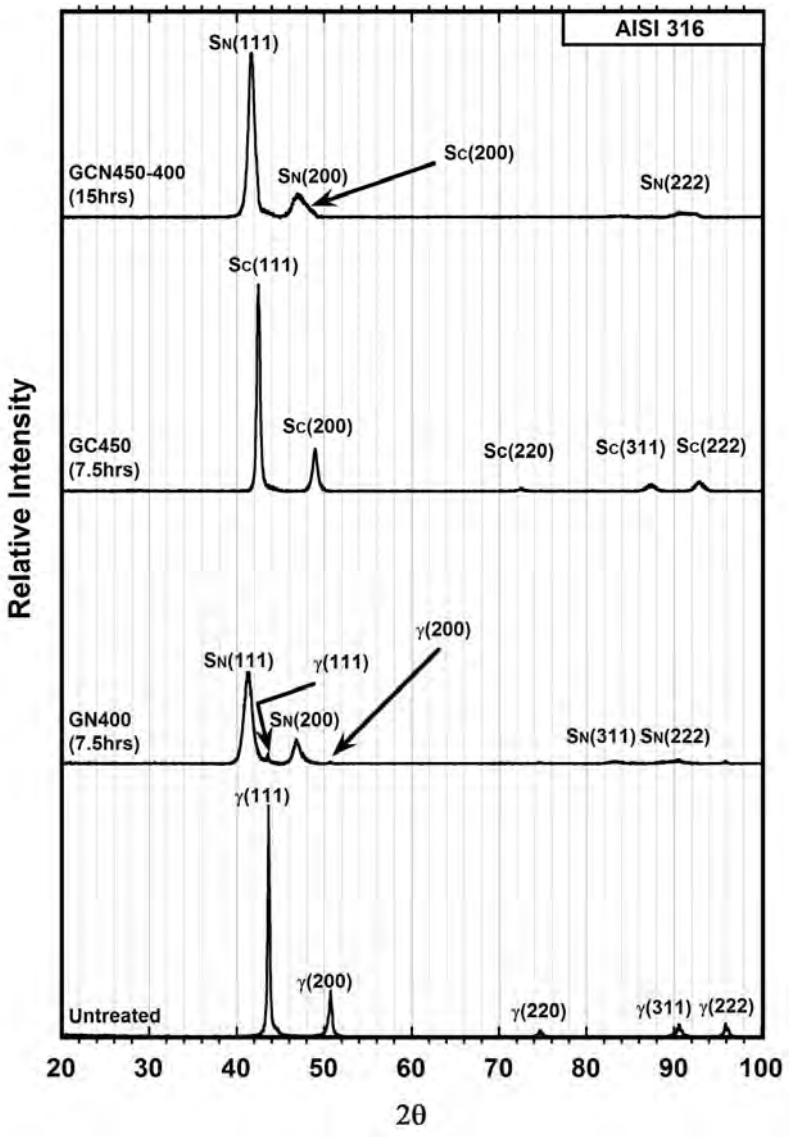

Figure 4-2.3.6 XRD patterns of AISI 316 Samples: Untreated; nitrided at 400°C for 7.5hrs (GN400); carburised at 450°C for 7.5hrs (GC450); and sequentially treated by carburising at 450°C for 7.5hrs followed by post-nitriding at 400°C for 7.5hrs (GCN450-400)
Cu Kα Radiation

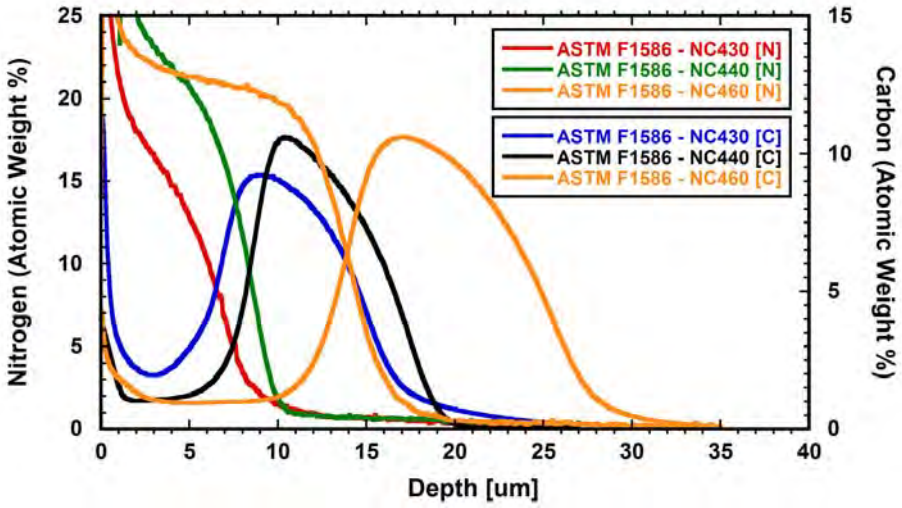

Figure 4-2.3.7 Chemical depth profiles of plasma carbonitrided ASTM F1586 samples at different temperatures

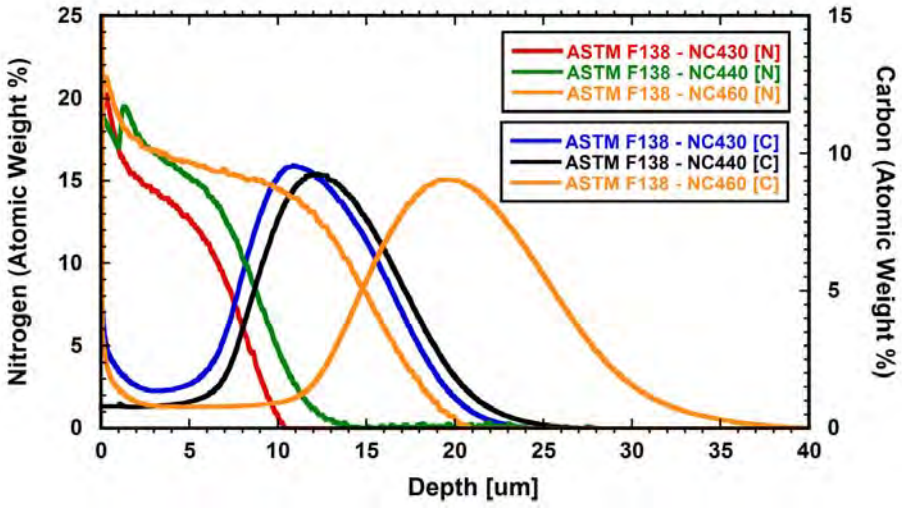

Figure 4-2.3.8 Chemical depth profiles of plasma carbonitrided ASTM F138 samples at different temperatures

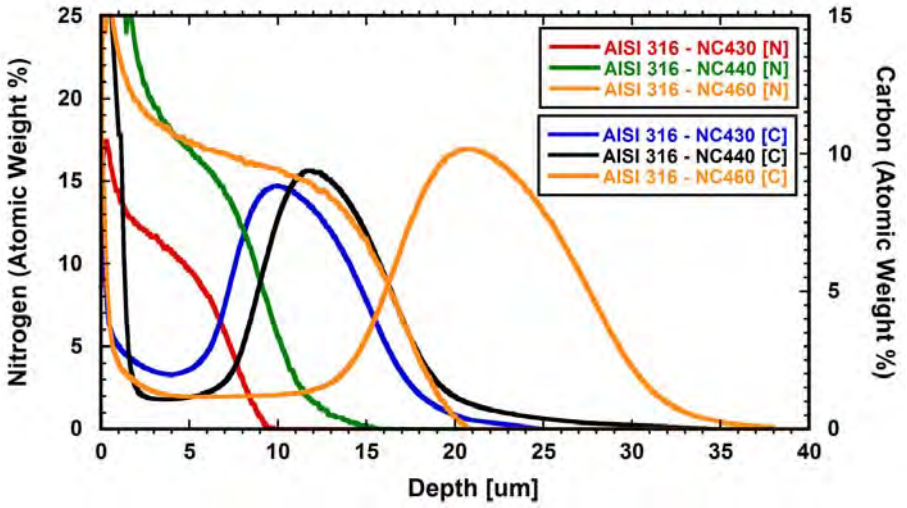

Figure 4-2.3.9 Chemical depth profiles of plasma carbonitrided AISI 316 samples at different temperatures

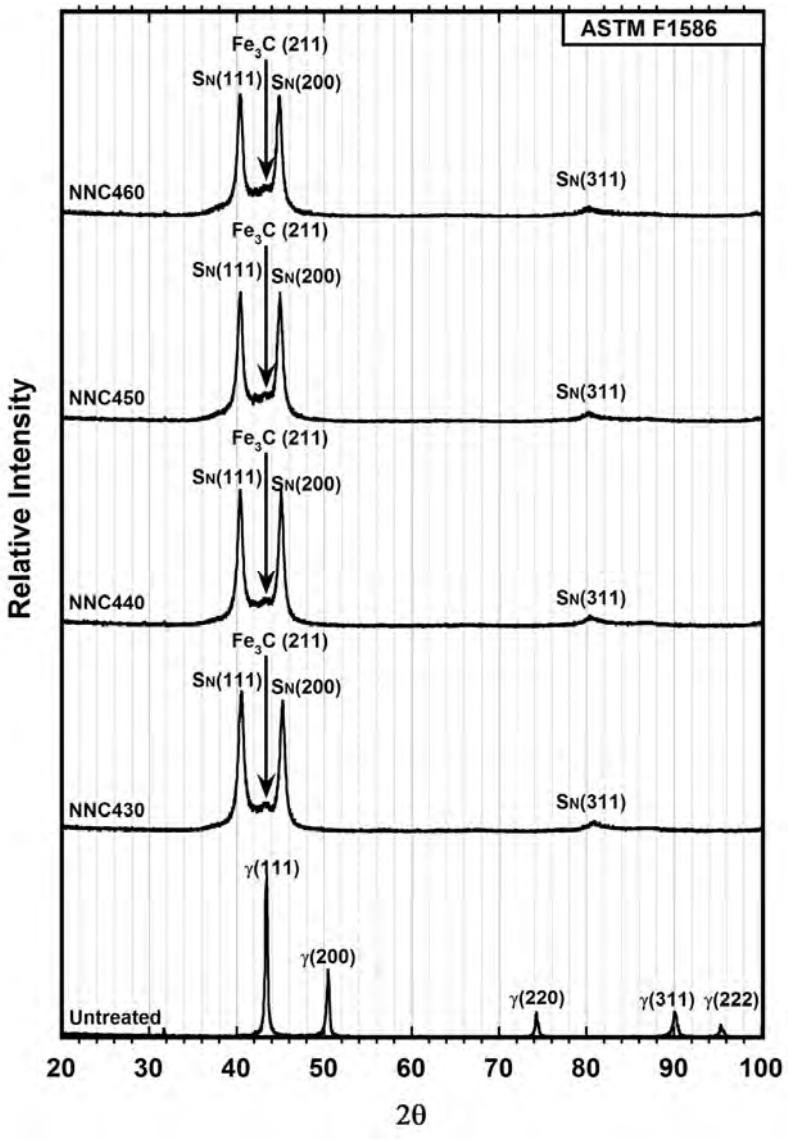

Figure 4-2.3.10 XRD profiles of ASTM F1586 samples which were carbonitrided at different temperatures as compared to that of the untreated material
Cu Kα Radiation

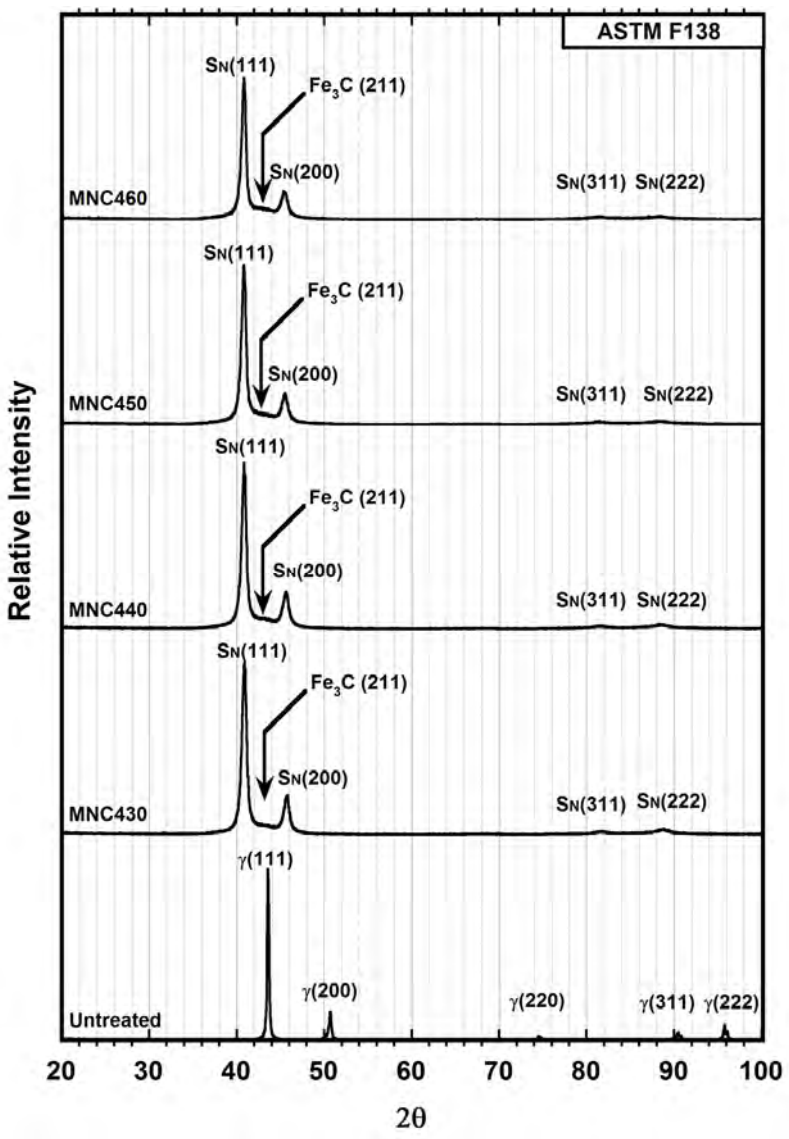

Figure 4-2.3.11 XRD profiles of ASTM F138 samples which were carbonitrided at different temperatures as compared to that of the untreated material
Cu Kα Radiation

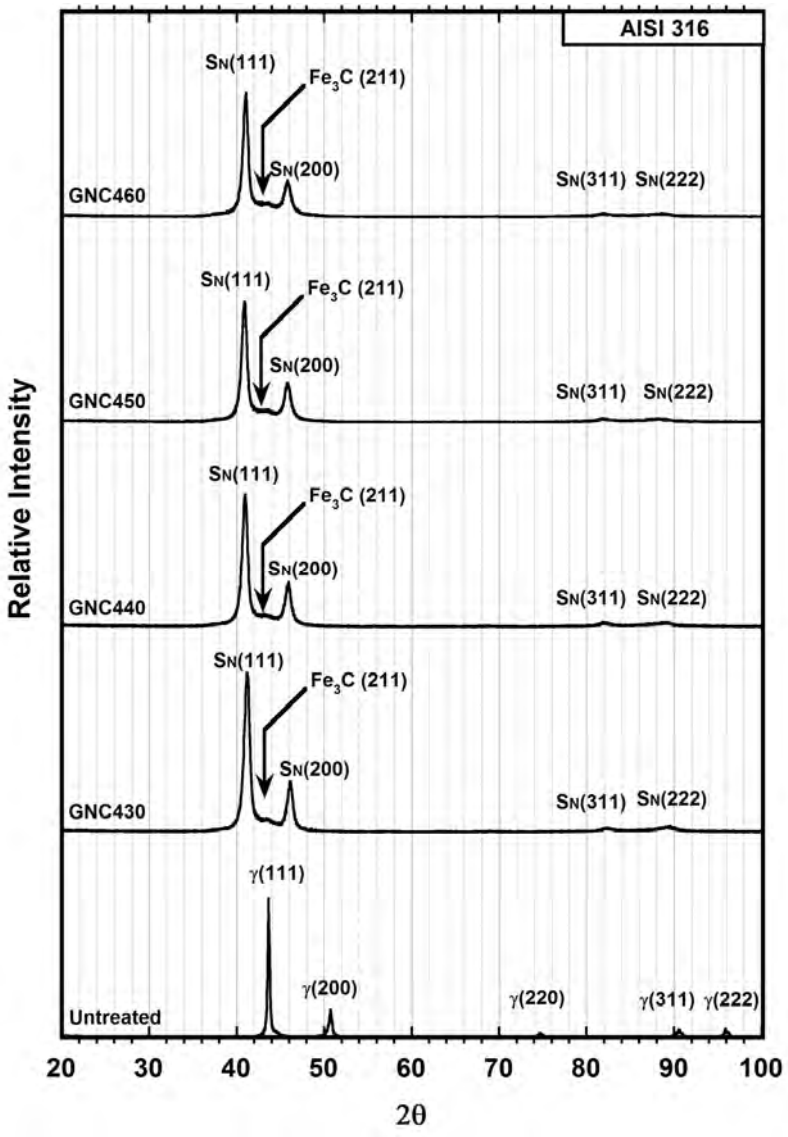

Figure 4-2.3.12 XRD profiles of AISI 316 samples which were carbonitrided at different temperatures as compared to that of the untreated material
Cu Kα Radiation

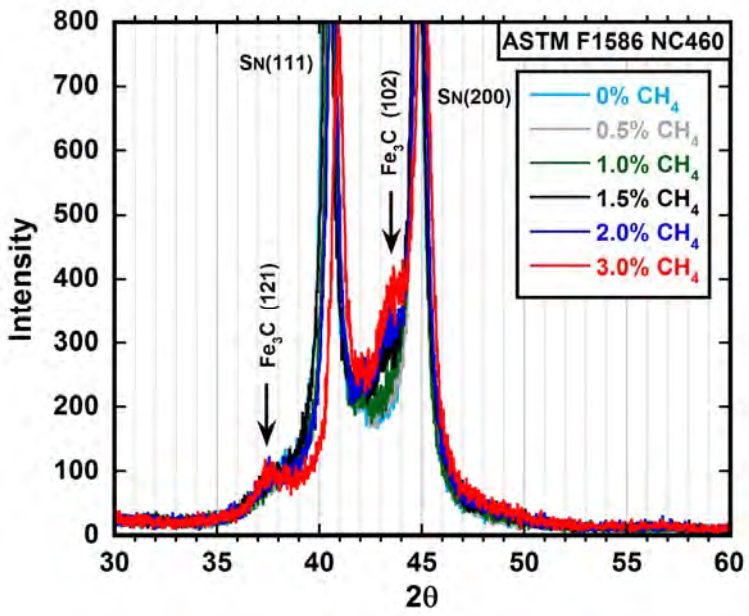

Figure 4-2.3.13 XRD profiles of ASTM F1586 samples which were carbonitrided at 460°C using different gas compositions as compared to ASTM F1586 nitrided at 460°C
Cu Kα Radiation

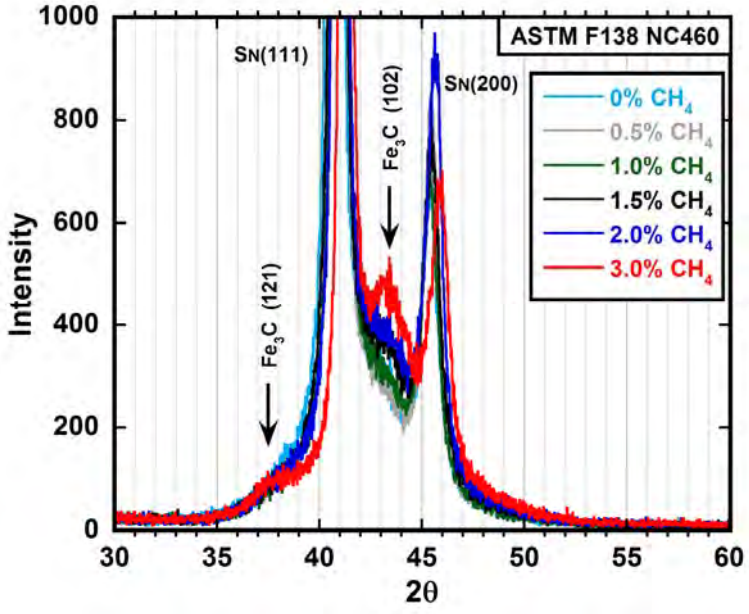

Figure 4-2.3.14 XRD profiles of ASTM F138 samples which were carbonitrided at 460°C using different gas compositions as compared to ASTM F138 nitrided at 460°C
Cu Kα Radiation

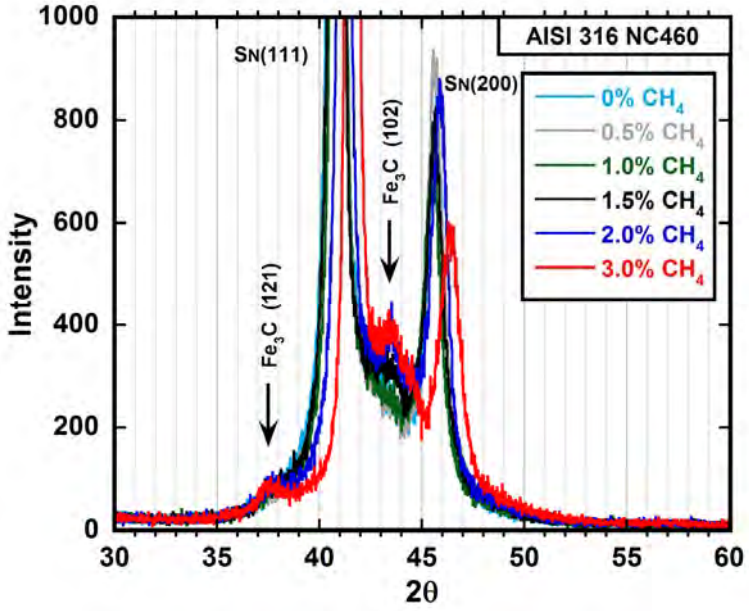

Figure 4-2.3.15 XRD profiles of AISI 316 samples which were carbonitrided at 460°C using different gas compositions as compared to AISI 316 nitrided at 460°C
Cu Kα Radiation

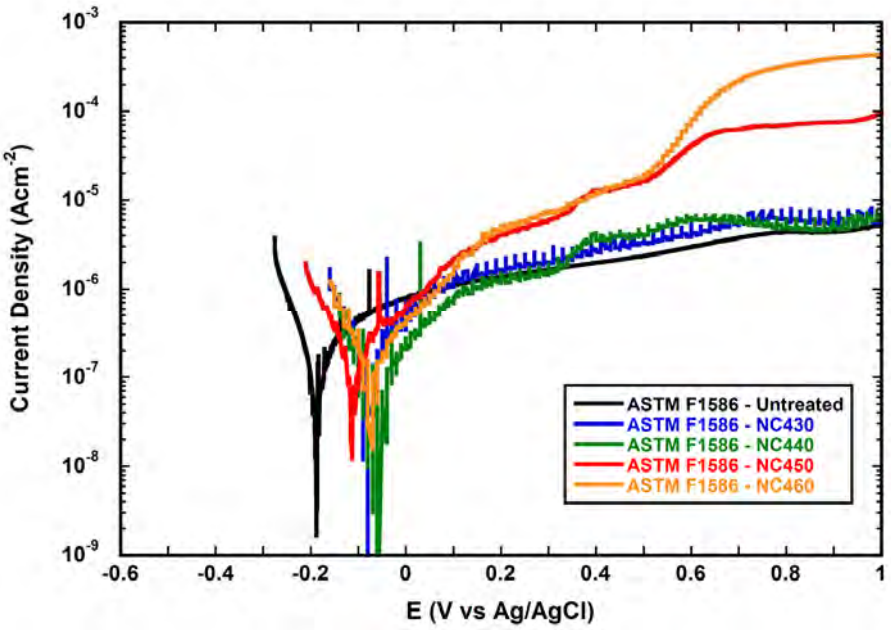

Figure 4-2.3.16 Potentiodynamic curves of ASTM F1586 samples plasma carbonitrided at different temperatures and electrochemically tested in full strength Ringer's solution.

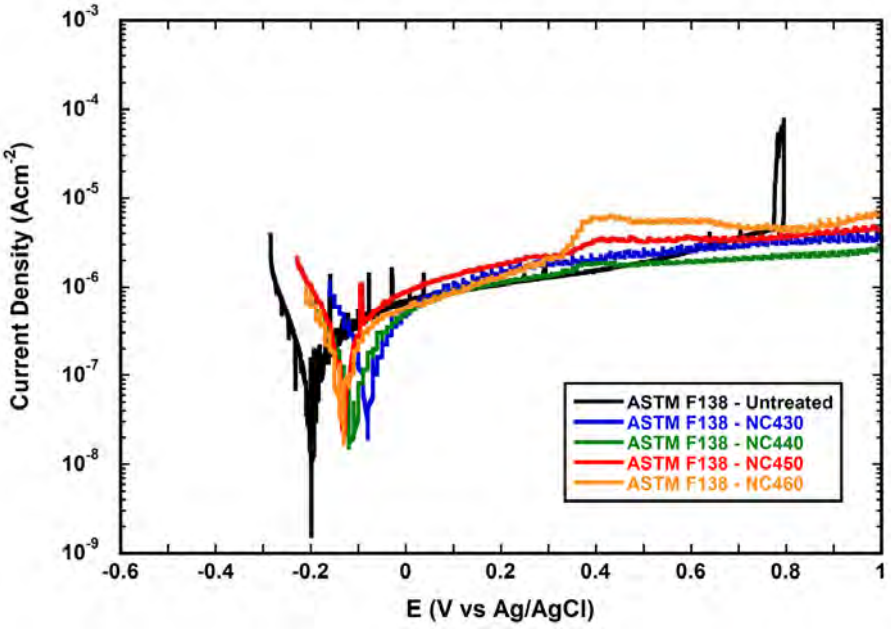

Figure 4-2.3.17 Potentiodynamic curves of ASTM F138 samples plasma carbonitrided at different temperatures and electrochemically tested in full strength Ringer's solution

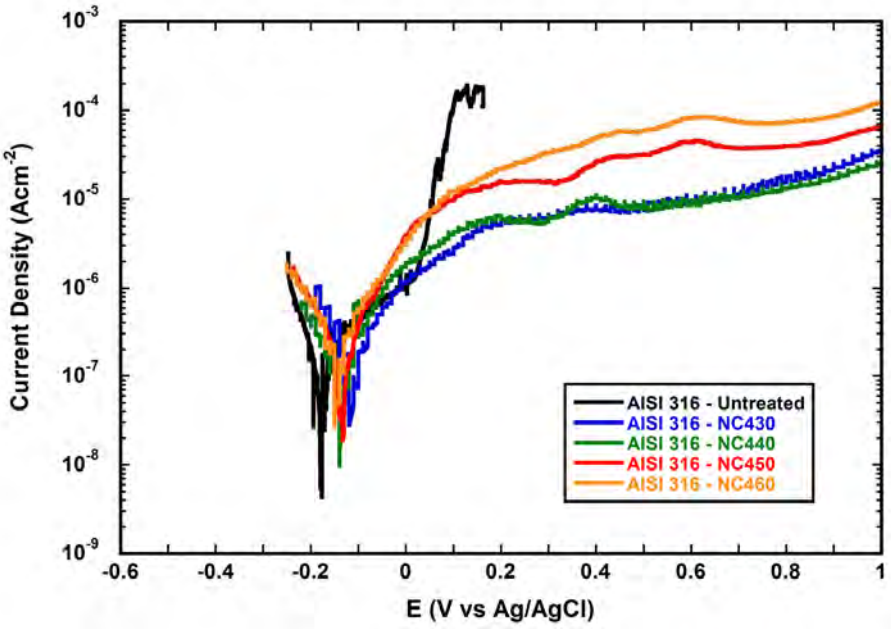

Figure 4-2.3.18 Potentiodynamic curves of AISI 316 samples plasma carbonitrided at different temperatures and electrochemically tested in full strength Ringer's solution

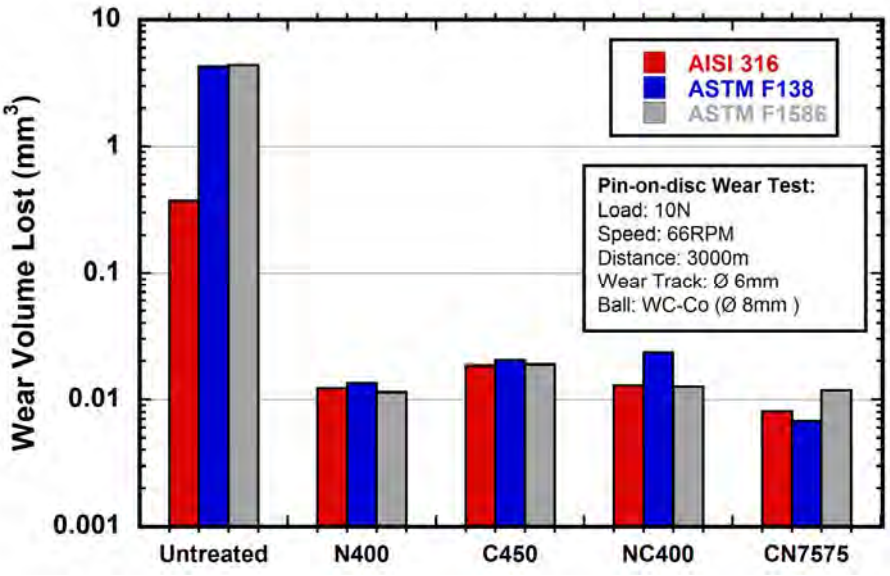

Figure 4-2.4.1 Wear lost during preliminary pin-on-disc wear test on ASTM F1586, ASTM F138 and AISI 316 in the: Untreated; nitrided at 400°C (N400); carburised at 450°C (C450); carbonitrided at 400°C (NC400); carburising at 450°C followed by post-nitriding at 400°C (CN7575)

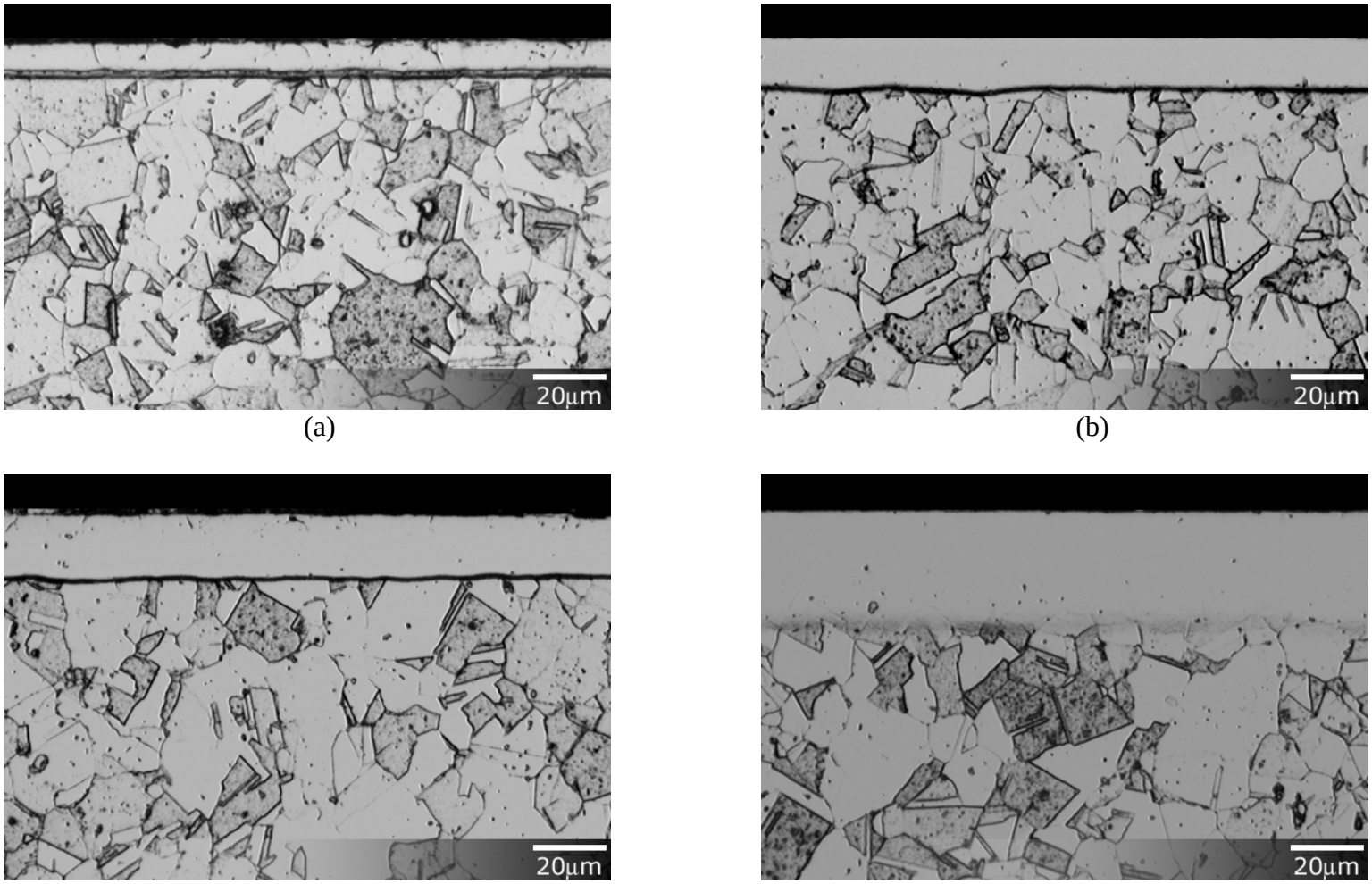

Figure 4-3.1.1 Microstructure of S-phase layer on ASTM F1586 using: (a) nitriding at 430°C; (b) carburising at 430°C; (c) carbonitriding at 430°C; and (d) carburising at 500°C

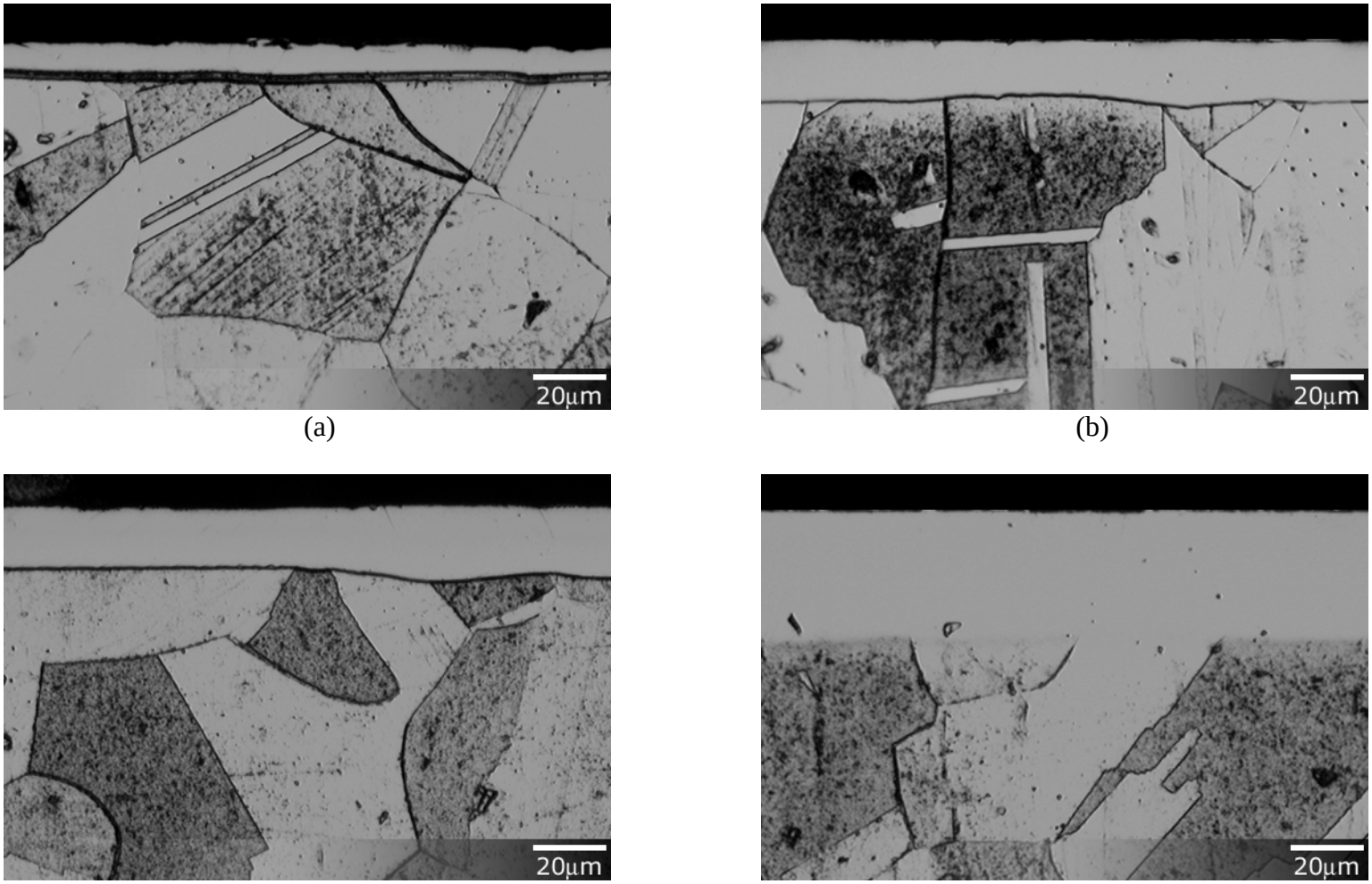

Figure 4-3.1.2 Microstructure of S-phase layer on ASTM F138 using: (a) nitriding at 430°C; (b) carburising at 430°C; (c) carbonitriding at 430°C; and (d) carburising at 500°C

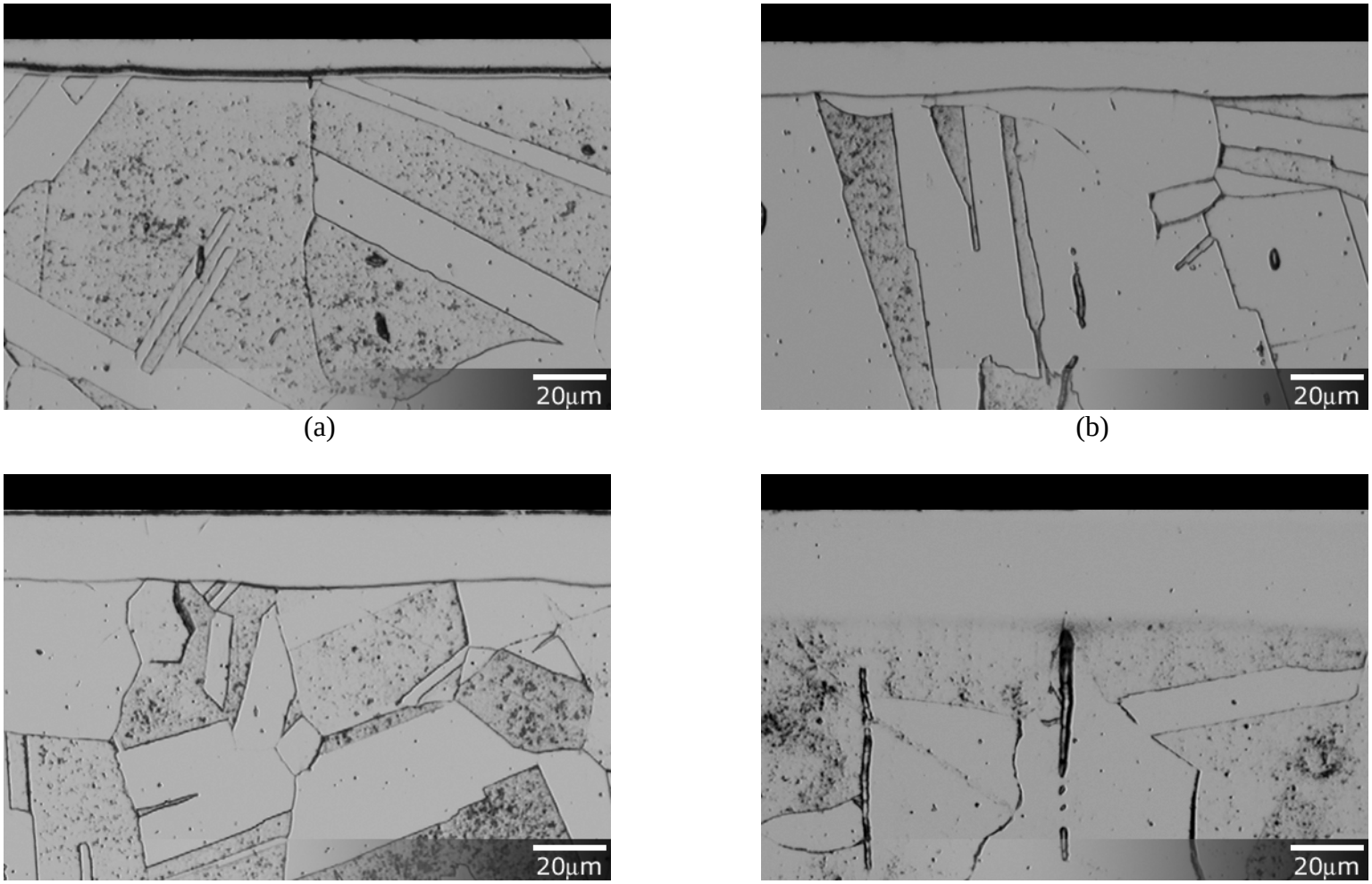

Figure 4-3.1.3 Microstructure of S-phase layer on AISI 316 using: (a) nitriding at 430°C; (b) carburising at 430°C; (c) carbonitriding at 430°C; and (d) carburising at 500°C

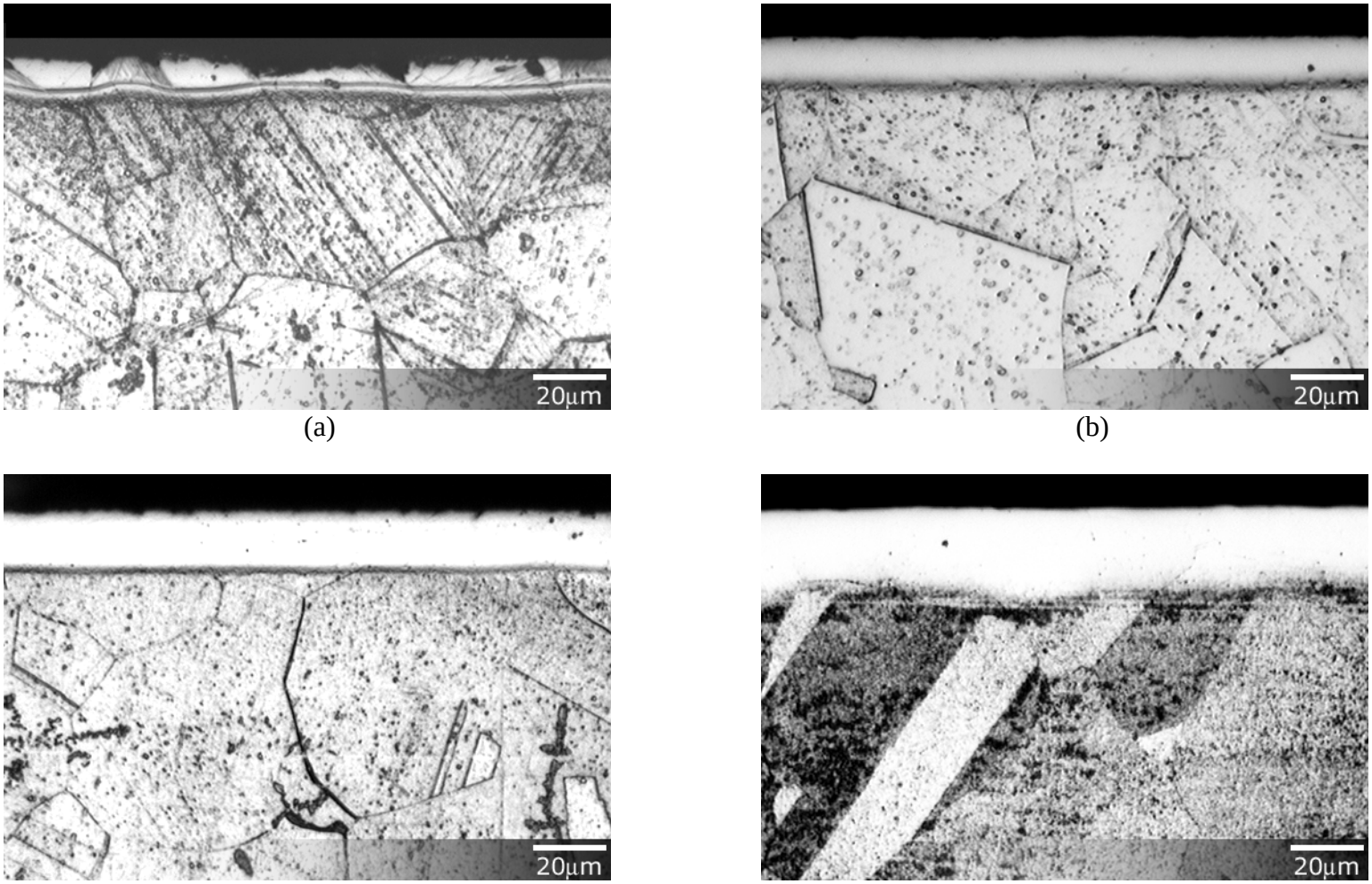

Figure 4-3.1.4 Microstructure of S-phase layer on ASTM F2581 using: (a) nitriding at 430°C; (b) carburising at 430°C; (c) carbonitriding at 430°C; and (d) carburising at 500°C

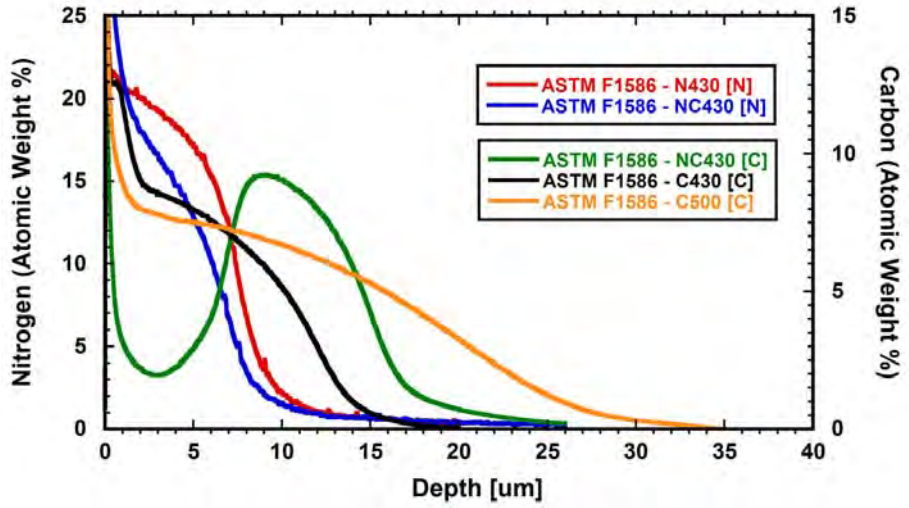

Figure 4-3.2.1 Chemical depth profile of S-phase layer on ASTM F1586 using: nitriding at 430°C (N430); carburising at 430°C (C430); carbo-nitriding at 430°C (NC430); and carburising at 500°C (C500)

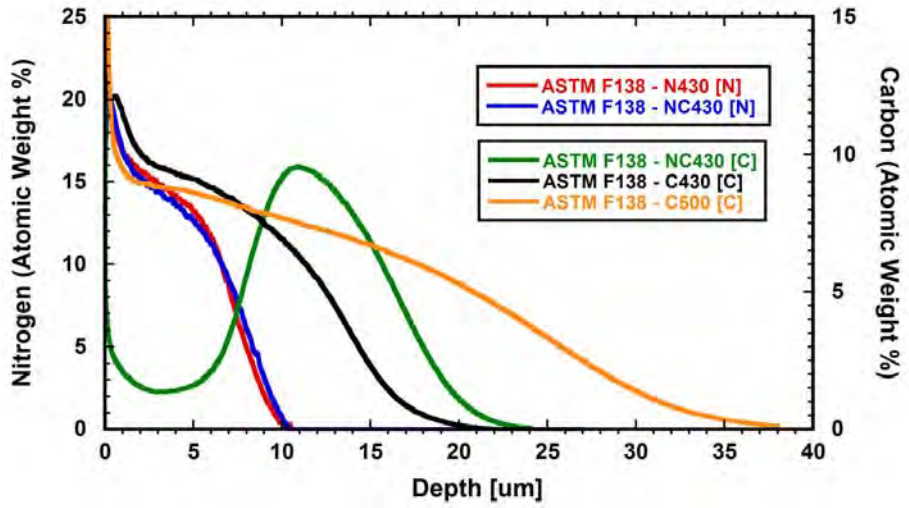

Figure 4-3.2.2 Chemical depth profile of S-phase layer on ASTM F138 using: nitriding at 430°C (N430); carburising at 430°C (C430); carbo-nitriding at 430°C (NC430); and carburising at 500°C (C500)

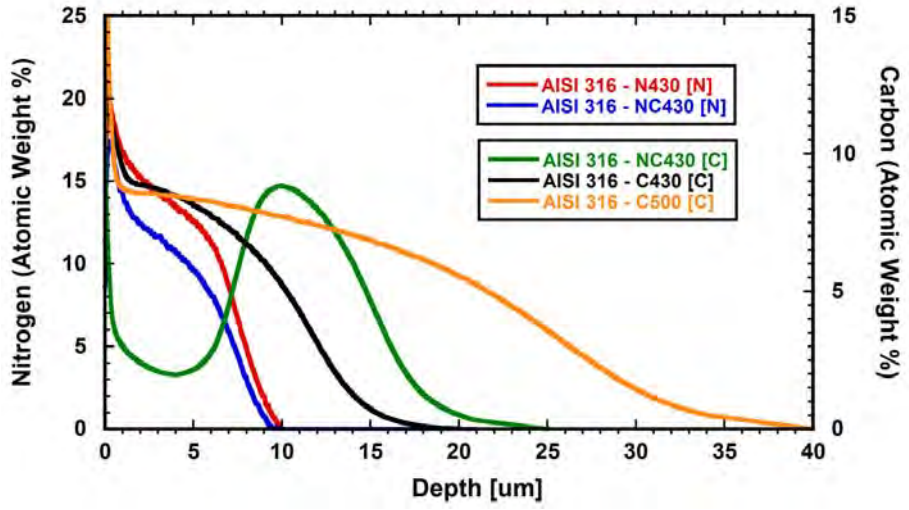

Figure 4-3.2.3 Chemical depth profile of S-phase layer on AISI 316 using: nitriding at 430°C (N430); carburising at 430°C (C430); carbo-nitriding at 430°C (NC430); and carburising at 500°C (C500)

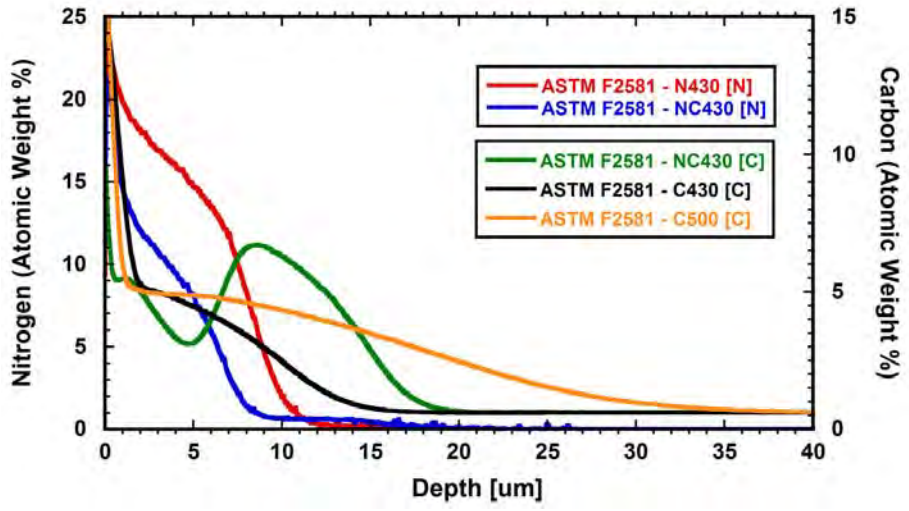

Figure 4-3.2.4 Chemical depth profile of S-phase layer on ASTM F2581 using: nitriding at 430°C (N430); carburising at 430°C (C430); carbo-nitriding at 430°C (NC430); and carburising at 500°C (C500)

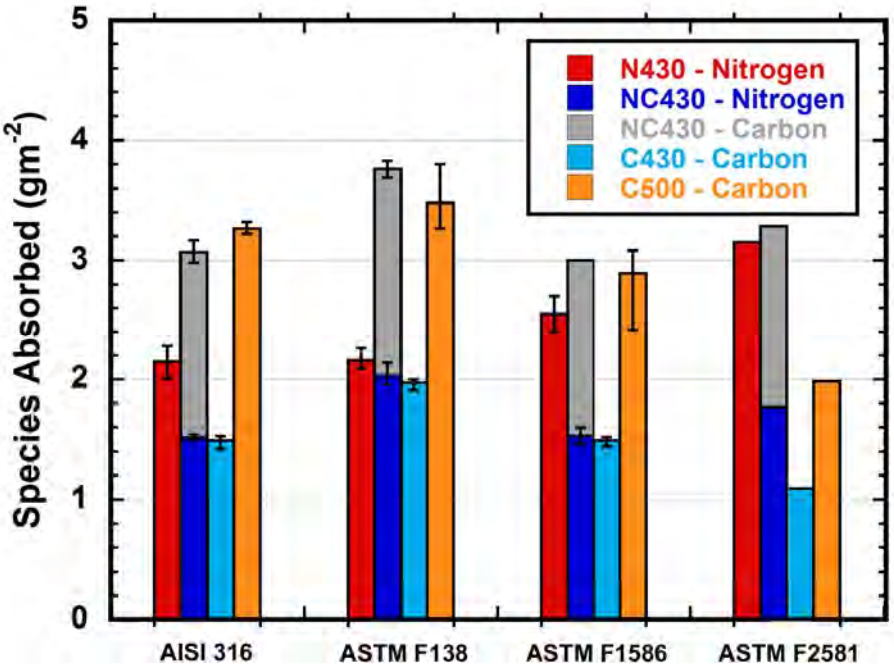

Figure 4-3.2.5 Species absorbed in AISI 316, ASTM F138, ASTM F1586 and ASTM F2581 after: nitriding at 430°C; carburising at 430°C; carbo-nitriding at 430°C; and carburising at 500°C
Error bar: Largest deviation from the mean of 3 values.

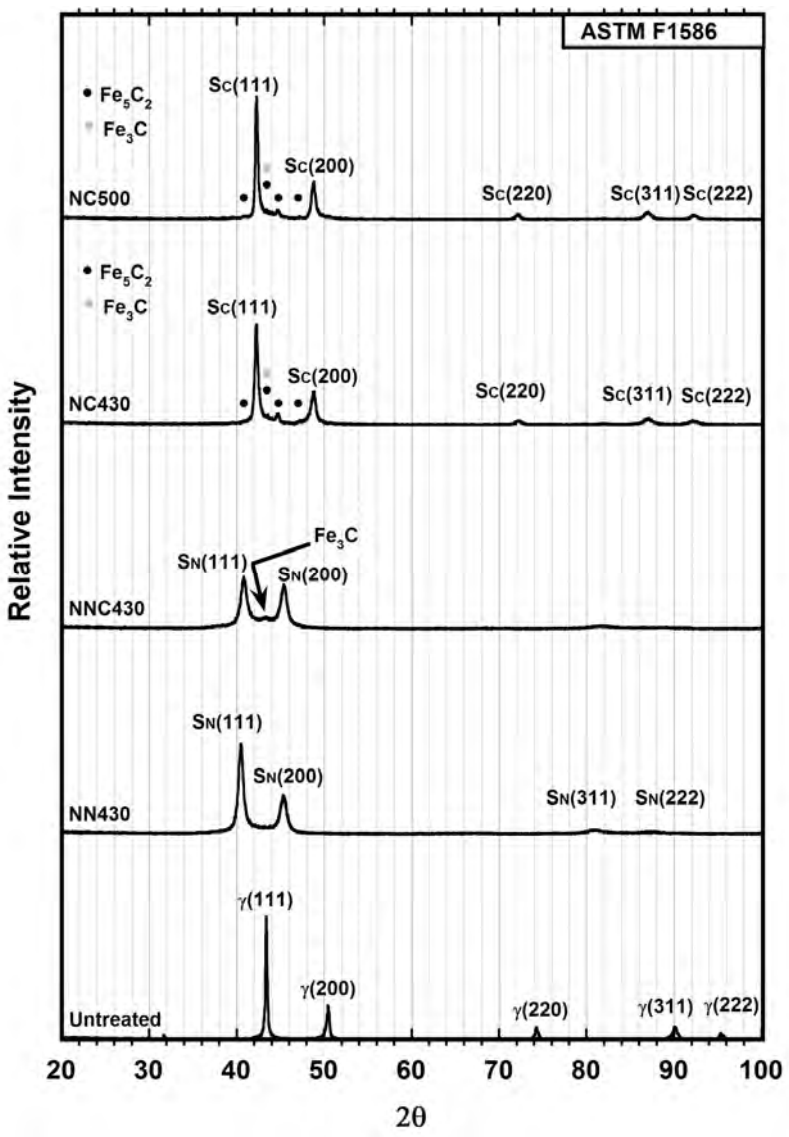

Figure 4-3.3.1 XRD patterns of untreated ASTM F1586 compared to modified layers formed on ASTM F1586 using: nitriding at 430°C (NN430); carburising at 430°C (NC430); carbonitriding at 430°C (NNC430); and carburising at 500°C (NC500). Cu Kα Radiation.

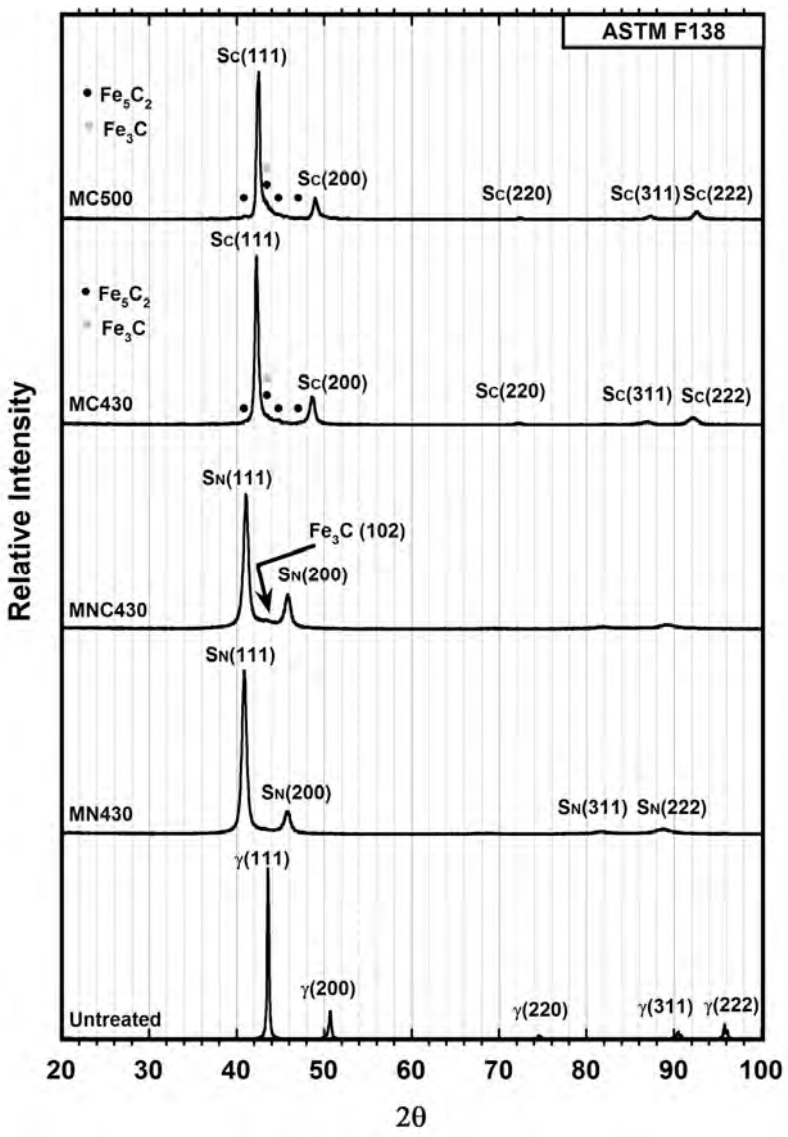

Figure 4-3.3.2 XRD patterns of untreated ASTM F138 compared to modified layers formed on ASTM F1586 using: nitriding at 430°C (MN430); carburising at 430°C (MC430); carbonitriding at 430°C (MNC430); and carburising at 500°C (MC500). Cu Kα Radiation.

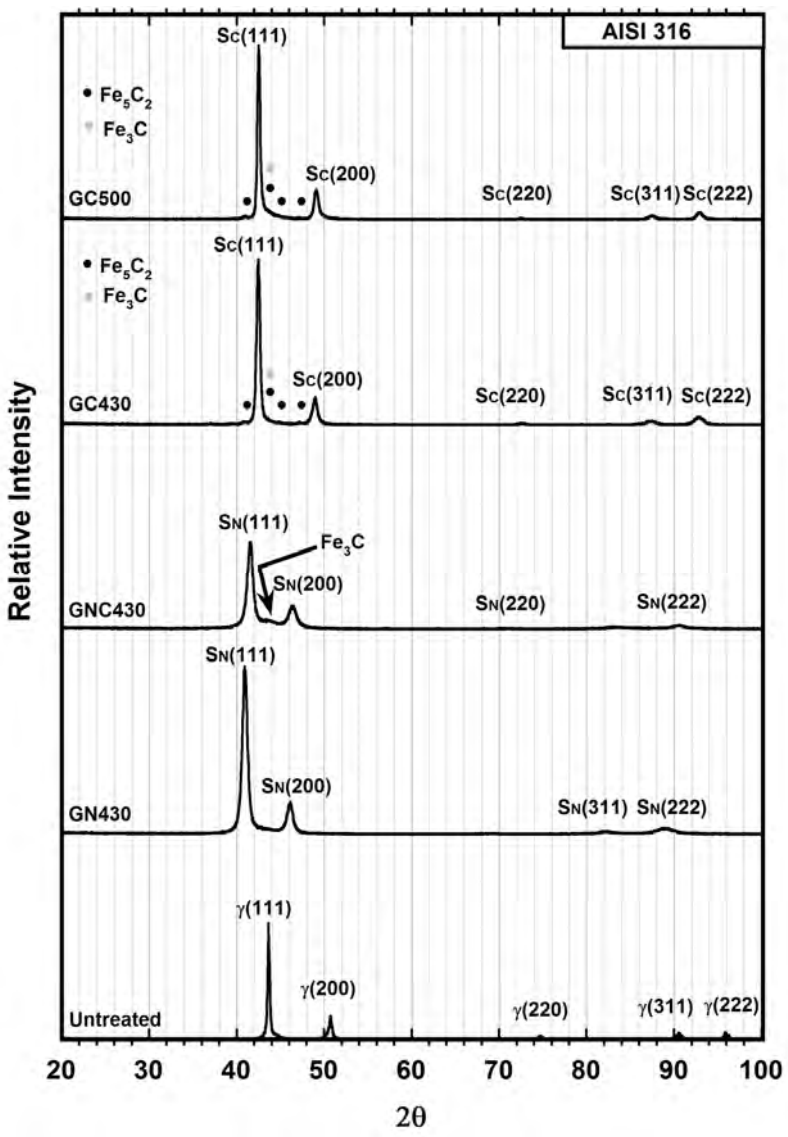

Figure 4-3.3.3 XRD patterns of untreated AISI 316 compared to modified layers formed on ASTM F1586 using: nitriding at 430°C (GN430); carburising at 430°C (GC430); carbonitriding at 430°C (GNC430); and carburising at 500°C (GC500). Cu Kα Radiation.

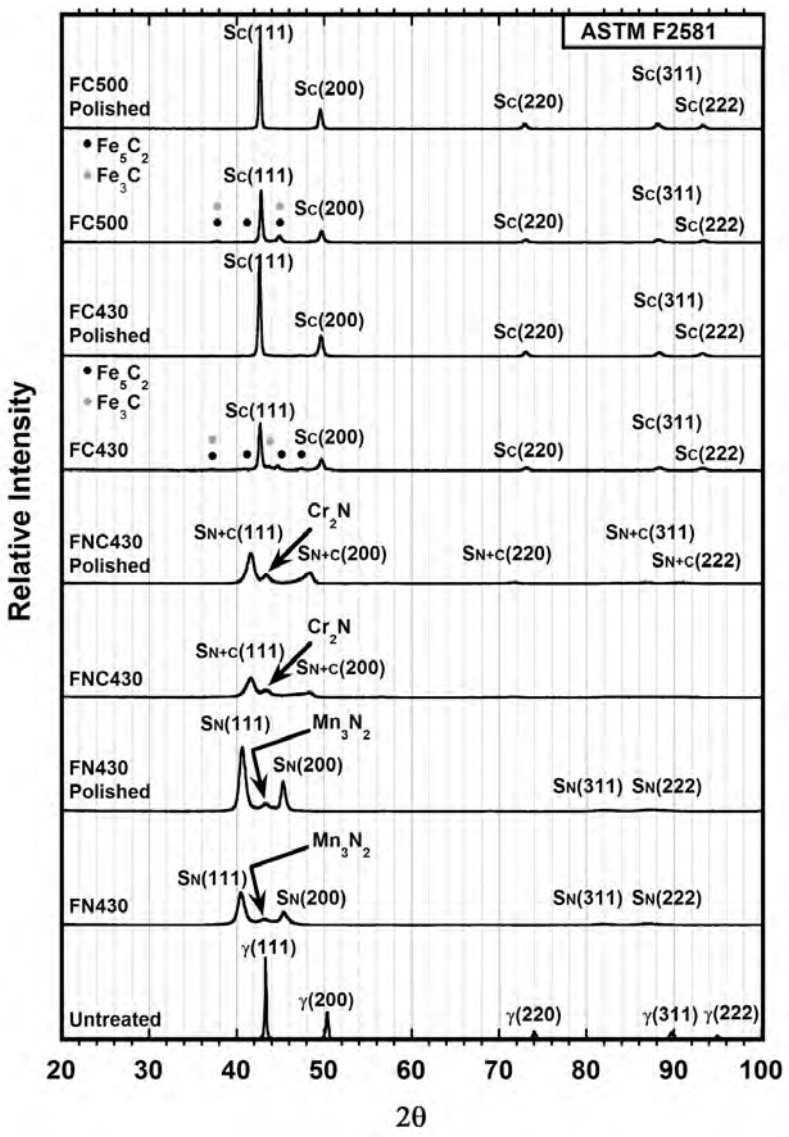

Figure 4-3.3.4 XRD patterns of untreated ASTM F2581 compared to modified layers formed on ASTM F2581 using: nitriding at 430°C (FN430); carburising at 430°C (FC430); carbonitriding at 430°C (FNC430); and carburising at 500°C (FC500). XRD patterns of treated samples with 1μm polished off their surface are also included. Cu Kα Radiation.

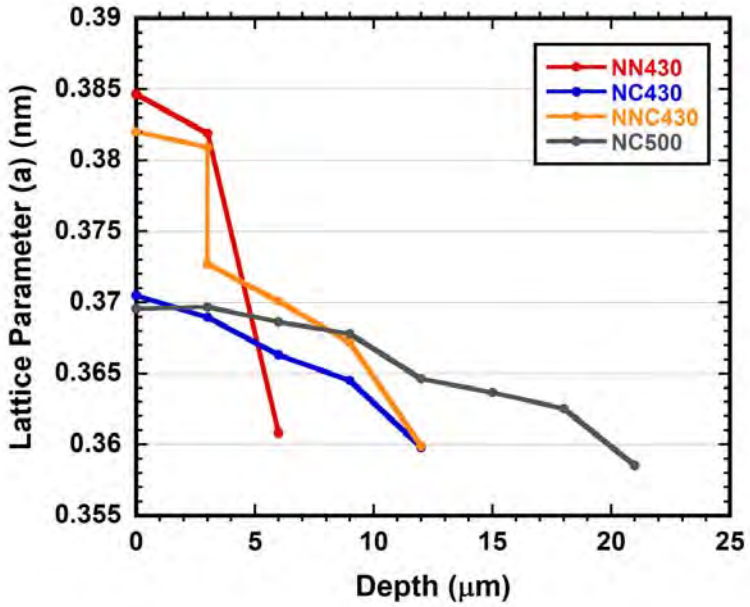

Figure 4-3.3.5 XRD depth profiles of S-phase layers formed on ASTM F1586 using: nitriding at 430°C (NN430); carburising at 430°C (NC430); carbonitriding at 430°C (NNC430); and carburising at 500°C (NC500). Calculations for the lattice parameters are based on the assumption that the crystal structure is face-centred-cubic.
Cu Kα Radiation.

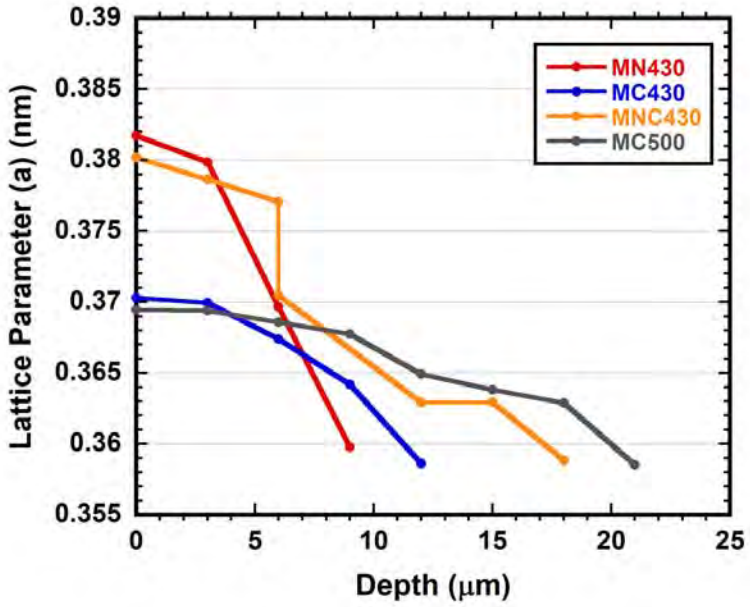

Figure 4-3.3.6 XRD depth profiles of S-phase layers formed on ASTM F138 using: nitriding at 430°C (MN430); carburising at 430°C (MC430); carbonitriding at 430°C (MNC430); and carburising at 500°C (MC500). Calculations for the lattice parameters are based on the assumption that the crystal structure is face-centred-cubic.
Cu Kα Radiation.

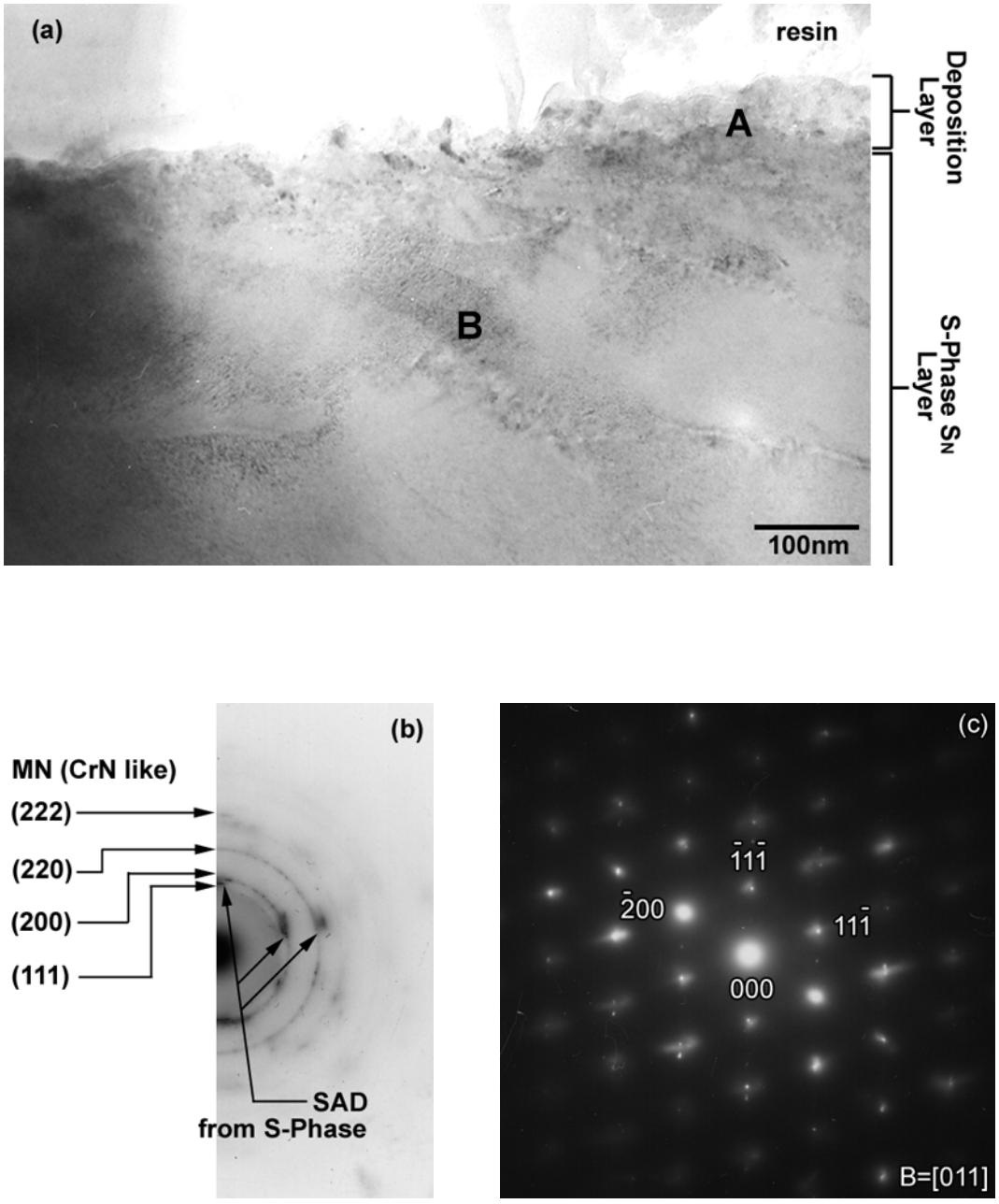

Figure 4-3.4.1 XTEM micrograph showing the layer structure - outer layer (A) and S-phase layer (B) - of plasma carbonitrided ASTM F1586 at 430°C (NNC430) together with corresponding SAD patterns of the outer layer (b) and the S-phase-layer (c)

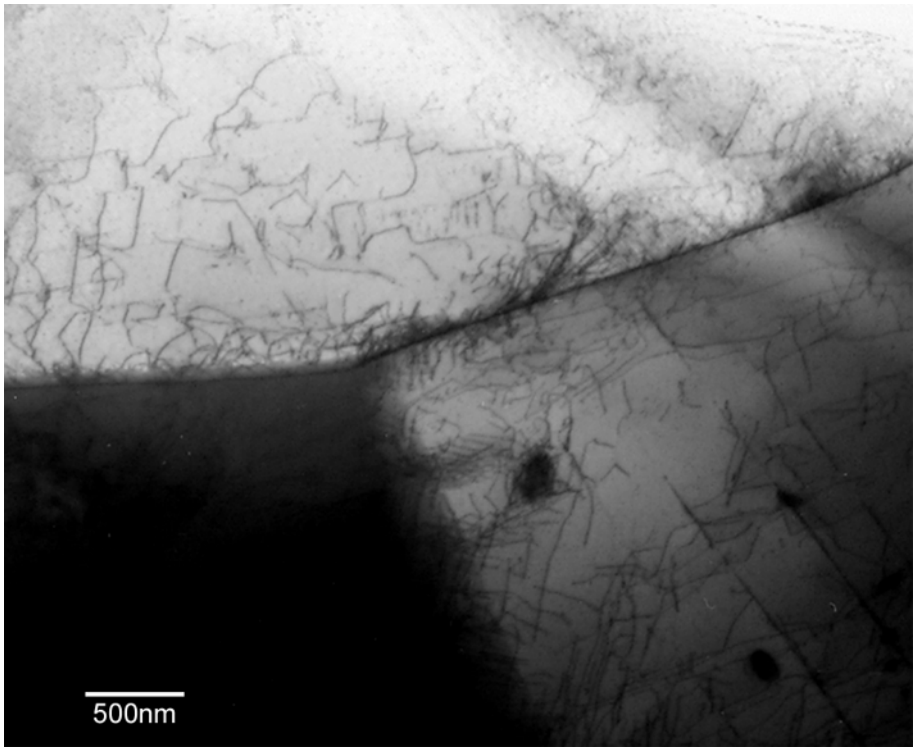

Figure 4-3.4.2 XTEM micrograph showing a high density of entangled dislocations in 430°C plasma carbonitrided ASTM F1586 (NNC430) sample

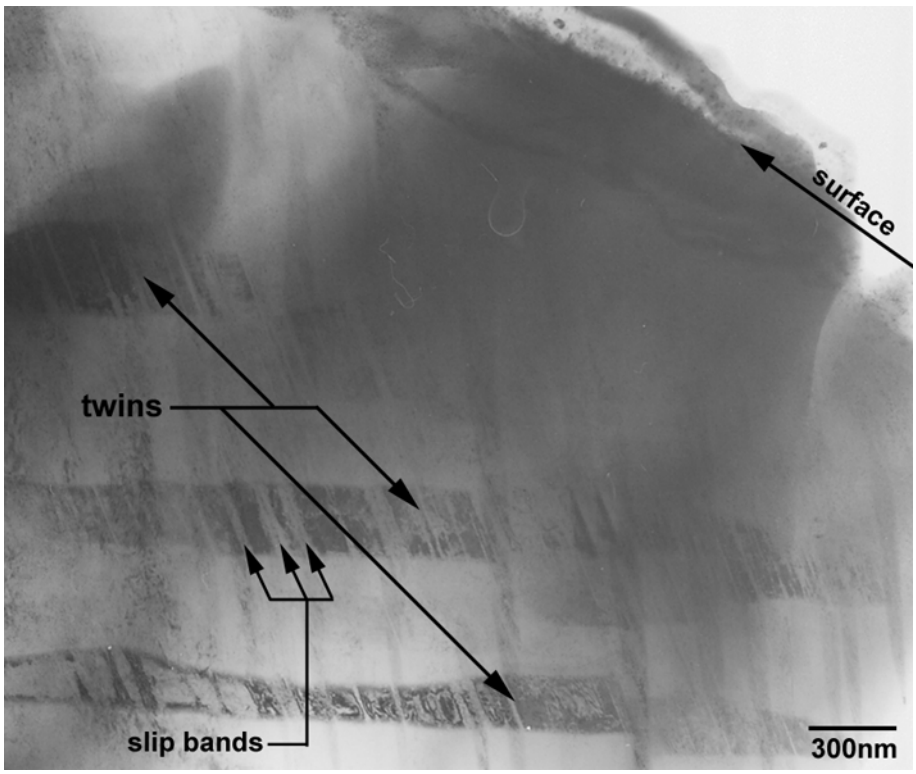

Figure 4-3.4.3 XTEM micrograph showing twins and slip bands in 430°C plasma carbonitrided ASTM F1586 (NNC430) sample

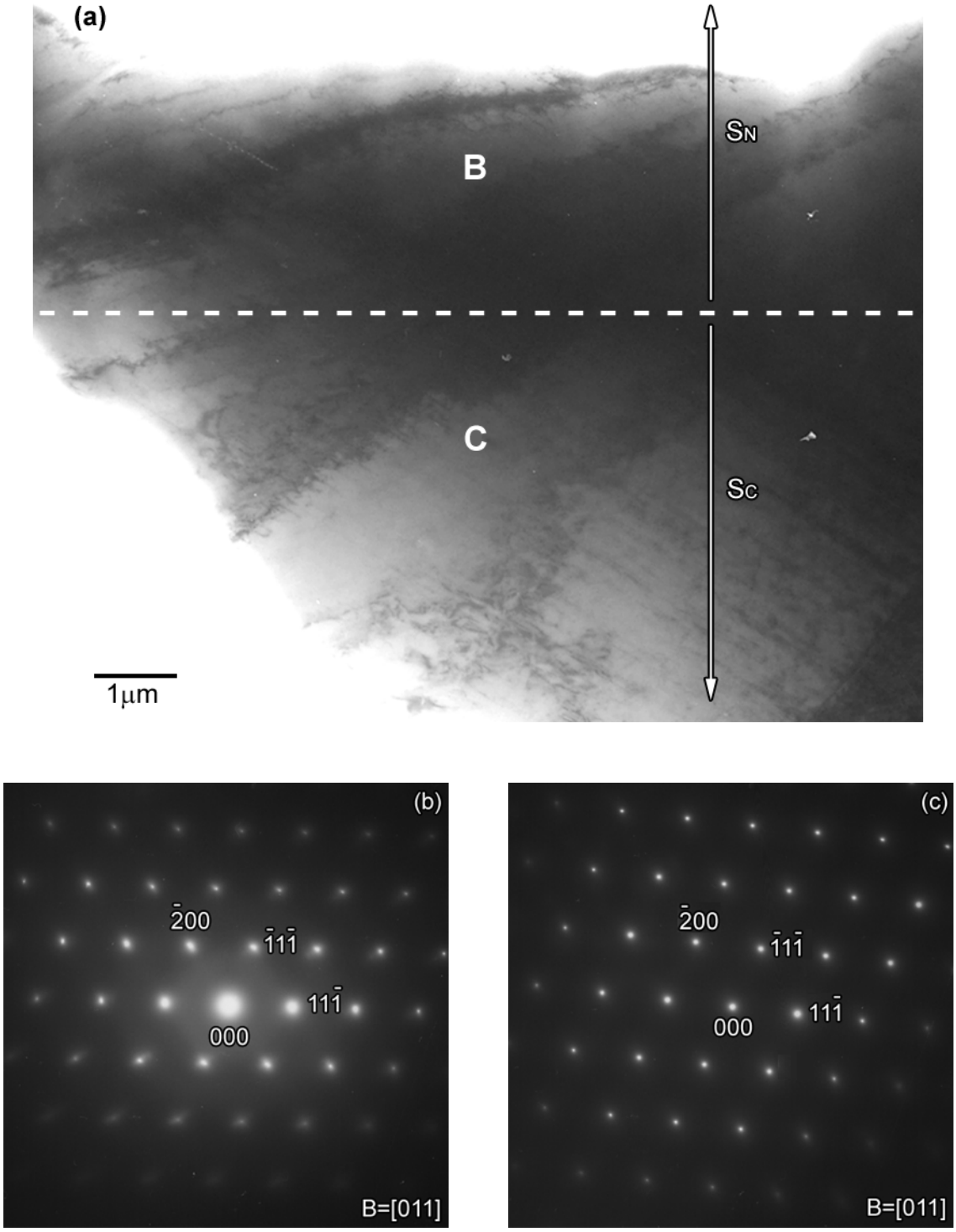

Figure 4-3.4.4 XTEM micrograph showing the interface between the nitrogen- and carbon-rich S-phase on ASTM F138 carbonitrided at 430°C (MNC430) together with SAD patterns of (b) nitrogen-rich S-phase and (c) carbon-rich S-phase

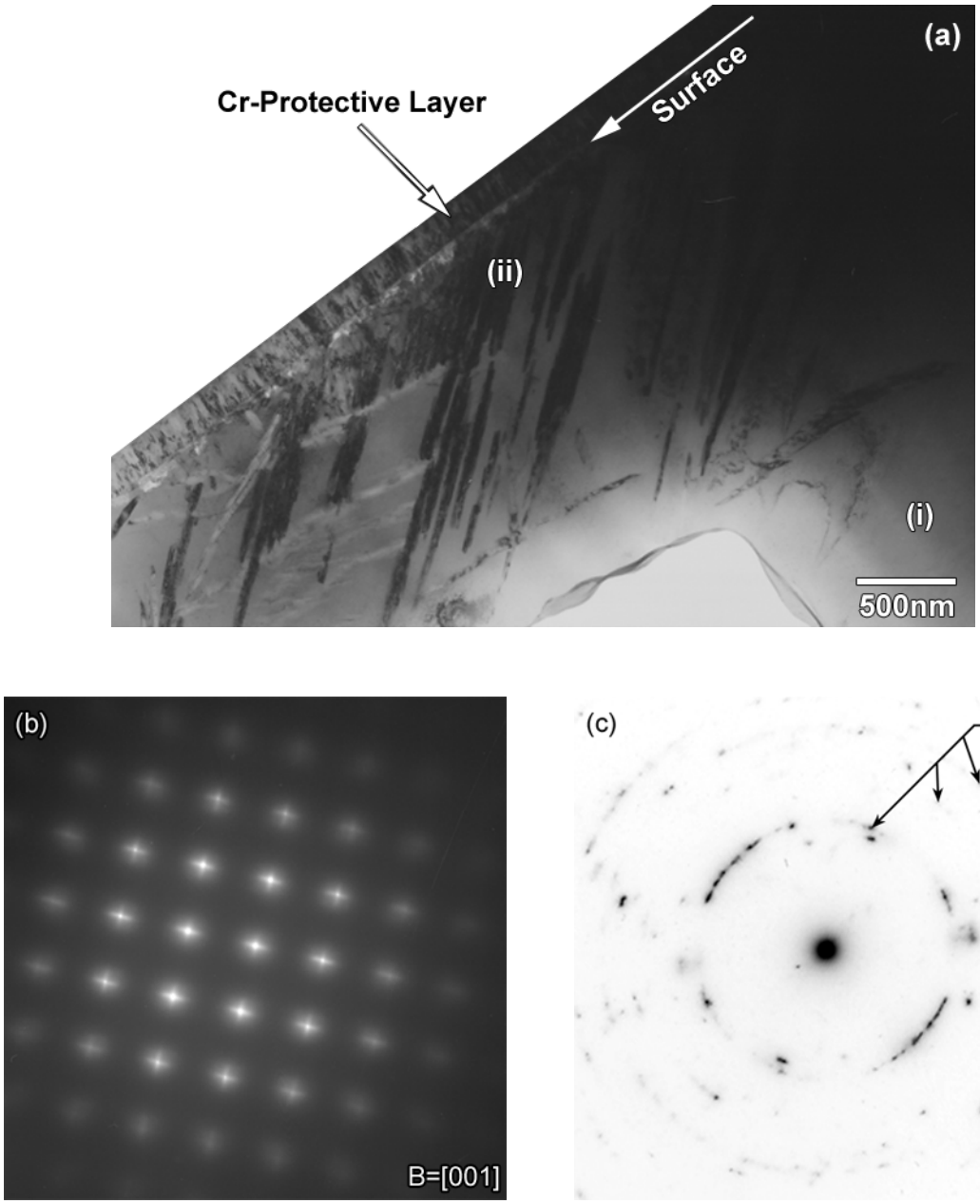

Figure 4-3.4.5 XTEM micrograph showing the outermost part of the layer of carburised ASTM F138 at 500°C (MC500) together with SAD patterns of (b) carbon-rich S-phase and (c) Hagg carbide (Fe_5C_2) precipitates

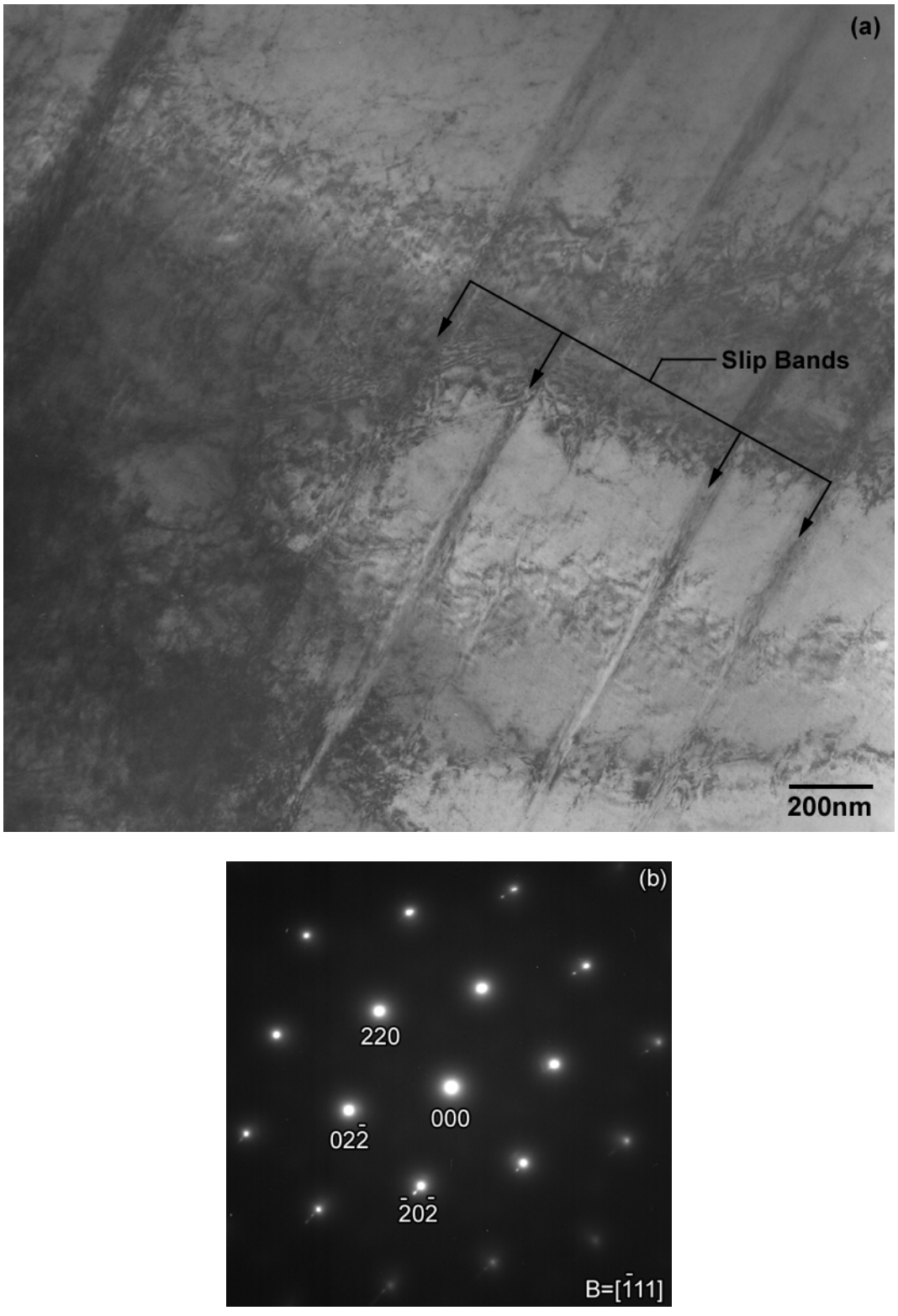

Figure 4-3.4.6 Plane-View TEM microstructure (a) and corresponding SAD patterns (b) of S-Phase layer on ASTM F2581 plasma nitrided at 430°C (FN430)

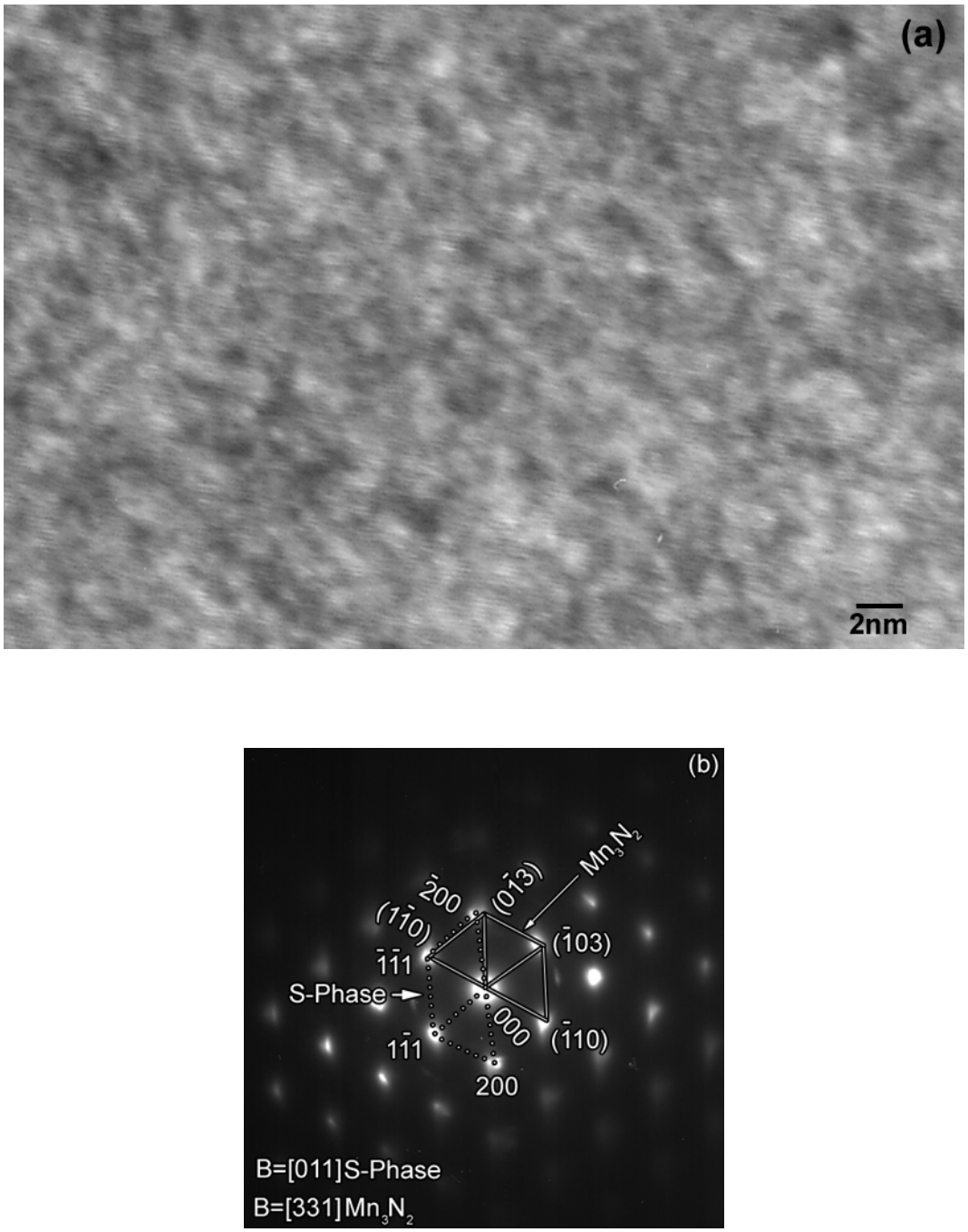

Figure 4-3.4.7 TEM microstructure of S-phase (a) formed on ASTM F2581 by plasma nitrided at 430°C (FN430) showing a ‘tweed’ structure together with the corresponding SAD pattern (b)

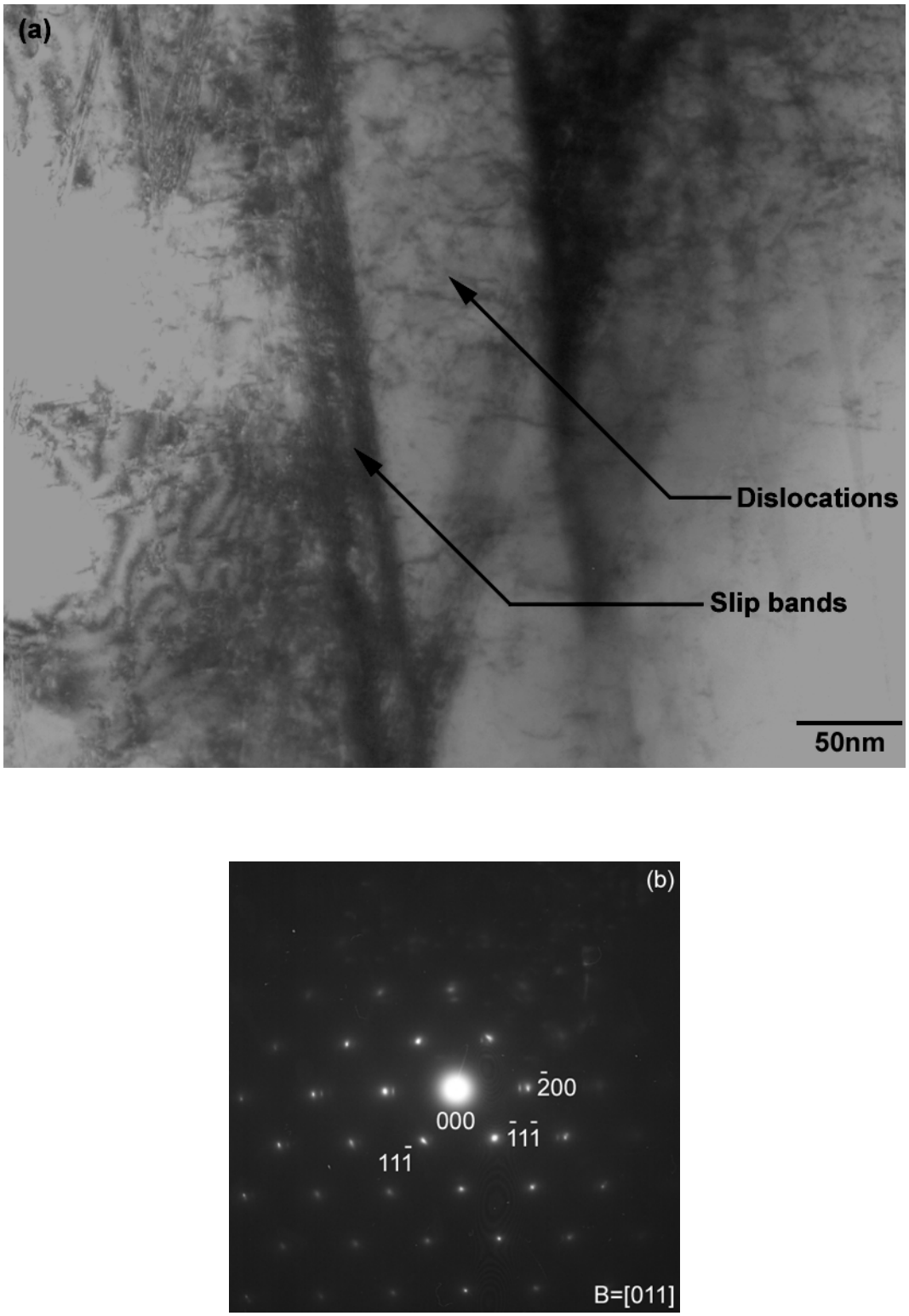

Figure 4-3.4.8 TEM microstructure of S-phase formed on ASTM F2581 by plasma carbonitriding at 430°C (FNC430) showing a high density of dislocation and slip bands (a) together with the corresponding SAD pattern (b)

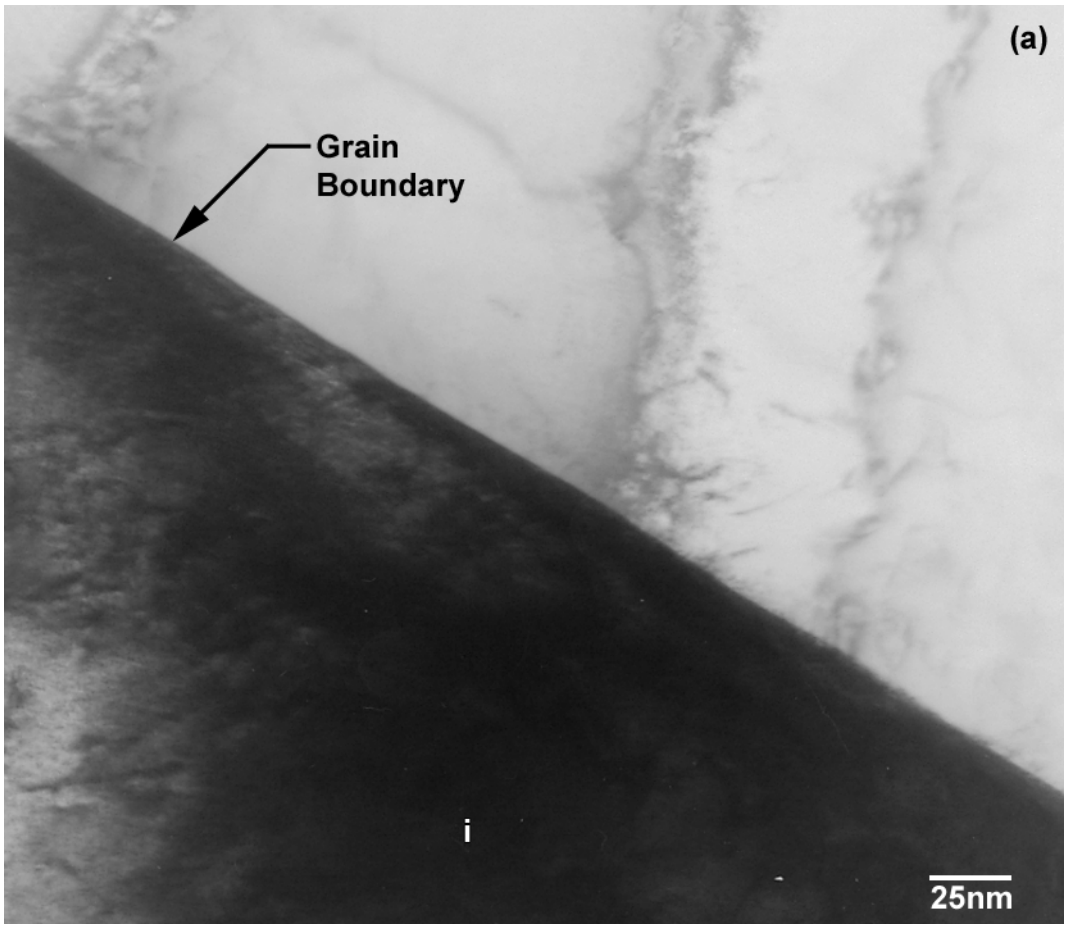

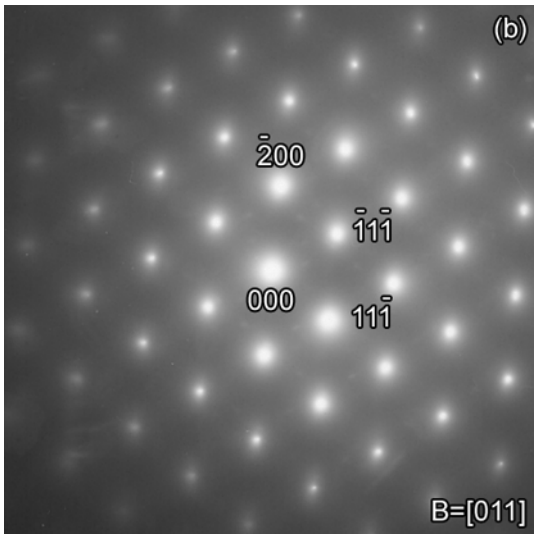

Figure 4-3.4.9 TEM microstructure of S-phase (a) formed on ASTM F2581 by plasma carburising at 500°C (FC500) together with the corresponding SAD pattern (b)

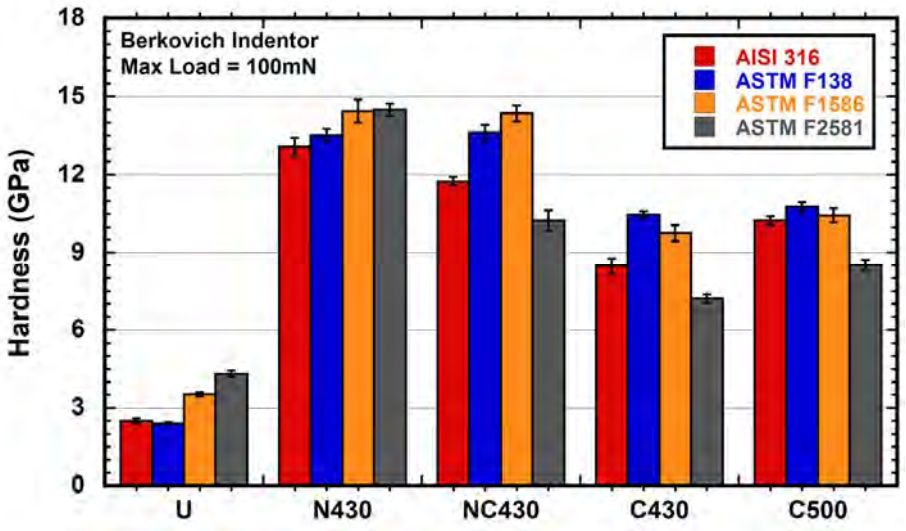

Figure 4-3.5.1 Nano-hardness of AISI 316, ASTM F138, ASTM F1586 and ASTM F2581 in the: untreated (U); nitrided at 430°C (N430); carbonitrided at 430°C (NC430); carburised at 430°C (C430); and carburised at 500°C (C500) condition
Error: Standard deviation of 15 points

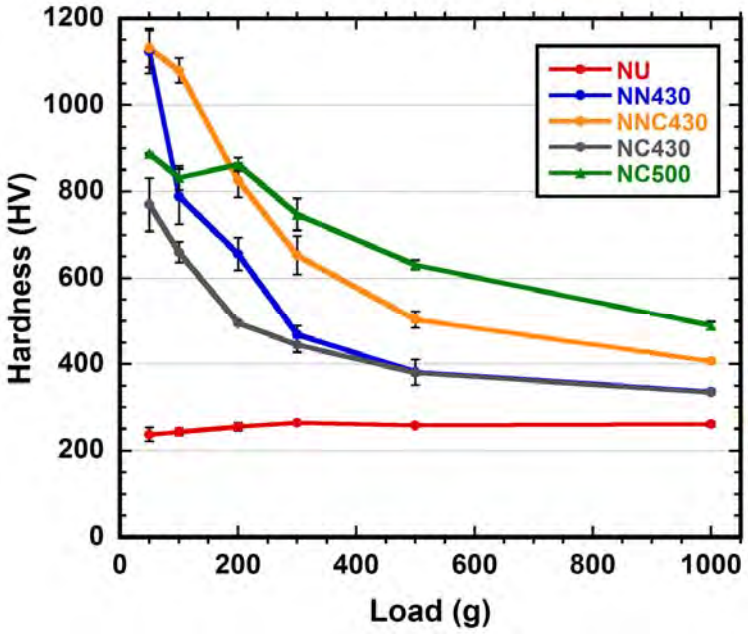

Figure 4-3.5.2 Surface micro-hardness at different loads on ASTM 1586 in the: untreated (NU); nitrided at 430°C (NN430); carbonitrided at 430°C (NNC430); carburised at 430°C (NC430); and carburised at 500°C (NC500) condition
Error: Standard deviation of 3 points

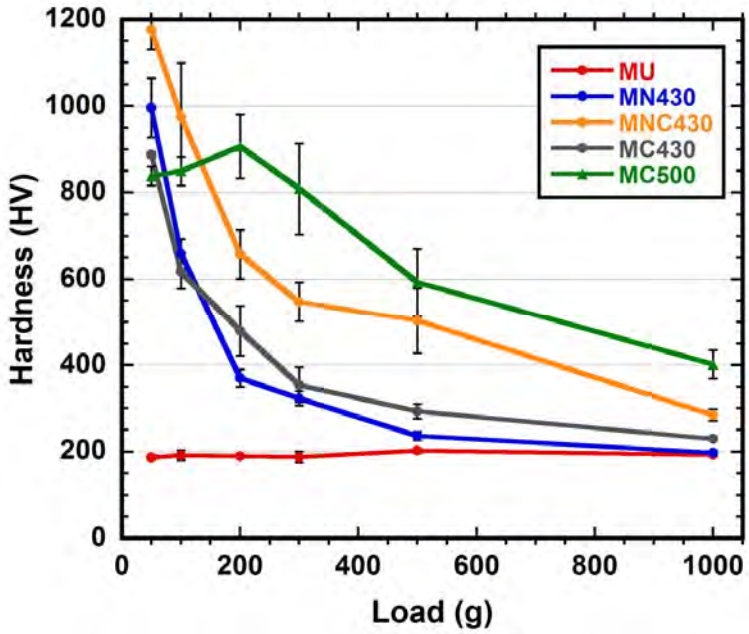

Figure 4-3.5.3 Surface micro-hardness at different loads on ASTM F138 in the: untreated (MU); nitrided at 430°C (MN430); carbonitrided at 430°C (MNC430); carburised at 430°C (MC430); and carburised at 500°C (MC500) condition
Error: Standard deviation of 3 points

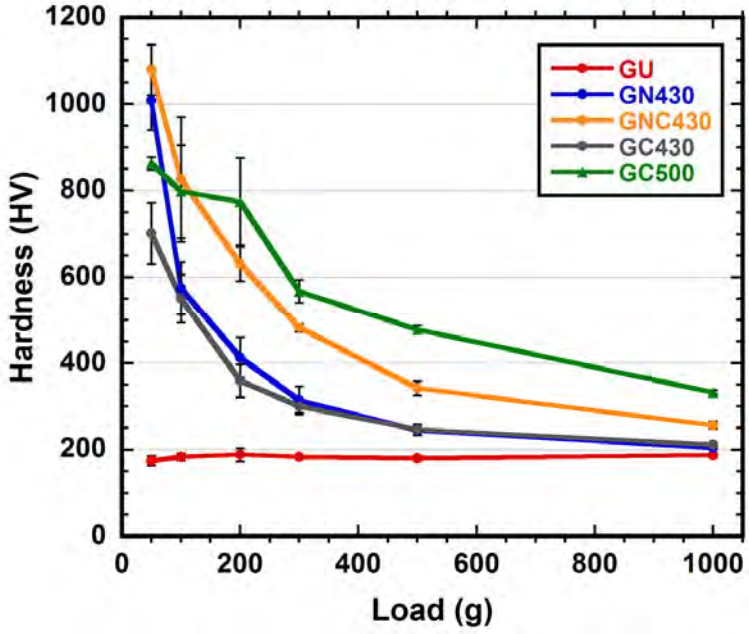

Figure 4-3.5.4 Surface micro-hardness at different loads on AISI 316 in the: untreated (GU); nitrided at 430°C (GN430); carbonitrided at 430°C (GNC430); carburised at 430°C (GC430); and carburised at 500°C (GC500) condition
Error: Standard deviation of 3 points

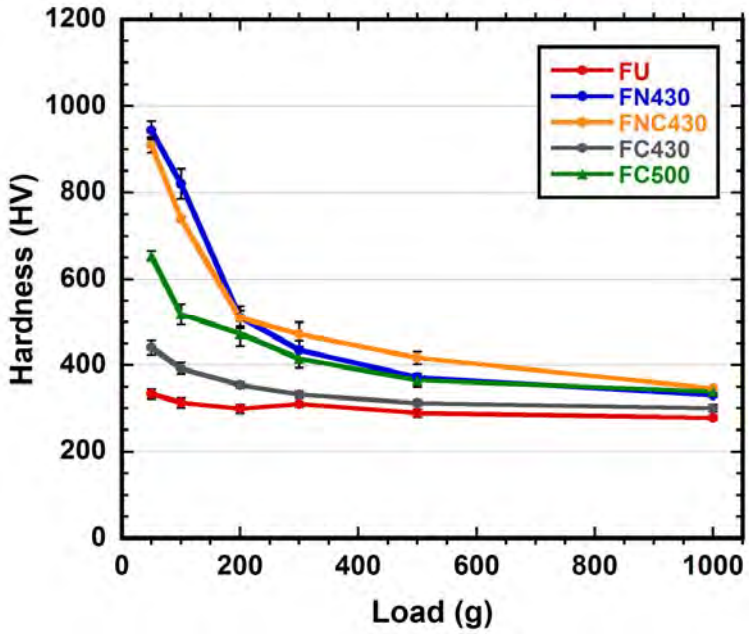

Figure 4-3.5.5 Surface micro-hardness at different loads on ASTM F2581 in the: untreated (FU); nitrided at 430°C (FN430); carbonitrided at 430°C (FNC430); carburised at 430°C (FC430); and carburised at 500°C (FC500) condition
Error: Standard deviation of 3 points

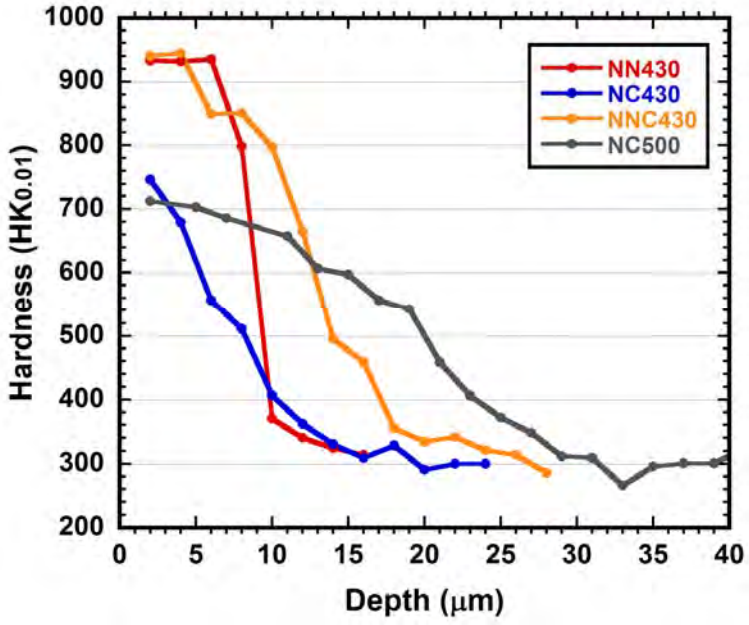

Figure 4-3.5.6 Hardness depth profiles of S-phase formed on ASTM F1586 by: nitriding at 430°C (NN430); carbonitriding at 430°C (NNC430); carburising at 430°C (NC430); and carburising at 500°C (NC500)

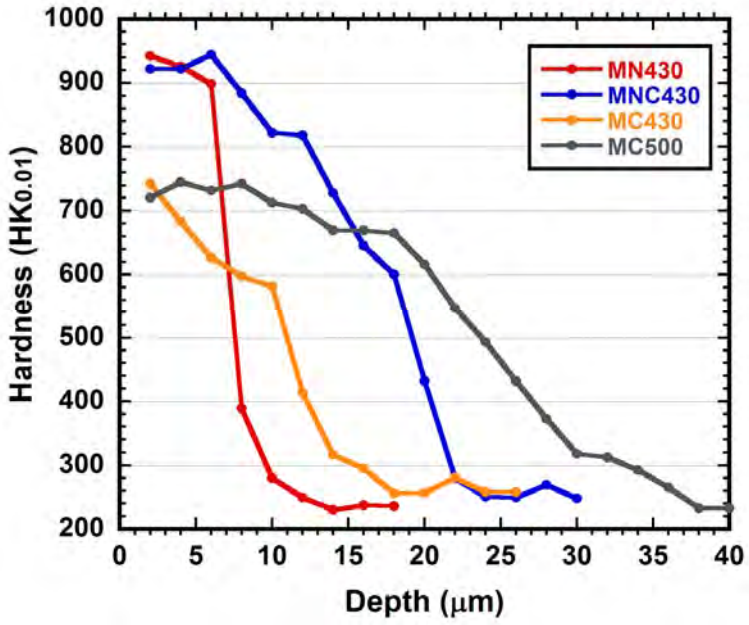

Figure 4-3.5.7 Hardness depth profiles of S-phase formed on ASTM F138 by: nitriding at 430°C (MN430); carbonitriding at 430°C (MNC430); carburising at 430°C (MC430); and carburising at 500°C (MC500)

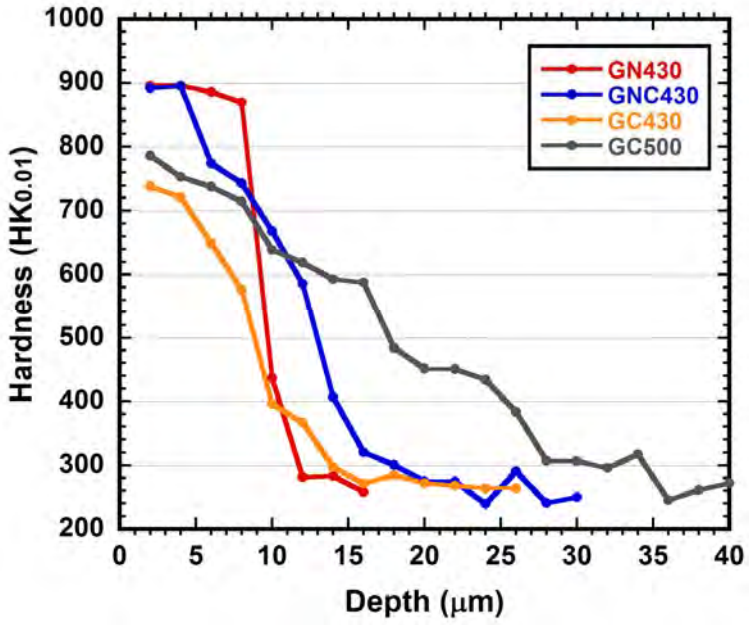

Figure 4-3.5.8 Hardness depth profiles of S-phase formed on AISI 316 by: nitriding at 430°C (GN430); carbonitriding at 430°C (GNC430); carburising at 430°C (GC430); and carburising at 500°C (GC500)

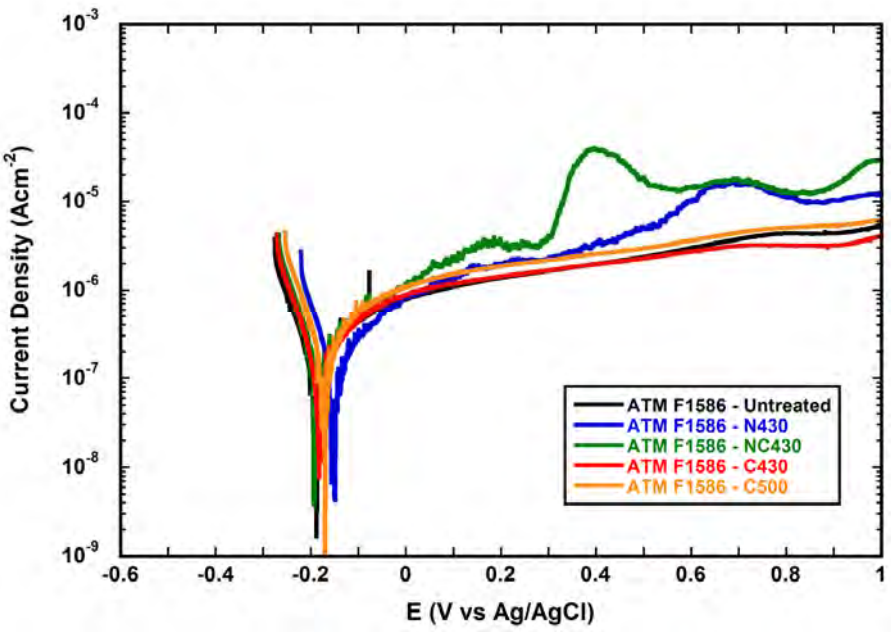

Figure 4-3.6.1 Potentiodynamic curves of ASTM F1586 in the: untreated (U); nitrided at 430°C (N430); carbonitrided at 430°C (NC430); carburised at 430°C (C430); and carburised at 500°C (C500) condition. Tests conducted at 37°C in full strength Ringer's Solution.

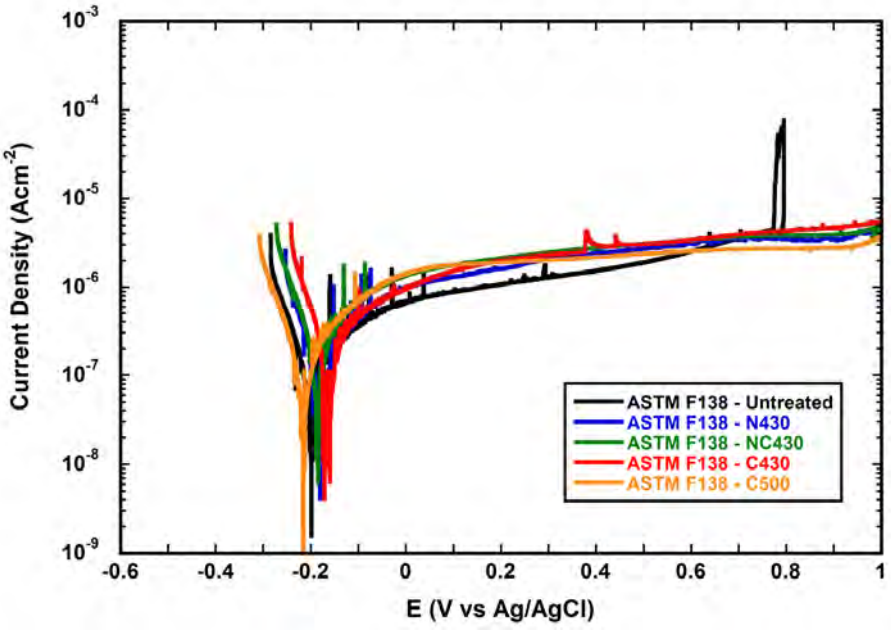

Figure 4-3.6.2 Potentiodynamic Curves of ASTM F138 in the: untreated (U); nitrided at 430°C (N430); carbonitrided at 430°C (NC430); carburised at 430°C (C430); and carburised at 500°C (C500) condition. Tests conducted at 37°C in full strength Ringer's Solution.

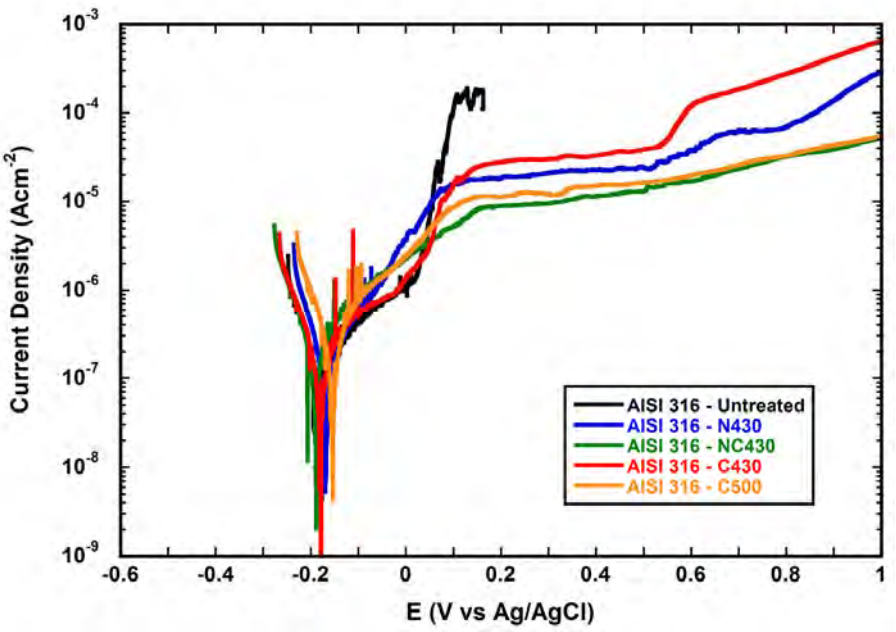

Figure 4-3.6.3 Potentiodynamic curves of AISI 316 in the: untreated (U); nitrided at 430°C (N430); carbonitrided at 430°C (NC430); carburised at 430°C (C430); and carburised at 500°C (C500) condition. Tests conducted at 37°C in full strength Ringer's Solution

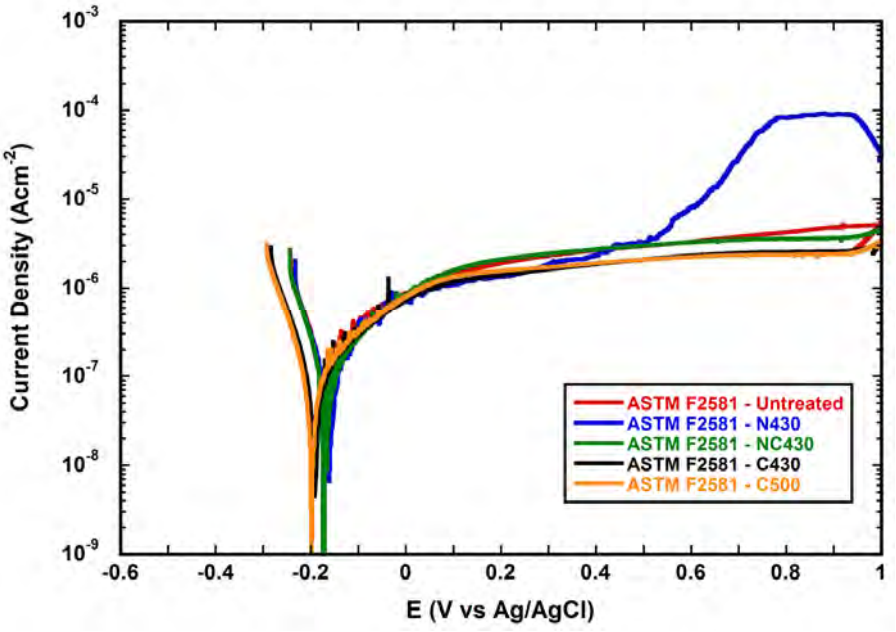

Figure 4-3.6.4 Potentiodynamic curves of ASTM F2581 in the: untreated (U); nitrided at 430°C (N430); carbonitrided at 430°C (NC430); carburised at 430°C (C430); and carburised at 500°C (C500) condition. Tests conducted at 37°C in full strength Ringer's Solution.

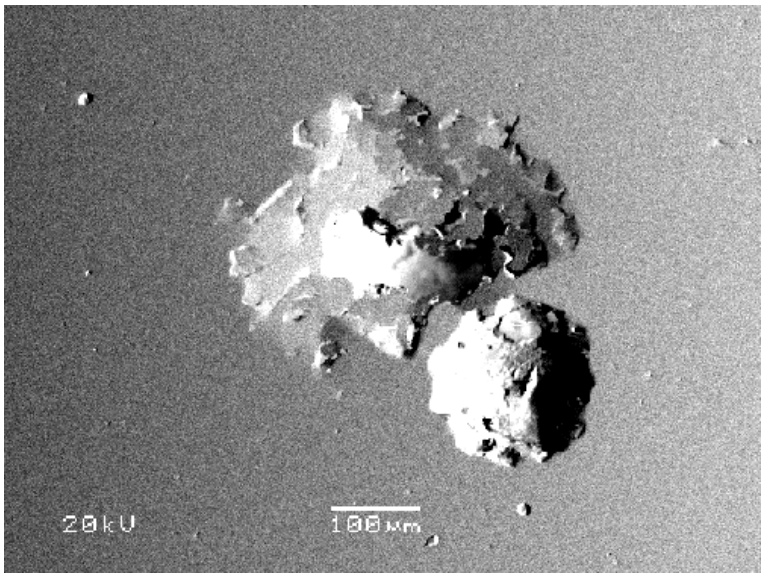

Figure 4-3.6.5 Pitting on untreated AISI 316 after electrochemical testing at a temperature of 37°C in full Strength Ringer's Solution. No signs of crevice corrosion were visible in this test.

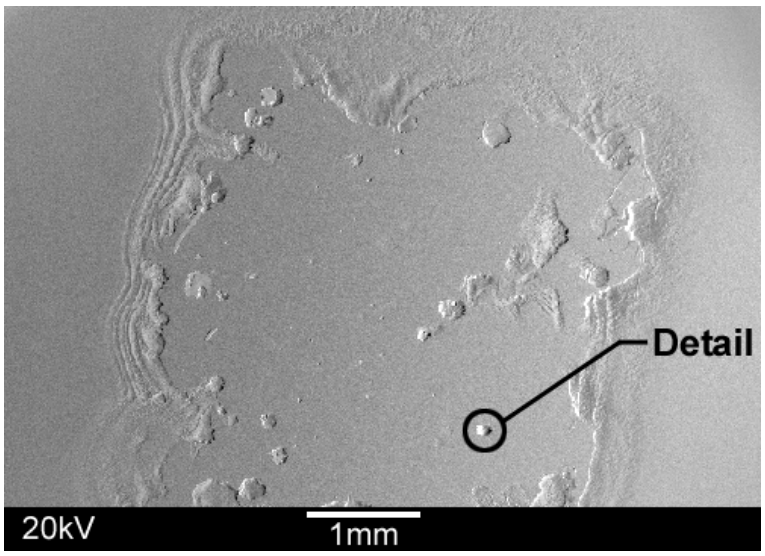

Figure 4-3.6.6 Crevice corrosion attack under lacquer used to create a testing area window. Untreated AISI 316 electrochemically tested at a temperature of 37°C in full strength Ringer's solution. The potentiodynamic curves presented in this work did not show any signs of crevice corrosion.

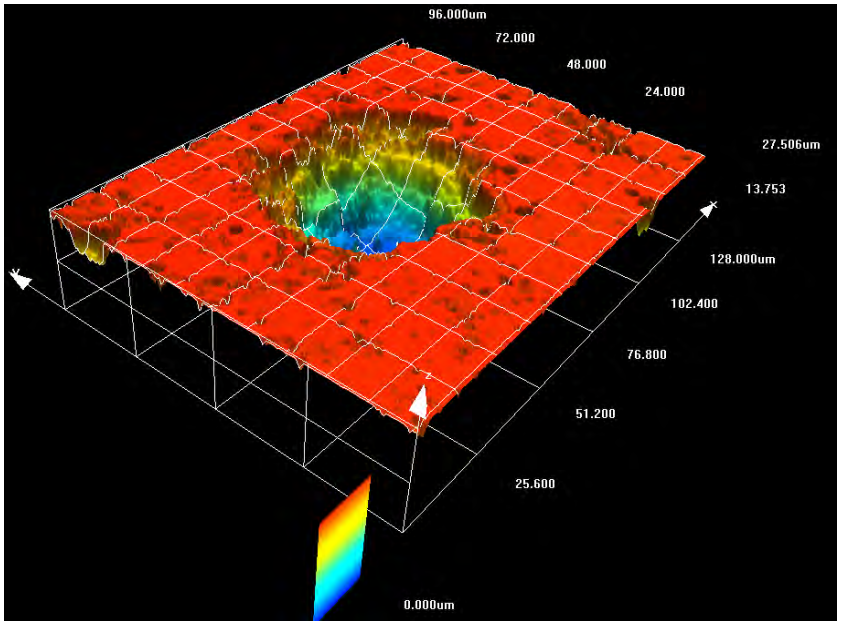

(a)

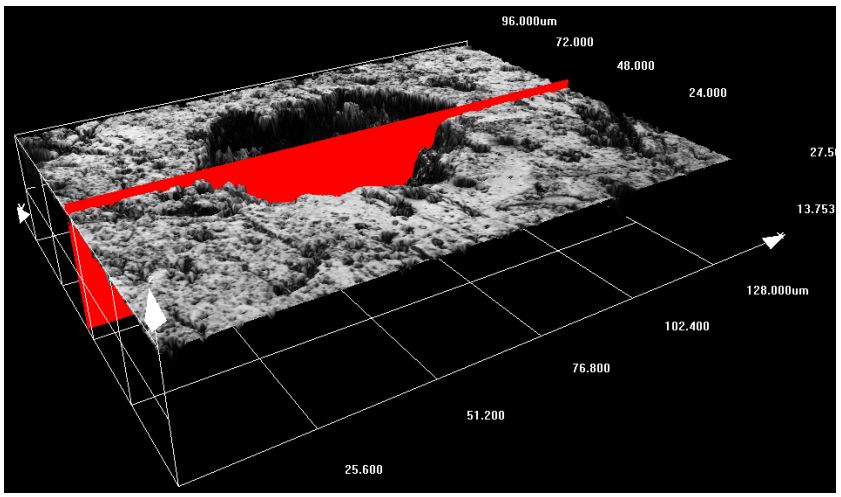

(b)

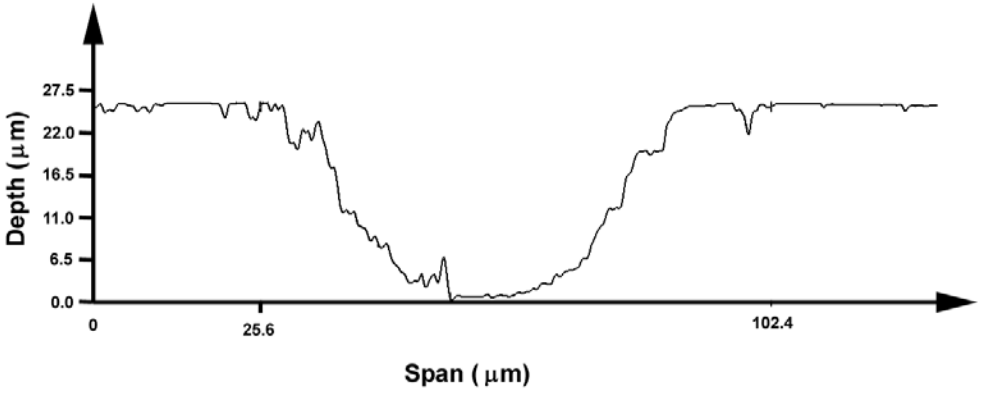

(c)

Figure 4-3.6.7 Crevice attack under lacquer on a selected area on untreated AISI 316 sample surface (detail marked in Figure 4-3.6.6). Laser confocal microscopy (a) in height 3-D mode, (b) in intensity 3-D mode and (c) profile of section cut by the red plane in image (a)

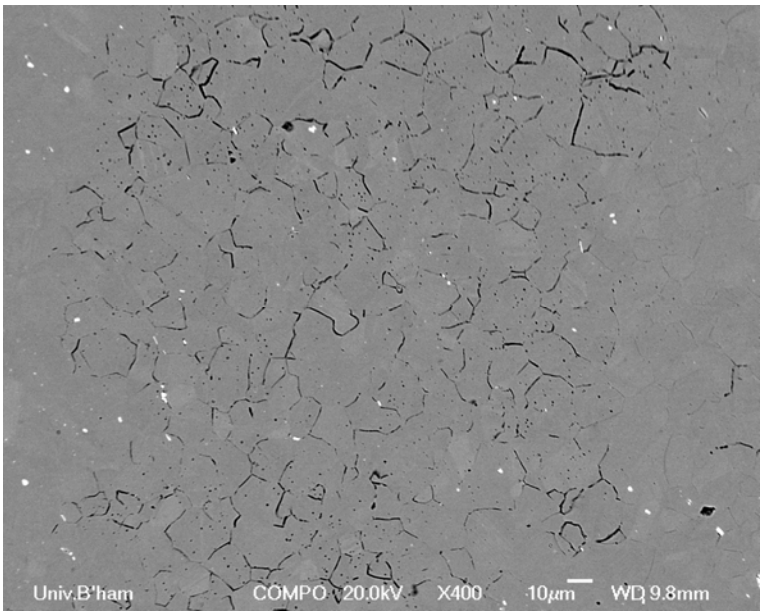

Figure 4-3.6.8 Intergranular corrosion on carbonitrided at 430°C ASTM F1586 sample (NNC430). Electrochemical testing in full strength Ringer's solution at 37°C

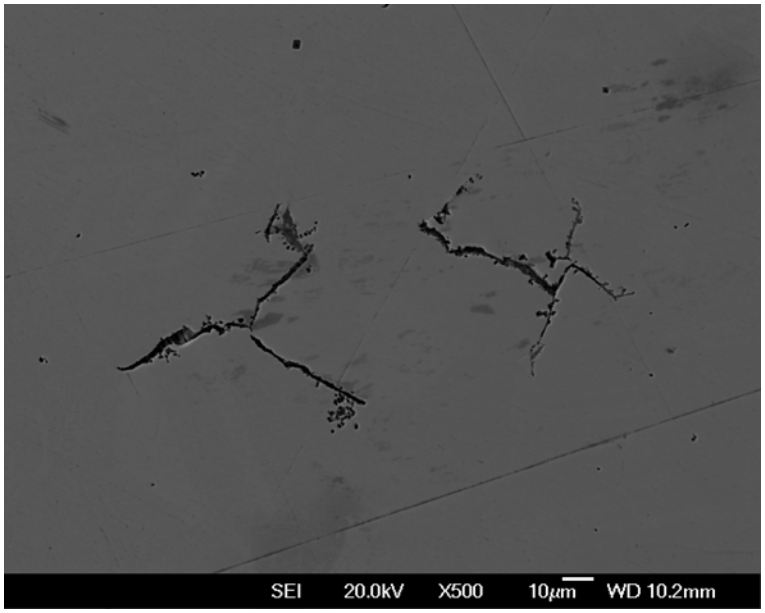

Figure 4-3.6.9 Intergranular corrosion on nitrided at 430°C ASTM F2581 sample (FN430). Electrochemical testing in full strength Ringer's Solution at 37°C.

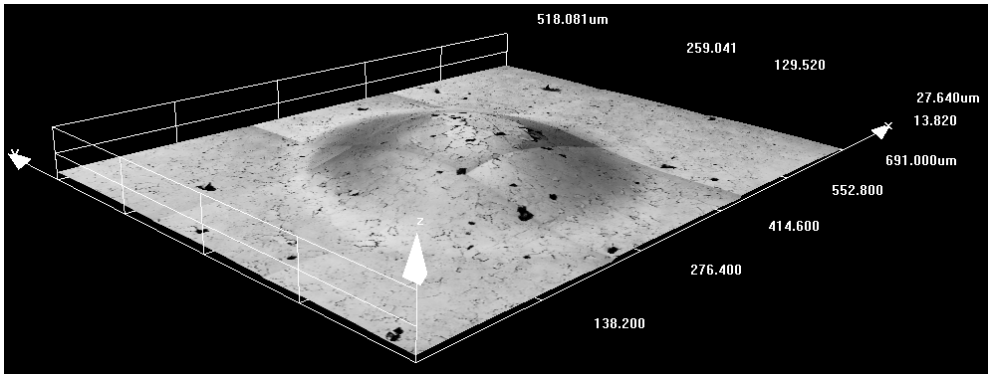

Figure 4-3.7.1 (a) Laser confocal microscope image (3-D intensity mode) of sensitization, grain pullout and layer bulging on ASTM F1586 sample carbo-nitrided at 430°C (NNC430). Crevice corrosion immersion test.

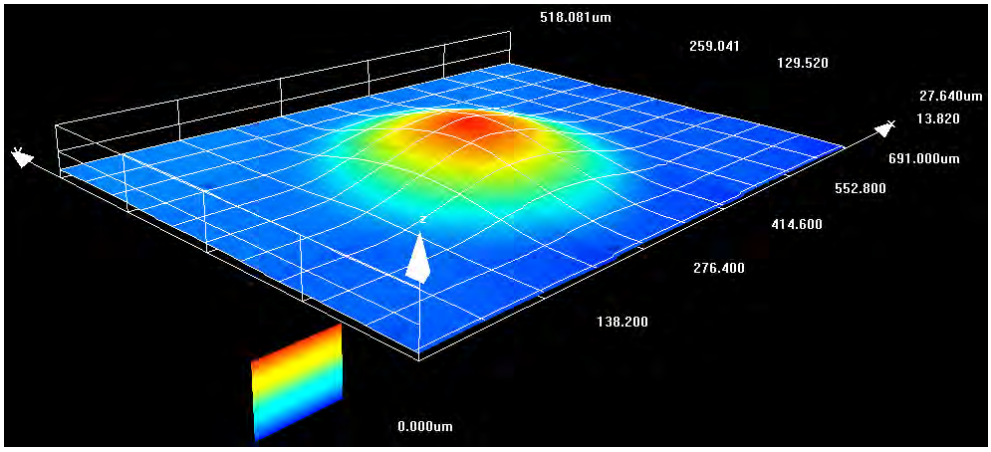

Figure 4-3.7.1 (b) Laser confocal microscope image (3-D height mode) of Figure 4-3.7.1 (b) showing layer bulging

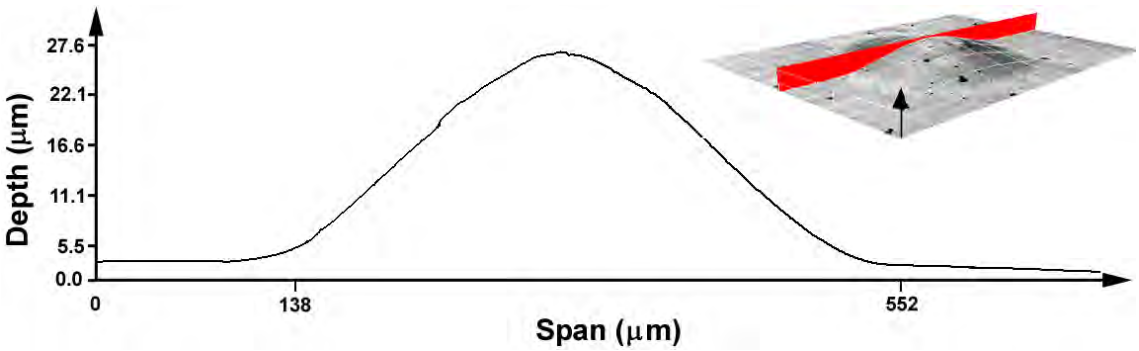

Figure 4-3.7.1 (c) Profile of bulge shown in Figure 4-3.7.1 (a). This profile was created by the intersecting plane (red) shown in the inset image

Figure 4-3.7.1 (d) Zoomed in laser confocal microscope detail (2-D intensity mode) from Figure 4-3.7.1 (a) showing grain pullout.

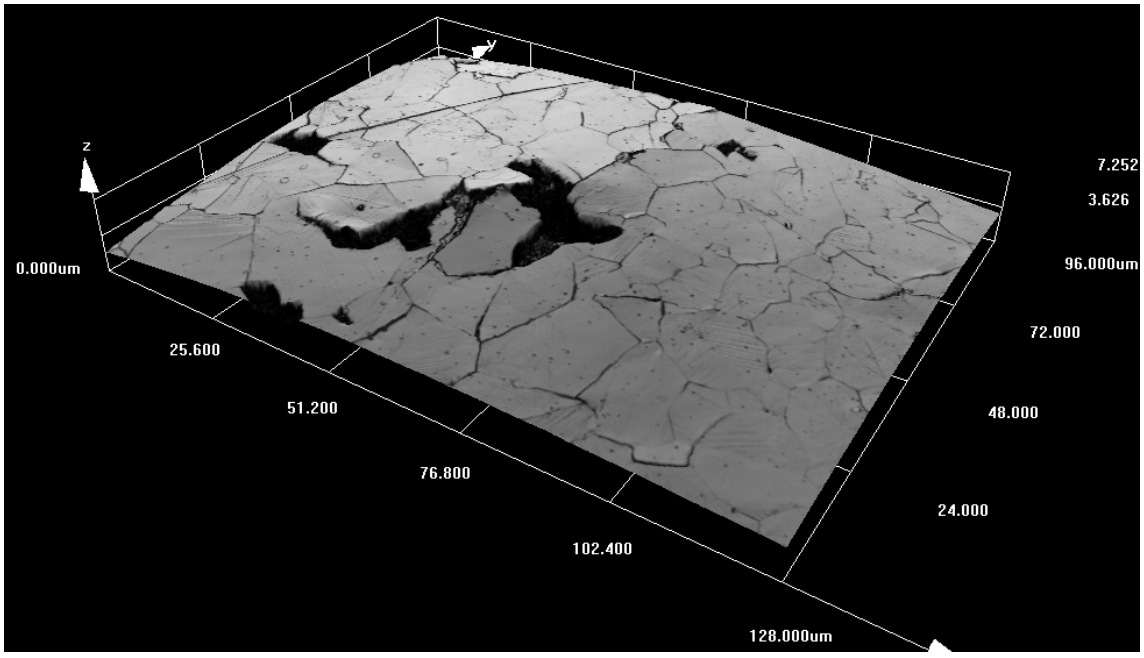

Figure 4-3.7.1 (e) 3-D intensity mode laser confocal microscope image of Figure 4-3.7.1 (d)

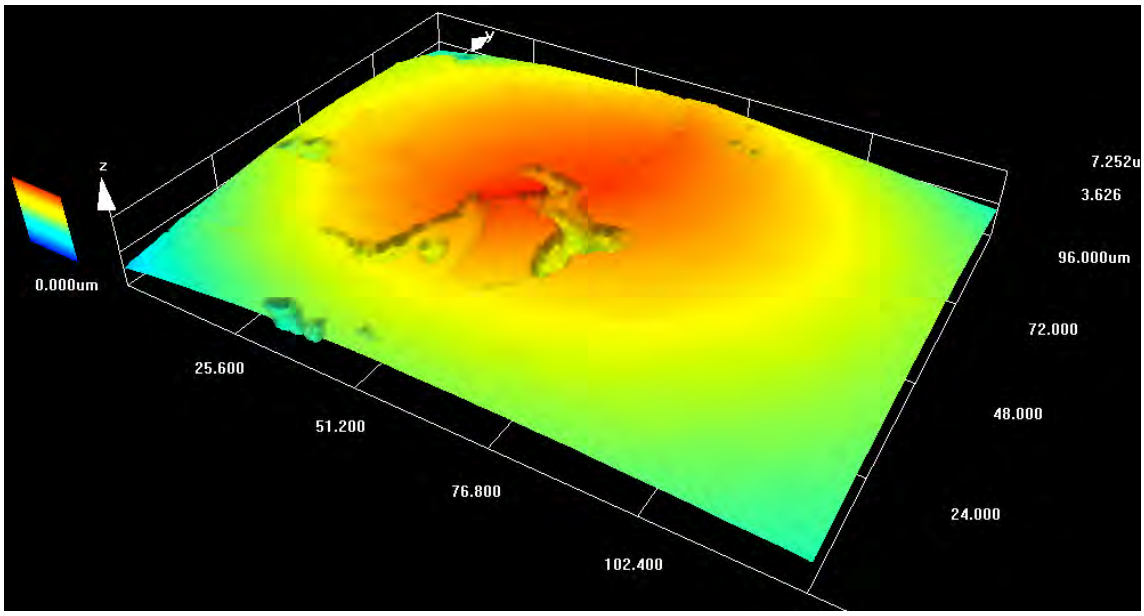

Figure 4-3.7.1 (f) 3-D height mode laser confocal microscope image of Figure 4-3.7.1 (d)

Figure 4-3.7.2 Cross-Section micrograph (polished) of ASTM F1586 sample carbo-nitrided at 430°C (NN430) after crevice corrosion immersion test

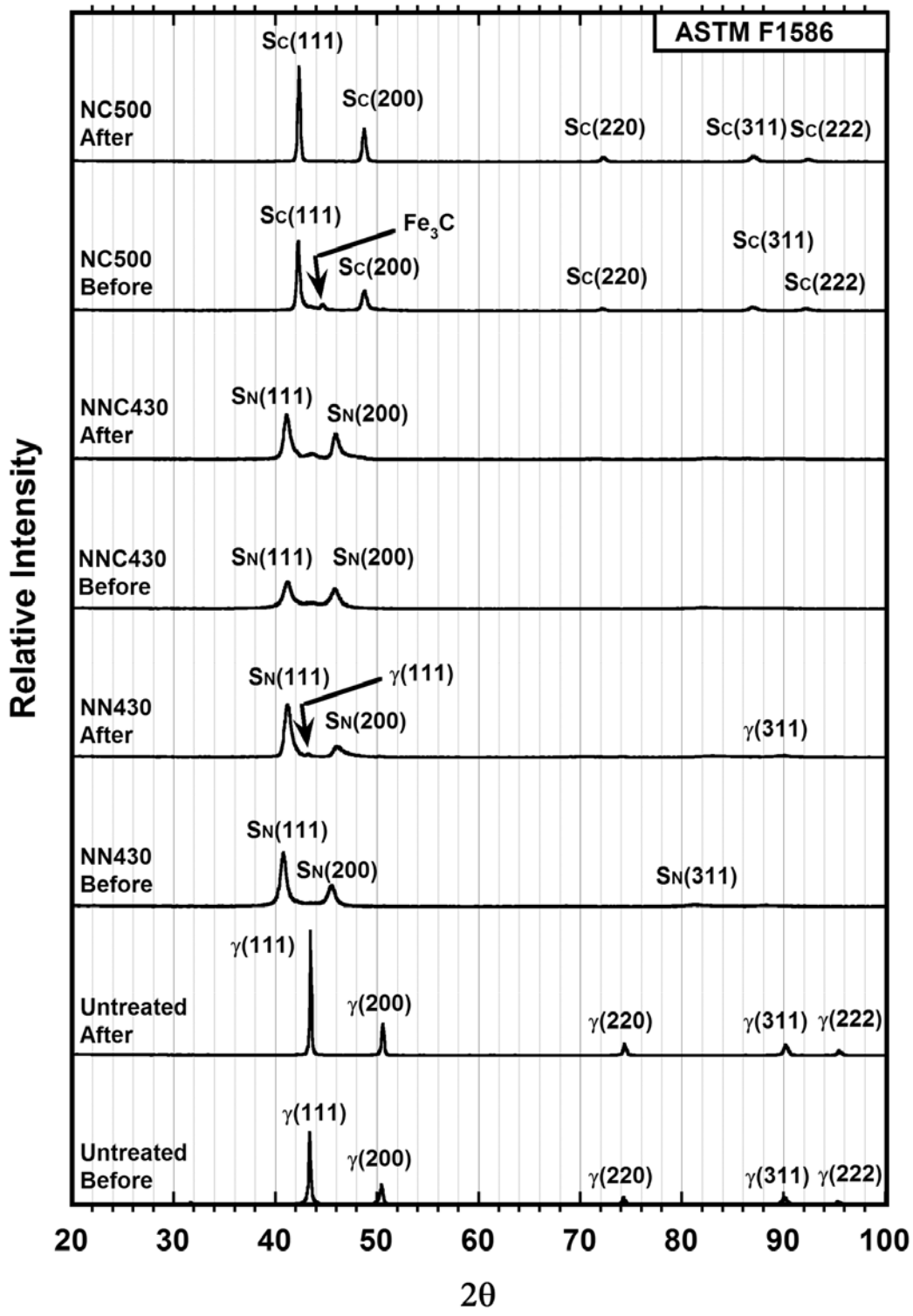

Figure 4-3.7.3 XRD profiles on treated and untreated ASTM F1586 samples before and after the crevice corrosion immersion test.

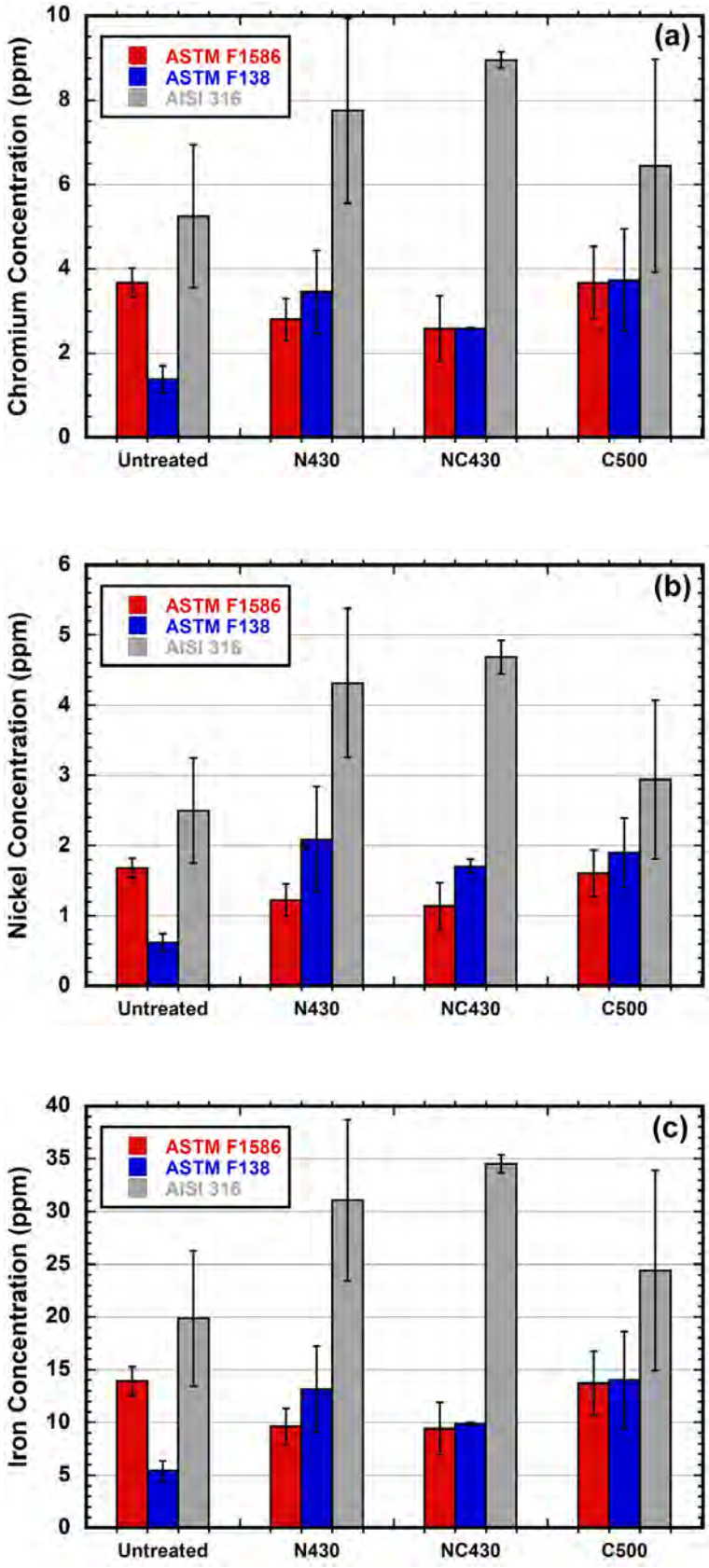

Figure 4-3.7.4 Ion concentrations – (a) chromium, (b) nickel and (c) iron – in the solution after the crevice corrosion immersion test.
Error: Deviation from the mean of 2 values

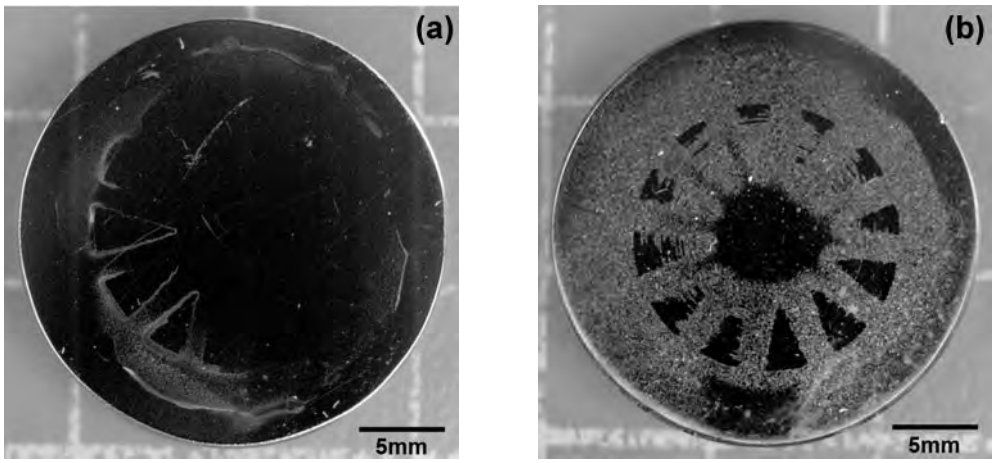

Figure 4-3.7.5 Macrographs of corroded ASTM F138: Untreated (MU) (a) and carbonitrided at 430°C (MNC430) (b)

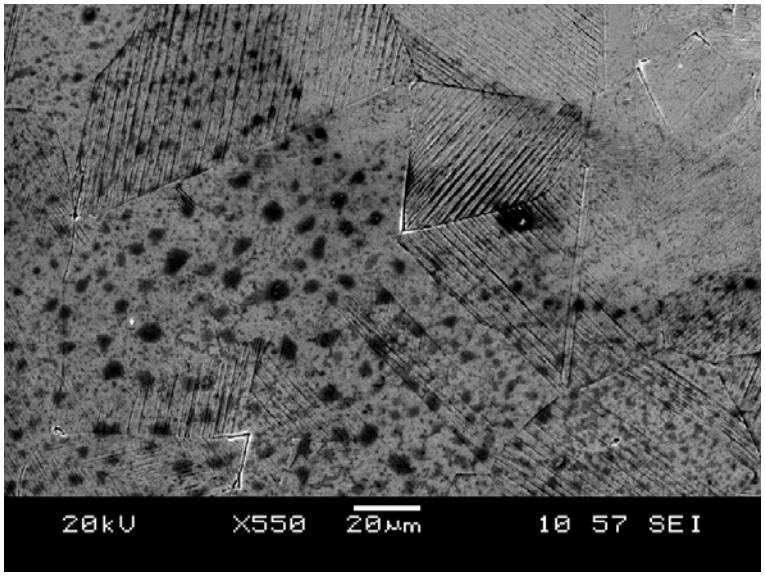

Figure 4-3.7.6 Corrosion morphology on carbonitrided ASTM F138 sample at 430°C (MNC430)

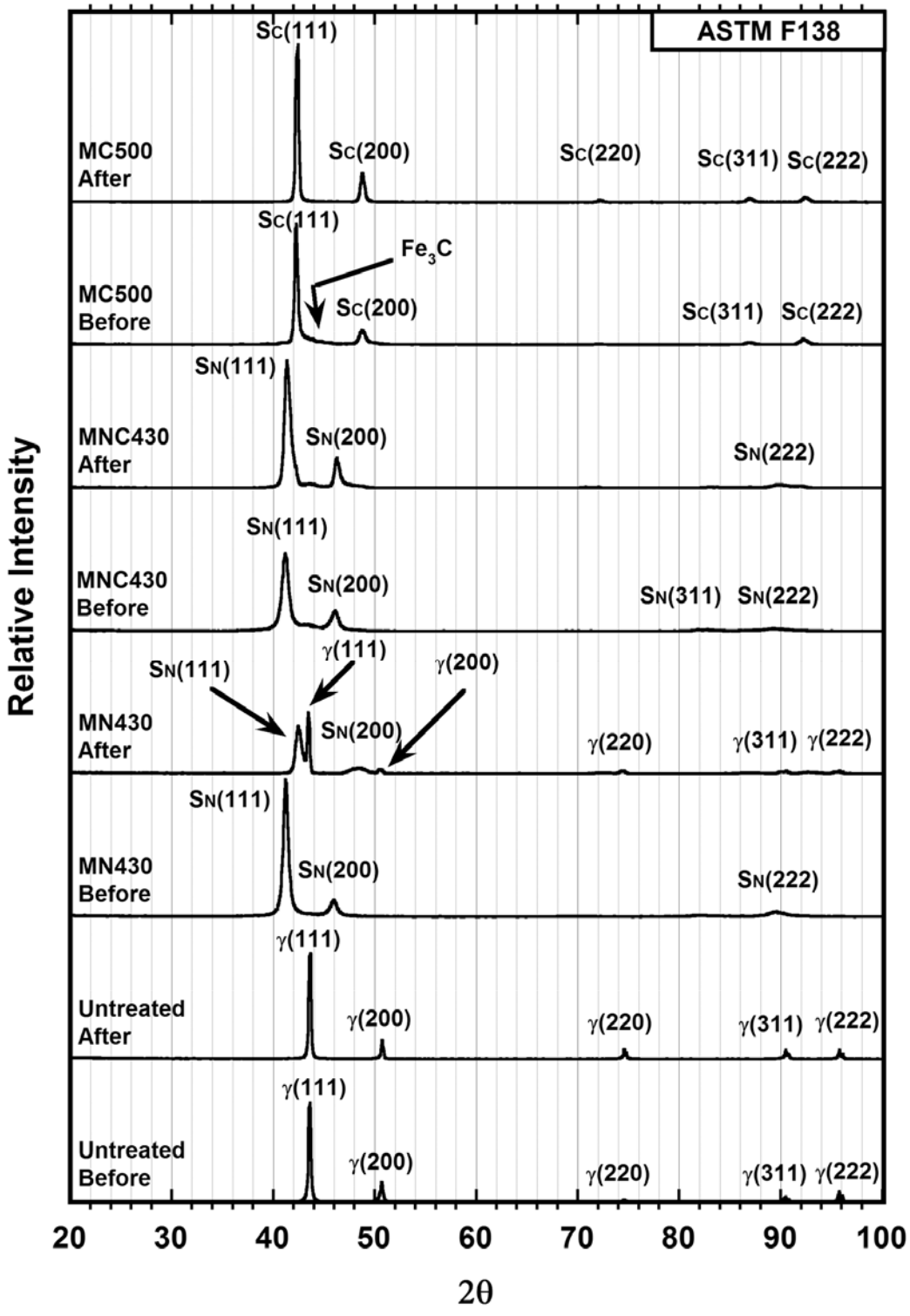

Figure 4-3.7.7 – XRD profiles on treated and untreated ASTM F138 samples before and after the crevice corrosion immersion test.

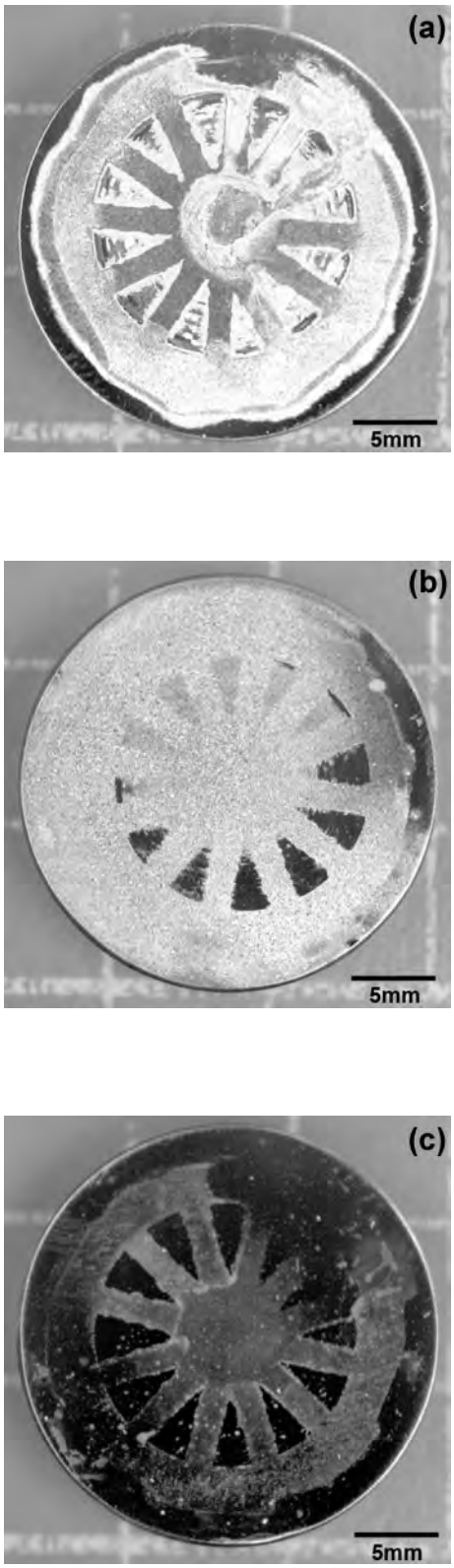

Figure 4-3.7.8 Macrographs of corroded AISI 316: untreated (GU) (a) carbonitrided at 430°C (GNC430) (b) and carburised at 500°C (GC500) (c)

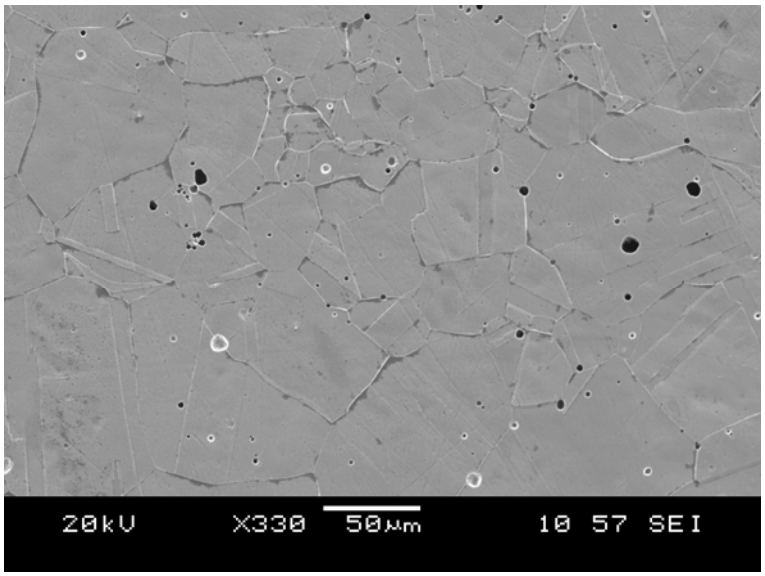

(a)

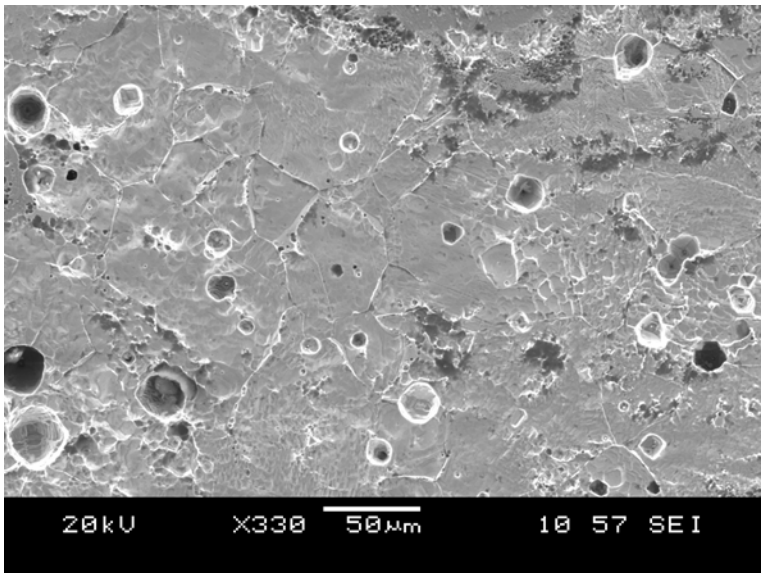

(b)

Figure 4-3.7.9 Untreated AISI 316 (GU): corrosion at exposed area (a) and under crevice former (b)

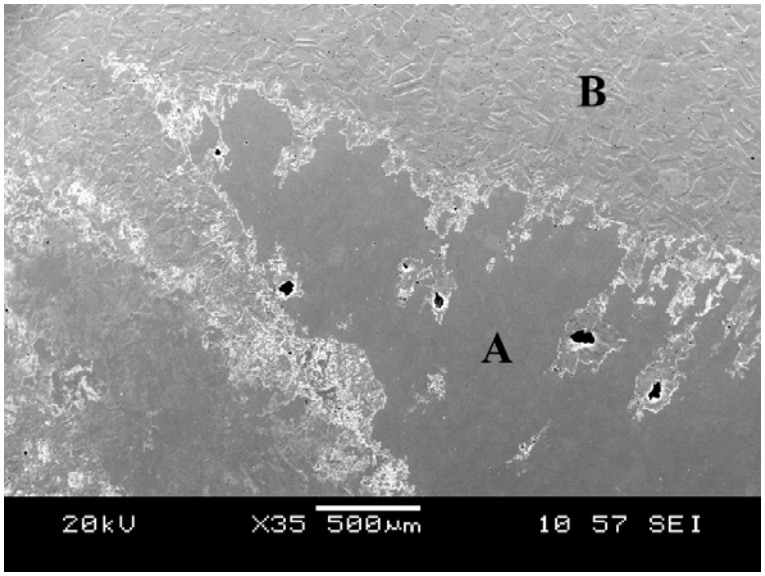

(a)

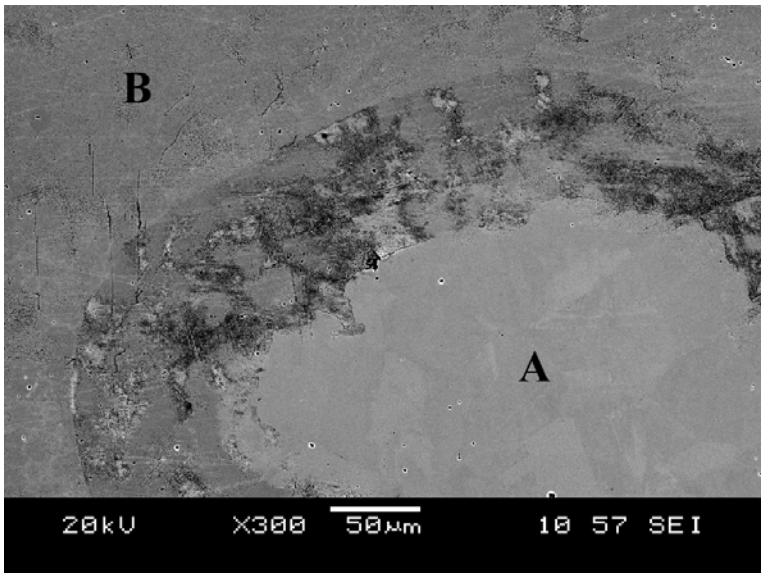

(b)

Figure 4-3.7.10 Corrosion under crevice former (marked A) and at exposed area (marked B) for 430°C nitrided (GN430) (a) and 500°C carburised (GC500) (b) AISI 316 samples.

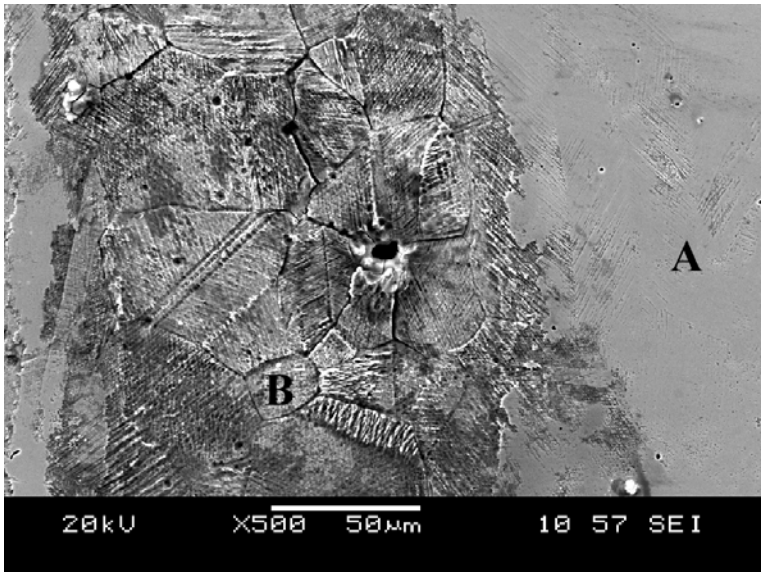

(a)

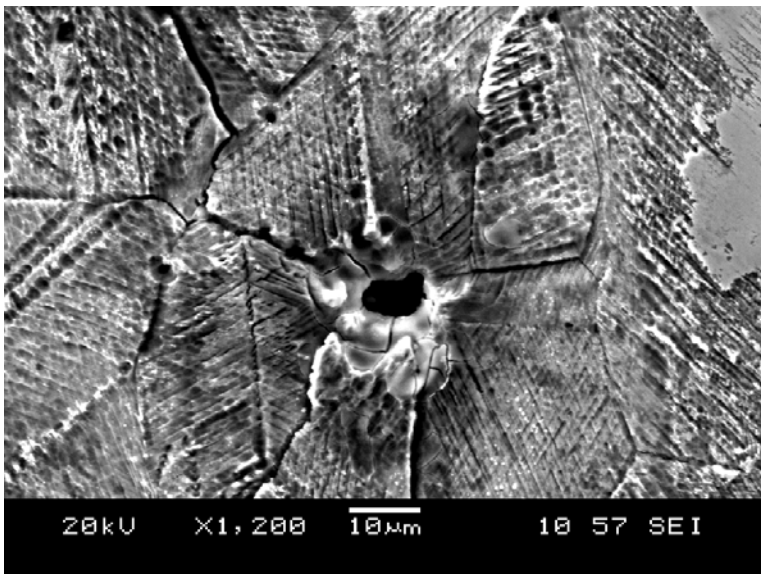

(b)

Figure 4-3.7.11 Corrosion under crevice former (marked A) and at exposed area (marked B) at low (a) and high (b) magnifications for 430°C carbonitrided AISI 316 sample (GNC430).

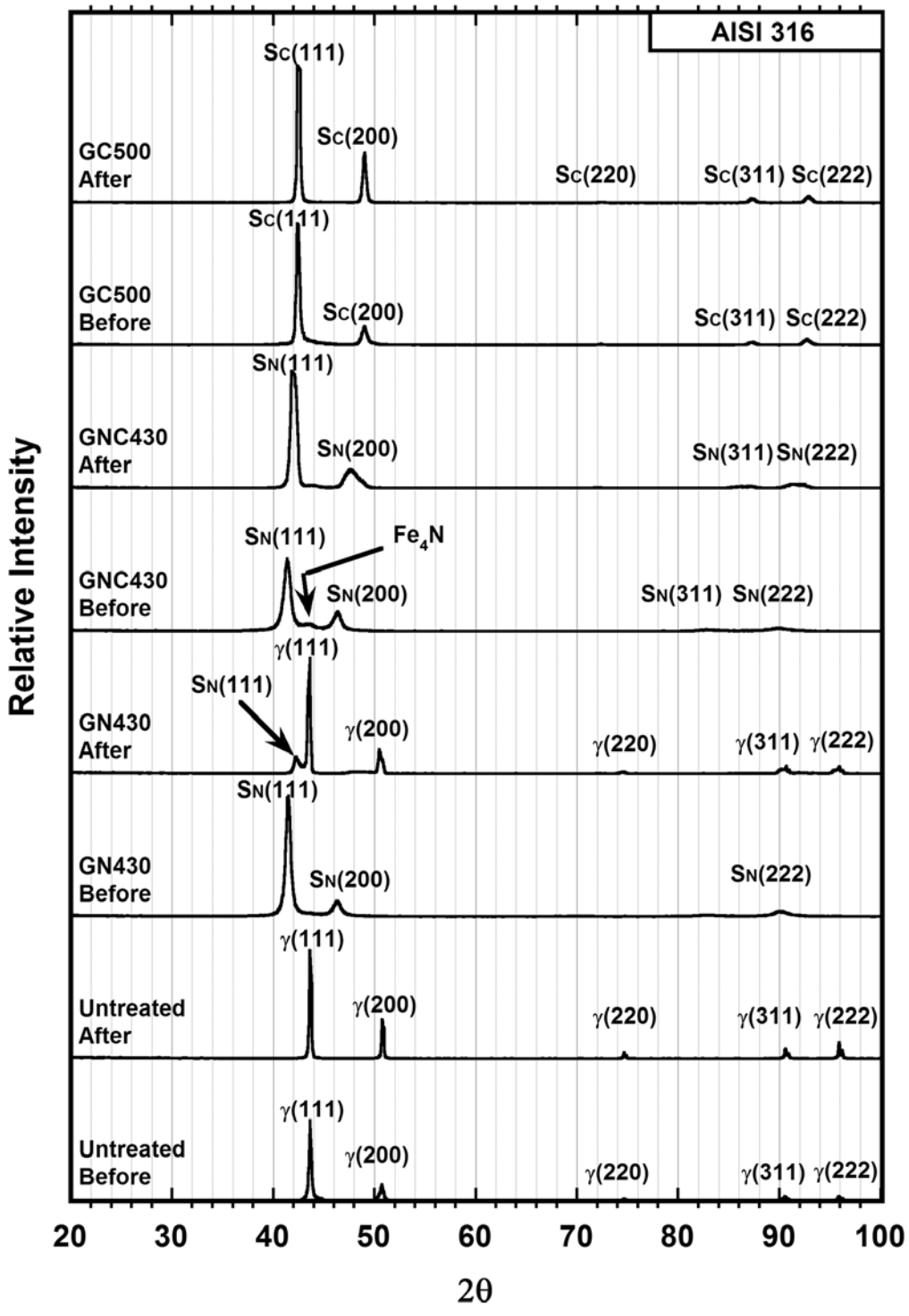

Figure 4-3.7.12 XRD profiles on treated and untreated AISI 316 samples before and after the crevice corrosion immersion test

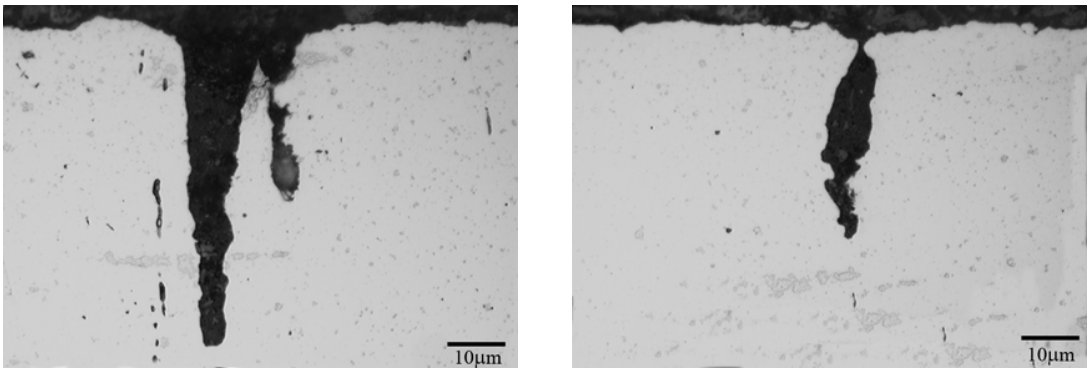

Figure 4-3.7.13 Cross-section micrograph (polished) of untreated AISI 316 (GU) showing pitting after crevice corrosion immersion test

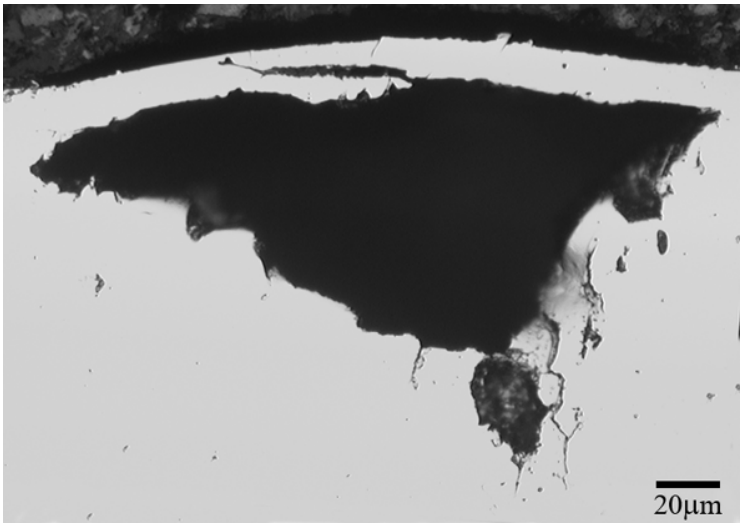

Figure 4-3.7.14 Cross-section micrograph (polished) of carbonitrided AISI 316 at 430°C (GNC430) showing bulging and corrosion under the layer after crevice corrosion immersion test

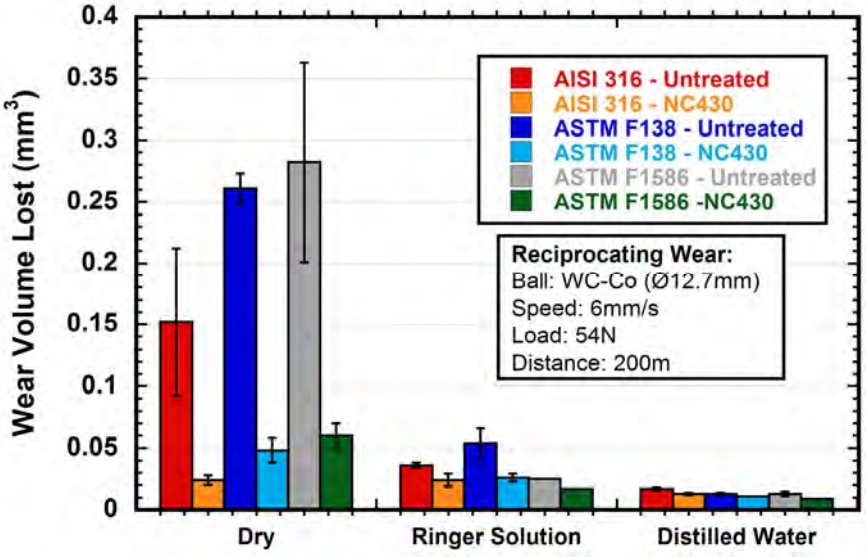

Figure 4-3.8.1 Wear volume lost in reciprocating wear using three different test conditions: air (dry), Ringer's solution and distilled water
Error: Deviation from the mean of 2 values

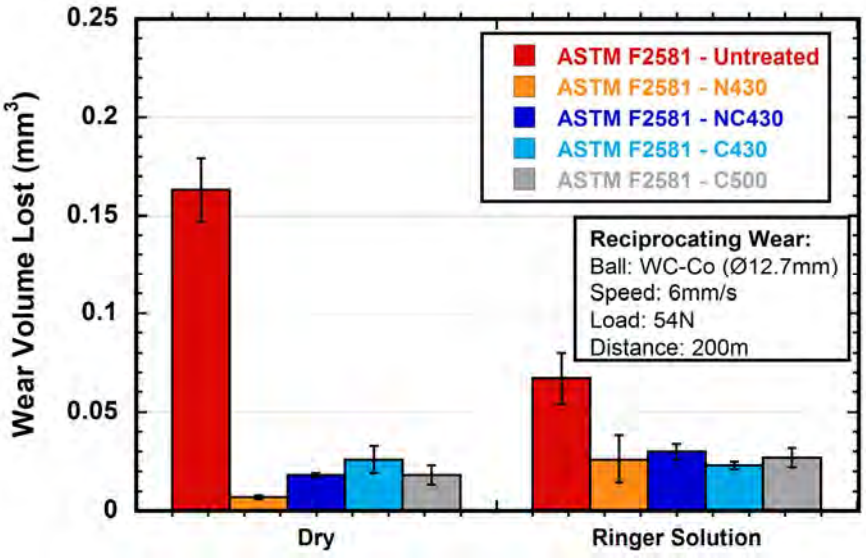

Figure 4-3.8.2 Wear volume lost during reciprocating wear on treated and untreated ASTM F2581 in two different test conditions: air (dry) and Ringer's solution
Error: Standard deviation of 6 values

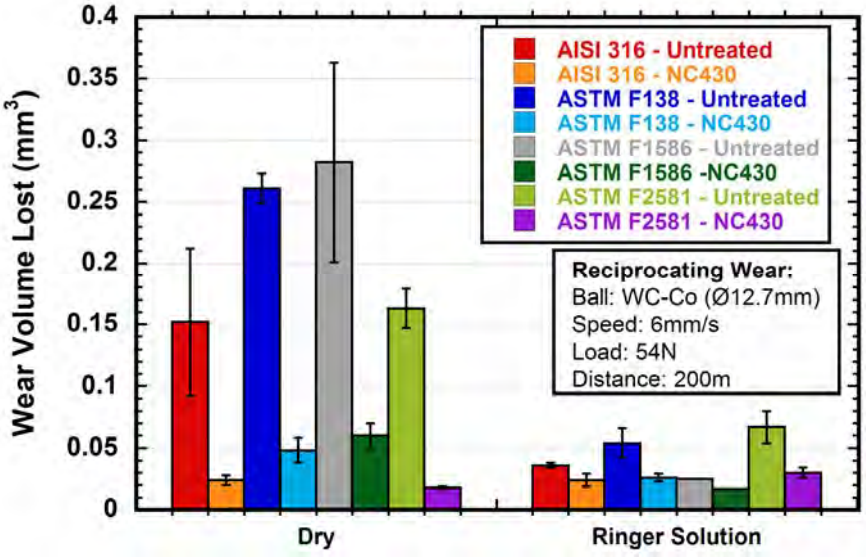

Figure 4-3.8.3 Wear volume lost during reciprocating wear: A comparison of all tested materials
Error for ASTM F2581: Standard deviation of 6 values
Error for other materials: Deviation from the mean of 2 values

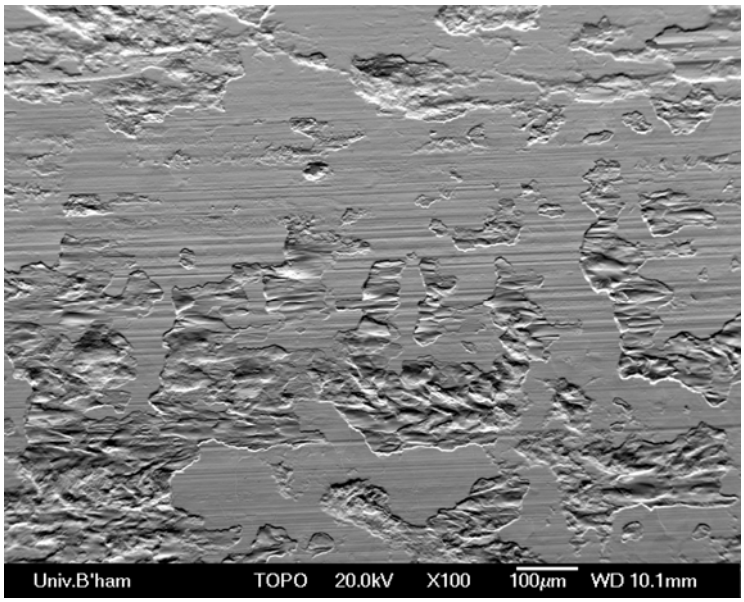

(a)

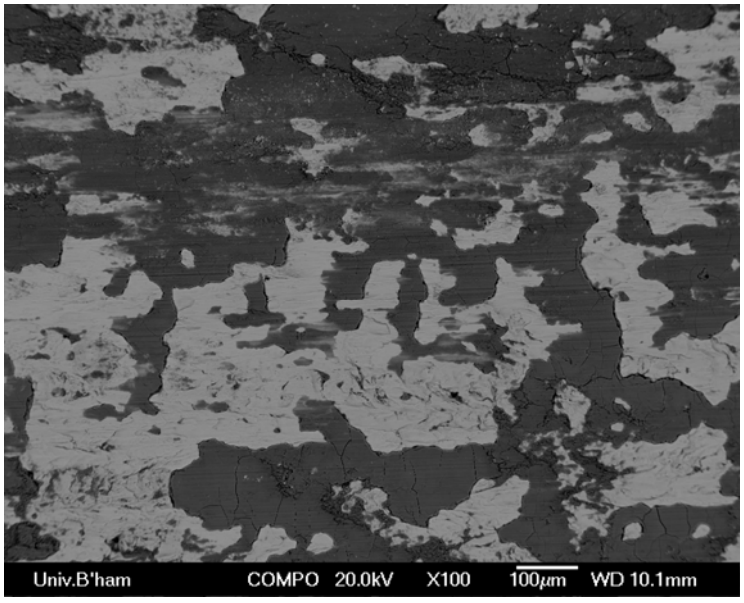

(b)

Figure 4-3.8.4 Back scattered SEM images in topography (a) and composition (b) mode of the centre part of wear track of untreated ASTM F138 (MU) against WC-cobalt sphere (dry condition)

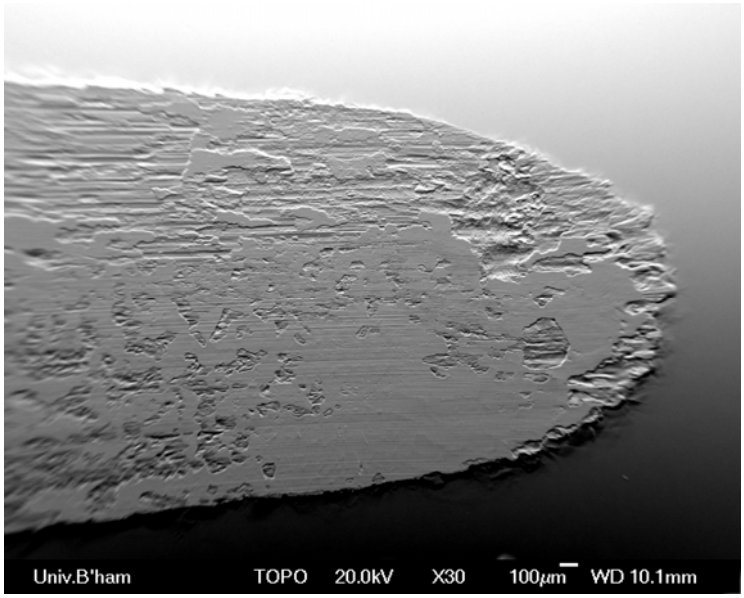

(a)

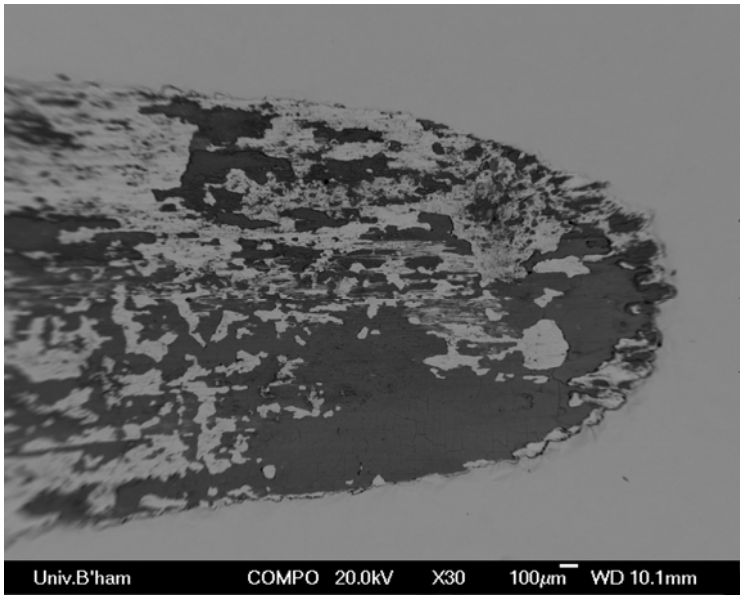

(b)

Figure 4-3.8.5 Back scattered SEM images in topography (a) and composition (b) mode of the edge part of the wear track of untreated ASTM F138 (MU) against WC-cobalt sphere (dry condition)

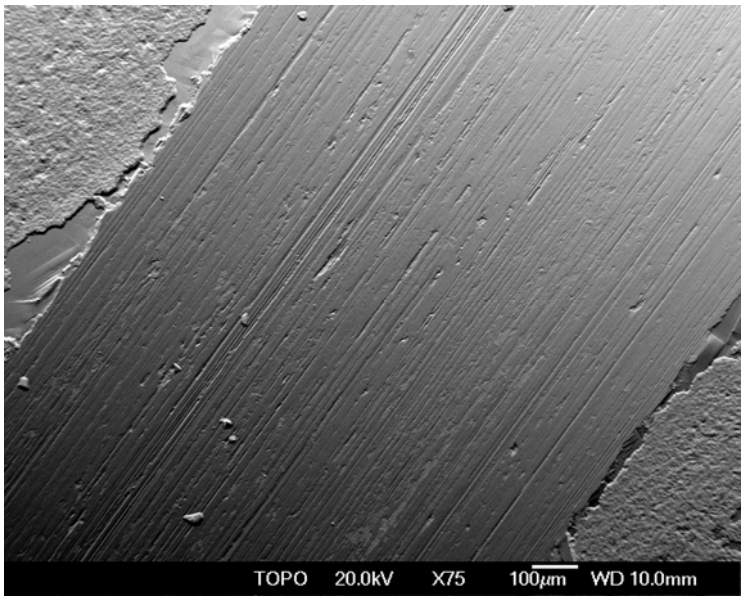

(a)

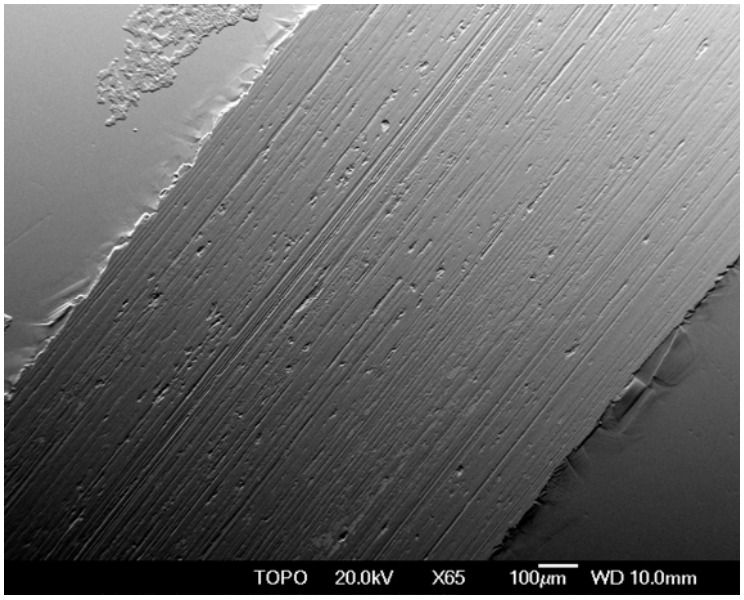

(b)

Figure 4-3.8.6 Back scattered SEM images in topography mode of (a) un-cleaned and (b) cleaned wear track on untreated ASTM F138 (MU) against WC-cobalt sphere (Ringer's solution)

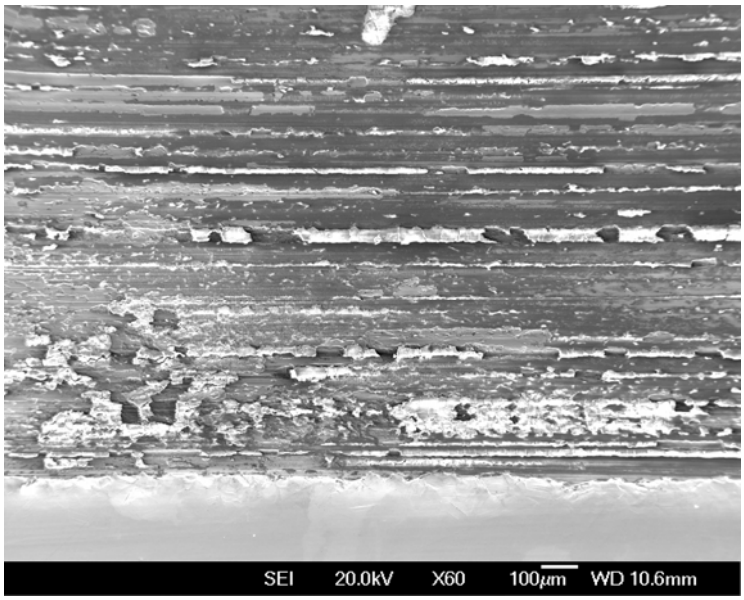

(a)

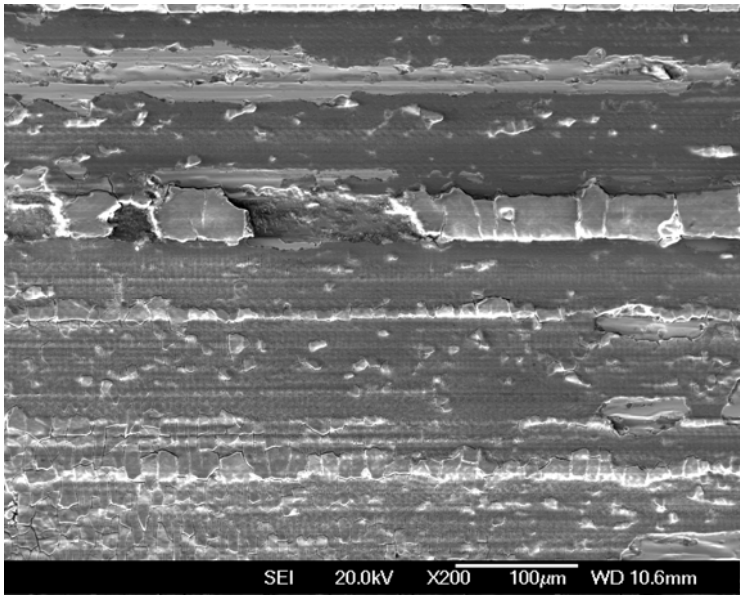

(b)

Figure 4-3.8.7 SEI SEM images of wear track, at (a) low and (b) high magnifications, on untreated ASTM F2581 (FU) against WC-Cobalt ball in dry conditions

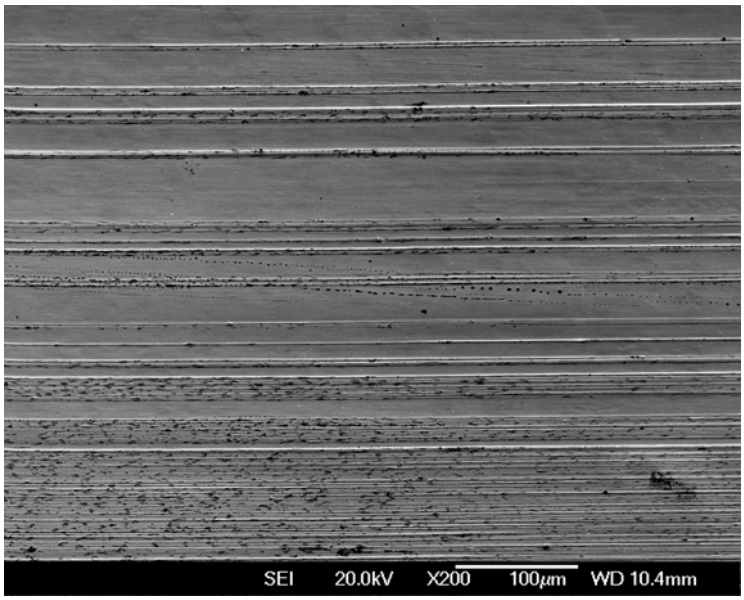

(a)

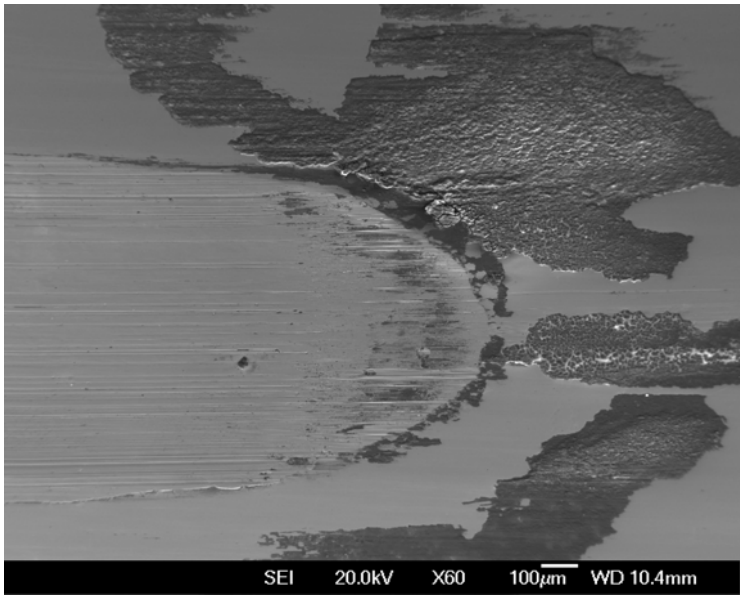

(b)

Figure 4-3.8.8 SEI SEM images of (a) edge and (b) centre of wear track on untreated ASTM F2581 (FU) against WC-Cobalt ball in Ringer's solution

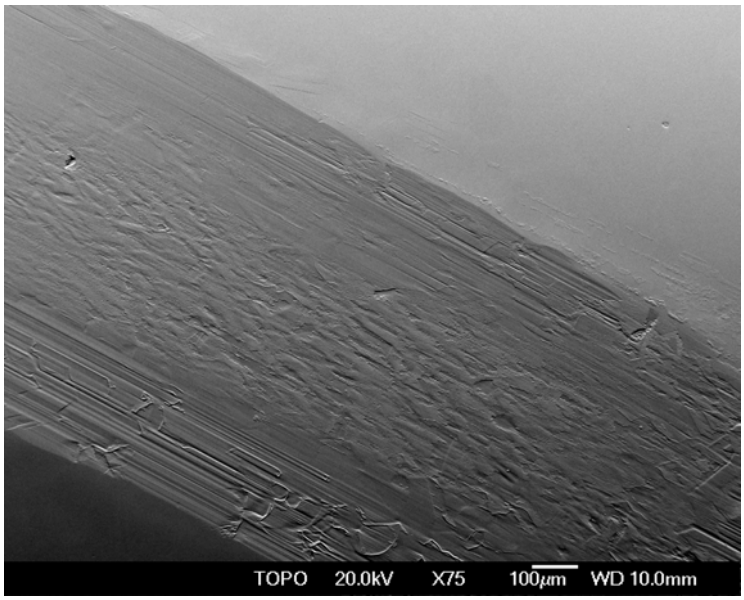

Figure 4-3.8.9 Back scattered SEM image in topography mode of wear track on 430°C carbonitrided ASTM F138 (MNC430) in Ringer's solution

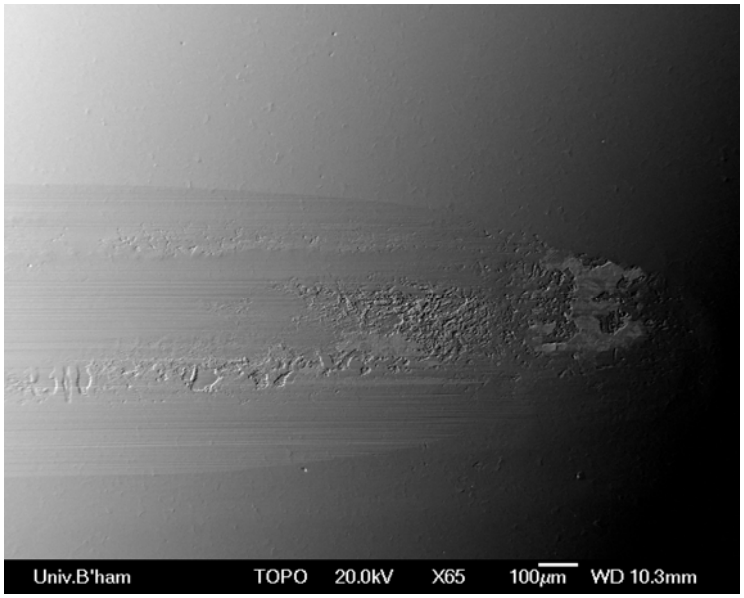

Figure 4-3.8.10 (a) Back scattered SEM image in topography mode of wear track on 430°C carbonitrided ASTM F1586 (NNC430) in Ringer's solution

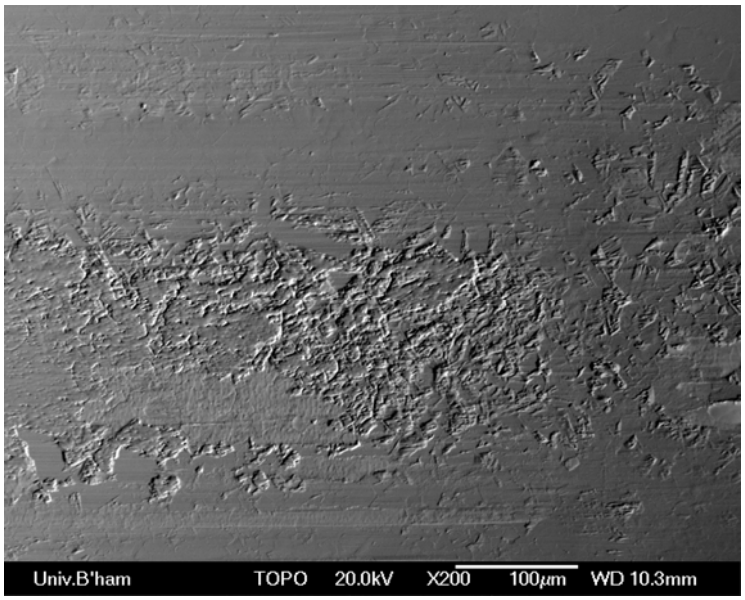

Figure 4-3.8.10 (b) Back scattered SEM image in topography mode of wear track on 430°C carbonitrided ASTM F1586 (NNC430) in Ringer's solution

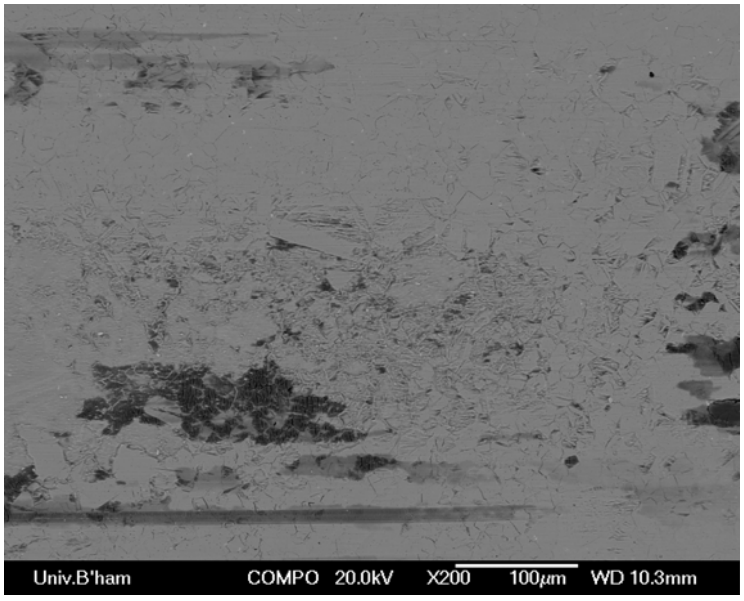

Figure 4-3.8.10 (c) Back scattered SEM image in composition mode of wear track on 430°C carbonitrided ASTM F1586 (NNC430) in Ringer's solution

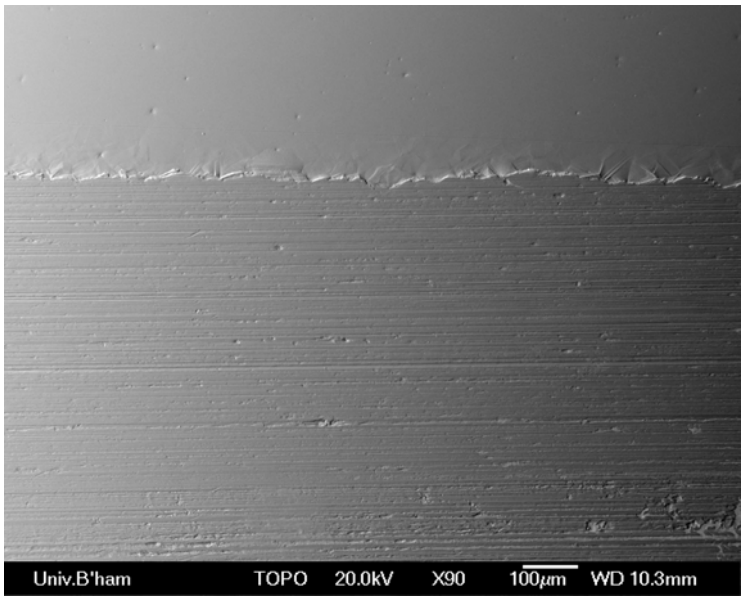

(a)

(b)

Figure 4-3.8.11 Back Scattered SEM images in (a) topography and (b) composition mode of wear track on 430°C carbonitrided AISI 316 (GNC430) in Ringer's solution

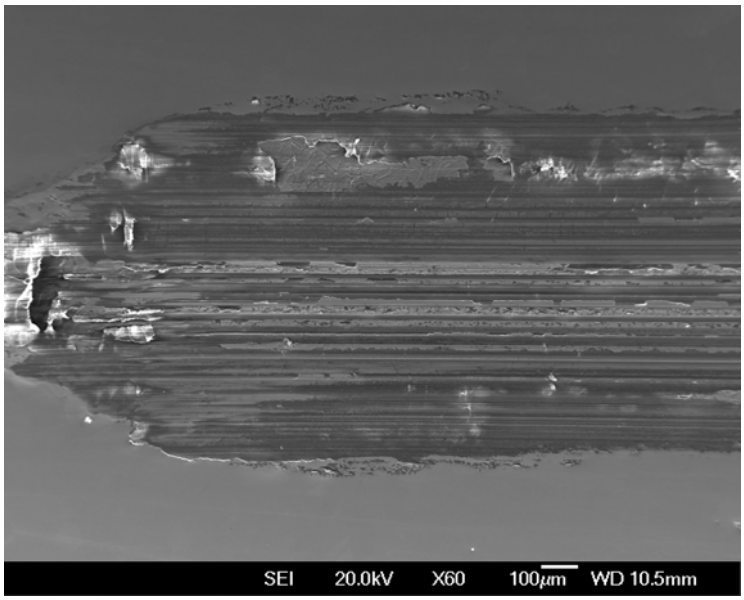

(a)

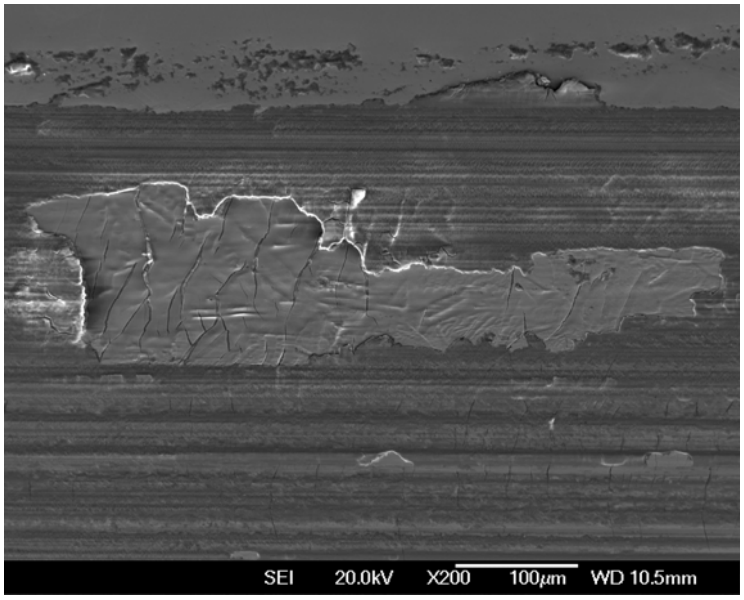

(b)

Figure 4-3.8.12 Secondary electrons SEM images of wear track at (a) low and (b) high magnifications on 430°C carbonitrided ASTM F2581 (FNC430) in dry conditions

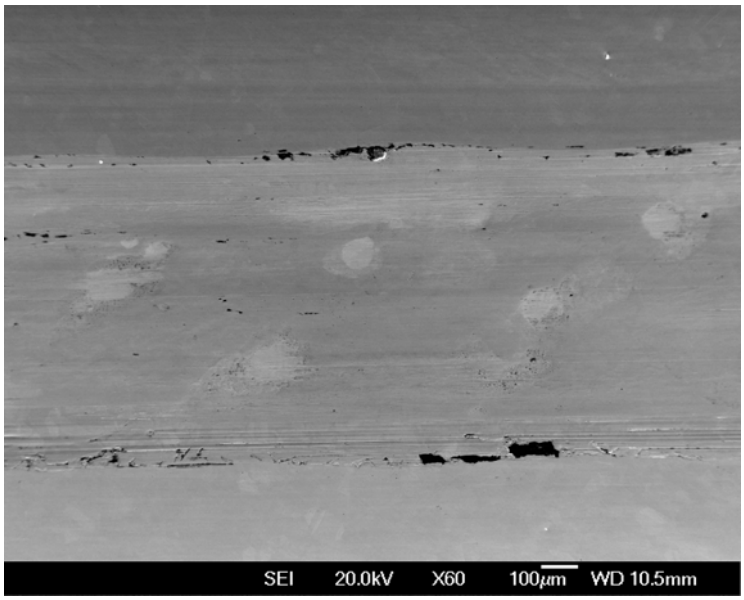

(a)

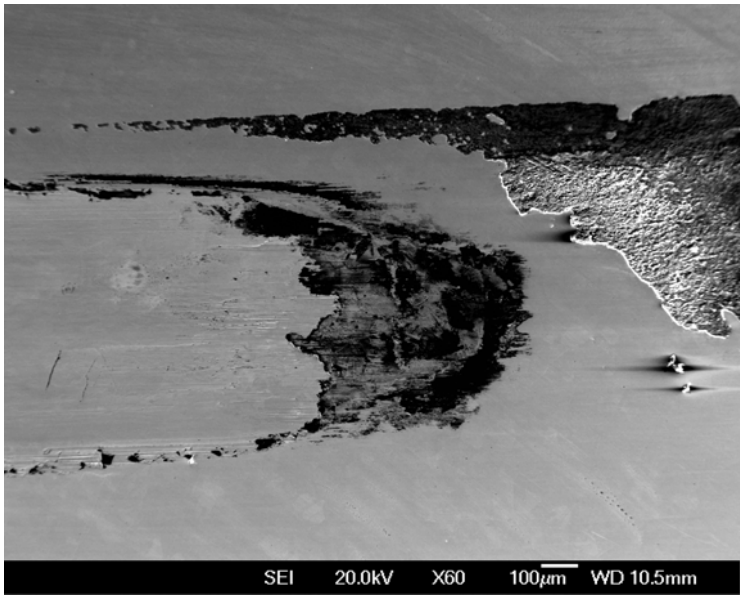

(b)

Figure 4-3.8.13 Secondary electrons SEM images at the (a) middle and (b) end of the wear track on 430°C carbonitrided ASTM F2581 (FNC430) in Ringer's solution

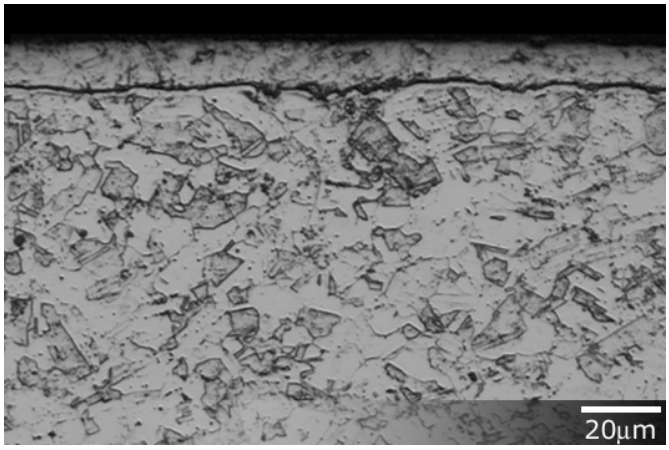

(a)

(b)

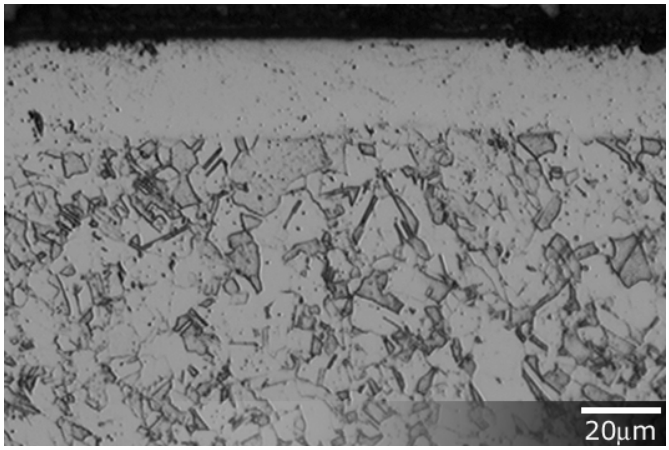

(c)

Figure 4-3.9.1 S-Phase Layers created on AISI 316 spheres by (a) nitriding at 430°C (N430), carbonitriding at 430°C (NC430) and (c) carburising at 500°C (C500)

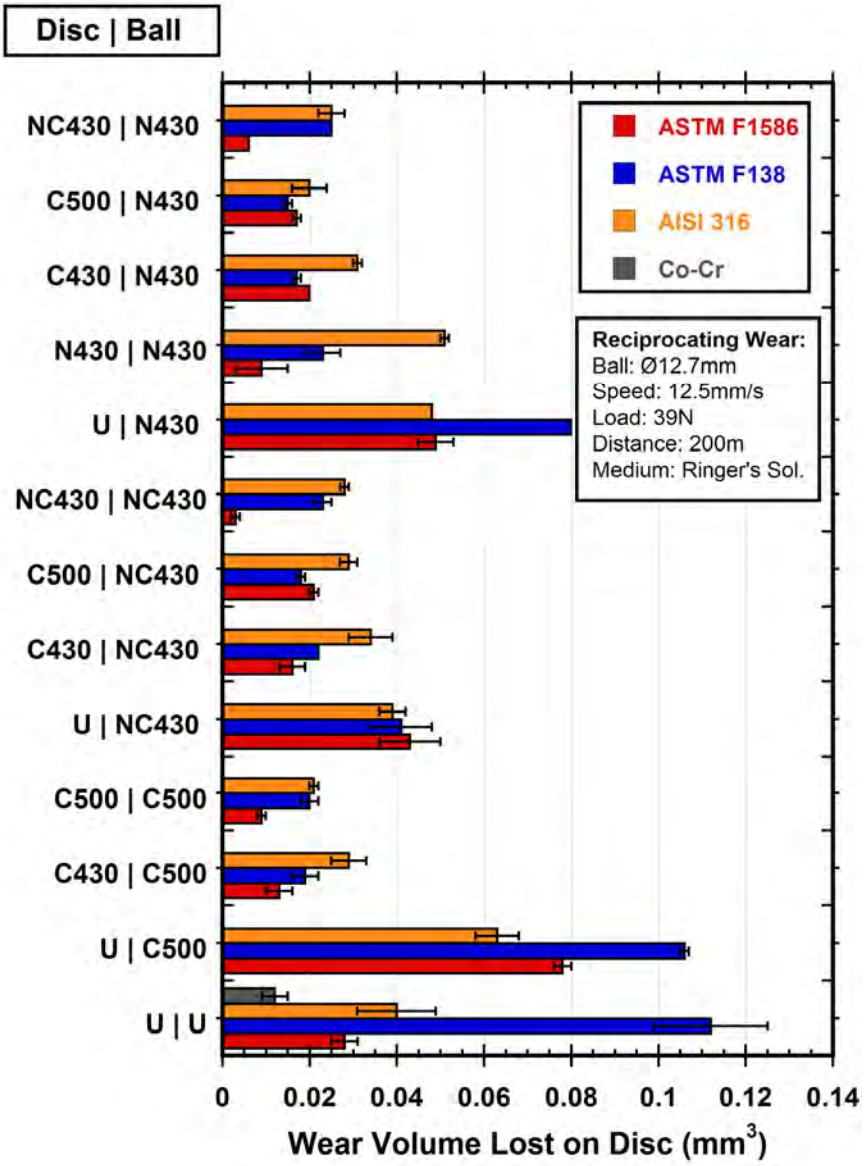

Figure 4-3.9.2 (a) Wear volume loss of disc after reciprocating wear tests in Ringer's solution
Error: Deviation from mean of 2 values

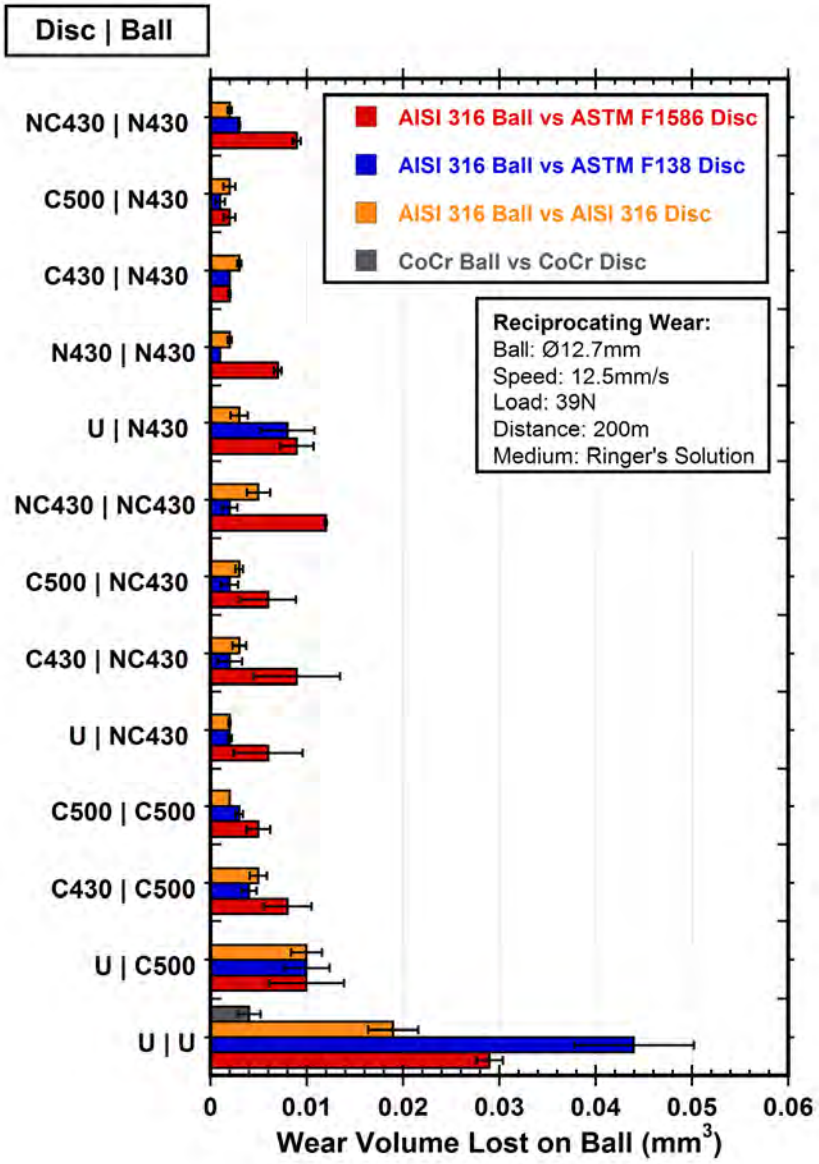

Figure 4-3.9.2 (b) Wear volume loss of spheres after reciprocating wear tests in Ringer's solution.
Error: Deviation from mean of 2 values

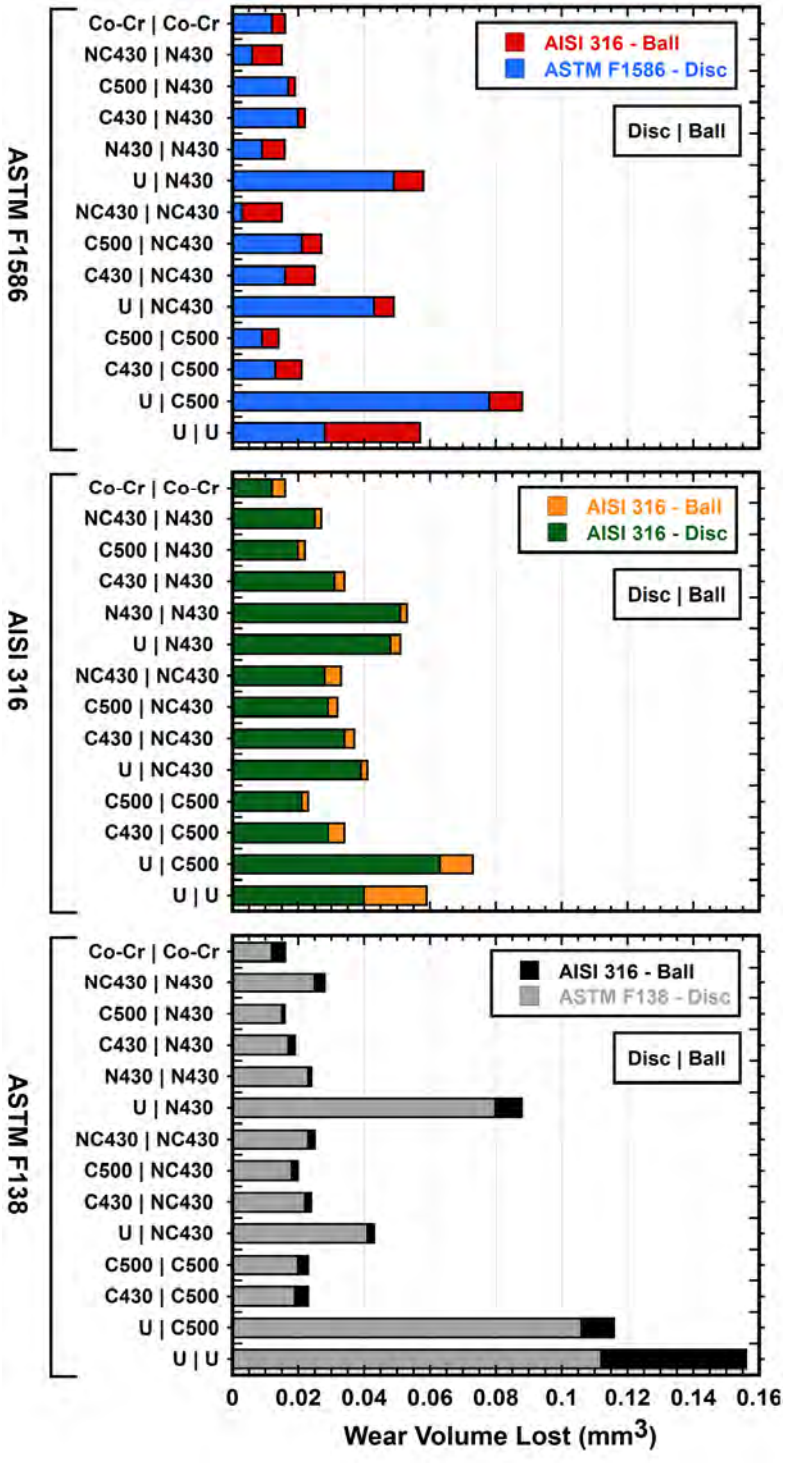

Figure 4-3.9.3 Combined wear volume loss of both discs and spheres after reciprocating wear tests in Ringer's solution

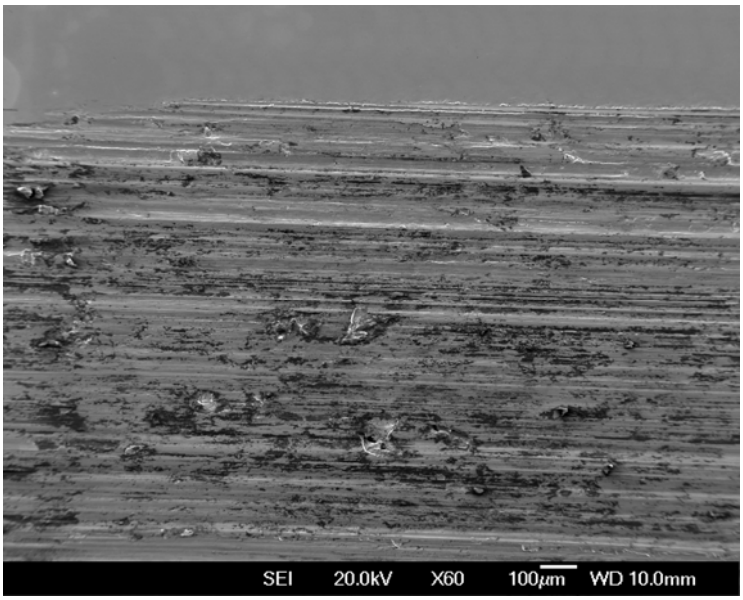

(a)

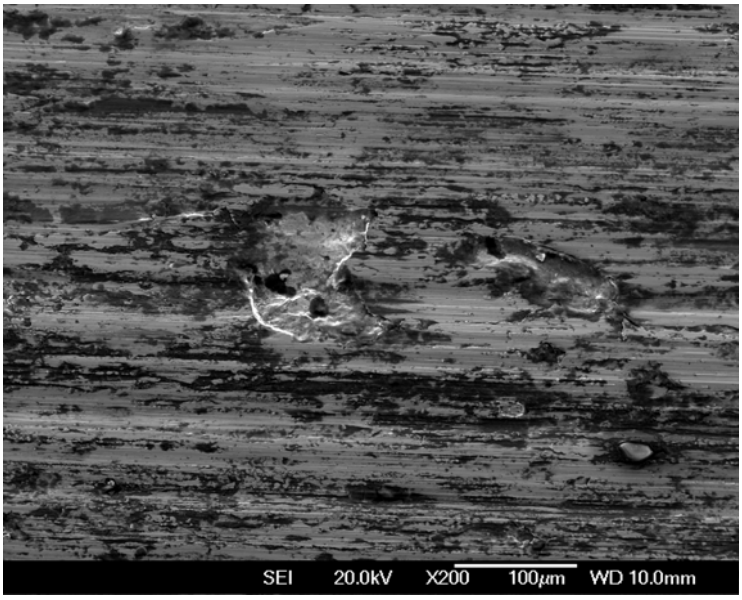

(b)

Figure 4-3.9.4 SEI SEM images at (a) low (b) high magnifications of wear track on disc. Reciprocating wear testing in Ringer's Solution of untreated AISI 316 sphere versus untreated ASTM 1586 (NU) disc.

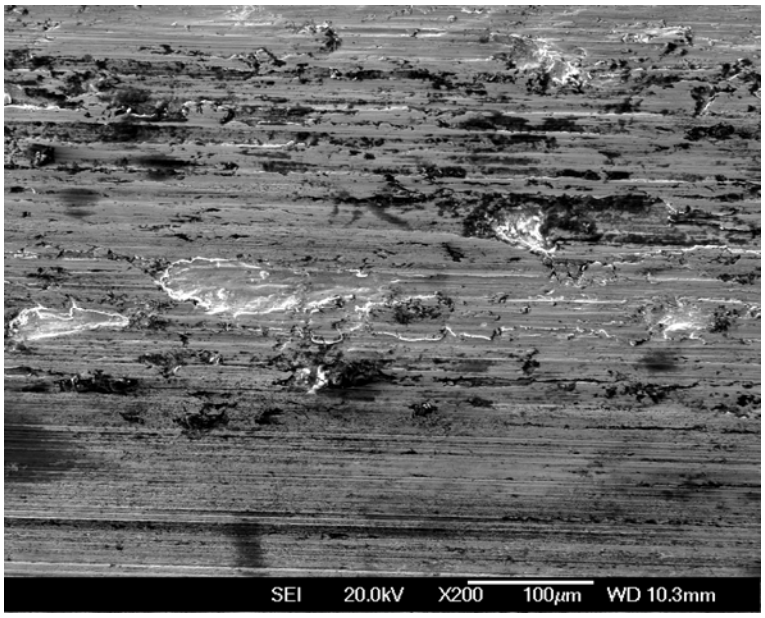

(a)

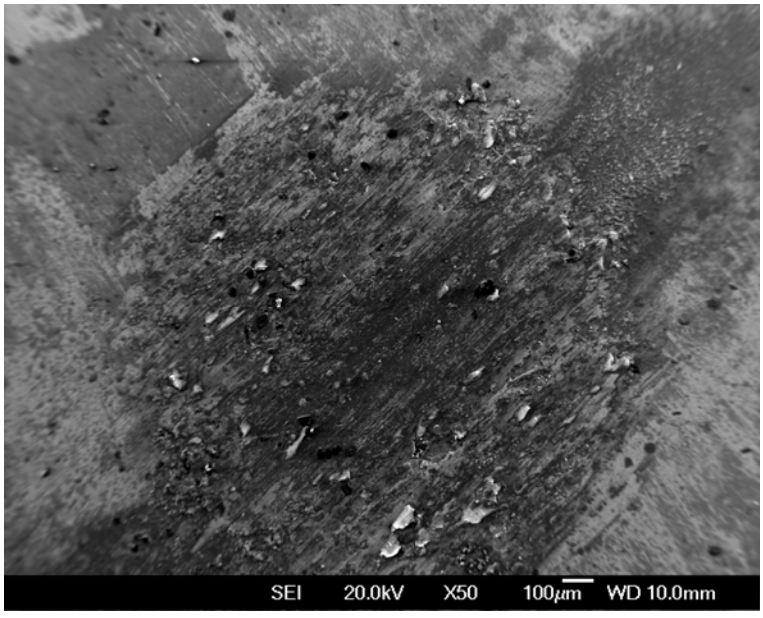

(b)

Figure 4-3.9.5 SEM images of wear track of untreated ASTM F138 disc (MU) (a) tested versus untreated AISI 316 ball (b) in Ringer's solution

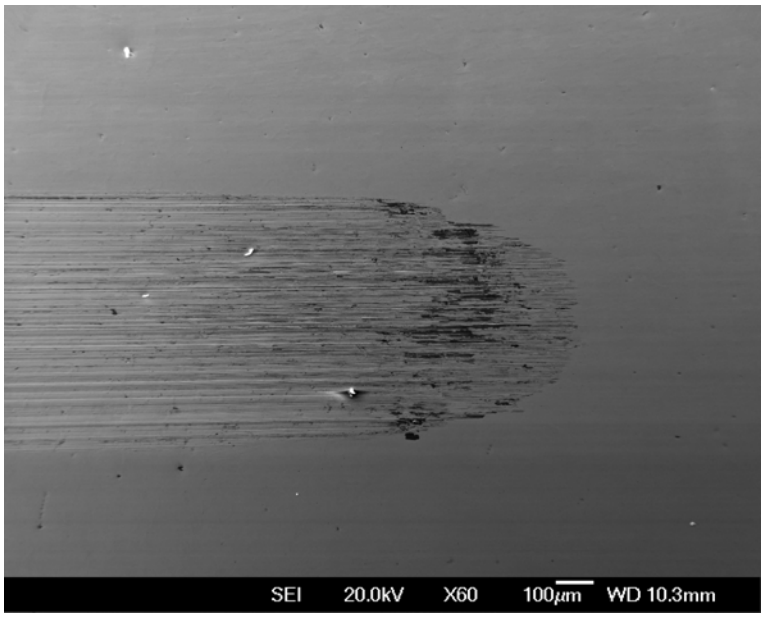

(a)

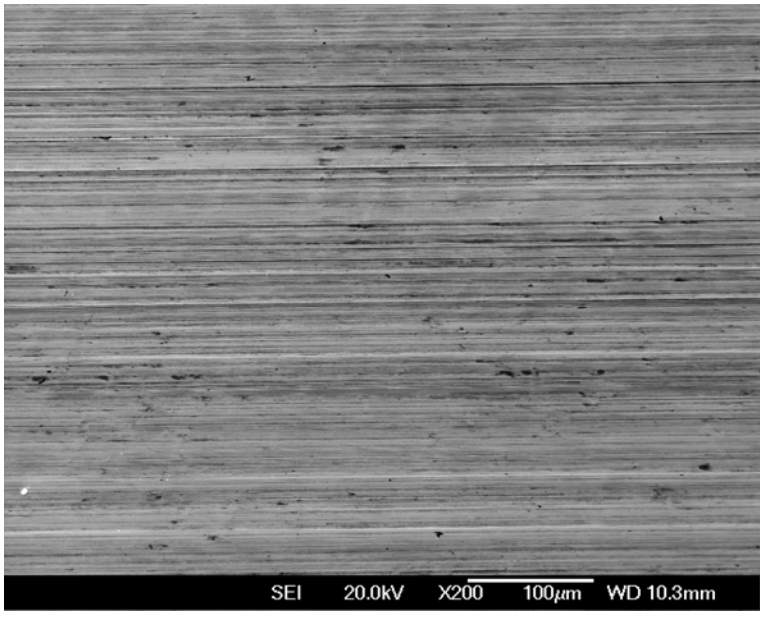

(b)

Figure 4-3.9.6 SEM images of wear track on disc at (a) low and (b) high magnifications of untreated Co-Cr disc tested versus untreated Co-Cr Ball in Ringer's solution

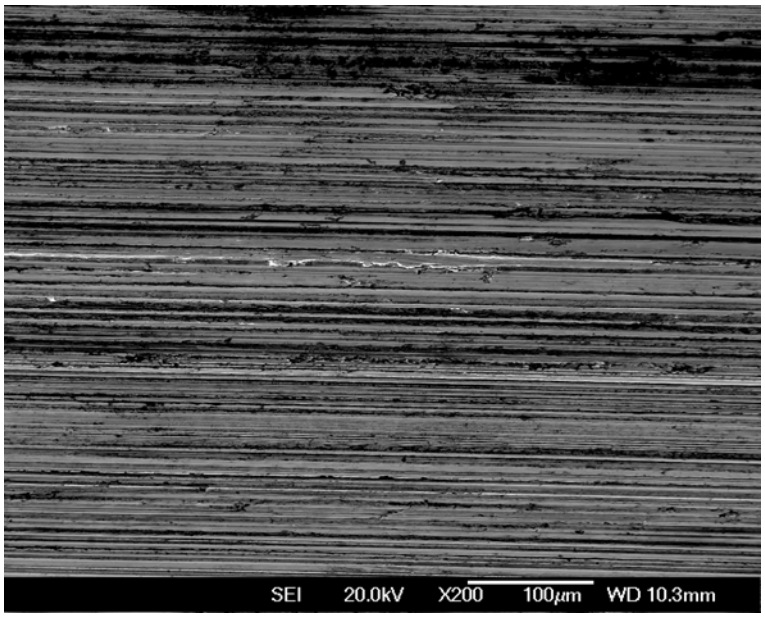

(a)

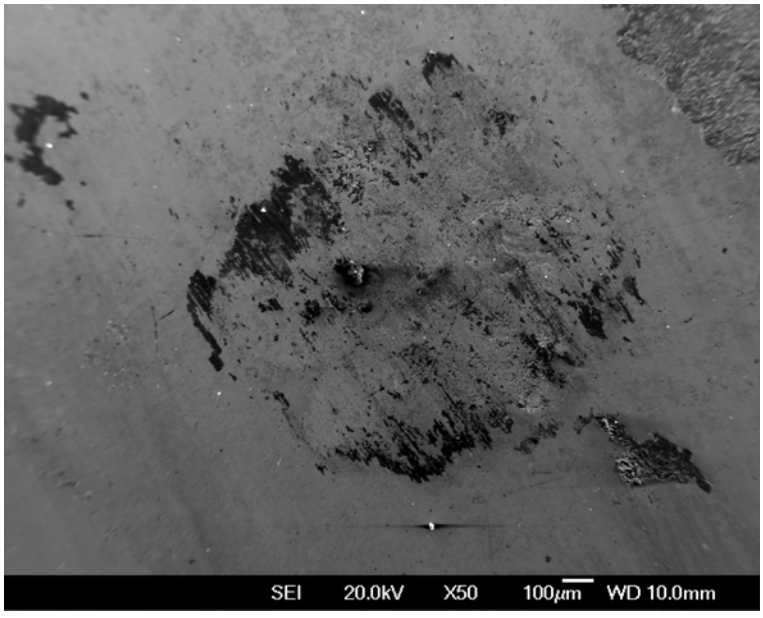

(b)

Figure 4-3.9.7 SEM image of wear track on disc (a) of untreated ASTM F138 disc (MU) tested versus 500°C carburised AISI 316 Ball (b) in Ringer's solution

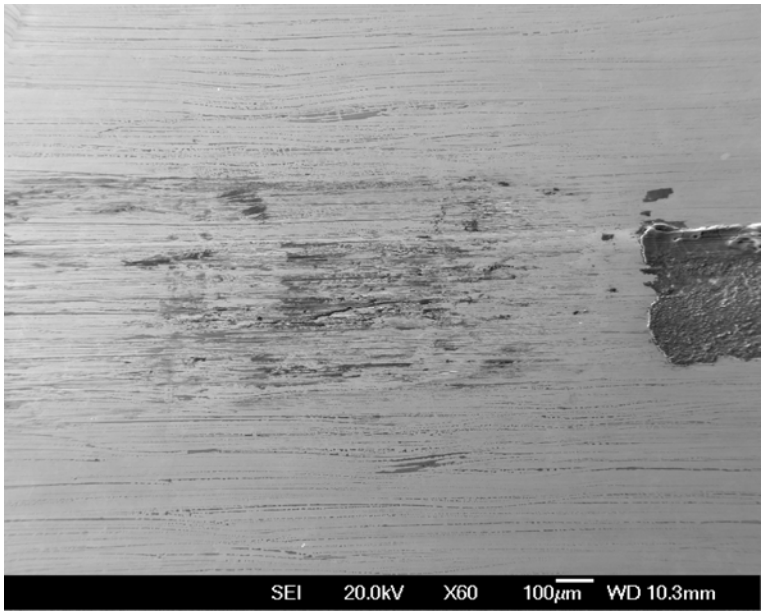

(a)

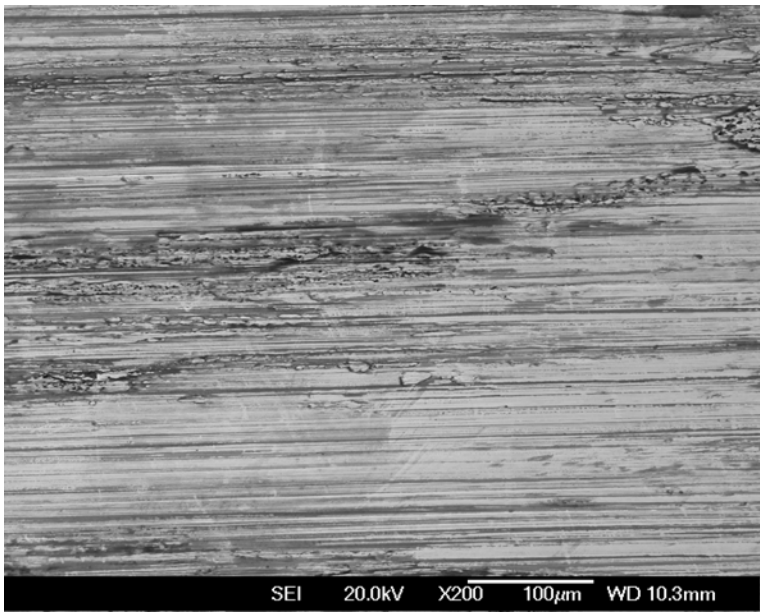

(b)

Figure 4-3.9.8 SEM image of wear track on disc at (a) low and (b) high magnifications of 500°C carburised ASTM F138 disc (MC500) tested versus 500°C carburised ball in Ringer's solution

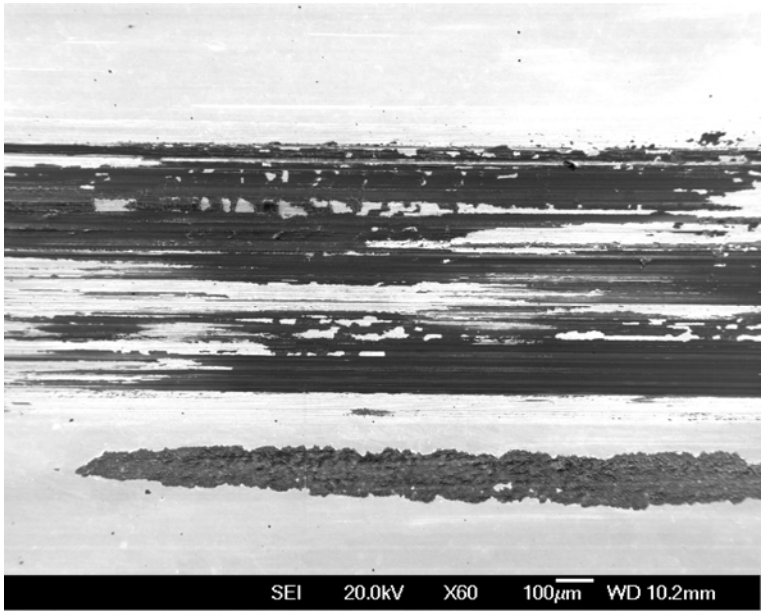

(a)

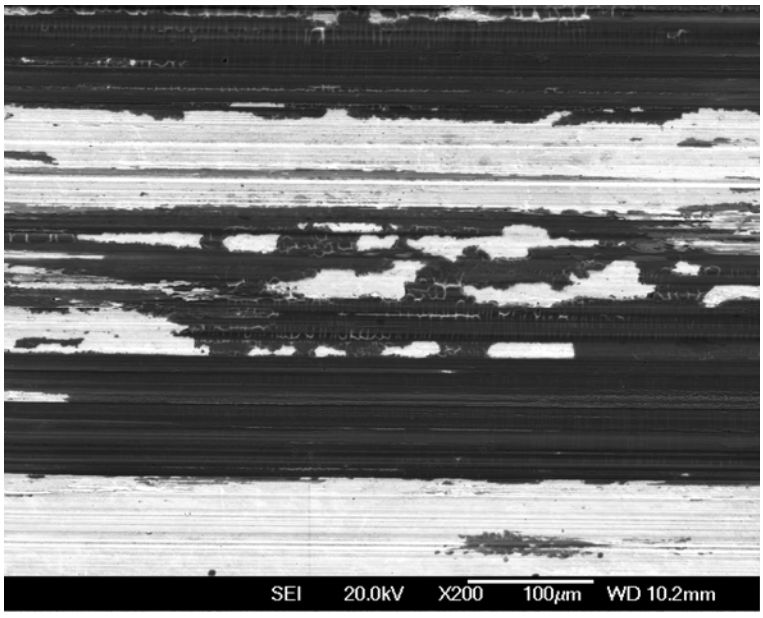

(b)

Figure 4-3.9.9 SEM images of wear track on disc at (a) low and (b) high magnifications of 500°C carburised ASTM F1586 disc (NC500) tested versus a 500°C carburised ball in Ringer's solution

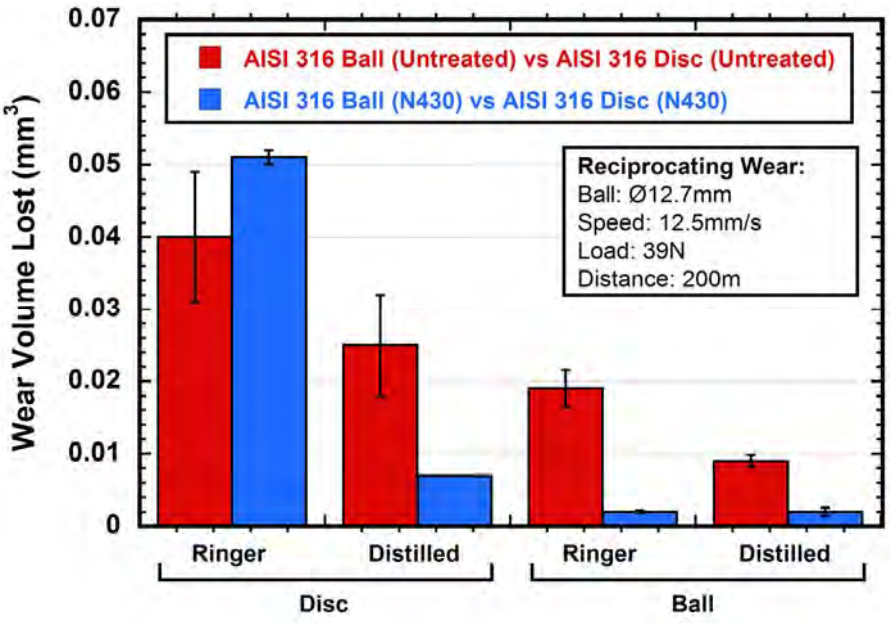

Figure 4-3.9.10 Wear volume loss of untreated AISI 316 disc versus untreated AISI 316 ball and nitrided AISI 316 ball versus nitrided AISI 316 disc in Ringer's solution and distilled water
Error: Deviation from mean of 2 values

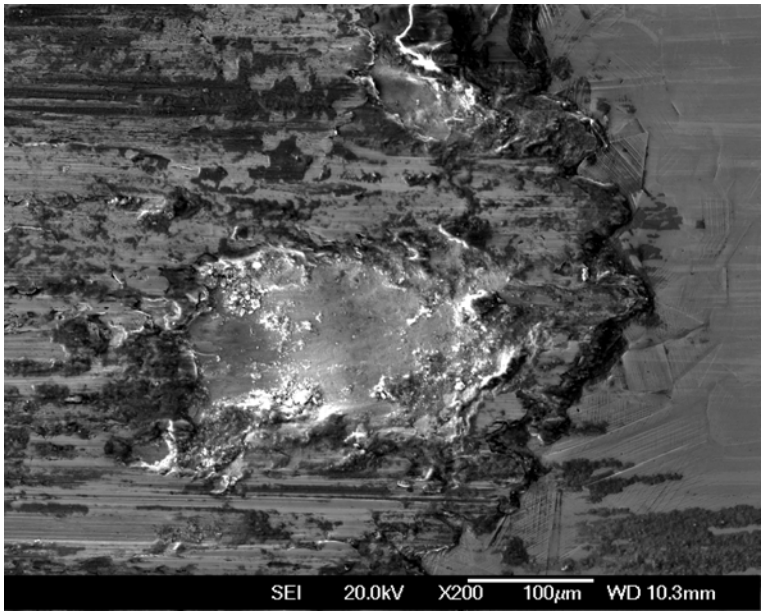

(a)

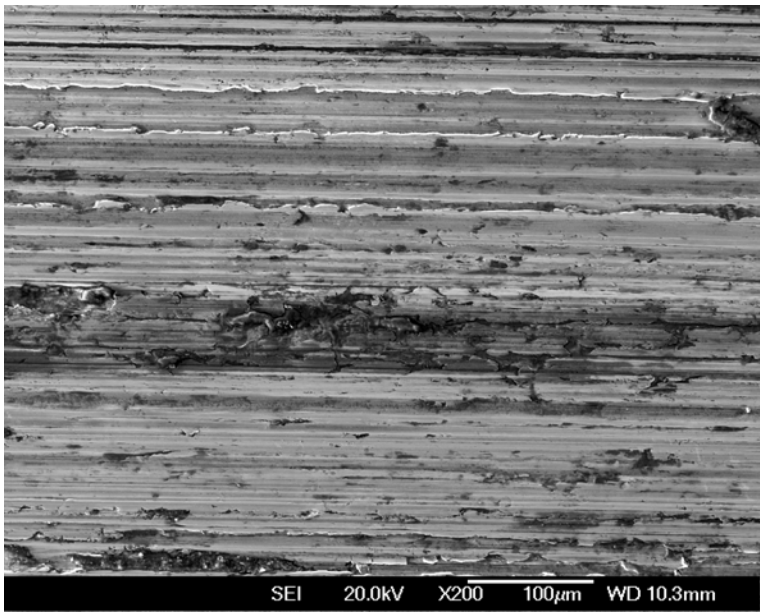

(b)

Figure 4-3.9.11 SEM images of (a) the end and (b) the middle of a wear track on untreated AISI 316 disc (GU) tested versus untreated AISI 316 ball in Ringer's solution

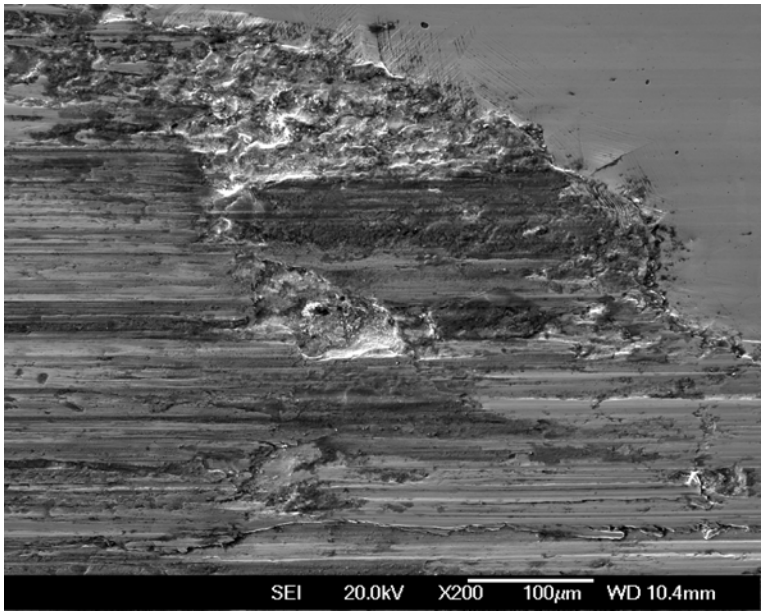

(a)

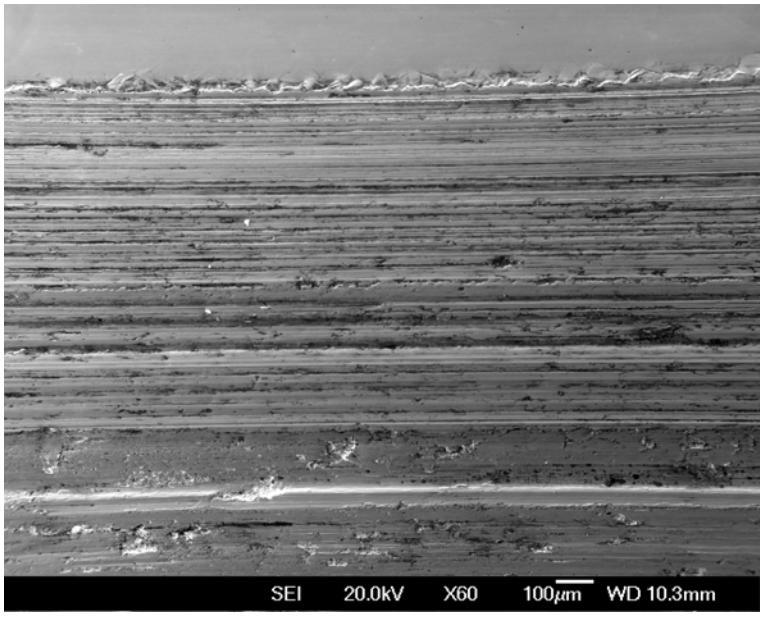

(b)

Figure 4-3.9.12 SEM images of the end (a) and central (b) part of a wear track on untreated AISI 316 disc (GU) tested versus untreated AISI 316 ball in distilled water

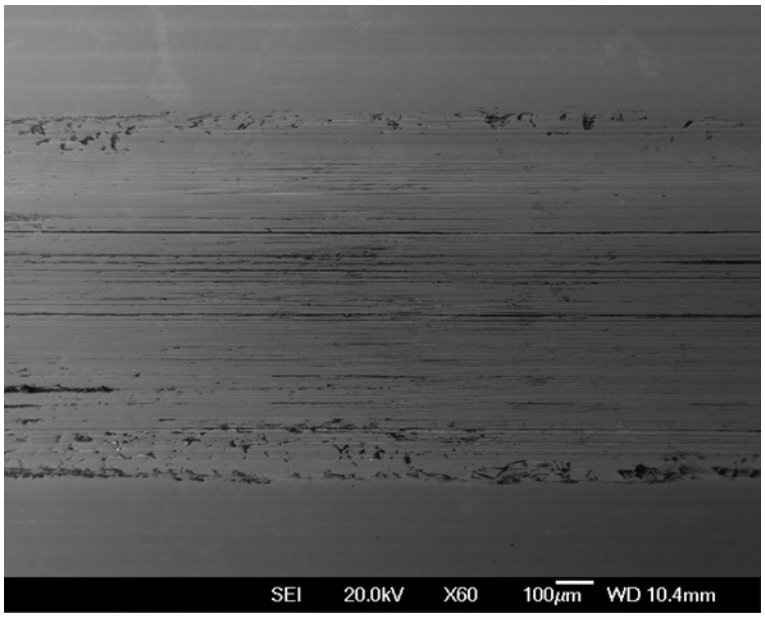

(a)

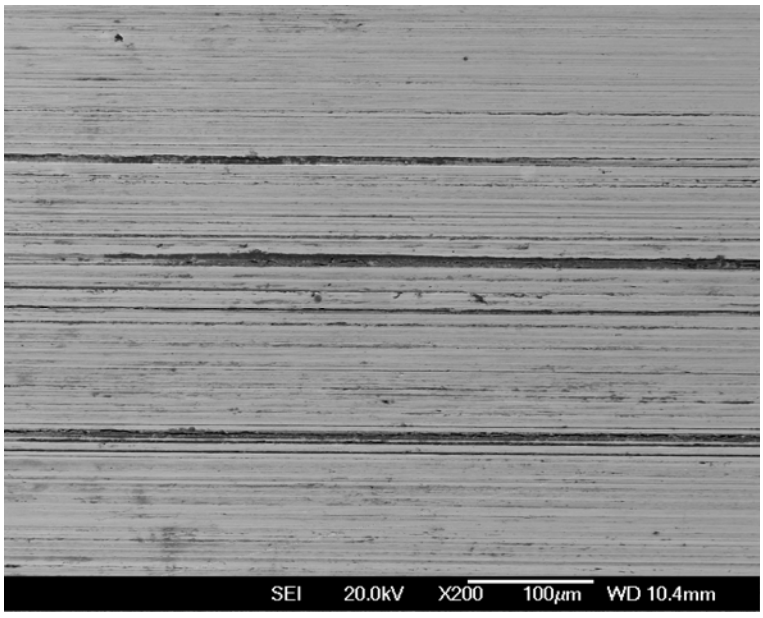

(b)

Figure 4-3.9.13 SEM images of the centre part of a wear track on disc at (a) low and (b) high magnifications of 430°C nitrided AISI 316 disc (GN430) tested versus 430°C nitrided AISI 316 ball in Ringer's solution

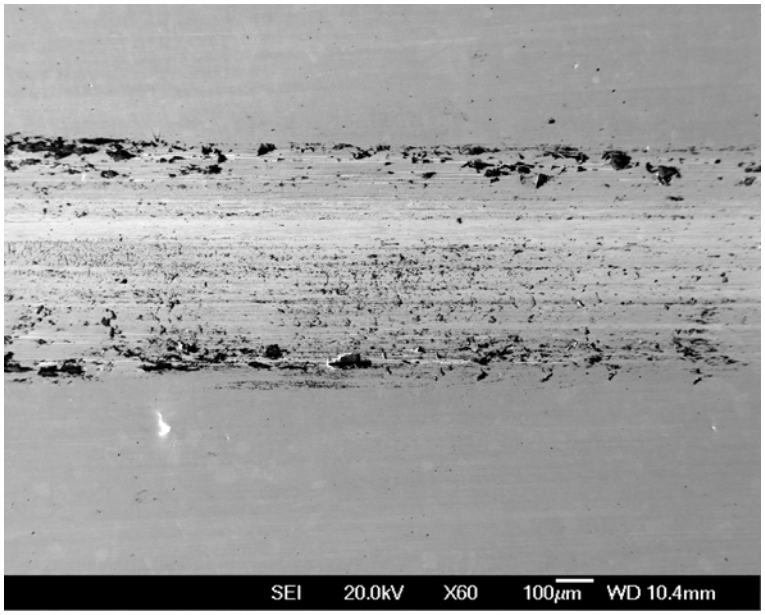

(a)

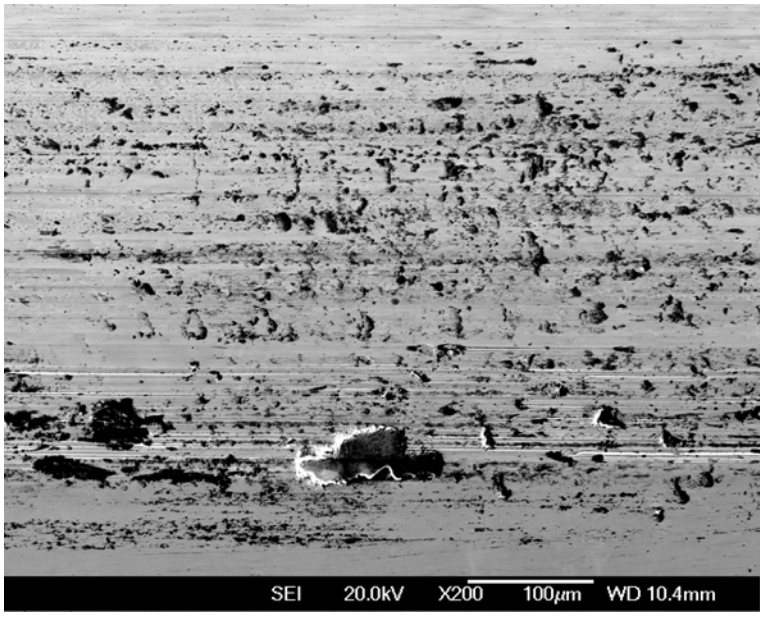

(b)

Figure 4-3.9.14 SEM images of the centre part of a wear track on disc at (a) low and (b) high magnifications of 430°C nitrided AISI 316 disc (GN430) tested versus 430°C nitrided AISI 316 ball tested in distilled water

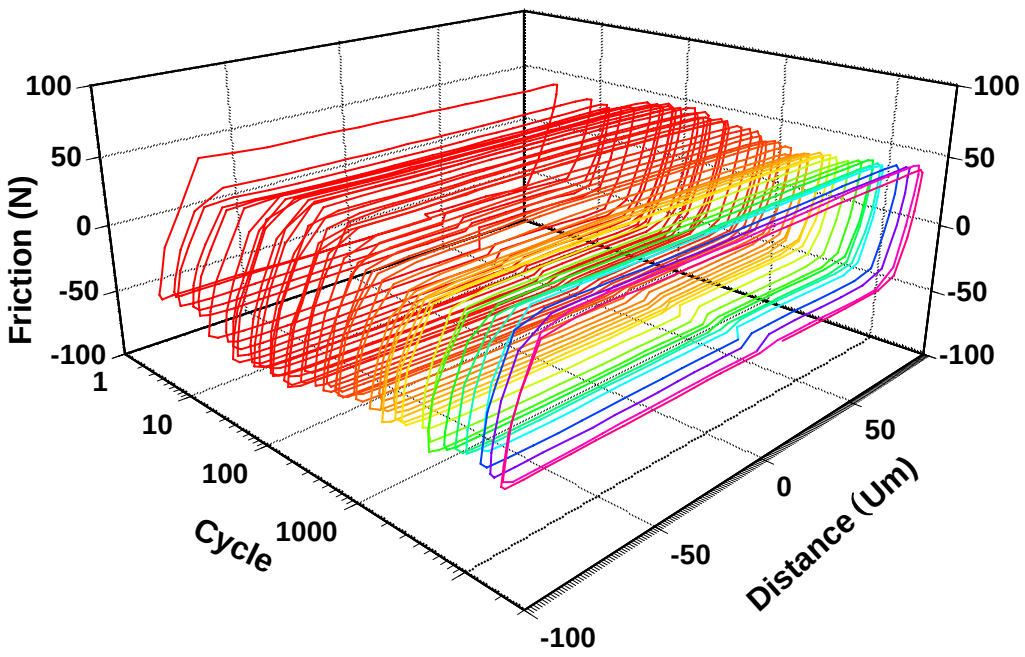

(a)

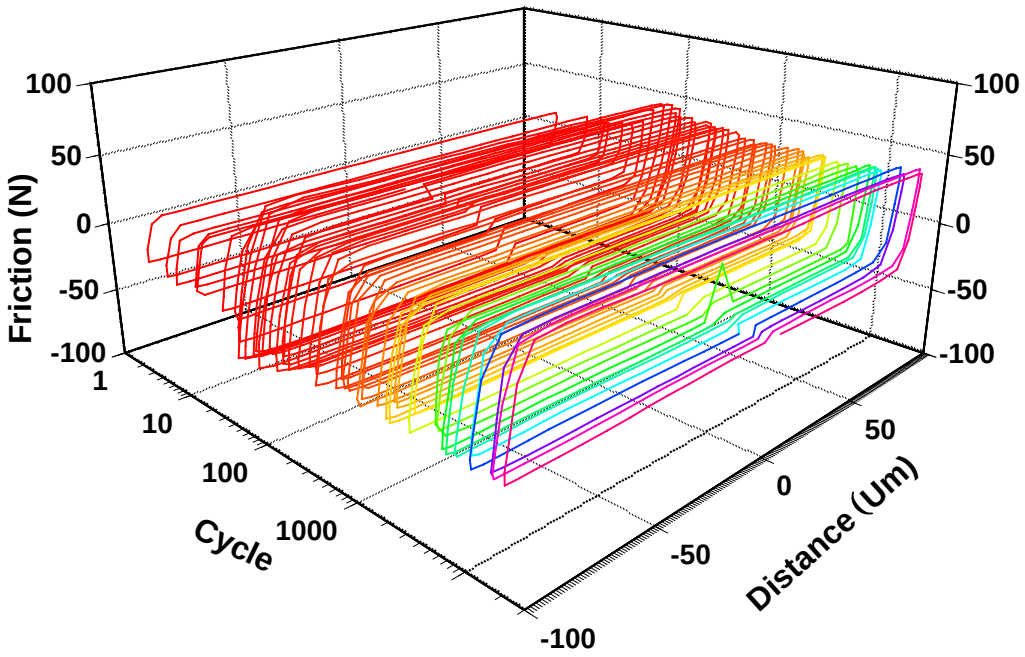

(b)

Figure 4-3.10.1 3-dimensional fretting-wear F_t-d-N curve for ASTM F2581 in the: untreated (FU) (a) and 500°C carburised (FC500) (b) condition. The parallelogram shape of the curves indicates a gross-slip fretting-wear mechanism. All the materials (ASTM F138, ASTM F1586 and ASTM F2581) treated and untreated showed similar fretting-wear mechanisms.

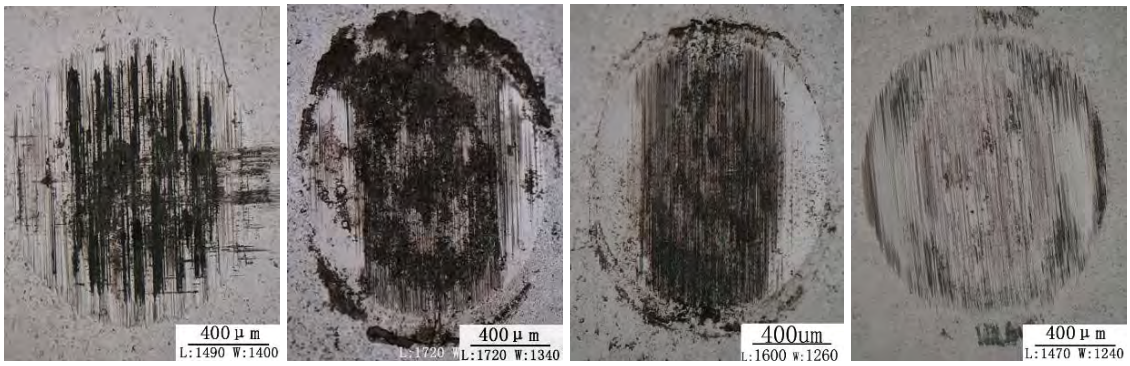

(a) - NU (b) - NN430 (c) - NNC430 (d) - NC500

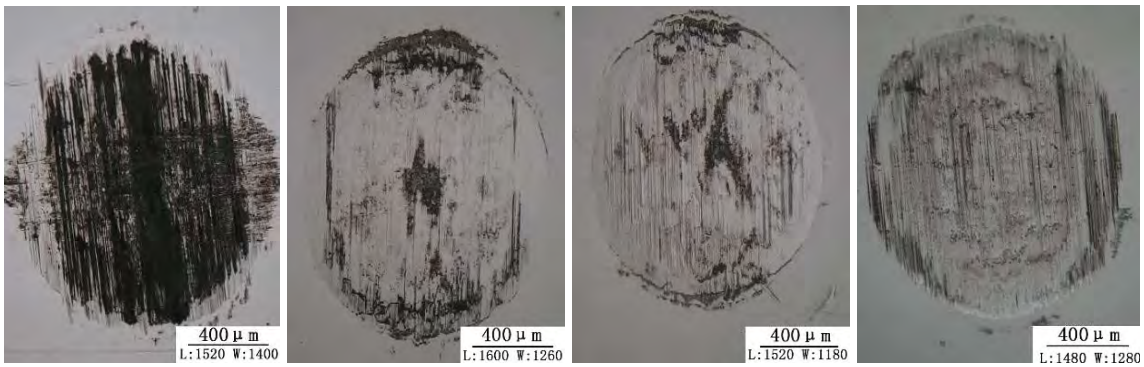

(e) – MU (f) – MN430 (g) –MNC430 (h) – MC500

(i) - FU (j) – FC500

Figure 4-3.10.2 (a-j) Optical microscope images of fretting-wear tracks on ASTM F1586 (a-d), ASTM F138 (e-h) and ASTM F2581 (i – j) in the: untreated (a, e & i); 430°C nitrided (b & f); 430°C carbonitrided (c & g); and 500°C carburised (d, h & j) tested in Ringer's solution for $2x10^4$ cycles.

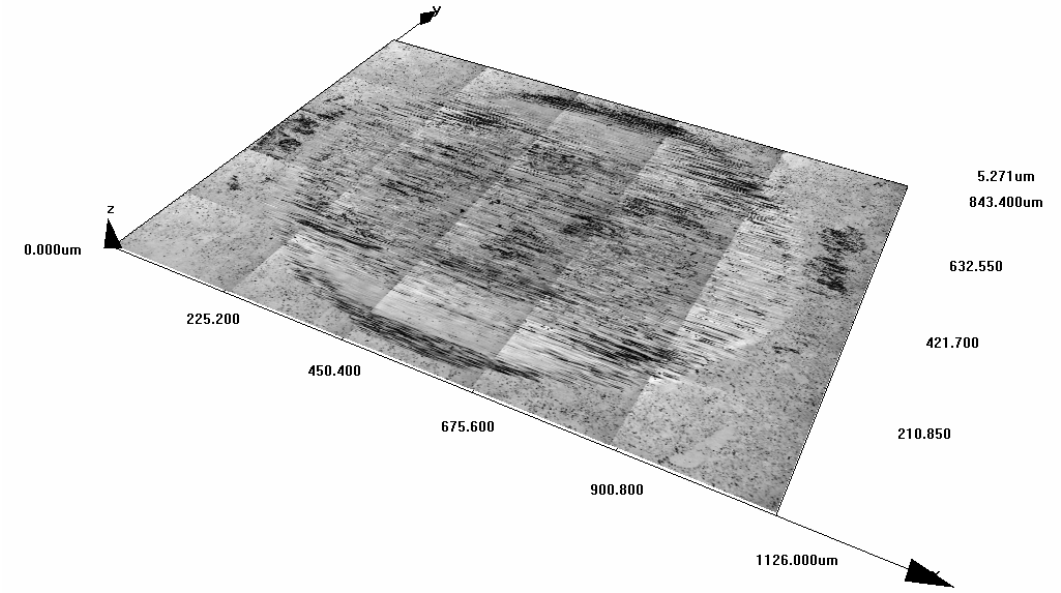

(a)

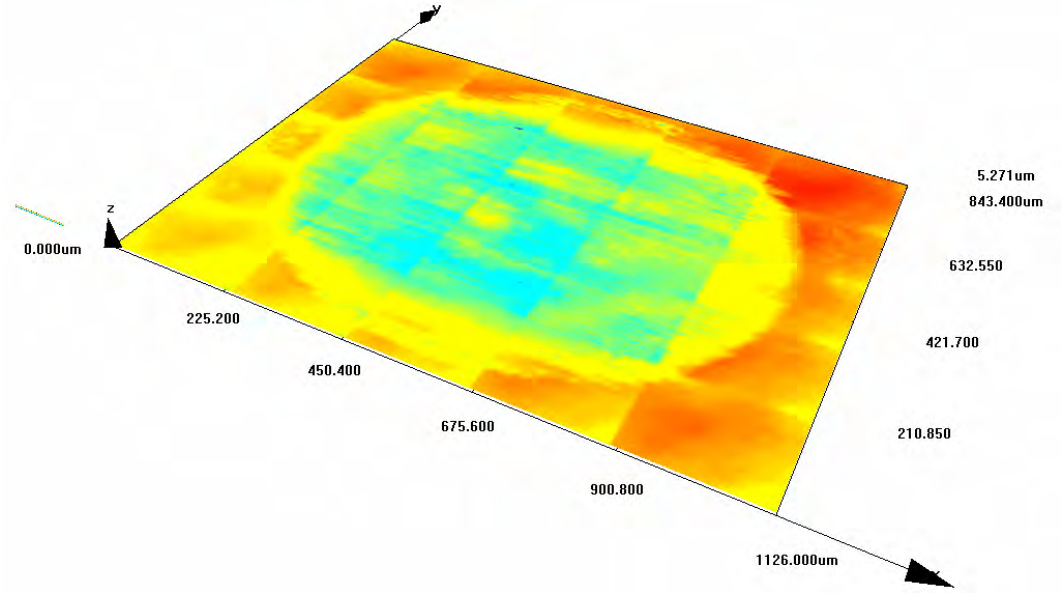

(b)

Figure 4-3.10.3 Typical 3-D laser confocal microscope images in (a) intensity and (b) height mode of fretting-wear track used to calculate the volume of material lost. This image is the fretting-wear track after $2x10^4$ cycles on a 500°C carburised ASTM F1586 sample

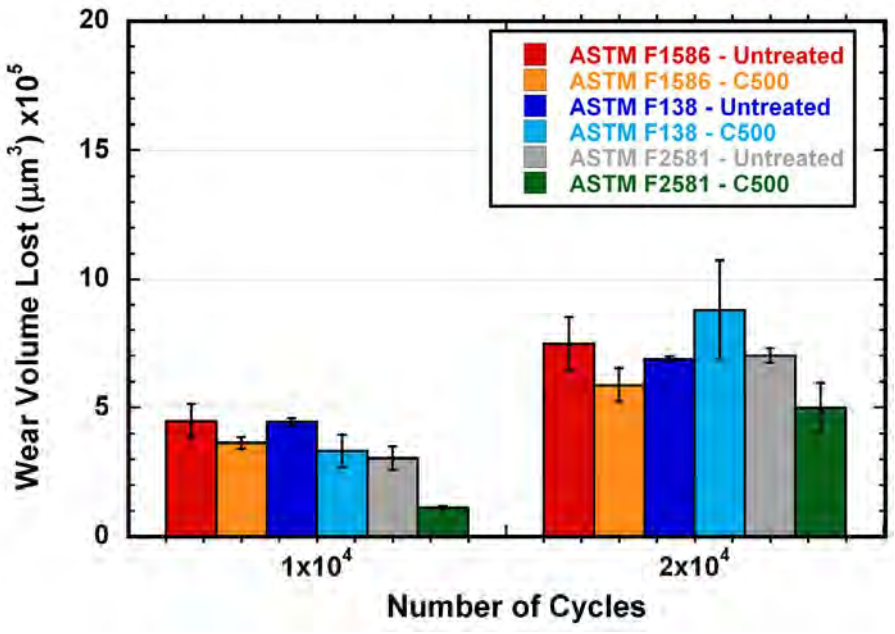

Figure 4-3.10.4 Wear loss during fretting-wear test in Ringer's solution for ASTM F138, ASTM F1586 and ASTM F2581 in the untreated and 500°C carburised conditions
Error for ASTM F2581: Standard deviation of 3 values
Error for the rest of materials: Deviation from the mean of 2 values

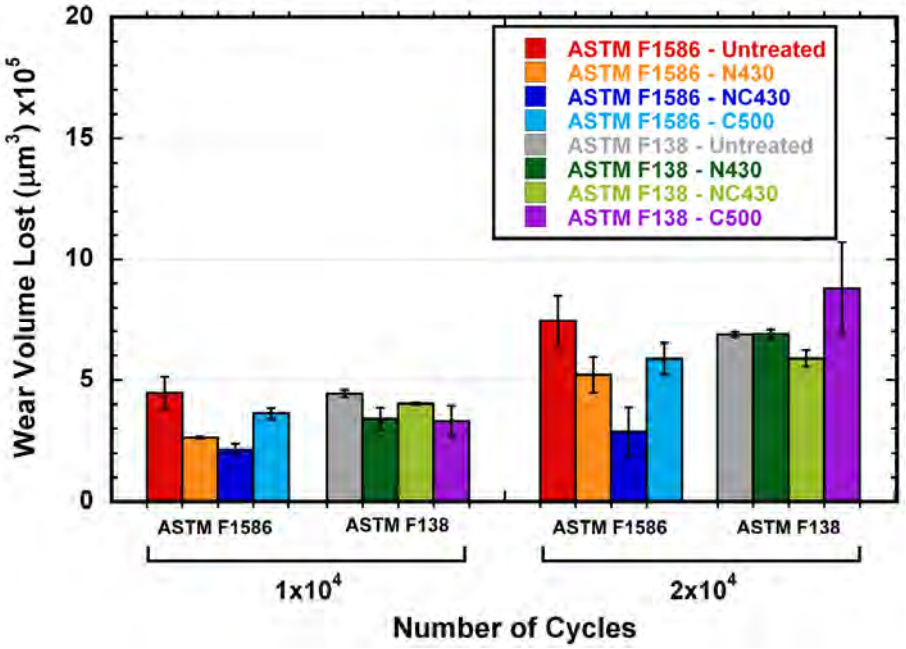

Figure 4-3.10.5 Wear loss during fretting-wear test in Ringer's solution for ASTM F138 and ASTM F1586 in the untreated, 430°C nitrided, 430°C carbonitrided and 500°C carburised conditions
Error: Deviation from the mean of 2 values

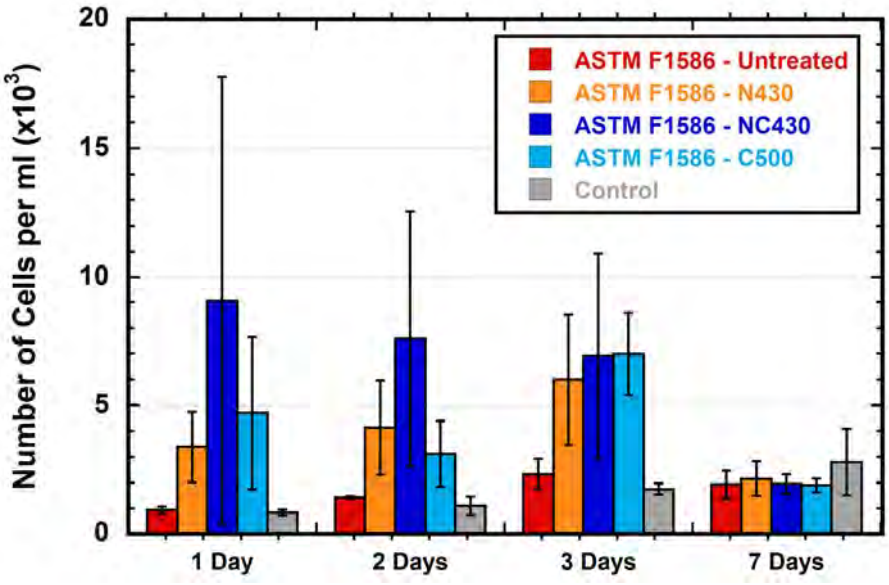

(a)

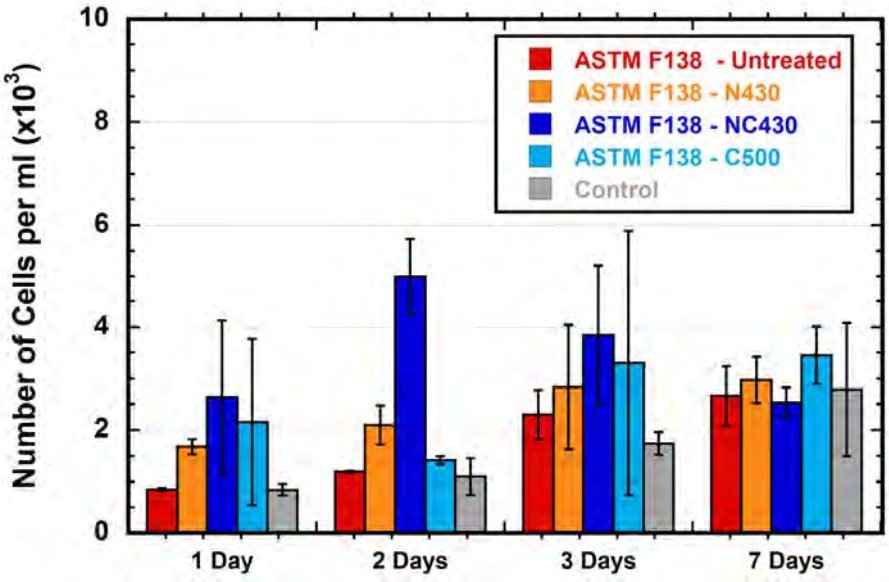

(b)

Figure 4-3.11.1 Osteoblasts proliferation kinetics on (a) ASTM F1586 and (b) ASTM F138
Error: Standard deviation of 3 values

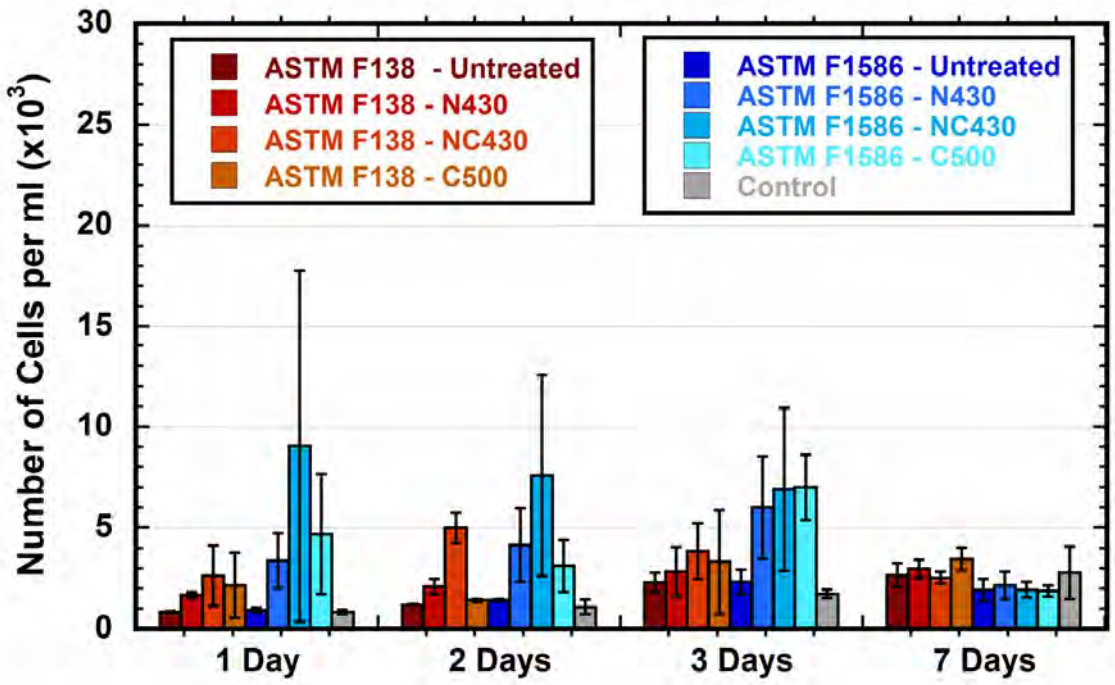

Figure 4-3.11.2 Osteoblasts proliferation kinetics on untreated and treated ASTM F1586 and ASTM F138
Error: Standard deviation of 3 values

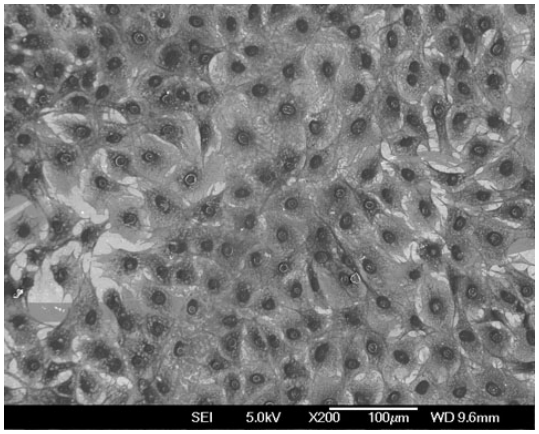

(a) ASTM F1586 – Untreated

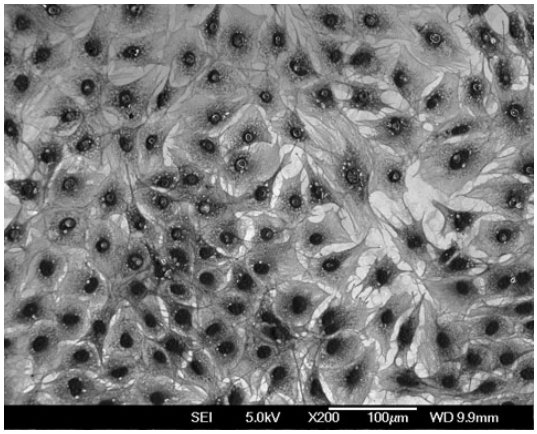

(b) ASTM F1586 – Nitrided at 430°C

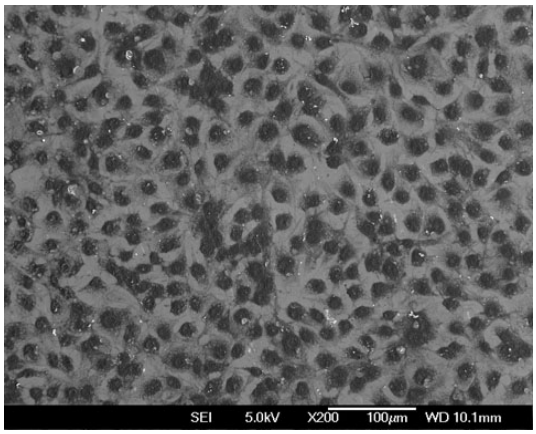

(c) ASTM F1586–Carbonitrided at 430°C

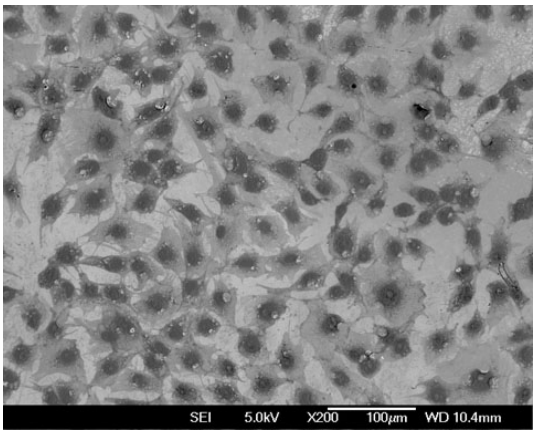

(d) ASTM F1586 – Carburised at 500°C

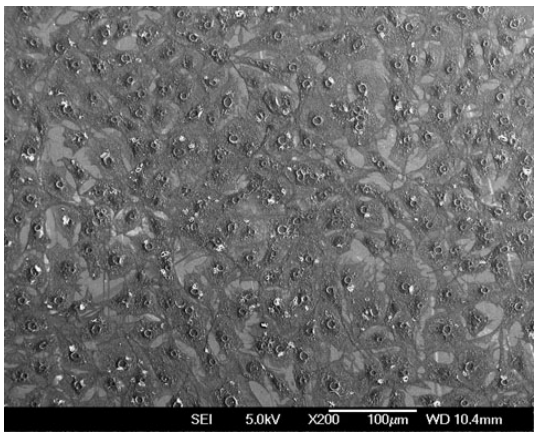

(e) Thermanox Control

Figure 4-3.11.3 (a-e) Scanning electron micrographs of osteoblasts after 1 day of culture on ASTM F1586 (High Tensile) and control

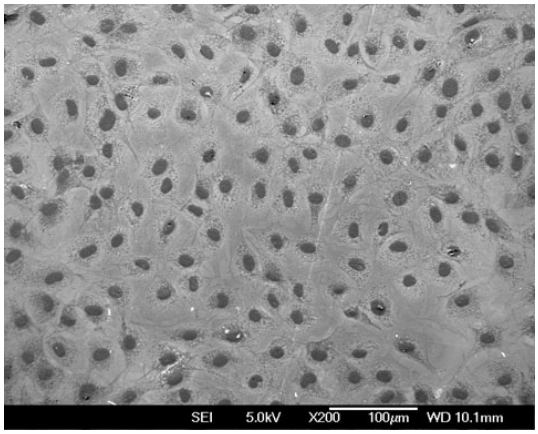

(a) ASTM F138 – Untreated

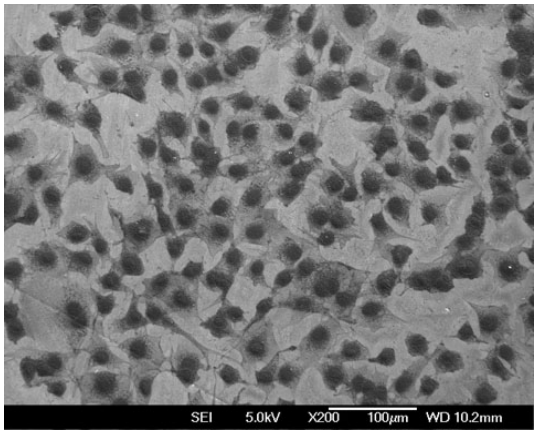

(b) ASTM F138 – Nitrided at 430°C

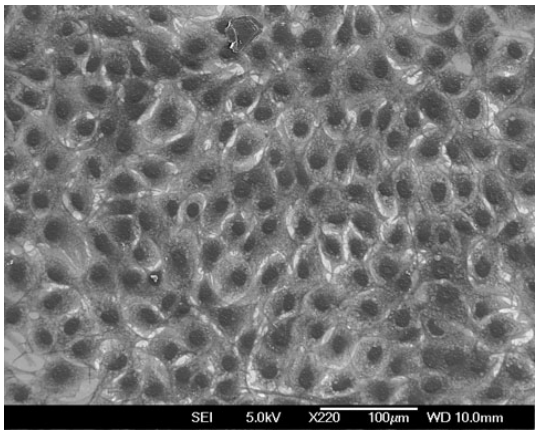

(c) ASTM F138 – Carbonitrided at 430°C

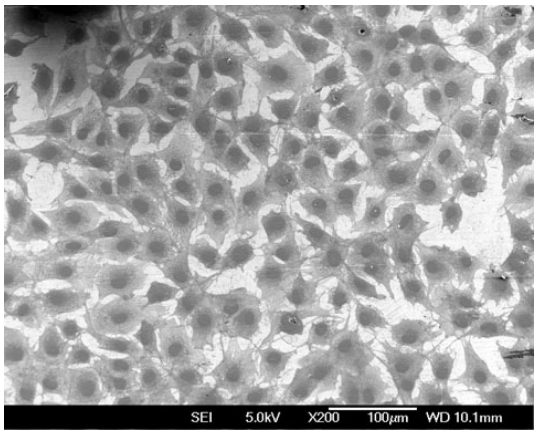

(d) ASTM F138 – Carburised at 500°C

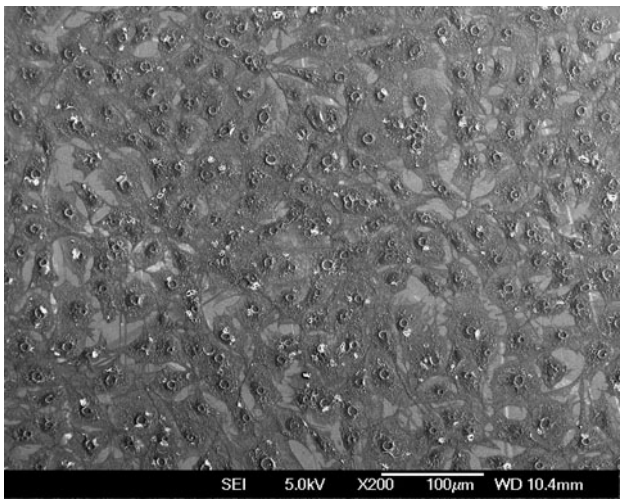

(e) Thermanox Control

Figure 4-3.11.4 (a-e) Scanning electron micrographs of osteoblasts after 1 day of culture on ASTM F138 (High Tensile) and control

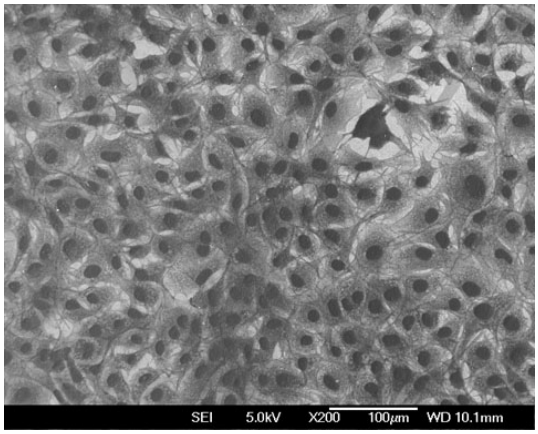

(a) ASTM F1586 – Untreated

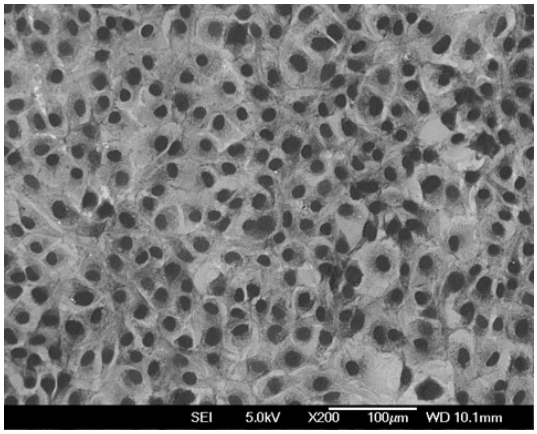

(b) ASTM F1586 – Nitrided at 430°C

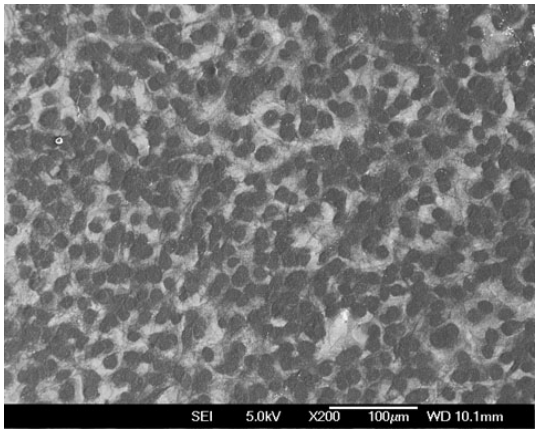

(c) ASTM F1586–Carbonitrided at 430°C

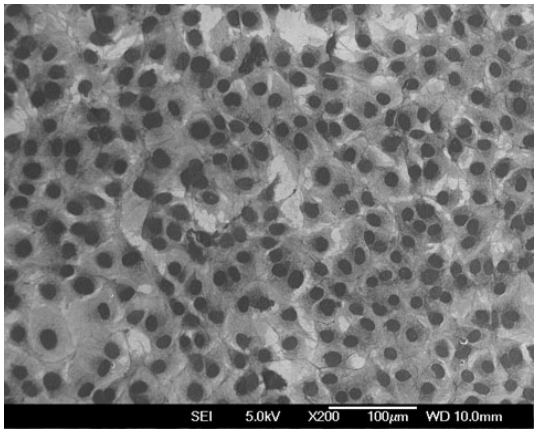

(d) ASTM F1586 – Carburised at 500°C

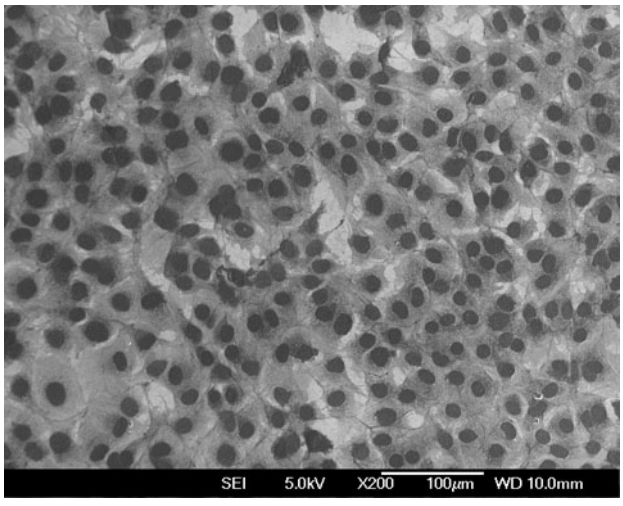

(e) Thermanox Control

Figure 4-3.11.5 (a-e) Scanning electron micrographs of osteoblasts after 2 days of culture on ASTM F1586 (High Tensile) and control

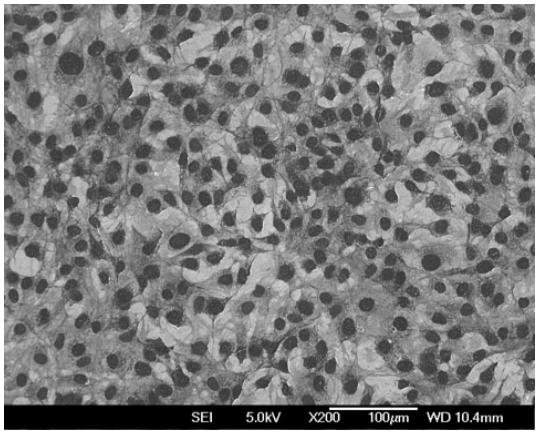

(a) ASTM F138 – Untreated

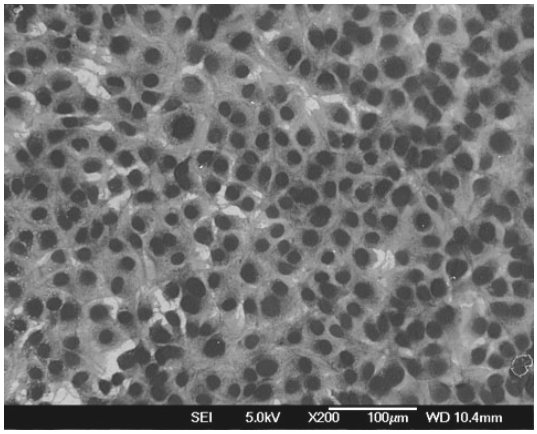

(b) ASTM F138 – Nitrided at 430°C

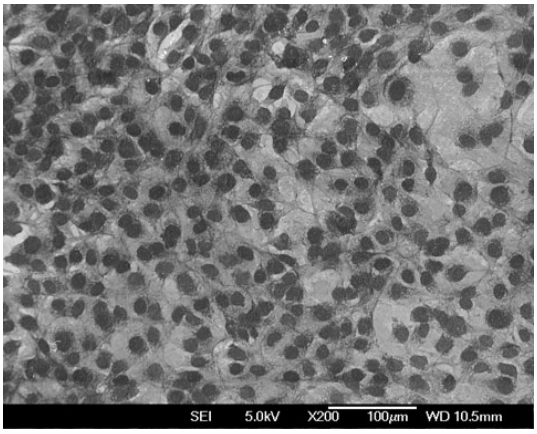

(c) ASTM F138 – Carbonitrided at 430°C

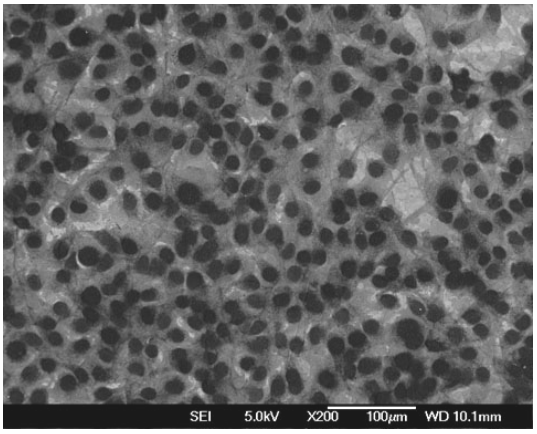

(d) ASTM F138 – Carburised at 500°C

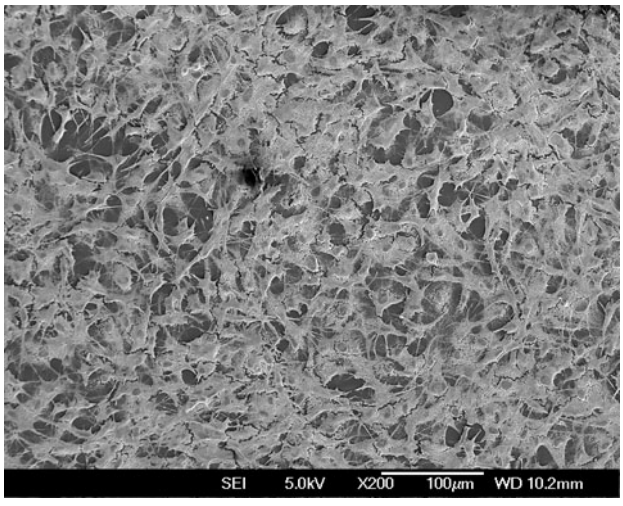

(e) Thermanox Control

Figure 4-3.11.6 (a-e) Scanning electron micrographs of osteoblasts after 2 days of culture on ASTM F138 (High Tensile) and control

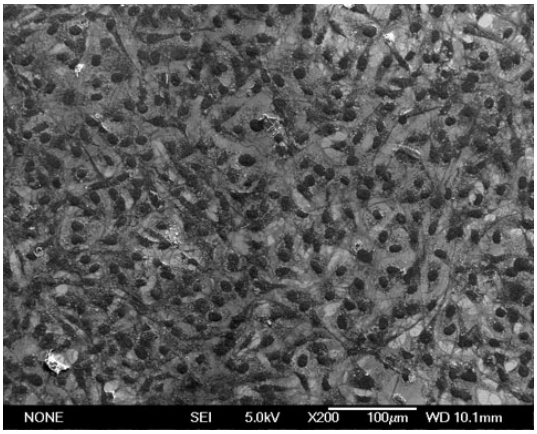

(a) ASTM F1586 – Untreated

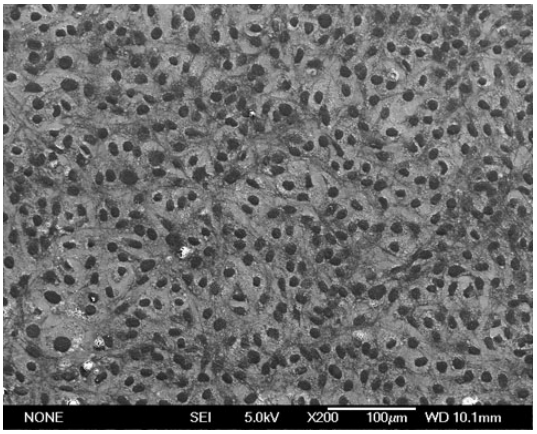

(b) ASTM F1586 – Nitrided at 430°C

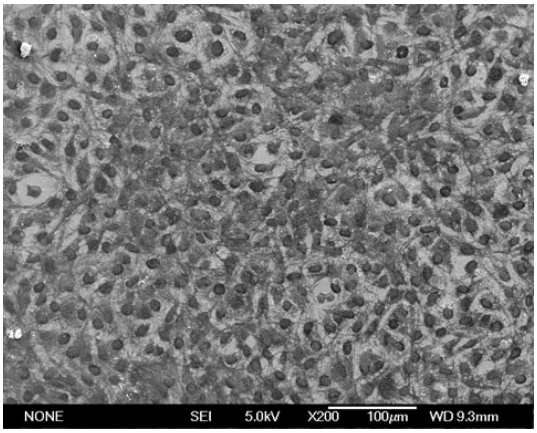

(c) ASTM F1586–Carbonitrided at 430°C

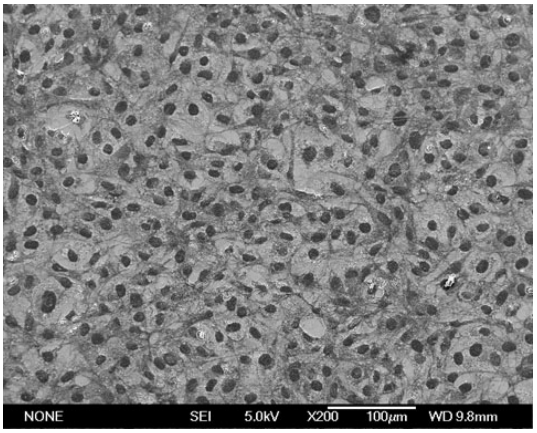

(d) ASTM F1586 – Carburised at 500°C

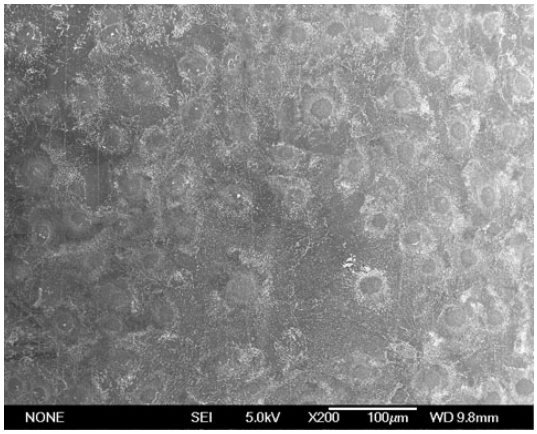

(e) Thermanox Control

Figure 4-3.11.7 (a-e) Scanning electron micrographs of osteoblasts after 3 days of culture on ASTM F1586 (High Tensile) and control

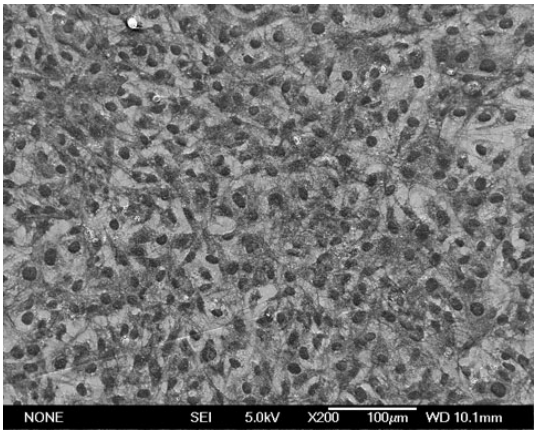

(a) ASTM F138 – Untreated

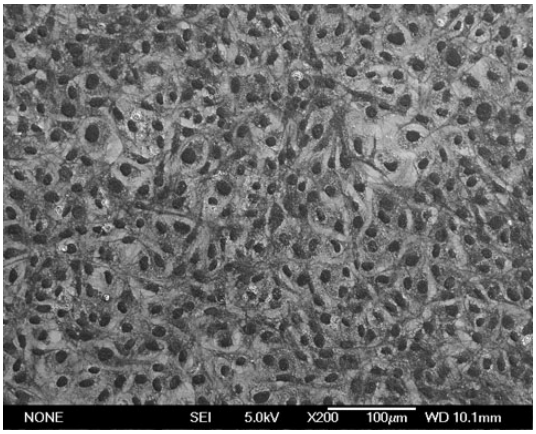

(b) ASTM F138 – Nitrided at 430°C

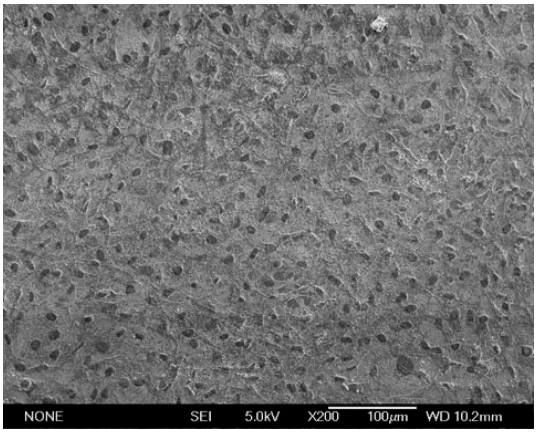

(c) ASTM F138 – Carbonitrided at 430°C

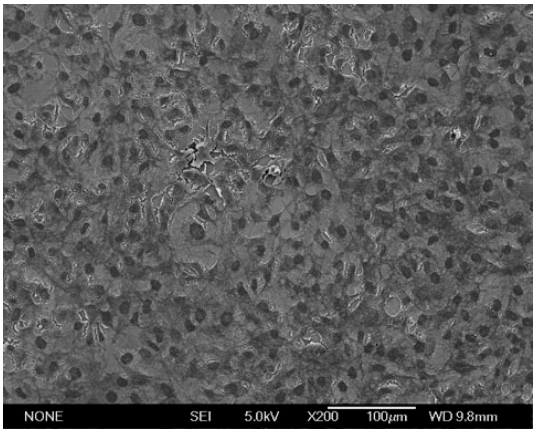

(d) ASTM F138 – Carburised at 500°C

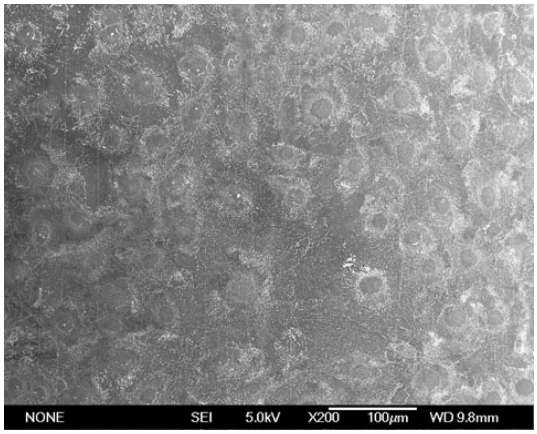

(e) Thermanox Control

Figure 4-3.11.8 (a-e) Scanning electron micrographs of osteoblasts after 3 days of culture on ASTM F138 (High Tensile) and control

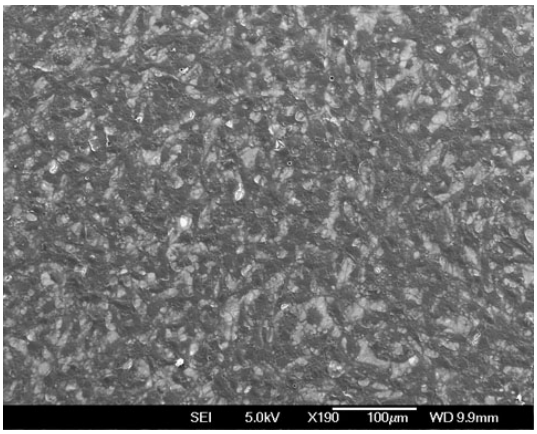

(a) ASTM F1586 – Untreated

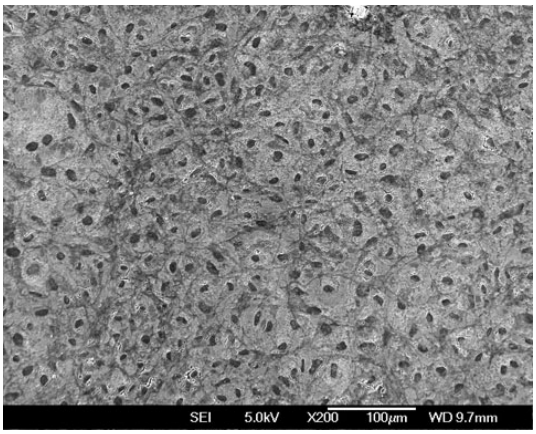

(b) ASTM F1586 – Nitrided at 430°C

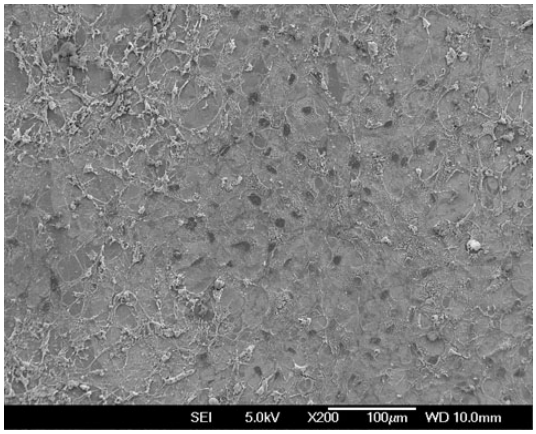

(c) ASTM F1586–Carbonitrided at 430°C

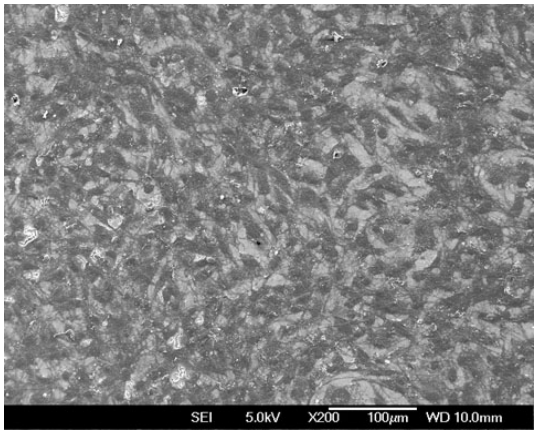

(d) ASTM F1586 – Carburised at 500°C

Figure 4-3.11.9 (a-d) Scanning electron micrographs of osteoblasts after 7 days of culture on ASTM F1586 (High Tensile)

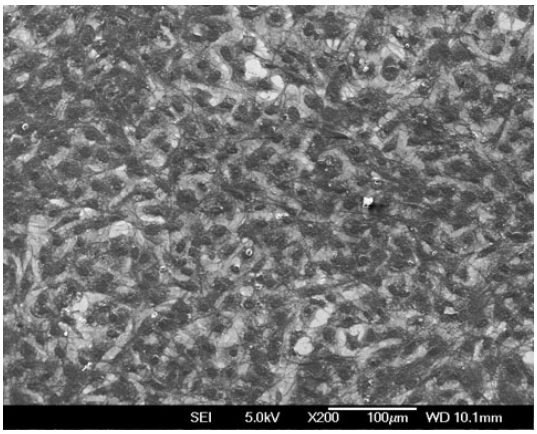

(a) ASTM F138 – Untreated

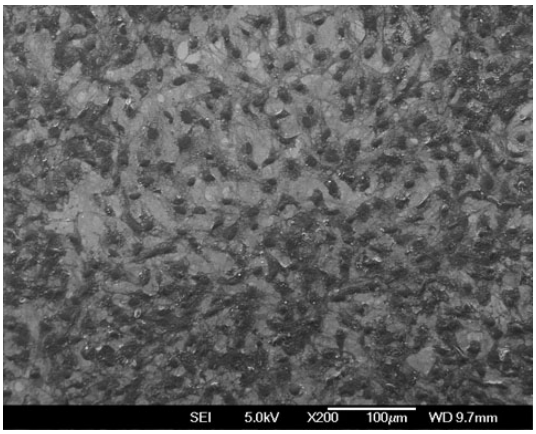

(b) ASTM F138 – Nitrided at 430°C

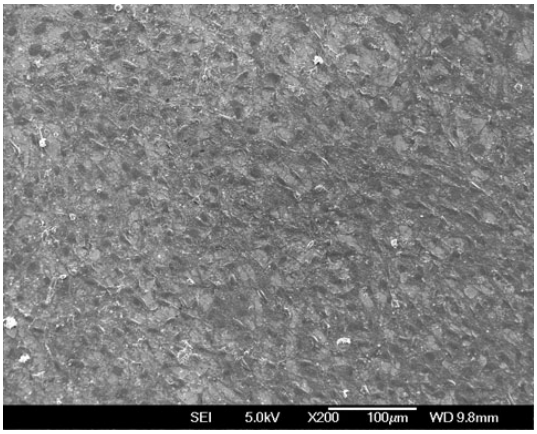

(c) ASTM F138 – Carbonitrided at 430°C

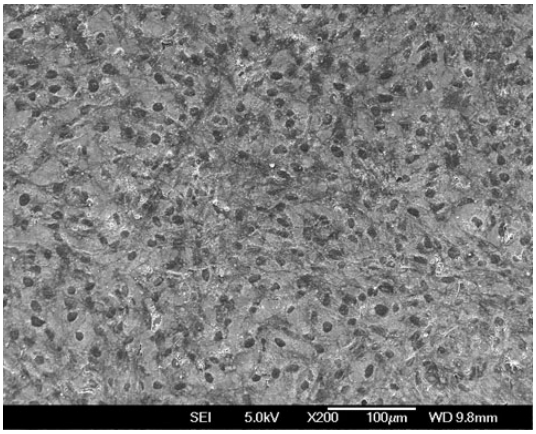

(d) ASTM F138 – Carburised at 500°C

Figure 4-3.11.10 (a-d) Scanning electron micrographs of osteoblasts after 7 days of culture on ASTM F138 (High Tensile)

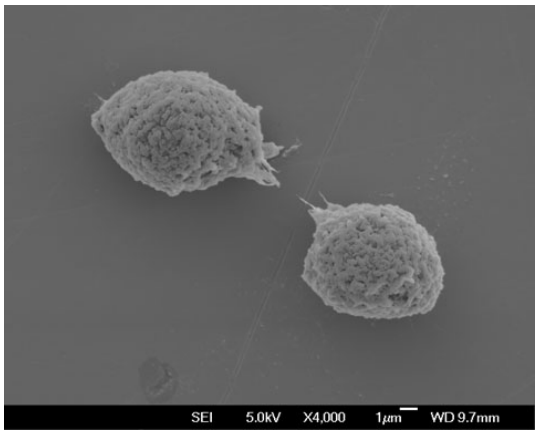

(a) Stage 1 of cell attachment

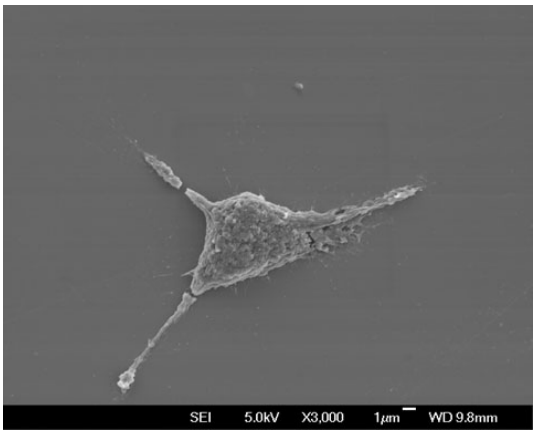

(b) Stage 2 of cell attachment

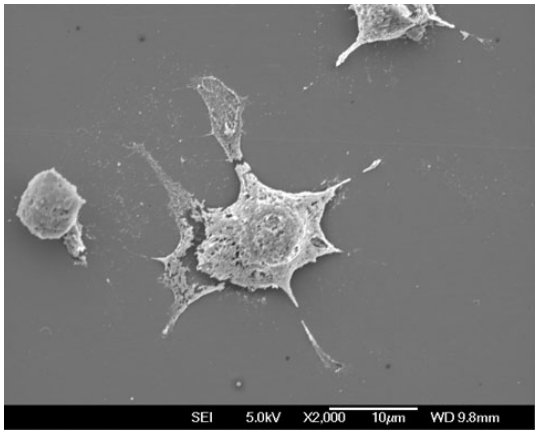

(c) Stage 3 of cell attachment

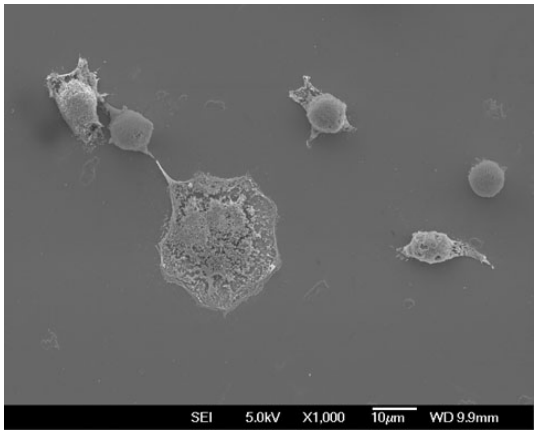

(d) Stage 4 of cell attachment

Figure 4-3.11.11 (a-d) Different stages of early stage attachment on biomedical stainless steel

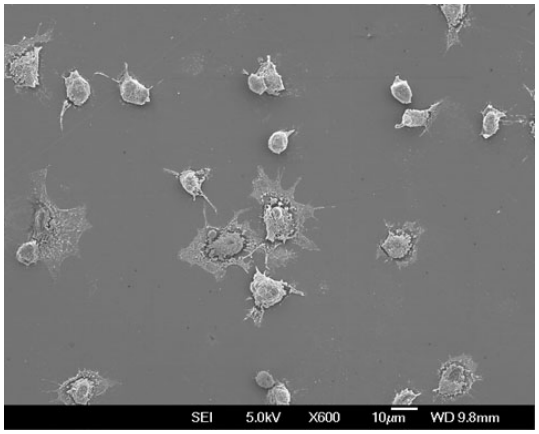

(a) ASTM F1586 – Untreated

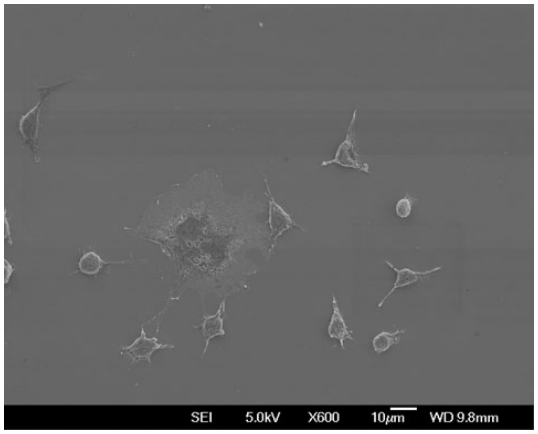

(b) ASTM F1586 – Nitrided at 430°C

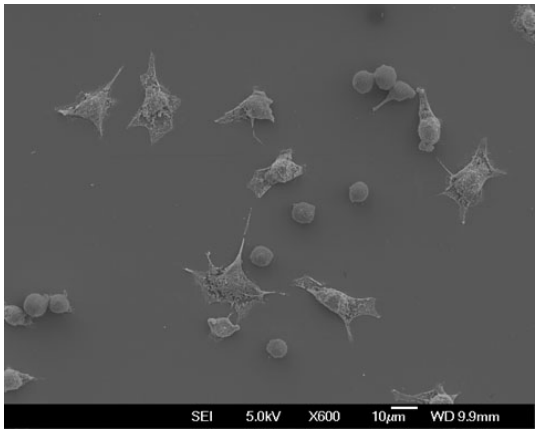

(c) ASTM F1586–Carbonitrided at 430°C

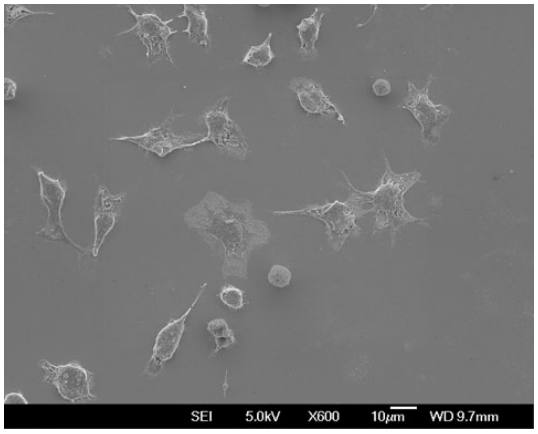

(d) ASTM F1586 – Carburised at 500°C

Figure 4-3.11.12 (a-d) Scanning electron micrographs of cell attachment on ASTM F1586 (High Tensile) after 30 minutes of incubation

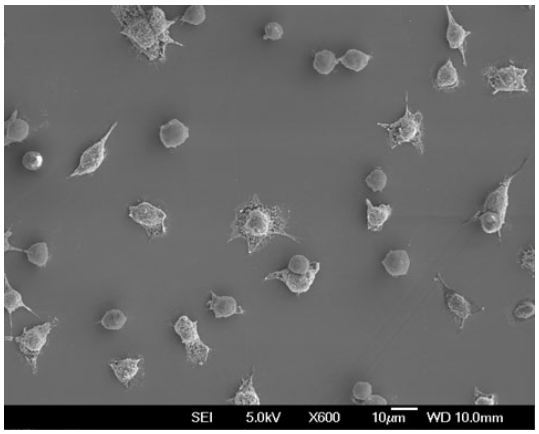

(a) ASTM F138 – Untreated

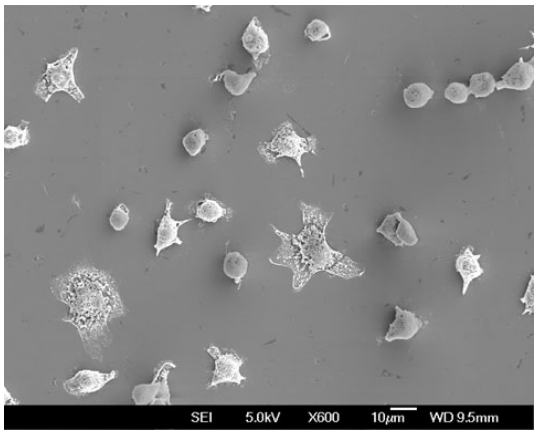

(b) ASTM F138 – Nitrided at 430°C

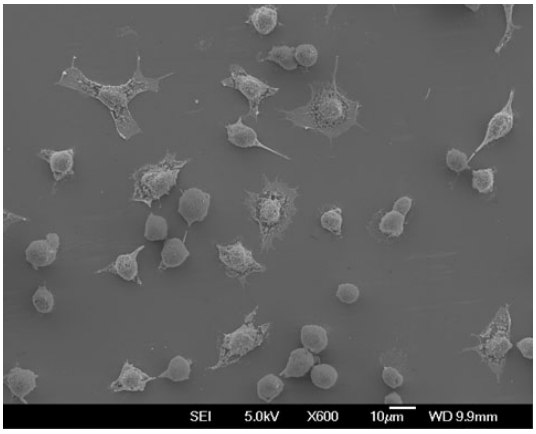

(c) ASTM F138 – Carbonitrided at 430°C

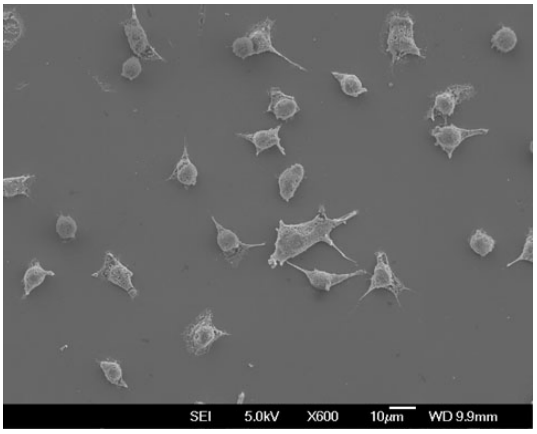

(d) ASTM F138 – Carburised at 500°C

Figure 4-3.11.13 (a-d) Scanning electron micrographs of cell attachment on ASTM F138 (High Tensile) after 30 minutes of incubation

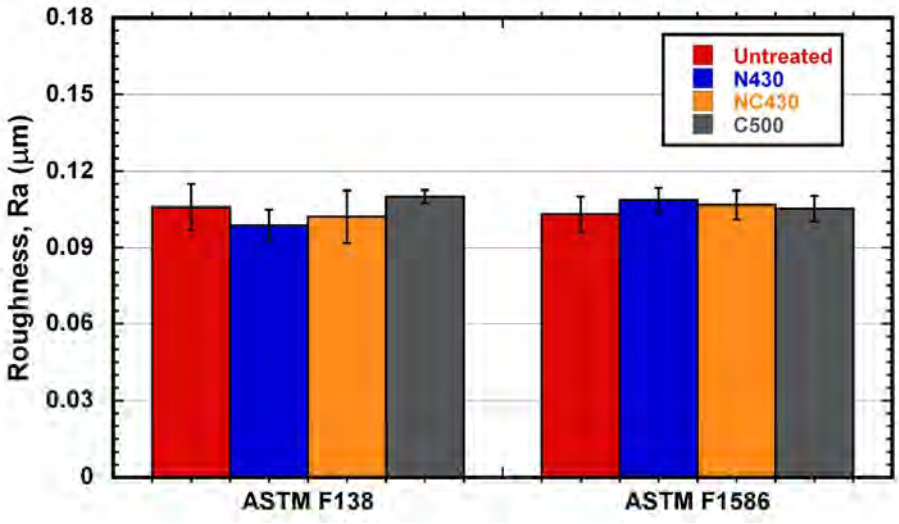

Figure 4-3.11.14 Surface roughness measurements on ASTM F138 and ASTM F1586 samples used in the biocompatibility experiments
Error: Standard deviation of 9 values (on 3 different samples)

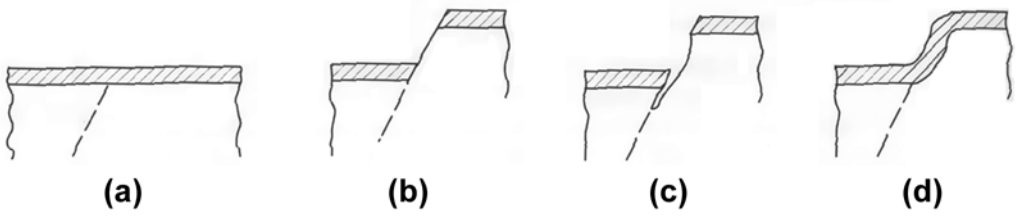

Figure 5-1 Schematic representation of (a) passive film, (b) passive film rapture by stress-induced slip resulting in exposure of bare substrate, (c) crack initiation by anodic dissolution initiating crevice corrosion conditions before repassivation of exposed substrate, and (d) repassivation of exposed substrate before crack initiation. Source: Reference [174]

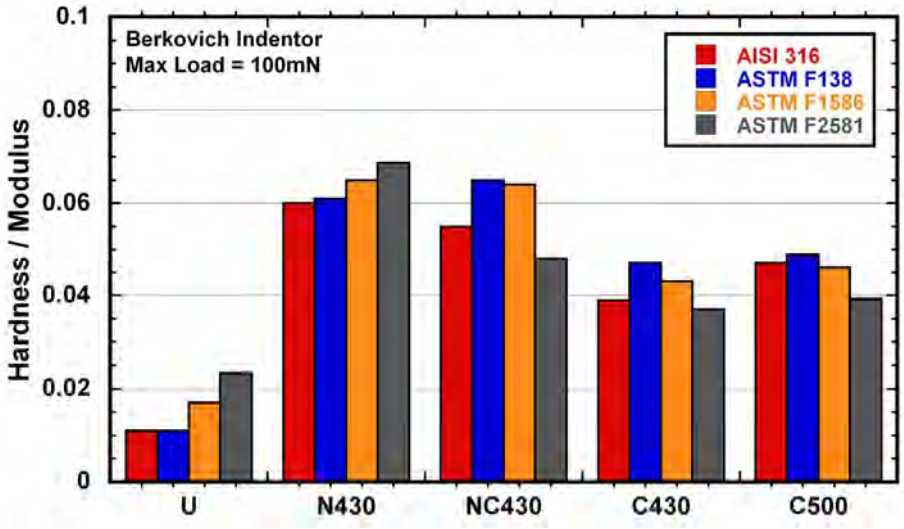

Figure 5-2 Ratio of hardness and modulus (H/E) of AISI 316, ASTM F138, ASTM F1586 and ASTM F2581 in the: untreated (U); nitrided at 430°C (N430); carbonitrided at 430°C (NC430); carburised at 430°C (C430); and carburised at 500°C (C500) condition

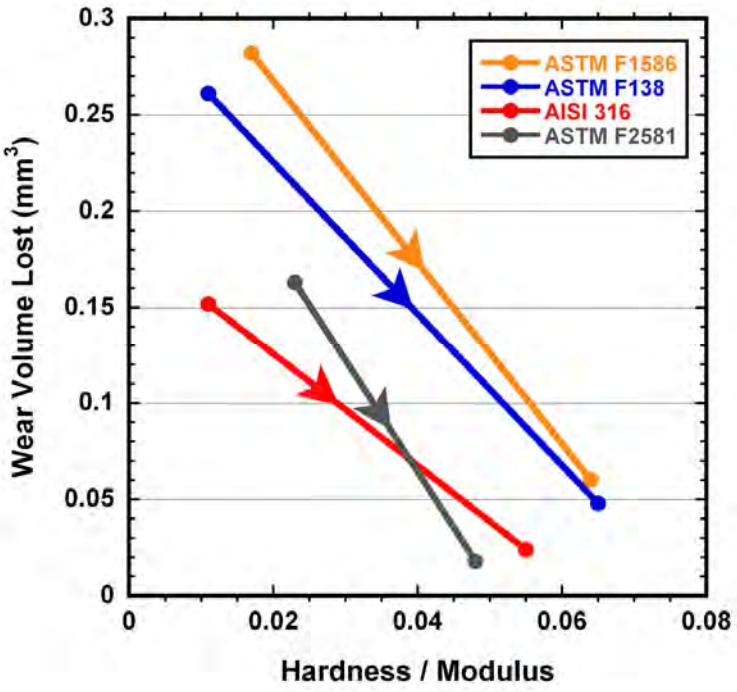

Figure 5-3 Correlation plot of H/E (ratio of hardness and modulus) with wear volume lost during "dry" reciprocating wear for untreated and carbonitrided at 430°C stainless steels used throughout this study.

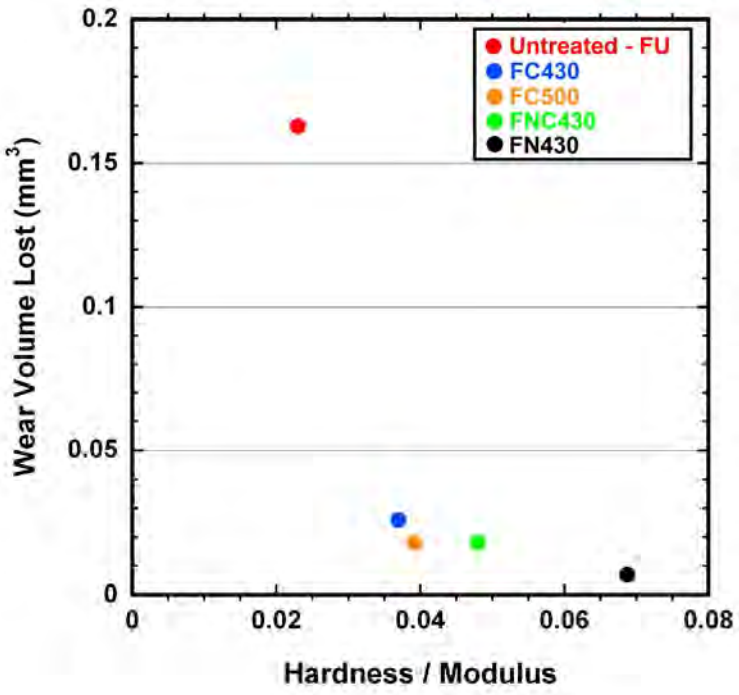

Figure 5-4 Correlation plot of H/E (ratio of hardness and modulus) with wear volume lost during "dry" reciprocating wear for untreated and treated ASTM F2581

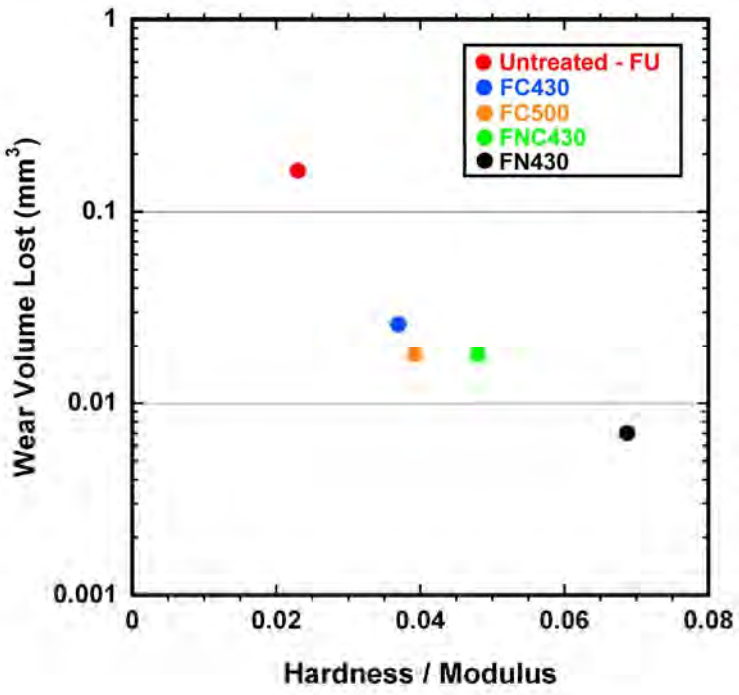

Figure 5-4 Correlation plot of H/E (ratio of hardness and modulus) with wear volume lost (log scale) during "dry" reciprocating wear for untreated and treated ASTM F2581

Chapter IX
Appendix

A-1 Calculation of the Difference in Nitrogen Species

Calculation of the difference of nitrogen species in a depth of 10μm inside ASTM F138 and ASTM F1586:

The nitrogen alloying content of ASTM F1586 from Table 3-4 is of 0.39 wt% whilst that of ASTM F138 is of 0.084 wt%. The density of both alloys is going to be taken as $8gcm^{-3}$.

Therefore utilising equation 3-1:

Difference in nitrogen species in 10μm = $0.01\times (0.39-0.084) \times 10 \times 8 = 0.2448gm^{-2}$

A-2 Calculation of the Contact Pressure and Area Radius

Example calculation: of the contact pressure and the contact area that occur throughout the pin-on-disc test. The calculations for the reciprocating wear test follow using the according variables.

Data can be obtained from Table A-8 and Table 3-5

Radius of sphere counterface (R): 4mm
Load (P): 10N
Young's Modulus of Austenitic Stainless Steel Disc (E_D): 220GPa
Young's Modulus of Tungsten Carbide Sphere (E_B): 600GPa
Poisson Ratio of Austenitic Stainless Steel Disc (υ_D): 0.3
Poisson Ratio of Tungsten Carbide Sphere (υ_D): 0.22

Substituting the values in Equations A-1

$$E_* = \frac{1}{\frac{1-\nu_D^2}{E_D} + \frac{1-\nu_B}{E_B}} \qquad \text{(A-1)}$$

E_* = 174GPa

Substituting the values in Equations A-2

$$\sigma = \frac{1}{\pi}\left(\frac{6E_*^2 P}{R^2}\right)^{1/3} \qquad \text{(A-2)}$$

Contact Pressure (σ) =1.55GPa

Substituting the values in Equations A-3

$$a = \left(\frac{3RP}{4E_*}\right)^{1/3} \qquad \text{(A-3)}$$

Contact Area Radius (a) = 0.06mm

A-3 Calculation of d-spacing from TEM

The camera constant used (Lλ) is 1.25nm. The shortest distance spot for nitrogen S-phase (R) is 5.7mm. According to equation A-4

$$d = \frac{L\lambda}{R} \qquad \text{(A-4)}$$

Therefore the d-spacing (d) = 0.219nm

This is then repeated for the other spots

A-4 Tables

Table A-1 Crystal Structure and lattice parameters of precipitates found

	PDF No	Name	Crystal System	a (Å)	b (Å)	c (Å)	Alpha (°)	Beta (°)	Gamma (°)	Volume of cell	Z
Fe_3C	035-0772	Cementite	Orthorombic	5.091	6.7434	4.526	90	90	90	155.38	4
Fe_5C_2	036-1248	Hagg Carbide	Monoclinic	11.563	4.573	5.058	90	97.7	90	265.04	4
Mn_3N_2	001-1158	Manganese Nitride	Tetragonal	2.966	2.966	6.471	103.25	103.25	90	107.70	2
Cr_2N	035-0803	Chromium Nitride	Hexagonal	4.484	4.811	4.811	120	90	90	89.89	3
$Cr_{23}C_6$	014-0407	Chromium Carbide	Cubic	10.638	10.638	10.638	90	90	90	1203.87	4
AISI 304	033-0397	Chromium Iron Nickel	Cubic	3.5911	3.5911	3.5911	90	90	90	46.31	4

Table A-2 Fe_5C_2 - Hagg Carbide (036-1248)

h	k	l	d [Å]	2θ
0	0	2	2.5063	35.799
2	0	-2	2.41816	37.15
0	2	0	2.28648	39.375
4	0	-2	2.0253	44.709
6	0	0	1.190972	47.576

Table A-3 Fe_3C - Cementite (035-0772)

h	k	l	d [Å]	2θ
1	2	1	2.38818	37.634
2	1	0	2.38147	37.744
0	0	2	2.26311	39.799
2	1	1	2.10737	42.88
1	0	2	2.06777	43.743
2	2	0	2.0313	44.57
0	3	1	2.01319	44.993

Table A-4 Mn_3N_2 - Manganese Nitride (001-1158)

h	k	l	d [Å]	2θ
1	0	3	2.4	37.44
1	1	0	2.1	43.04
0	0	6	2.02	44.83
2	0	0	1.48	62.72
2	0	2	1.45	64.17
2	1	3	1.26	75.37
0	0	10	1.22	78.3
2	0	6	1.2	79.86

Table A-5 Cr_2N - Chromium Nitride (035-0803)

h	K	l	d [Å]	2θ
1	1	0	2.40568	37.35
1	1	1	2.12005	42.61
2	0	0	2.08322	43.4
2	0	1	1.88878	48.13
1	1	2	1.64046	56.01
2	2	1	1.16193	83.04
2	2	2	1.05999	93.21

Table A-6 $Cr_{23}C_6$ - Chromium Carbide (035-0783)

h	k	l	d [Å]	2θ
4	2	2	2.17615	41.461
5	1	1	2.05199	44.097
6	0	0	1.77666	51.388

Table A-7 AISI 304 (033-0397)

h	k	l	d [Å]	2θ
1	1	1	2.07500	45.583
2	0	0	1.79610	50.792
2	2	0	1.26970	74.699
3	1	1	1.08280	90.697
2	2	2	1.03680	95.968

Table A-8 Modulus and Poisson ratio of materials used for tribological tests

Material	Modulus, E (GPa)	Poisson ratio, ν
Stainless Steel	220	0.3
Cobalt-Chromium	230	0.3
Tungsten Carbide	600	0.22

Values obtained from data sheets of supplier

A-5 Figures

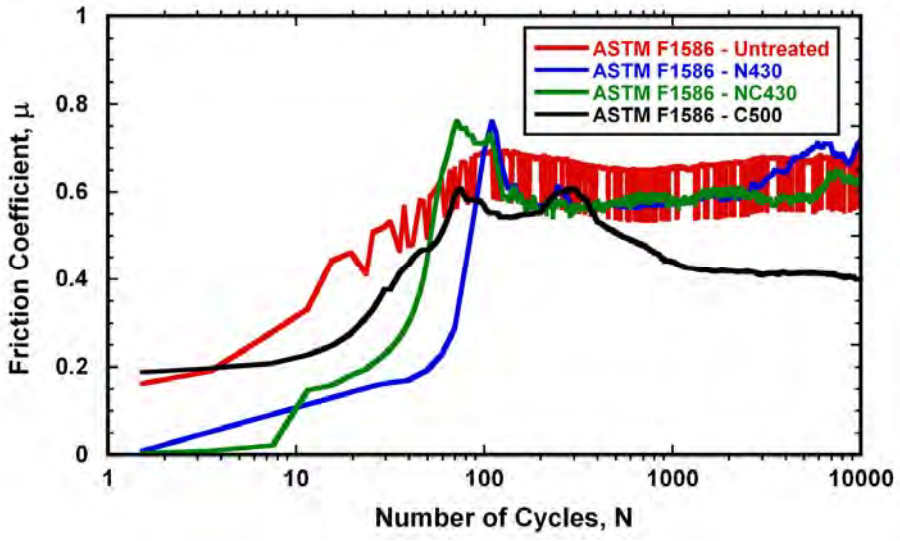

(a) 10000 cycles

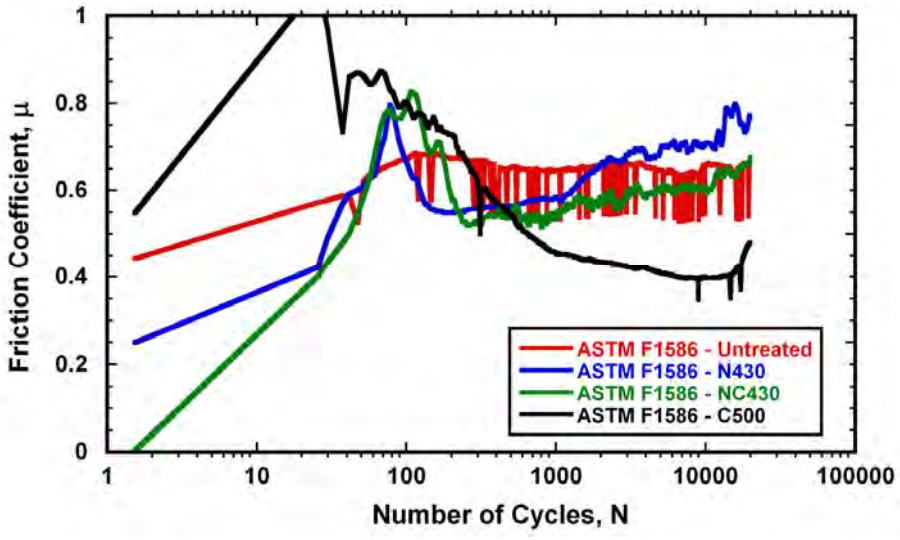

(b) 20000 cycles

Figure A-1 Friction coefficient versus number of cycles plot during fretting-wear of treated and untreated ASTM F1586 in Ringer's solution.

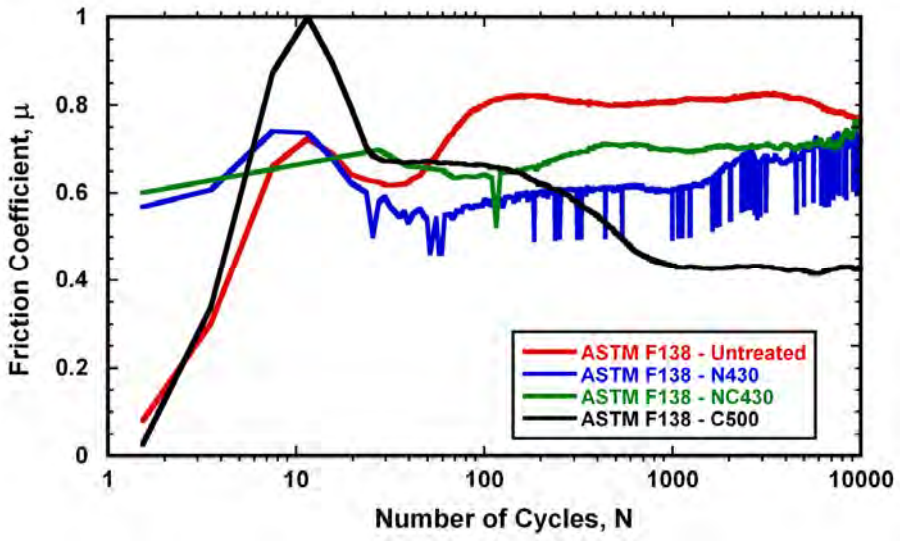

(a) 10000 cycles

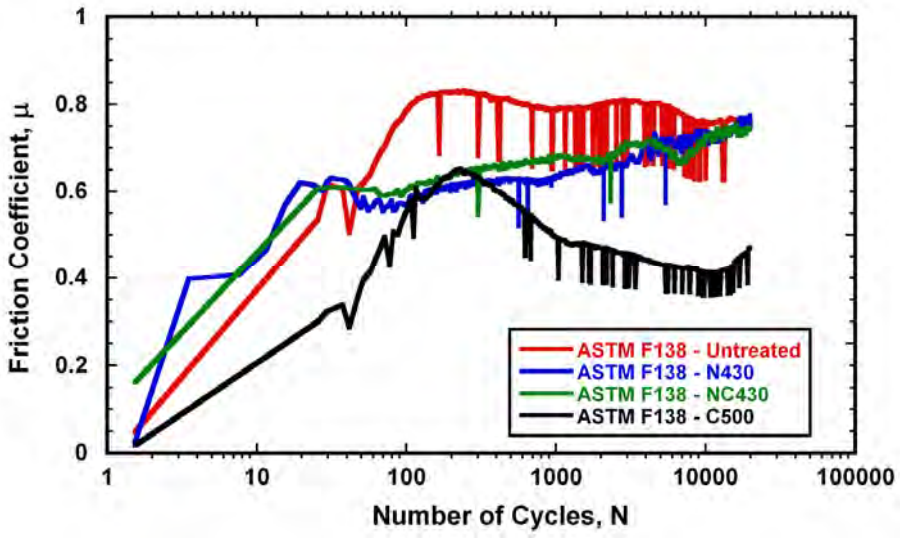

(b) 20000 cycles

Figure A-2 Friction coefficient versus number of cycles plot during fretting-wear of treated and untreated ASTM F138 in Ringer's solution.

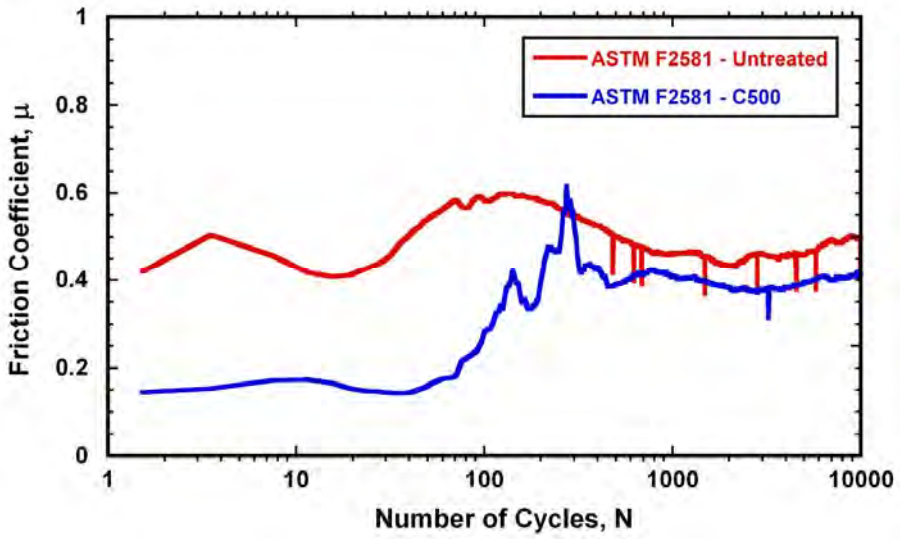

(a) 10000 cycles

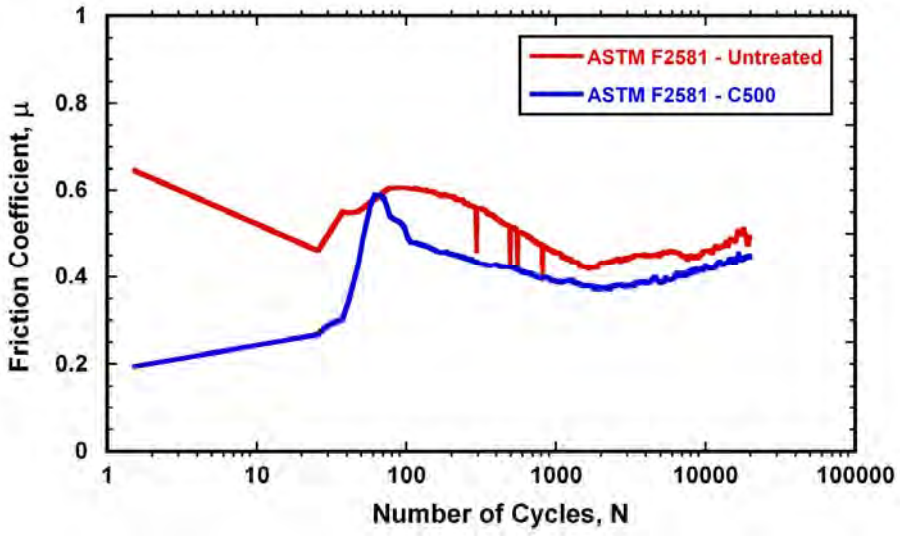

(b) 20000 cycles

Figure A-3 Friction coefficient versus number of cycles plot during fretting-wear of 500°C and untreated ASTM F2581 in Ringer's solution.